ADAPTIVE-OPTIC APPROACH TO MITIGATING AERO-OPTIC DISTURBANCES FOR A FORCED SHEAR LAYER

A Dissertation

Submitted to the Graduate School

of the University of Notre Dame

in Partial Fulfillment of the Requirements

for the Degree of

Doctor of Philosophy

by

Alice M. Nightingale

_____

Eric J. Jumper, Co-Director

_____

Bill Goodwine, Co-Director

Graduate Program in Aerospace and Mechanical Engineering

Notre Dame, Indiana

December 2010

ADAPTIVE-OPTIC APPROACH TO MITIGATING AERO-OPTIC DISTURBANCES FOR A FORCED SHEAR LAYER

Abstract

by

Alice M. Nightingale

Non-uniform, variable-density fields, resulting from compressibility effects in turbulent flows, are the source of aero-optical distortions which cause significant reductions in optical system performance. As a laser beam transverses through an optically active medium, containing index-of-refraction variations, several optical phenomena occur including beam wander, image distortion, and beam defocus. When encountering a variation in the index field, light waves refract causing an otherwise planar wavefront of a laser beam to become aberrated, contributing to the adverse effects mentioned above. Adaptive-Optics (AO) is a technique used to correct for such spatially and temporally varying aberrations on an optical beam by applying a conjugate waveform correction prior to the beams transmission through the flow. Conventional AO systems are bandwidth limited by real-time processing issues and wavefront sensor limitations.

Therefore, an alternative to the conventional AO approach has been proposed, developed and evaluated with the goal of overcoming such bandwidth limitations.

The alternative AO system, presented throughout this document, consists of two main features; feed-forward flow control and a phase-locked-loop AO control strategy. Initially irregular, unpredictable large-scale structures within a shear layer are regularized using flow control. Subsequently, the resulting optical wavefront, and corresponding optical signal, emerging from the regularized flow becomes more periodic and predictable effectively reducing the bandwidth necessary to make real-time corrections. A phase-lock-loop controller is then used to perform real-time corrections. Wavefront corrections are estimated based upon the regularized flow, while two small aperture laser beams provide a non-intrusive means of acquiring amplitude and phase error measurements. The phase-lock-loop controller uses these signals as feedback to synchronize the deformable mirror's waveform to that of the shear layer by adjusting its amplitude and phase. A third-order analog phase-lock-loop controller has been designed and a prototype board assembled; the higher order controller was designed to accommodate for any step and ramp changes in phase. The control system was assessed and validated through numerical simulations. The prototype controller was then constructed and several experimental tests were run using a function generator signal as the input. The frequency and phase of the input signal was varied throughout the testing process and the phase-lock-loop controller was able to successfully synchronize its output signal with the changing sinusoidal input. This work represents a key step in the successful development of an automated AO controller capable of applying real-time corrections to an optical beam for high-speed aero-optic applications.

This work is dedicated with love to my family. To my best friend and husband, Jason, whose patience, love and continual support has guided me through this challenging journey. Your courage to follow your dreams and the faith you place in our Lord is a true inspiration. I could not have done this without you! To our children, Ruthie and Noah, whose smiling faces and unconditional love is a constant reminder of God's love and the true blessings in life. It is also dedicated to my parents, Paul and Sherry Duesing, and to Jason's parents, Ron and Debbi Nightingale, for whose love, support, and encouragement I am most grateful.

CONTENTS

FIGURES

TABLES

NOMENCLATURE

Symbol	Description	Units
A	amplitude	
a	aperture radius	
C_δ	vorticity thickness constant	
C_Λ	optical coherence length constant	
c_p	specific heat at constant pressure	J/kg/K
d	forcing displacement	
f	optical frequency	Hz
f_f	forcing frequency	Hz
f_n	optical natural frequency	Hz
g	acceleration of gravity	m/s^2
I	irradiance	W/sr
I_o	maximum achievable on-target irradiance	W/sr
i	imaginary number	
J_1	first order Bessel function	
K_{GD}	Gladstone-Dale constant	m^3/kg
k	wave number of the optical wave	m^{-1}
n	index-of-refraction	
Ma	Mach number	

OPL	Optical Path Length	μm
OPD	Optical Path Difference	μm
p	pressure	N/m^2
p_∞	free stream pressure	N/m^2
R	ratio of upper to lower stream velocities	
R_0	distance between source and aperture plane	m
R_0'	distance between aperture and observation planes	m
r	radial position from vortex center	m
	radial position of irradiance pattern in observation plane	m
r'	radial distance from beam center to aperture plane	m
$r_{Singular}$	critical radius	
SR	Strehl ratio	
s	direction along the path a light ray travels	
	ratio of lower to upper stream densities	
T	temperature	K
T_{ad}	adiabatic temperature	K
t	time	s
t_r	transmission function of the optical aperture	
U_c	convective velocity	m/s
U_L	upper stream velocity	m/s
U_U	upper stream velocity	m/s
u	streamwise velocity	m/s
v	cross-stream velocity	m/s

x	streamwise coordinate	
	horizontal location within observation plane	
x'	horizontal location in aperture plane	
y	cross-stream coordinate	
z	spanwise coordinate	
	perpendicular location within observation plane	
z'	perpendicular location in aperture plane	
Γ	vortex strength	
Λ_n	optical coherence length	m
γ	specific heat ratio	
δ_i	initial half shear layer thickness	m
δ_ω	vorticity thickness	m
θ	jitter angle	rad
	momentum thickness	m
λ	wavelength	μm
ν	propagation velocity of individual spherical wavelet	m/s
ρ	density	kg/m^3
τ	time delay between Malley probe beams	s
ϕ	wavefront's phase shift	rad
φ	aberration function of OPD in the aperture	rad
ω	wavefront's angular frequency	rad/s

ACKNOWLEDGMENTS

I would like to express my deepest appreciation to all the people, departments and organizations that made this work possible. To my co-advisors, Dr. Eric J. Jumper and Dr. Bill Goodwine, thank you for allowing me to work on this project, for believing in me, and for all your invaluable help you provided throughout the process. To Dr. Michael Lemmon for all the guidance you so willingly and generously provided. To Stanislav Gordeyev, Meng Wang, Dave Cavalieri, Mike Zenk, Mark Rennie, Greg Brownell, and Joel Preston, thank you for your assistance during my graduate career. To Marilyn Walker, Nancy Davis, Nancy O'Connor, Evelyn Addington, Judy Kenna, Donna Fecher, and the entire AME department faculty and staff, thank you for the resources and services you provided on a regular basis. To the Aero-optics group members and my fellow graduate students, thanks for all your help and for your friendships. A special thanks to friends Carolyn Baughman, Tricia Barry, and Andrea Gregory for your help caring for Ruth and Noah while I worked on this dissertation. And finally, thank you to the organizations that sponsored this research: the Air Force Office of Scientific Research, Air Force Research Laboratory's Directed Energy and Air Vehicles Directorates, Air Force Material Command, USAF, under Grant Numbers FA9620-03-1-0019 and FA9550-06-1-0160, and to the Directed Energy Professional Society for its support.

CHAPTER 1:

INTRODUCTION

1.1. Fluid-Optics Overview

Fluctuations in a medium's index of refraction through which light is propagated are the cause of several observable phenomena. In the case of air, index of refraction is, for the most part, directly related to the air's density. The appearance of water on dry pavement is a common example of a mirage that occurs on hot or humid summer days. As light rays encounter pockets of air density gradients, due to hot air near the pavement's surface, they are refracted upward creating an image of the sky that appears to originate from the ground. Another familiar example is that of "twinkling" stars. This occurs when light from stars pass through rapidly varying density fluctuations in the Earth's atmosphere caused primarily by temperature variations. This atmospheric turbulence acts like a collection of lenses redirecting or refracting the light in a random time-varying manner producing the twinkling phenomenon, technically known as stellar scintillation [1, 2].

Evidence of atmospheric fluctuations not only occurs in the twinkling of stars, but also in projected optical signals. Optical systems require the propagation of optical signals through turbulent flow fields such as atmospheric turbulence and aero-optic disturbances. Atmospheric effects are the result of small amplitude aberrations which

amass over long propagation distances. On the other hand, aero-optic effects are caused by inhomogeneities in air density within a near-field turbulent medium including boundary layers, wakes, free shear layers, *etc.* These turbulent flows may be viewed as additive phase aberrations advancing and/or retarding points along the wavefront, defined as a line of constant phase. The subsequently distorted optical wavefront and its real-time correction have been the subject of study for optical designers throughout the past several hundred years.

1.1.1. Brief History of Adaptive-Optics

With the dawn of telescopic imaging in the early 1600's, the need for real-time imaging improvements began. As early as 1704, Isaac Newton acknowledged the negative effect turbulence has on imaging systems writing,

> "If the theory of making telescopes could at length be fully brought into practice, yet there would be certain bounds beyond which telescopes could not perform. For the air through which we look upon the stars is in perpetual tremor" [1, 2].

Throughout the next few hundred years, several discoveries were made dealing with the propagation and behavior of light: the area of study known as *optics*. In 1953, Horace Babcock, an American astronomer, introduced the concept of adaptive optics for the first time [1, 2]. Adaptive-optics (AO) is "the control of light in a real-time closed-loop fashion" [2]. It is the technique of applying the conjugate waveform to the optical wavefront prior to its transmission through an aberrating medium, effectively restoring a planar wavefront. Although his idea could not be implemented at that time due to a lack of available technology, the concept would serve as a springboard for future development of real-time wavefront correction control systems. In the early 1970's technological

advancements made it feasible to begin developing feedback control systems used to perform real-time imaging corrections for low frequency disturbances. During the next several years a considerable amount of research was dedicated to advancing the area of adaptive optics. Today the use of AO systems is common place in correcting telescopic images and reducing atmospheric aberrations on aircraft mounted optical systems [1]; however, there is still an ever-present need for further advancements in the case of high speed aero-optic disturbances.

The adaptive-optic process consists of three main components or steps within the control loop; sensing the aberration, reconstructing the appropriate correction, and applying the conjugate correction to the optical beam prior to transmission. In order for this principle to work effectively, the accuracy of each conjugate correction is extremely important. An error in the conjugate correction often produces an output optical signal whose quality is worse than its input. [2] For example, let us assume that at time, t_0, the AO control process begins and the aberration present at that point in time is as shown in Fig. 1.1 (A). If a perfect conjugate correction were applied (shown in Fig. 1.1 (B)), the emerging wavefront will become planar (Fig. 1.1 (C)). This represents an ideal optical correction in which the emerging planar wavefront would produce a perfectly focused laser beam.

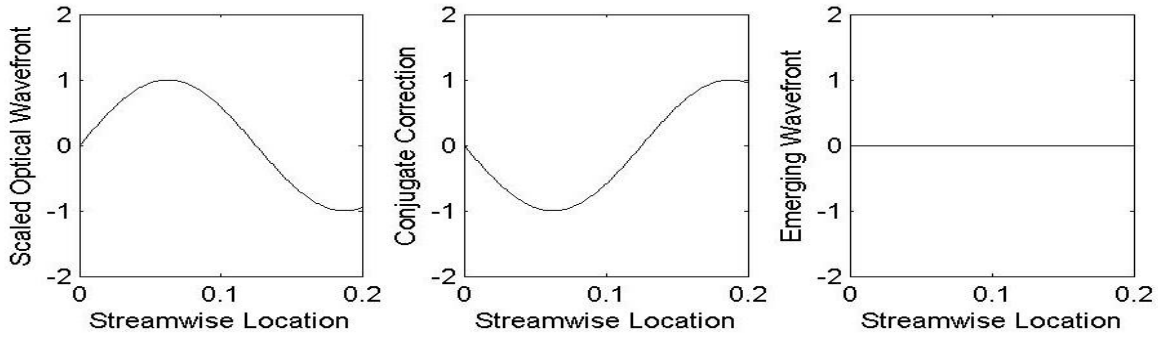

Figure 1.1: (A). Optical aberration caused by a flow field at time t_0 (B). Perfect conjugate correction for the aberration shown in Fig. 1.1 (A) (C). Emerging planar optical wavefront given the perfect conjugate correction shown in Fig. 1.1 (B) applied to the wavefront shown in Fig. 1.1 (A).

However, the AO control loop does not happen instantaneously. Rather, sensing, reconstructing and applying the conjugate correction takes a certain amount of time, Δt, during which the aberrating flow field is continually changing. As the speed or frequency at which the aberrations within the flow field are moving and changing increases so does the discrepancy between the applied correction and the necessary correction after Δt. Once the frequency of aberrations exceeds a certain threshold, described in more detail in Chapter 2, AO corrections become ineffective and in fact destructive. Referring back to the example shown in Figs. 1.1, if the aberrations are occurring too fast for the controller, the conjugate correction will have some amount of associated phase lag. For example, the actual optical aberration present after Δt may look something like the wavefront shown in Fig. 1.2 (A) where the conjugate correction happens to be 180º out of phase. If the conjugate correction shown in Fig. 1.2 (B) was applied to the actual wavefront shown in Fig. 1.2 (A), the emerging wavefront would become even more aberrated (Fig. 1.2 (C)). Thus, system latencies alone result in

significant bandwidth limitations. And for high speed aero-optic flows, time delays associated with current AO control systems make such corrections virtually impossible.

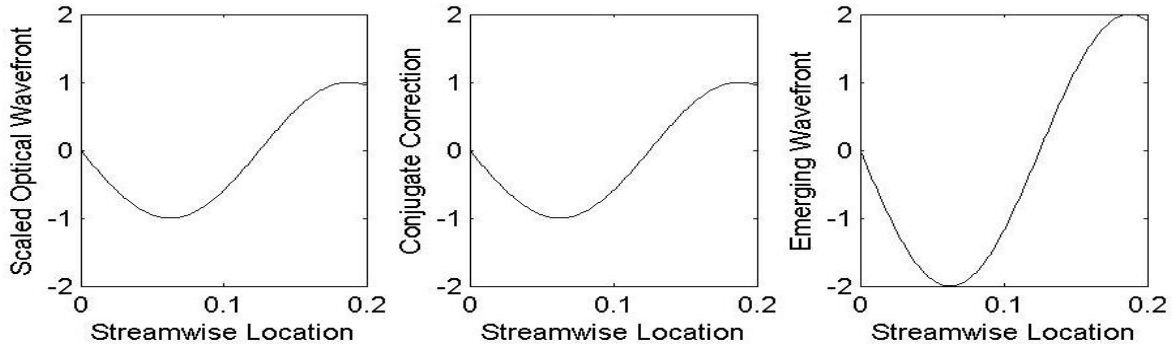

Figure 1.2: (A). Actual optical aberration caused by a high speed flow field after Δt (B). Conjugate correction constructed by an AO control system whose process began at time t_0 (C). Emerging optical wavefront given the conjugate correction shown in Fig. 1.2 (B) is applied to the wavefront shown in Fig. 1.2 (A).

1.1.2. Recent Advancements in Aero-Optics

Aero-optics refers to the study of wavefront distortions caused by index-of-refraction fluctuations in the near field. The near field is defined as the region where the propagation length is on the same order as the aperture size; this refers to the flow field near the exit pupil of an outgoing beam or the receiving aperture of an imaging system [3]. Due to the wavelength dependence of a beams maximum irradiance, aero-optic effects proved inconsequential until recently with the movement towards visible-wavelength laser systems. For an unaberrated beam with a given aperture (diameter), laser power, and propagation distance, the far-field irradiance increases with decreasing wavelength as shown in Figure 1.3 (A). This relationship has promoted the use of shorter wavelength lasers which in turn has caused the aero-optic problem to become even more substantial. As shown in Figure 1.3 (B), a given aero-optic disturbance that produces

95% maximum irradiance for a wavelength of 10.6 microns reduces to less than 10% for wavelengths below ~ 1.5 microns [3].

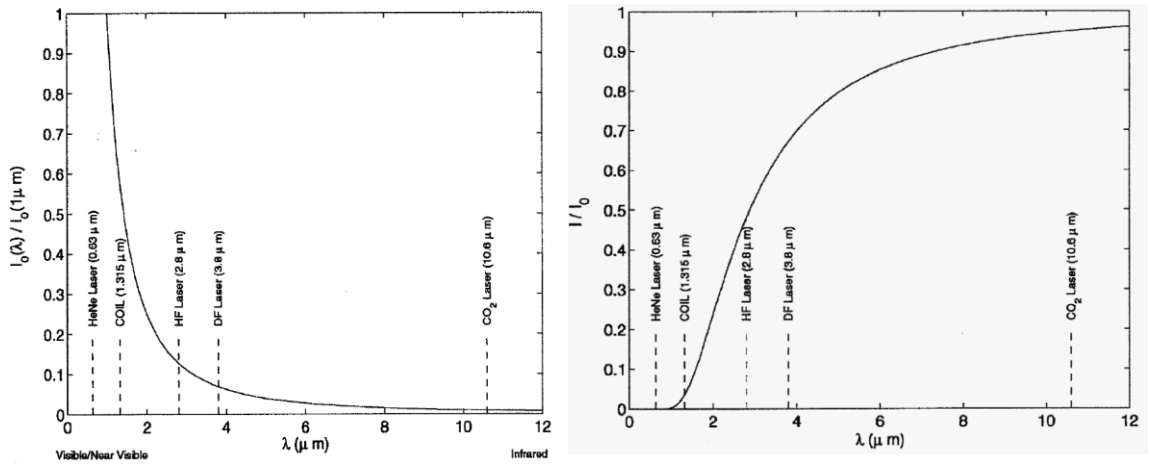

Figure 1.3: (A). Peak irradiance of diffraction limited spot versus laser wavelength (B). Ratio of target irradiance to maximum achievable irradiance (system performance) versus laser wavelength [3].

With the increased use of shorter wavelength lasers over the past decade, it has become imperative to perform real-time corrections of aero-optic disturbances. Current AO systems successively correct for low frequency disturbances present in atmospheric turbulence, however these systems become bandwidth limited as the frequency increases. In the case of aero-optic disturbances, frequencies commonly exceed 1 kHz requiring wavefront capture rates of at least 100 kHz due to stability and update criteria discussed in Section 2.2.2. Such bandwidth requirements exceed the ability of available technology. This research seeks to overcome these limitations by proposing an alternative approach to the conventional AO system.

1.2. Motivation

Optical systems, including free-space communication platforms and airborne laser weapon systems, transmit and receive optical signals that must propagate through variable density flow fields which adversely affect system performance. Various types of turbulence may be encountered by the optical signal within the systems field of regard including turbulent boundary layers, wakes, and free shear layers. Due to the high frequency content and unpredictable nature of a free shear layer, this form of turbulence presents a significant problem with detrimental performance implications. Figure 1.4 shows an example of a variable-density shear layer forming as the air separates across an airborne turret [4].

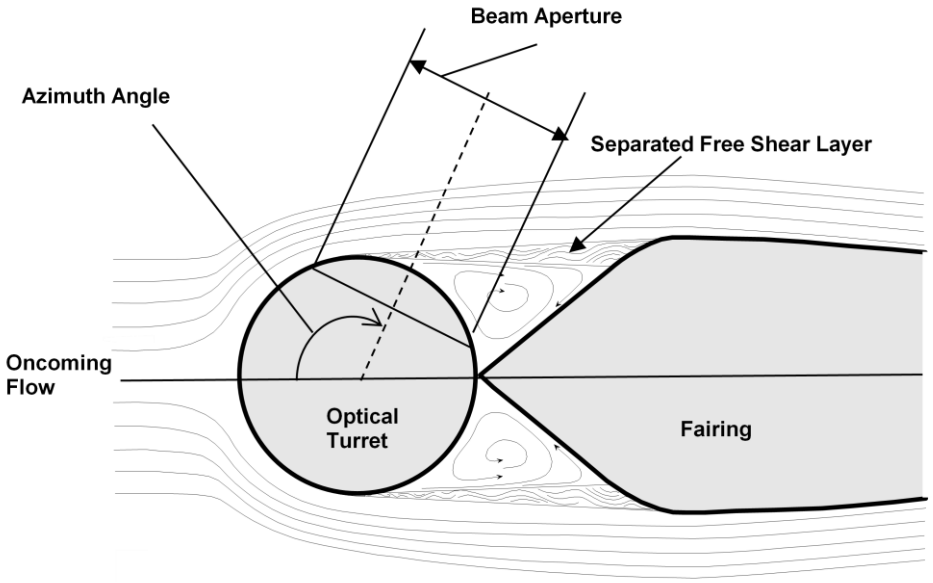

Figure 1.4: Shear layer formed over a turret/fairing combination.

As the flow goes unstable and begins to roll over itself and downward into the cavity between the turret and fairing combination, a recirculation region is formed creating a lower speed flow compared with the upper free stream velocity. This

difference in velocity causes the flow to roll-up forming vortical structures which grow as they convect downstream creating a separated free shear layer (see Figure 1.4). In flight conditions where the free stream Mach number routinely exceeds 0.6 [3], the aerodynamic flows contain temporal and spatial frequencies more than an order of magnitude greater than the atmospheric disturbances that are currently being corrected using AO systems. When the optical signal encounters this region of flow significant beam degradation occurs.

As the azimuth angle, defined as the angle between the centerline of the oncoming flow and the centerline of the outgoing beam (refer to Fig. 1.4), increases the quality of the beam and consequently the performance of an optical system making use of the signal greatly reduces. This is due primarily to the separated free shear layer flow. In order to maximize the system's utility it is important to maintain a large field of regard, defined as the range of points in space that the laser beam can be successfully propagated. Therefore, it becomes necessary to perform AO corrections for large azimuth angles thus improving the system's field of regard.

1.3. Research Objective

The overall goal of this research is to design, simulate, and construct a prototype of an alternative AO controller that may be used to perform real-time corrections to an aberrating optical wavefront emerging from a regularized free shear layer. Due to bandwidth limitations faced by current AO systems and technology, an alternative approach to correcting high-speed optical aberrations must be explored. Numerical

simulations were first conducted to investigate the optical nature of a free shear layer flow. During this process, a method of optically characterizing the flow was proposed which provided extremely valuable insight into effectively "controlling" the flow's large-scale structures. Numerical simulations were verified experimentally, demonstrating the feasibility of using flow control to regularize a high-speed shear layer. Regularized large-scale coherent structures produce emerging optical signals that are much more periodic, thus providing *a priori* knowledge of the flow which can be used to reduce bandwidth requirements placed on the AO control strategy. The periodic nature of an optical signal propagating through the regularized flow may now be used as a reference signal within a phase-lock-loop controller. The combination of flow control used to regularize the shear layer's large-scale structures and a phase-lock-loop feedback controller used to apply conjugate corrections to a laser beam propagating through the flow, will be the primary focus of this dissertation and the means to achieving our research objective.

CHAPTER 2:

BACKGROUND

2.1 Optics

Since the early 1990s, the optical characteristics of free shear layers have been the subject of investigation. The cause of the optical aberrations in shear layers was found to be the large scale structures that naturally "roll up." More specifically, it was found that the radial pressure gradients (and the associated density deficit) required to support the curvature of the structure along with the high pressure/density regions between coherent structures substantiate the cause for a large part of the optical aberrations. Such large scale turbulent structures, loosely referred to as compressibility effects, cause variations in the flow field density [5]. This in turn produces a variable index-of-refraction field, n, which is related to density, ρ, through the Gladstone Dale constant, K_{GD}, by

$$n(x,y,t) = 1 + K_{GD}\rho(x,y,t)\,. \tag{2.1}$$

Such variations in the index-of-refraction field impose aberrations on an otherwise planar optical wavefront propagating through the flow. The path that a ray follows through a variable flow field as well as the time taken to transverse that path is dependent upon the index-of-refraction field. When a beam encounters fluctuations in index-of-refraction, portions of the optical wavefront become advanced or retarded, deviating the wavefront from its otherwise planar form. These distortions are commonly quantified using optical

path length (OPL) and optical path difference (OPD). *OPL(t,x)* is defined as the integral through a variable index-of-refraction field, *n(t,x,y)*, with respect to the ray's path of travel. Due to small deviations in the ray's path from the initial direction of propagation, *OPL(t,x)* can be approximated by integrating along the axis corresponding to the initial direction of propagation;

$$\mathrm{OPL}(t, x) = \int_{\mathrm{ray}} n(t, x, y)ds \approx \int_{y_1}^{y_2} n(t, x, y)dy. \tag{2.2}$$

Removing the spatial mean ($\overline{OPL(t_o)}$) at each time step produces

$$\mathrm{OPD}(t_o, x) = \mathrm{OPL}(t_o, x) - \overline{\mathrm{OPL}}(t_o) \tag{2.3}$$

where *OPD(t,x)* represents the conjugate of the optical wavefront defined as a locus of points along which the beam's phase is constant [6].

According to Huygen's Principle, a wavefront can be decomposed into several secondary spherical wavelets, with radius $v\Delta t$ (where v is the wave's propagation velocity), radiating from the locus of points defining the initial wavefront. At some later time, $t + \Delta t$, a new wavefront can be defined as the envelope of these secondary wavelets revealing that a wavefront will propagate in a direction normal to itself. Concomitantly, if a small-aperture laser beam is directed through an aberrating flow field, it will emerge normal to the outgoing aberrated wavefront at an angle, $\theta(t,x)$, defined by

$$\theta(t, x) = \arctan\left(-\frac{d\,OPD(t, x)}{dx}\right). \tag{2.4}$$

When a small-aperture laser beam is projected through an aberrating flow field, $\theta(t,x)$ varies in time producing a series of angles referred to as beam "jitter" [6]. These small-

aperture jitter signals play a significant role in this research; they are used to characterize a shear layer's optical properties (Section 3.1.3) and provide a non-intrusive means of acquiring feedback information for the proposed alternative AO controller (Chapter 4).

Far-field intensity pattern, or irradiance pattern, is another important term used throughout this dissertation. Such visible patterns provide a useful means of evaluating a system's response. Irradiance patterns, defined as the constructive and destructive interference of light waves, may be determined from *OPD(t,x)* using Fourier optics. Fraunhofer diffraction, also known as far-field diffraction, is the phenomenon that occurs when spherical waves become essentially planar at the point of observation. This arises when the source and observation point are sufficiently far apart or through the use of lenses creating a planar wavefront at the observation plane. In each case, the following Fraunhofer approximation becomes valid for calculating the peak electric field [6],

$$\widetilde{E}(x,z) = \frac{i}{\lambda} A \frac{e^{-ik(R_0+R_0')}}{R_0 R_0'} \int\int_{-\infty}^{\infty} t_r(x',z') e^{\frac{ik}{R_0'}(xx'+zz')-ik\varphi(x',z')} dx'dz', \qquad (2.5)$$

where A is the amplitude of the incident wave, λ is the wavelength, k is the wave number, R_0 defines the distance between the source and the aperture, R_0' is the distance between the aperture and point of observation, $t_r(x',z')$ is the transmission function, $\varphi(x', z')$ is the function defining OPD (the wavefront at the aperture) and x' and z' represent a point in the aperture over which the integration is performed. The incidence of flux density, also referred to as irradiance (I), is proportional to the square of the electric fields amplitude and can therefore be determined from Eq. (2.5). In the case of a perfectly planar wavefront (i.e., no phase variations) with circular aperture, an image known as an Airy

disk is formed in the far field. As shown in Figure 2.1, a bright central lobe forms (Airy disk) with concentric rings surrounding it. These rings are due to the intensity distribution described by the following result obtained using Eq. (2.5) for far-field irradiance in polar coordinates,

$$I(r) \propto \left[\frac{2J_1(kar'/R_0')}{kar'/R_0'} \right]^2, \tag{2.6}$$

where $J_1()$ represents a Bessel function of the first-order, a represents the aperture radius, and r' is the radial distance from the beams center in the aperture plane [2, 3, 6]. Figure 2.1 was created by numerically propagating a perfectly planar wavefront through a circular aperture. The irradiance distribution shown below was normalized by dividing the resulting field by the maximum or peak intensity value.

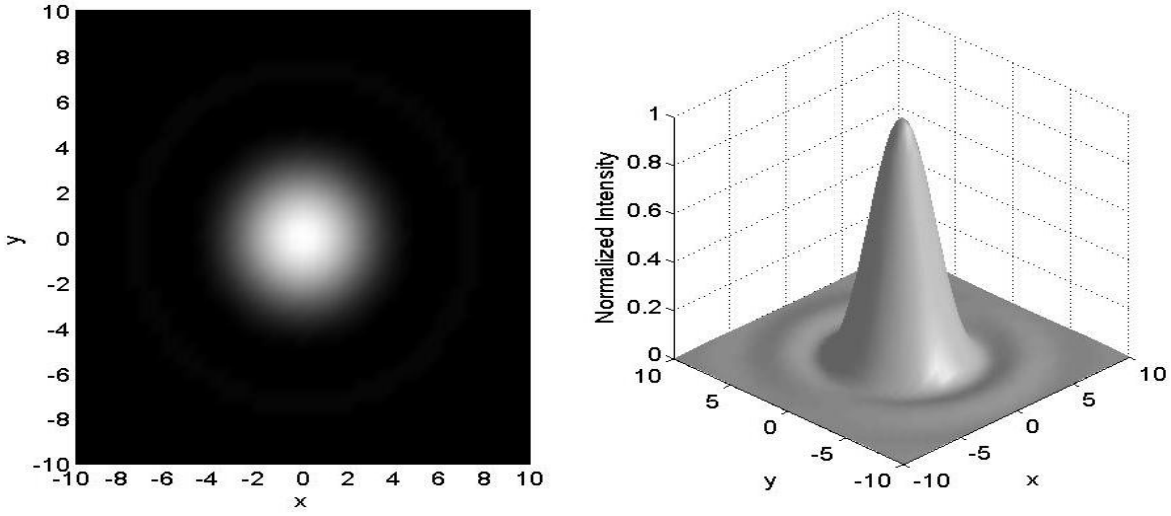

Figure 2.1: 2-D Fraunhofer diffraction pattern (Airy disk) for a planar wavefront with circular aperture (left) and a 3-D visualization of the same diffraction pattern (right).

When aberrations are imposed on a wavefront, significant degradation in image quality occurs. On-axis intensity is greatly reduced due to beam wander and beam

spreading. As the beam moves off target and/or the central diffraction spot is broken up into several smaller intensity lobes, the operation of an optical system making use of such a signal becomes severely impaired. Figure 2.2 shows an example of a far field diffraction pattern induced by a wavefront containing a plus or minus 1μm peak to peak sinusoidal aberration whose OPD_{rms} is approximately 0.7 μm. The one-dimensional sinusoidal aberration was uniformly spread in the cross-stream direction and numerically propagated through a circular aperture. The resulting intensity pattern was normalized by the maximum irradiance produced in the ideal case (i.e., planar wavefront). As shown in the figures below, the on-axis (0,0) and surrounding intensity for the aberrated wavefront in Fig. 2.2 has decreased appreciably compared to the on-axis intensity of the planar wavefront shown in Fig. 2.1. A wavelength of 600 nm was used to create the results in both Fig. 2.1 and Fig. 2.2.

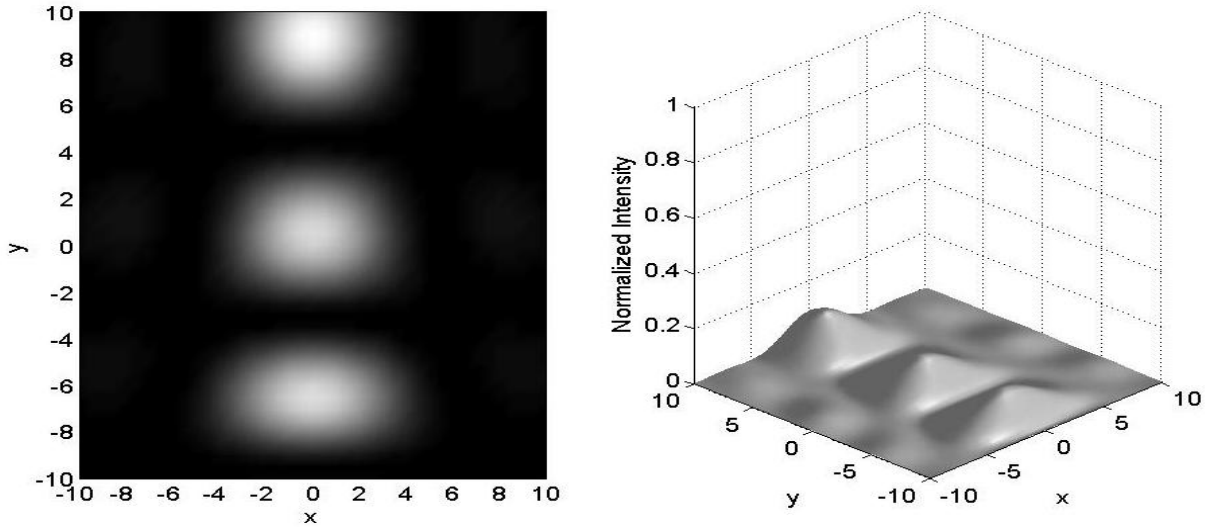

Figure 2.2: 2-D Fraunhofer diffraction pattern (Airy disk) for an aberrated wavefront with circular aperture (left) and a 3-D visualization of the same diffraction pattern (right).

The performance of an optical system is commonly characterized by this on-axis intensity. The Strehl ratio (*SR*) is defined as the ratio of actual on-axis intensity, *I*, to the maximum achievable on-axis intensity, I_o,

$$SR = \frac{I}{I_o}, \tag{2.7}$$

producing a value between zero and one, where a Strehl ratio of one represents a perfectly focused on-target beam (as shown in Fig. 2.1) [6]. The overall tilt, or average slope of the wavefront across the aperture, is typically removed prior to calculating the Strehl ratio to produce a more accurate estimation of the beam's quality [2]. In this case Strehl ratio is measured as the ratio of actual tilt-removed on-axis intensity to maximum achievable on-axis intensity, and when used will be specifically stated as such. The terms and equations described in this section will be referred to throughout the following dissertation, specifically when discussing optical performance.

2.2 Conventional Adaptive-Optic (AO) System

Systems that sense aberrations, and construct and apply the proper conjugate waveforms at regular time intervals are termed *AO systems* [2]. A conventional AO system operates in consecutive steps; the first step is to sense the aberration for which a conjugate must be constructed. Since optics is linear, this aberration can be determined by measuring the aberrated wavefront from a source propagating through the aberrating flow from either direction. For projecting systems, determining the aberration (or the remaining residual aberration after a correction has been made) at any given instant is

done by sensing the aberration from an incoming optical signal. The wavefront aberration is measured using a *WaveFront Sensor (WFS)*. Once the wavefront's figure is measured a *Conjugate Constructor (CC)*, also referred to as a "*reconstructor*," determines the distorted pattern that must be sent to a *deformable mirror (DM)*. The conjugate waveform (or some portion of it) is then sent to a DM, whose electro-mechanical characteristics, including its source of excitation (i.e., amplifiers) limit the rate at which it can be deformed. The conjugate wavefront is placed on the laser prior to its propagation through the aberrating turbulence by first reflecting it off the DM. Such AO corrections are applied to the DM at regular time intervals with the goal of reducing wavefront aberrations and consequently increasing on-axis intensity.

The conventional AO process discussed above is depicted in Fig. 2.3. Since a perfect correction is impossible due to latencies and wavefront approximations, a certain amount of error remains on the reflected beam which is directed onto the WFS. The residual error is measured and a signal sent to the CC which approximates a fraction of the error, based on system gain requirements. The wavefront correction is then applied to the DM closing the feedback loop [2]. Each component within the system possesses its own set of time delays and bandwidth constraints. In general the CC is typically much faster than the WFS and, at present, does not form the bandwidth-limiting step. The following section describes some bandwidth constraints and limitations associated with this conventional AO approach in more detail; this includes update rates, time delays, slew rates, and more.

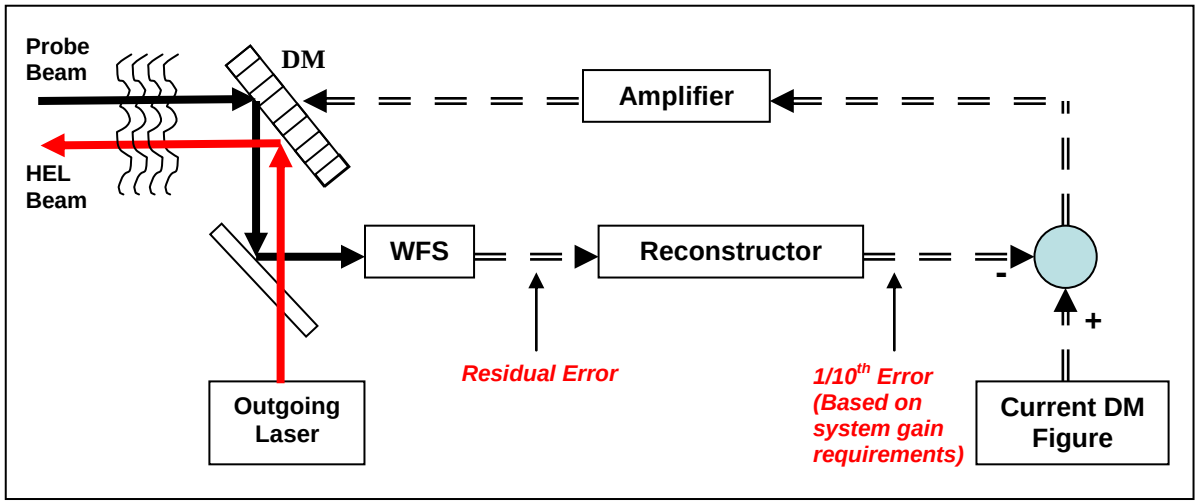

Figure 2.3: Closed-loop depiction of the conventional AO system, consisting of a WFS, reconstructor (CC), and DM.

2.3 Limitations of the Conventional AO Approach

As mentioned above, each component of an AO system exhibits certain bandwidth limitations restricting the systems capabilities and effectiveness in high speed applications. Such limitations become quite significant in the case of aero-optic disturbances where frequencies commonly exceed 1 kHz. Given the current technology, the WFS commonly creates the bottleneck within the system; however each component also plays its own role in the overall system response characteristics. These performance limitations are due primarily to update requirements, cutoff frequency, system latency, and slew rate limitations as will be expanded upon in the following sections.

2.3.1 System Update Requirements

In the conventional AO approach, the feedback control system represents one of the bandwidth-limiting steps, or components, in the AO system. This step has been

extensively studied by Tyson [2] and others. In the end it appears that only ~ $1/10^{th}$ of the residual error can be removed per DM update (usually the clock time of the WFS) to maintain system feedback stability. In other words, typically the system gain is approximately 0.1. Given higher gain values small amounts of error in the correction signal may produce an output beam possessing even more distortion than its incoming counterpart (as shown by the example depicted in Fig. 1.2), thus resulting in system instabilities.

The aberrating flow field itself sets yet another bandwidth requirement on the AO system. As described by Tyson [2] and re-examined and affirmed specifically for aero-optic disturbances by Cicchiello and Jumper [7], an aberration must be removed approximately ten times per disturbance clearing cycle to restore 80% of its diffraction-limiting performance, equivalent to a 1 dB correction ($dB = -10\log_{10}[(\text{Corrected } OPD_{rms} / \text{Uncorrected } OPD_{rms})]$). Recall that an ideal planar wavefront produces the maximum diffraction-limiting performance (i.e., 100% or 0 dB) while a Strehl ratio of 0.8 or higher is generally desired [40]. Taken together with the system stability update requirement discussed prior, a WFS must operate approximately one hundred times faster than the flows aberrating disturbances. These two bandwidth characteristics for an AO system are summarized in Fig. 2.4 given an aberrating flow that initially reduces the Strehl ratio to less than 0.1. The horizontal axis represents the frequency at which the disturbances pass through the beams aperture and the vertical axis shows the required WFS framing rate. Three slanted lines provide a means of estimating the required WFS framing rate for a specified disturbance bandwidth given three different desired Strehl ratios: 0.8, 0.5, or 0.3.

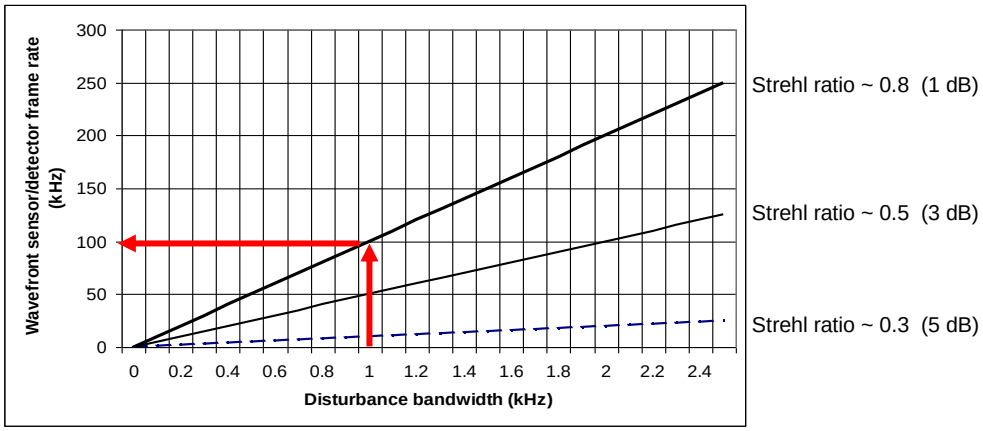

Figure 2.4: Bandwidth requirements for a wavefront sensor based on an aberrating flow that initially reduces the Strehl ratio to less than 0.1 and control system limitations for the conventional AO approach [8].

An example is shown in Fig. 2.4 according to the red arrows. It shows that for the conventional AO approach, in which an aberration has a clearing frequency through the aperture of 1 kHz, the WFS must frame at 100 kHz in real time in order to restore a Strehl ratio from 0.1 up to 0.8. The fastest real-time wavefront sensors that exist today operate at an order of magnitude lower than this. Even if a real-time wavefront sensor were available, other components in the AO system would form a barrier to correcting a 1 kHz aberration; yet the aberrations posed by a high-Mach subsonic shear layer are at least 1 kHz [3, 9, 10, 11].

2.3.2 Nonlinear Effects

Many electronic devices and components such as amplifiers exhibit nonlinear characteristics which can significantly affect both its magnitude and phase response. Two such nonlinear features are harmonic distortion and slew rate. Harmonic distortion refers to the process of harmonics being added to a signal as it passes through a device

due to nonlinear effects. The output signal being altered or distorted results in a more complicated transfer function. Here the term *slew rate* is used in its control context rather than being mistaken for the motion of a beam through the atmosphere. Slew rate is defined as the maximum rise rate of an output voltage to a step input voltage, which is the common use of this term in control theory. In other words, slew rate is the maximum rate of change that a signal can achieve placing limitations on its response characteristics. This can lead to nonlinear effects given a sinusoidal input if the slew rate, *SR*, does not meet the following condition:

$$SR > 2\pi fA, \tag{2.8}$$

where *f* refers to input frequency and *A* is the peak amplitude of the signal. Amplifiers used to transfer the conjugate correction signals to the DM actuators commonly exhibit these nonlinear characteristics and as such place certain limitations on the overall system response. Slew rate also affects the ability of a DM to form the desired conjugate correction. These last two statements will be illustrated more fully in the following two sections.

2.3.3 Conjugate Correction Requirements

In addition to the update requirements and nonlinear effects described above, there exist certain requirements on the conjugate correction itself. The AO system, or more specifically the DM, must be capable of producing a waveform correction with a minimal amount of error. Otherwise the applied correction could have a negative effect producing an output wavefront containing more distortion than was first present. The ability of the DM to generate the appropriate form or shape depends primarily on the

following three factors: the number of actuators comprising the DM, the spacing between actuators, and the slew rate (defined previously in Section 2.3.2) limit of the actuators. Section 2.4.3 refers to each of these issues when examining the constraints of Notre Dame's DM. The following section discusses the effect the limitations introduced above have on Notre Dame's AO System.

2.4 Limitations of the Conventional AO Approach

Notre Dame purchased a conventional AO system eight years prior to the writing of this dissertation. The AO system located in the Hessert laboratory at the University of Notre Dame, was developed by Xinetics and consists of two different control loops; a DM performs conjugate corrections and a tip/tilt mirror removes the average slope, or tilt, across the beam's aperture. Each feedback loop contains various components possessing frequency response characteristics crucial to overall system performance. The Notre Dame system consists of four key elements: a Shack-Hartman wavefront sensor, a wavefront reconstruction processor, an amplifier and a deformable mirror. Each component has its own set of time delays and bandwidth constraints. While the data presented in this section pertains specifically to the Notre Dame AO System, similar bandwidth restrictions also negatively affect other AO systems. This analysis will serve to further underscore the need to address and overcome current bandwidth limitations that plague the conventional AO approach.

Bandwidth limitations concerning several different components of Notre Dame's AO System will be addressed. The information and figures presented represent a

collection of data obtained through experimental testing and manufacturer testing. Limitations relating to the amplifier, DM, and wavefront sensor are analyzed below.

2.4.1 Amplifier

In order to characterize the DM amplifier's bandwidth limitations, frequency response analyses were performed. Experimental tests were conducted to determine key operational features, such as cutoff frequencies, latencies, and slew rate limitations. A more detailed description of the system identification techniques referred to here may be found in Appendix A.

The conjugate correction feedback loop, as part of Notre Dame's AO control system, consists of 5 NI-PXI (National Instruments) boards each containing 8 channels corresponding to the 37 DM actuators where three channels are unused. Control signals are relayed from each of the NI-PXI board channels through an amplifier which amplifies each signal by three times the input voltage. The amplified signals are then sent directly to each of the DM actuators which may be modeled as a capacitor.

Experimental tests were conducted to determine the frequency response of the DM amplifier. Bode diagrams were constructed depicting the amplifier's behavior as a function of input frequency. Sinusoidal input signals ranging in amplitude from 1 Volt to 8 Volts and ranging in frequency from 100 Hz to 20 kHz were sent into the amplifier. The input and output signals were measured simultaneously using a data acquisition system with a sampling rate of 500 kHz. Data was acquired over twenty-five consecutive time periods, i.e. $25T$ where T is the time period associated with the sinusoidal input frequency. Two amplitude measurements and two phase delay measurements were taken

from each of the twenty-five time periods resulting in 50 amplitude measurements and 50 phase delay measurements for each frequency test. Amplitude was measured as the maximum and minimum peak values over a time period and phase delay was measured as the phase shift between the input and output signals at the zero cross-over points. Note that amplitude and phase delay measurements were obtained after removing the signal's mean or DC bias. Each set of data (50 measurements) was averaged and plotted on a frequency response diagram showing magnitude and phase response characteristics where the magnitude data was determined by normalizing the output amplitude by the averaged input amplitude. The range of values obtained at each input frequency was used to determine the signal's uncertainty for each measurement.

The raw signals were also transformed into the Fourier domain for further analysis using Matlab's discrete Fourier transform commands. The output signal's amplitude and phase delay were determined from the signal's Fourier transform at the input frequency as a means of verifying the measurements described previously. The frequency spectrum obtained from the Fourier transform was also used to locate any harmonics present in the output signal which would indicate harmonic distortion. Square wave inputs were used to study the DM amplifier's response to step changes in voltage. This data was also used to determine any slew rate limitations.

The DM Amplifier represents a key component in Notre Dame's AO control system. The amplifier is used to transfer the conjugate correction signal to the DM actuators. It provides an amplification of 3X the input voltage resulting in an output signal of +/- 30 Volts peak to peak riding on a 70 Volt bias signal, i.e. when the input is 0.0 Volts the output is 70 Volts. The amplifier accepts a maximum input signal of +/- 10

Volts; therefore frequency response testing was conducted using sinusoidal waveforms with amplitudes ranging from 1 Volt to 8 Volts. Input frequencies ranged from 100 Hz to 20 kHz. In order to test the amplifier under conditions similar to those experienced during normal operation, a 2.2 μF capacitor was connected to the output of the amplifier, simulating the effects of an individual piezoelectric actuator. Sinusoidal signals were input into the amplifier using a function generator and the output voltage was measured across the simulated actuator (capacitor). The input and output signals were acquired at a 500 kHz sampling rate. Figure 2.5 shows the ratio of output to input averaged amplitude versus frequency for eight different input amplitudes. Figure 2.6 shows the corresponding averaged phase delays encountered between the input and output signals over the same range of input amplitudes and frequencies.

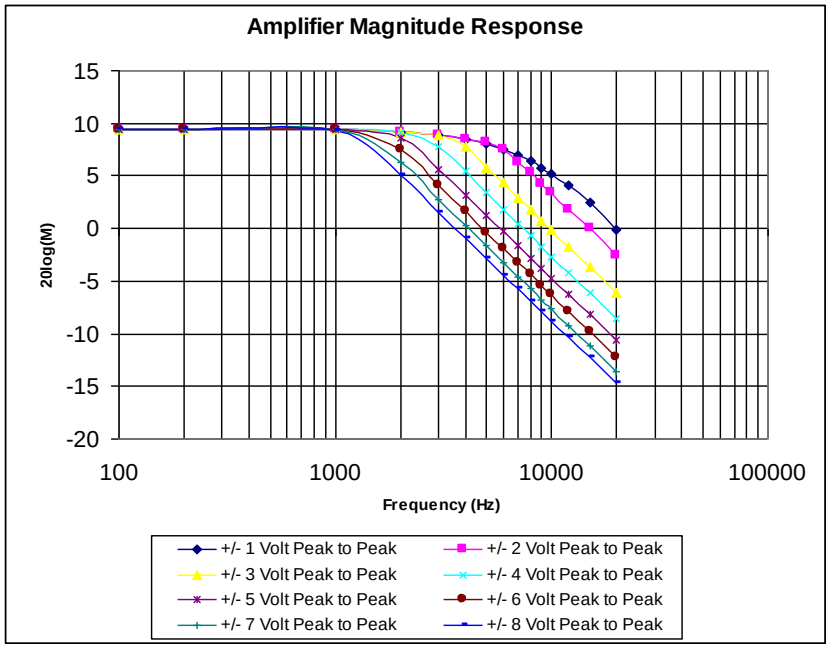

Figure 2.5: Magnitude response results for Notre Dame's DM Amplifier determined experimentally.

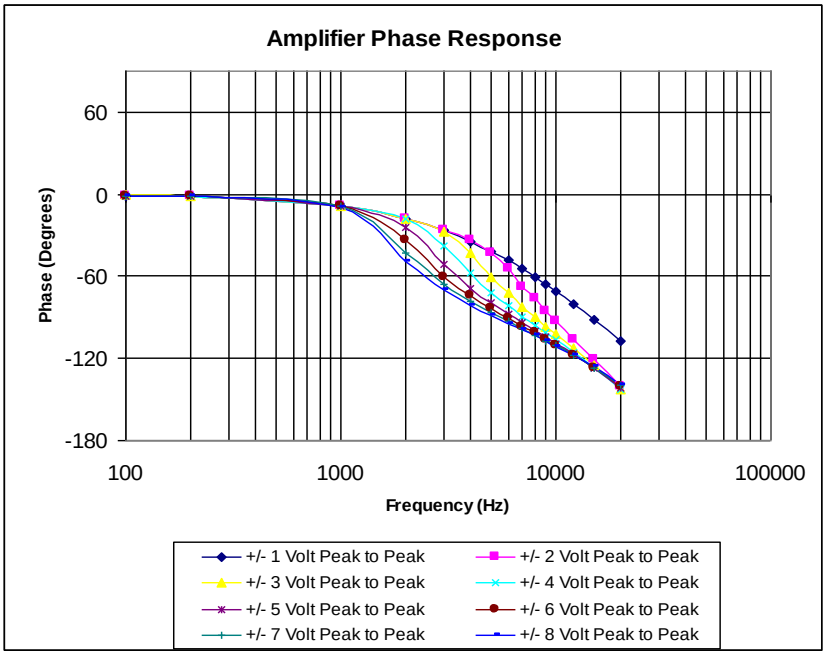

Figure 2.6: Phase response results for Notre Dame's DM Amplifier determined experimentally.

As evident from Figs. 2.5 and 2.6, the DM Amplifier exhibits linear characteristics to approximately 1 kHz, at which point both magnitude and phase begin to significantly fall off for large input amplitudes; the exception to this linear response for frequencies below 1 kHz is the linear negative slope on the Fig. 2.6 phase plot. This is an indication of a pure time delay which will be further discussed later.

Examination of the raw signal provides further insight into the source of the amplifier's nonlinear response. Step inputs were applied at four different amplitudes to determine any slew rate limitations. Figure 2.7 shows four different step response tests overlaid with one another for both rising (left) and falling (right) edge response, revealing a positive slew rate of approximately 0.18 Volts/μs and a negative slew rate of approximately 0.15 Volts/μs. Note that the output signal has been scaled by a factor of

1/3 so as to remove the DM amplifier's amplification rate aligning the final values of the input and output signals.

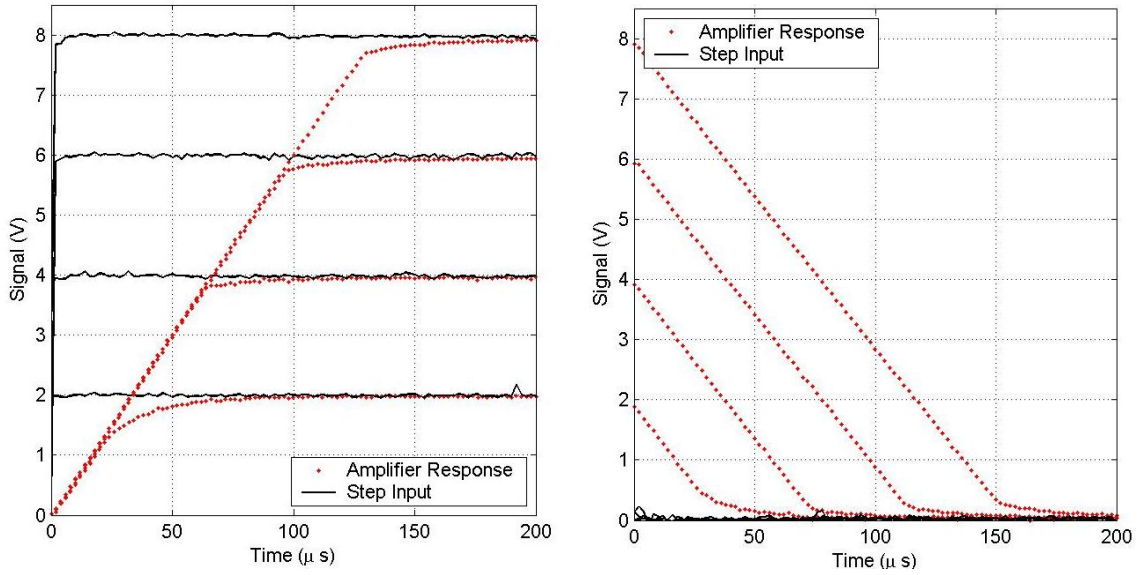

Figure 2.7: Step response tests performed on the DM Amplifier given four different input amplitudes: 2, 4, 6, and 8, showing a clear slew rate limit of approximately 0.18 Volts/μs (0.06 Volts/μs X3 due to the amplifier's amplification of 3 times the input signal).

The amplifier's slew rate limitations may also be seen in the frequency response data shown below in Fig.2.8. Figure 2.8 (A) represents a case where the slew rate limit has not yet been reached, whereas (B) and (C) show two different cases in which the output signal experiences nonlinear effects due to slew rate limitations. For the given range of input frequencies tested, the amplifier displayed positive slew rates between 0.15 and 0.158 Volts/μs and negative slew rates between 0.13 and 0.137 Volts/μs. Again, the output signals have been scaled by 1/3 to more clearly show the slew rate effects.

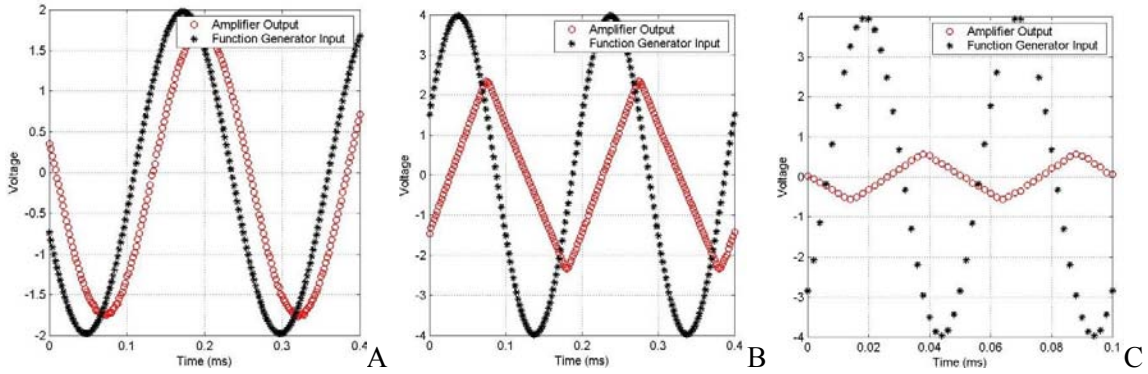

Figure 2.8: (A). Frequency response tests performed on the DM Amplifier showing slew rate limits ranging between 0.13 and 0.16 Volts/μs (after rescaled by 3X) given an input amplitude of 2 Volts and a frequency of 4 kHz, (B). an input amplitude of 4 Volts and a frequency of 5 kHz, and (C). an input amplitude of 4 Volts and a frequency of 20 kHz.

Using the data given above, an approximation to the DM amplifier's magnitude and phase response was derived. Negligible nonlinear effects were observed in the frequency response data given an input amplitude of 1 Volt. Therefore, a transfer function was fit to the +/- 1 Volt peak to peak magnitude response data points shown in Fig. 2.5. The best fit corresponded to a transfer function consisting of a low pass filter with a cutoff frequency of approximately 7.5 kHz with an additional pure time delay of 25 μs. The response characteristics from this transfer function were then applied in conjunction with slew rate limitations, noting that there exists a maximum output amplitude restriction given by,

$$\left|A_o\right|_{\max} \cong \frac{SR}{4f_d}, \tag{2.9}$$

based on the amplifier's slew rate, SR, and the input or disturbance frequency, f_d. These characteristics were used to estimate or model the magnitude response data measured experimentally. The good agreement between the measured data and the modeled

response shown in Fig. 2.9 indicates that the nonlinear effects are due primarily to slew rate limitations and the pure time delay referred to above imposed by the amplifier.

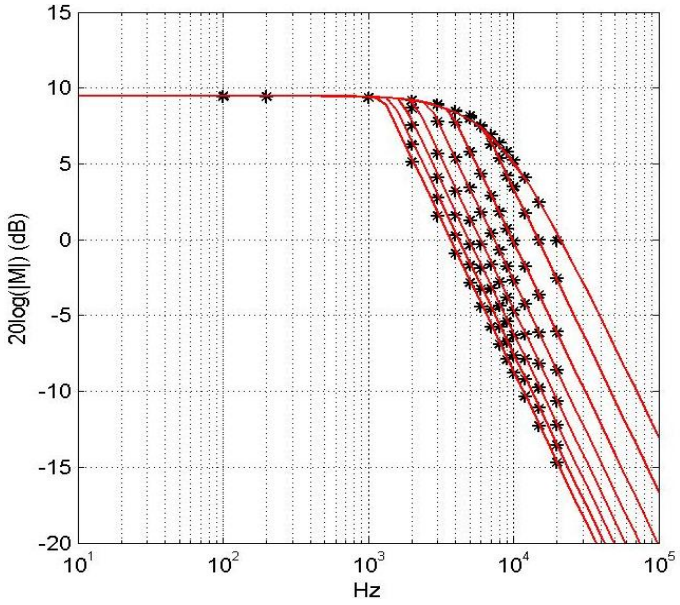

Figure 2.9: Experimental magnitude response data (*'s) and the modeled magnitude response (solid lines) using an estimated transfer function along with the amplitude restrictions placed on the output due to the DM amplifier's slew rate limits.

Due to the triangular output signal shown in Fig. 2.8 (B) and (C) there does exist a higher order harmonic at twice the input frequency in some cases. However, its associated power is approximately two orders of magnitude smaller than that of the fundamental and therefore only a slight amount of harmonic distortion occurs.

2.4.2 Deformable Mirror

The Xinetics DM consists of 37 piezoelectric actuators mounted to the back of a flexible membrane. Seven evenly spaced rows of actuators (separated by 7 mm), with each of the three corner actuators removed, makes up an approximate 42 mm diameter

circular aperture used for corrections (Fig. 2.10). Each actuator has a stroke length of +/- 4 μm given an input signal of +/- 10 Volts. The dynamic capabilities of the mirror depend on the frequency response of the amplifier and actuators discussed above, the number of cycles that can be accurately formed across the mirror's aperture, as well as the bandwidth constraints for applying discrete time control commands to the amplifier and DM. This section studies the effect that each of these limitations has on the AO system's correction capabilities.

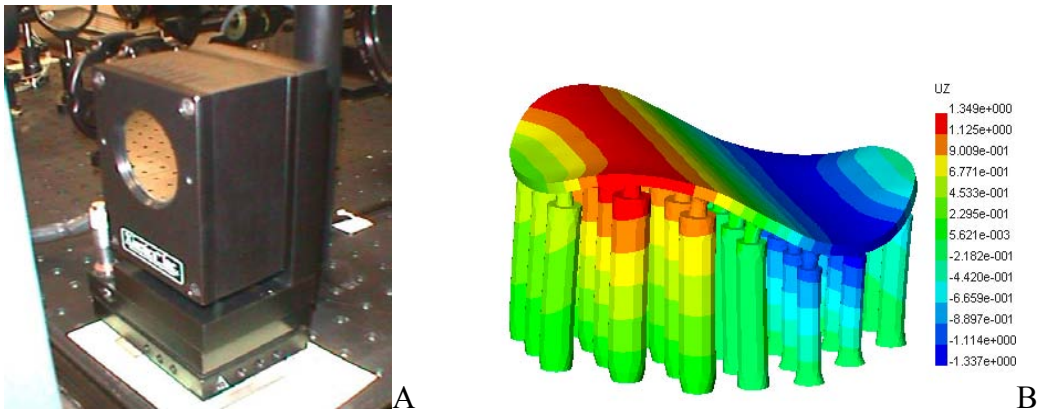

A B

Figure 2.10: (A). Xinetics DM photograph and (B). 3-D model of the mirror and actuators.

Based on the number of actuator rows as well as the spacing between them, the DM is limited by the number of full cycles that can be accurately formed across the aperture. Since a bi-quadratic fit represents a good model for the DM's shape and given that there are only seven rows of actuators, the mirror is capable of constructing one full cycle of disturbance very well. However, as the number of cycles of disturbance across the aperture increases so does the error. Figure 2.11 illustrates the requirements necessary to produce an acceptable AO correction based on the number of actuators per

disturbance wavelength given various aperture sizes as reported by Duffin [43]. It is clear from these results that at least three actuators per disturbance wavelength are necessary to achieve any amount of correction. Furthermore, as the DM aperture size increases with respect to the disturbance wavelength the number of actuators needed to attain the same amount of correction also increases.

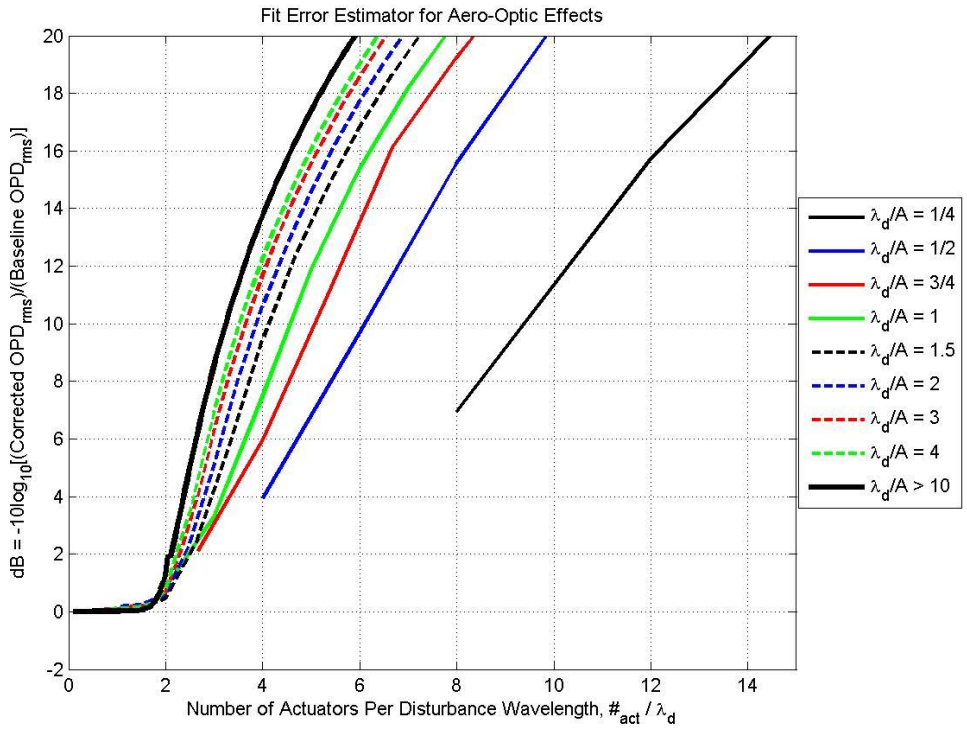

Figure 2.11: Requirements for the number of actuators needed to apply an acceptable correction as reported by Duffin [43].

In addition to the number of actuators per disturbance wavelength, the slew rate limitations discussed previously place another constraint on the amount of correction attainable. Moreover, if the AO system uses discrete time updates to control the DM actuators, yet another variable is introduced. Figures 2.12 show two different simulations of an individual actuator's "response" given five updates per quarter disturbance

wavelength. The "response" curves shown in Figs. 2.12 represent the voltage patterns that would be felt by the piezoelectric actuators while the plots shown in Figs. 2.13 represent the mirror displacements that would occur if the mirror responded with no time delays, overshoots, *etc*. introduced by the mirrors own response characteristics. The first case (Fig. 2.12 (A)) demonstrates the actuator's "response" when the slew rate limit given by Eq. (2.8) is satisfied (i.e., the limit has *not* been exceeded). In this example the actuator rises and falls at the maximum slew rate during each individual update yet is still able to achieve the target stroke height over each discrete update period. The second case (Fig. 2.12 (B)) shows the actuator's "response" when the slew rate limit given by Eq. (2.8) is not satisfied (i.e., the limit has been exceeded). In this case, the actuator is unable to reach the target stroke height during each discrete time period therefore causing the actuator to maintain the maximum slew rate from peak to peak. Note that this simulation agrees with the actual experimental data for the amplifier's response shown in Fig.2.8 (B) and (C).

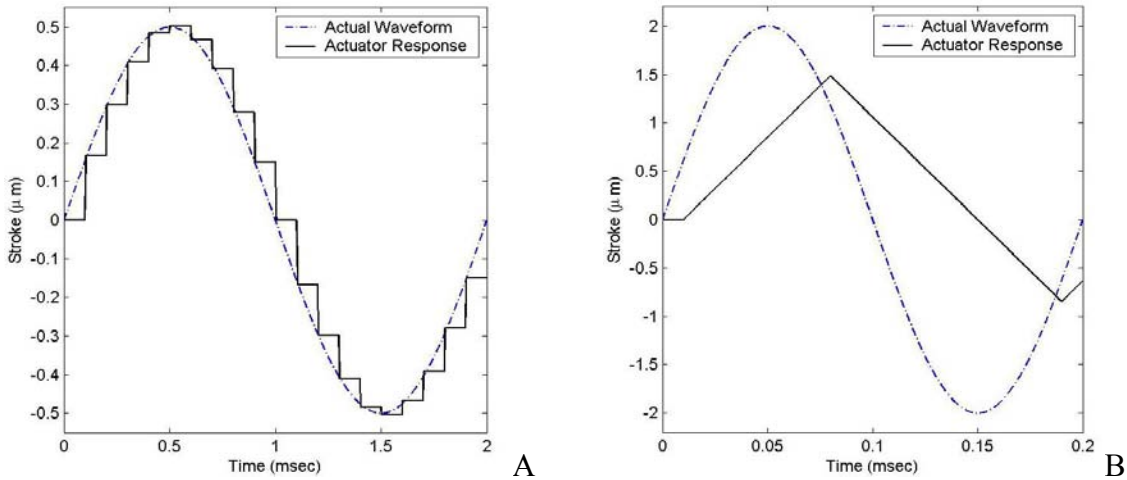

Figure 2.12: Simulated time response of an individual actuator plotted against the input waveform given discrete time updates where (A). $SR > 2\pi fA$ and (B). where $SR < 2\pi fA$.

The next logical question is how the "response" of an individual actuator translates to the overall wavefront correction capabilities. Figures 2.13 show three different time series of OPD, again not including the mirror's own response characteristics. Fig. 2.13 (A) shows the progression in time of a one-dimensional aberrating wavefront. This waveform then becomes the input signal used to produce the middle plot given discrete time updates. Therefore, Fig. 2.13 (B) depicts a time series of the DM actuators' one-dimensional OPD "response" associated with the wavefront shown in Fig. 2.13 (A). If the DM waveform shown in Fig. 2.13 (B) were used to correct for the aberrating wavefront shown in Fig. 2.13(A), Fig. 2.13 (C) represents the resulting time series of residual error. This example does show a significant reduction in OPD. However, as would be expected, given a similar analysis of the case shown in Fig. 2.12 (C) where the slew rate limit has been reached, a far less desirable outcome is produced.

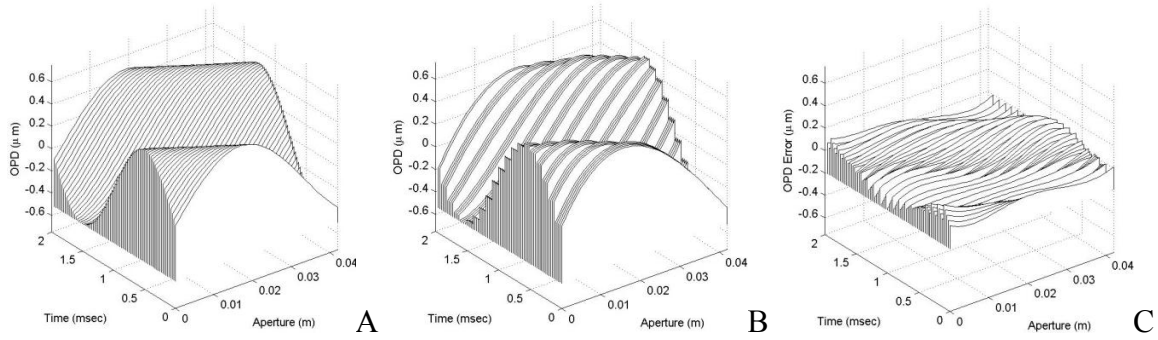

Figure 2.13: Simulated time series of OPDs corresponding to (A). a specified wavefront aberration, (B). twice the DM's conjugate correction given discrete time updates, and (C). the resulting wavefront error where $SR > 2\pi fA$.

These correction capabilities were quantified using the root-mean-squared of the difference between an actuator's ideal temporal surface, Ω_{ideal}, and its "actual" temporal surface, Ω_{actual}, absent the mirrors own characteristics, described as,

$$\delta_{rms} = \sqrt{\frac{1}{T_d}\sum(\Omega_{ideal} - \Omega_{actual})^2}\ , \tag{2.10}$$

where T_d is the disturbance time period. Since the aberrations for this analysis are given by sinusoidal functions, the following equation may also be used in replacement of Eq. (2.10),

$$\overline{OPD_{rms}^{residual}} = \overline{\sqrt{\frac{1}{A_p}\sum(OPD_{ideal} - OPD_{actual})^2}} \tag{2.11}$$

where A_p represents the mirror's aperture and the overbar indicates a time-averaging over one disturbance time period, T_d. The same results are produced using either Eq. (2.10) or Eq. (2.11) since time-averaging the OPD error at any location along the mirror's aperture looks the same as one full-disturbance time period elapses.

Figure 2.14 shows several different sets of simulation results for various ratios of slew rate (SR) to $2\pi f_d A$. As indicated by the range of plots shown below, there exists a limit on the amount of achievable correction independent of the number of updates per disturbance period when the slew rate drops below half of the limit given by Eq. (2.8). On the other hand, for slew rates exceeding approximately twice the limit given by Eq. (2.8), the mirror's correction ability improves only minimally. Although, in this case increasing the number of updates per disturbance cycle does continue to provide improvement.

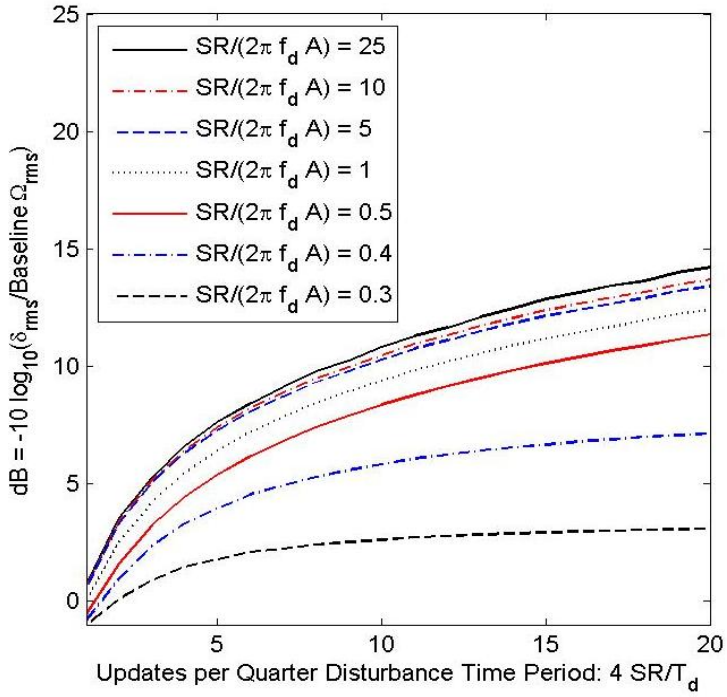

Figure 2.14: Correction restrictions due to the optical disturbance and slew rate limitations.

2.4.3 Wavefront Sensor

As described previously, wavefront sensing rates are dependent upon both system gain requirements, in order to maintain system stability, and the number of full corrections needed to attain a specified increase in on-axis intensity. The ability of the conventional AO system to accurately sense and correct a disturbance depends upon system latencies, τ_2, disturbance frequencies, f_d, and update frequencies, f_u, as illustrated by Duffin's analysis [27] shown below in Fig. 2.15. The horizontal axis represents the ratio of update frequency to disturbance frequency while the vertical axis represents the correction (dB = -10log$_{10}$[(Corrected OPD_{rms} / Uncorrected OPD_{rms})]). For corrections below the 0 dB line, the use of a conventional AO system would actually worsen the wavefront aberrations. It is also clear from Fig. 2.15 that as system latency (τ_2) increases

system performance declines given a constant disturbance frequency (f_d). It should also be noted that the ratio of update frequency to disturbance frequency must be at least three for any amount of correction to occur, even when considering the ideal case with no system latencies. There also exists a ratio for a given time delay beyond which improvements in system performance are negligible. Horizontal solid bars are used to indicate the asymptote for each curve in Fig. 2.15 [27].

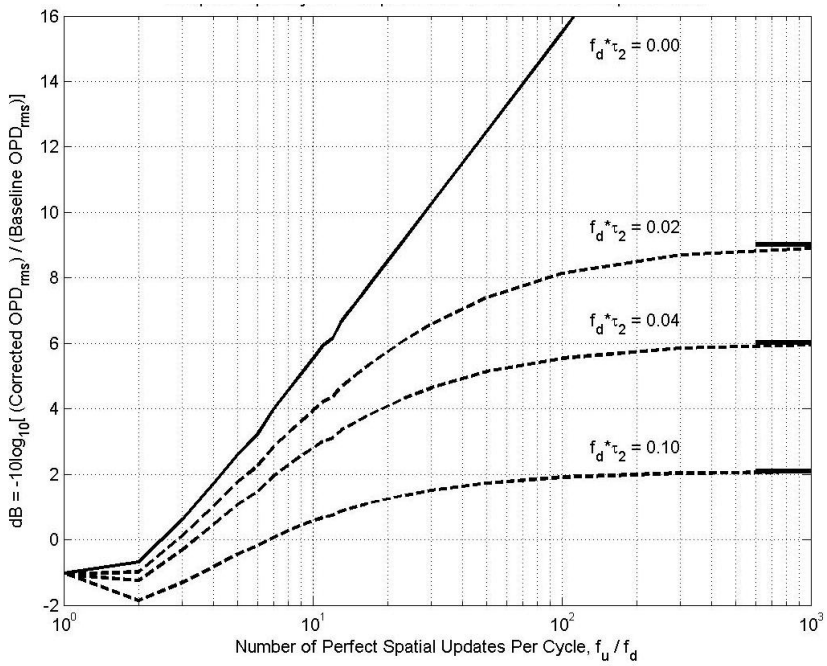

Figure 2.15: Correction dB versus DM update rate/frequency ratioed to the disturbance frequency for various latencies as reported by Duffin [27].

As an example, a latency of 25 μs associated with Notre Dame's DM Amplifier alone would require an update rate of approximately 6 kHz given an 800 Hz disturbance to achieve a 50% reduction in the residual OPD_{rms} (i.e., -3 dB); this in turn would require a 60 kHz wavefront frame rate in real time given a system gain of 0.1. The Shack-Hartman wavefront sensor used in Notre Dame's AO system only frames at a rate of 1

kHz. Even state-of-the-art wavefront sensors whose framing rates are an order of magnitude greater than Notre Dames would be incapable of making this correction. In this case the latency issue of the amplifier alone exceeds the limitations set by current technology; therefore an alternative AO approach is necessary. Moreover, frequencies commonly found in high speed aero-optic disturbances may be even greater than 800 Hz and the desired increase in system performance is often more than 50%, raising the necessary wavefront sensing rate even higher. While improvements are continually being made to technology and time delays reduced, there will always be some component of the AO system limiting its bandwidth capabilities. Therefore, the motivation behind this research is to approach the problem from a different perspective. Rather than trying to improve the speed of various system components this research has focused on reducing the bandwidth necessary to make real-time corrections.

2.5 Numerical Model

A significant portion of this research involves the use of a numerical model to simulate a free shear layer, its corresponding velocity fields and evolving thermodynamic properties, along with the form of the emerging wavefronts once propagated through the flow. Simulations were conducted to study the optical characteristics of an unforced shear layer along with its optical response to forcing. In addition, the code was used to test the effects of real-time AO corrections applied to an emerging aberrated wavefront. Developed by Hugo and Jumper [3, 11], and improved by Fitzgerald and Jumper [5, 12], this code was first used to develop wavefront sensors and later to discover the physics of

the aberrating mechanism in a matched-total-temperature shear layer [5]. It simulates two flows of different velocity, but identical total temperature, on either side of a stationary splitter plate. As the flows merge a free shear layer is formed. The model starts by calculating the unsteady velocity field using a discrete vortex method. A thermodynamic overlay is then performed to determine the thermodynamic properties from the computed velocity field. The following sections provide a more detailed description of these steps.

2.5.1 Discrete Vortex Method (DVM)

Several inviscid and pseudo-inviscid methods have been successfully used to model roll-ups in a shear layer caused by the Kelvin-Helmholtz instability mechanism [5]. The current study was performed using a pseudo-inviscid, two-dimensional discrete vortex method (DVM) developed at Notre Dame [5, 12]. The shear layer is modeled using two semi-infinite vortex sheets, solved analytically, on either side of a finite vortex sheet solved numerically (computational domain). A splitter plate is simulated using a string of positionally-fixed vortices while the remaining vortices within the computational domain are allowed to move and convect based on the induced velocity from all other vortices and the overall convective velocity of the flow. The rotational core associated with each discrete vortex is modeled using a temporal growth rate, simulating momentum diffusion. The model also uses vortex insertion and vortex merging when the distance between two adjacent vortices exceeds or drops below a specified value, respectively to ensure stability [5, 12]. Each vortex is assigned an initial strength, $d\Gamma$, at the splitter plate given by

$$d\Gamma = (U_U - U_L)dl\,, \tag{2.12}$$

where *dl* represents the spacing between adjacent vortices, and U_U and U_L represent the upper and lower stream velocities above and below the splitter plate, respectively. At each discrete point within the computational domain the velocity induced by all surrounding point vortices is calculated by

$$dU_\theta(r) = \frac{d\Gamma}{2\pi r} \tag{2.13}$$

when *r* is greater than some critical value, $r_{Singular}$, and by

$$dU_\theta(r) = \frac{d\Gamma}{2\pi r_{Singular}^2} r \tag{2.14}$$

otherwise, where r is the distance from the center of each vortex to the point of evaluation. Once the overall convection velocity is taken into account and the entire velocity field is computed at the given time step, new positions for each vortex at the subsequent time step are determined. A new velocity field is calculated using the equations above and the process is repeated.

2.5.2 Weakly Compressible Model (WCM)

Once the velocity fields are available from the DVM, another numerical code designated the *Weakly-Compressible Model* (WCM), is used to overlay the thermodynamic properties onto each velocity field. The unsteady Euler equations,

$$\frac{\partial p}{\partial x} = -\rho\left[\frac{\partial u}{\partial t} + u\frac{\partial u}{\partial x} + v\frac{\partial u}{\partial y}\right]$$
$$\frac{\partial p}{\partial y} = -\rho\left[\frac{\partial v}{\partial t} + u\frac{\partial v}{\partial x} + v\frac{\partial v}{\partial y}\right] \tag{2.15}$$

are back solved using a four-point central difference scheme to calculate the pressure gradients from which the pressure field is computed. The adiabatic heating/cooling equation and the perfect gas law are used to find the initial temperature and density fields. These iterations are repeated until the density field converges. At this point another iteration loop is run using the Hilsch approximation,

$$\frac{T(t,x,y)}{T_{ad}(t,x,y)} = \left(\frac{p(t,x,y)}{p_{\infty}}\right)^{\frac{\gamma-1}{\gamma}}, \tag{2.16}$$

to solve for the temperature variations within the flow field. The density iteration cycle is then repeated followed by the temperature iteration cycle until pressure, density, and temperature converge at each time step [5, 12]. The index-of-refraction field, *n(t,x,y)*, is determined using the Gladstone-Dale constant from which OPL and OPD are computed using Eq. (2.2) and Eq. (2.3). Once the optical wavefronts are obtained, jitter signals, far field diffraction patterns, and Strehl ratios may be computed as described earlier.

2.5.3 DVM/WCM Experimental Validation

The results obtained using the DVM and WCM have been found to be in good agreement with experimental results. Good comparison between mean velocity profiles from the numerical model and incompressible and weakly-compressible experimental shear layers validate the DVM computations (Fig. 2.16 (A)). Further validation of the

DVM simulation results were obtained by comparing the vorticity thickness computed using the DVM with the vorticity thickness predicted by literature (Fig. 2.16 (B)) [13]. The DVM simulated a vorticity thickness growth rate of approximately 0.139, which is within 8.6 % of the empirical predicted value [5].

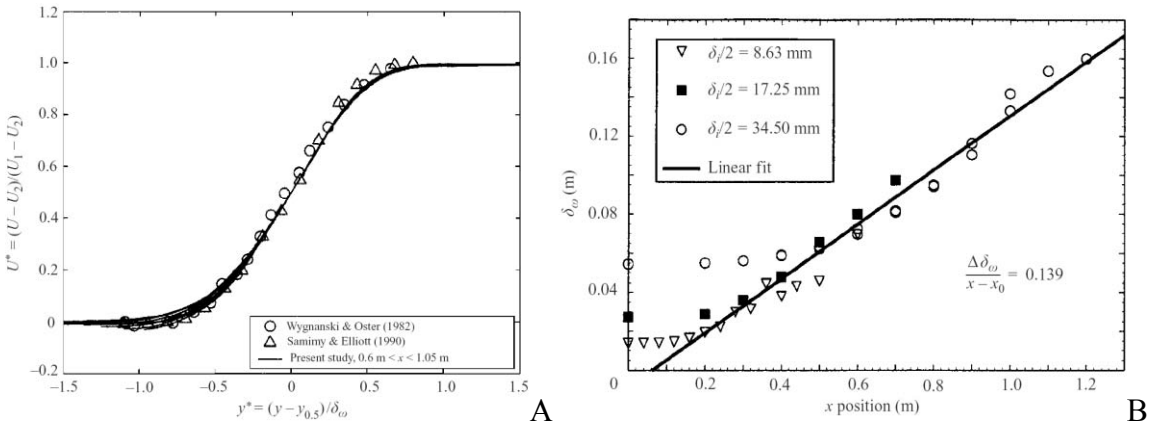

A B

Figure 2.16: (A). Mean velocity profile comparison between the DVM (numerical simulation performed by Fitzgerald), an incompressible shear layer (Oster and Wygnanski), and a weakly-compressible shear layer (Saminy and Elliot) [5, 12] (B). Vorticity thickness growth rate of a free shear layer simulated using the DVM with varying initial core radius values [5, 12].

The results from the WCM were also validated experimentally. Figure 2.17 shows a qualitative comparison between a DVM/WCM computed vorticity plot with its corresponding Schlieren image shown on the left and an experimental flow visualization shown on the right [5, 9, 11, 12]. As reported by Fitzgerald and Jumper [5], the DVM/WCM accurately models the large-scale structures present in the flow. Figure 2.18 shows the similarities between the pressure wells formed within a vortical structure produced numerically by the WCM and experimentally [9]. Although only 2-D, the discrete vortex method and Weakly-Compressible Model provides good insight into the

underlying shear layer mechanism. While it does not simulate the entire range of turbulent scales in a shear flow, it does predict the large-scale motion and more importantly the optical aberrations induced by such a flow very well. When a laser beam is propagated through a turbulent shear layer, the large-scale structures convecting downstream ultimately determine the form of the outgoing beam. This is due primarily to the large density deficit within each of the large-scale structures. Not only does it support the curvature allowing such structures to persist downstream, but it is this significant density gradient which, along with the local „stagnation' or saddle point between coherent structures forming a high-pressure region, largely contributes to the emerging wavefront's aberrations.

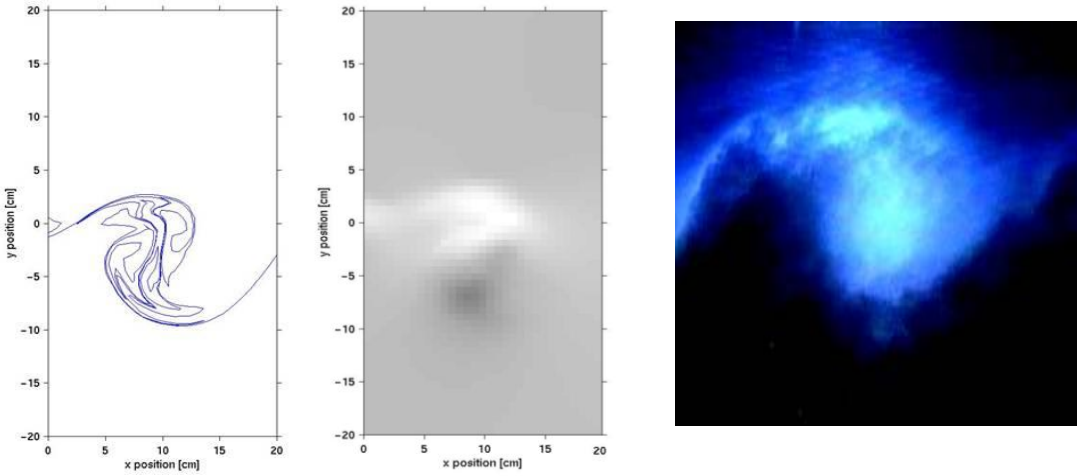

Figure 2.17: Comparison between DVM vorticity plot and Schlieren image (left) and an experimental flow visualization image (right) [5, 9, 11, 12].

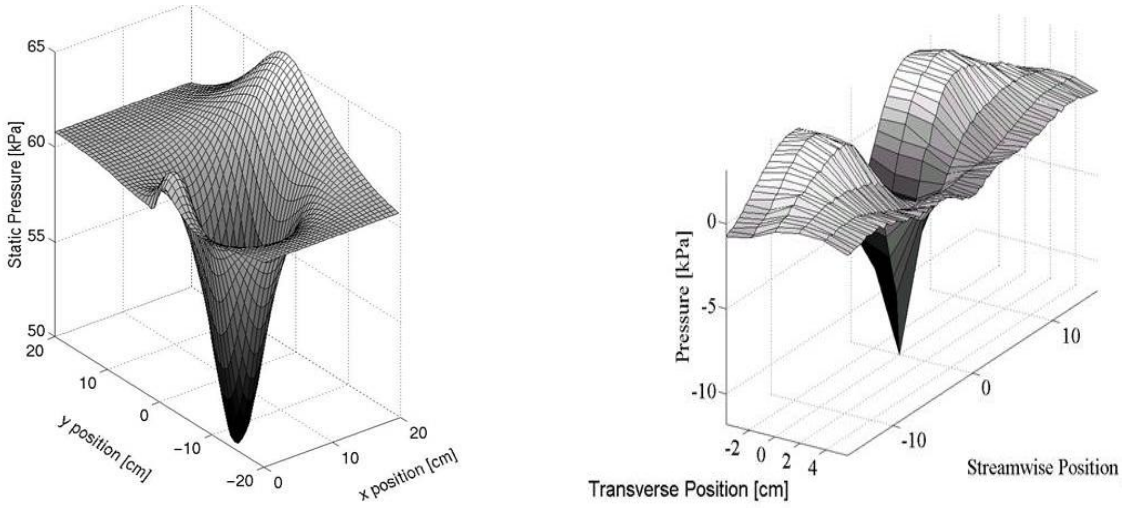

Figure 2.18: Comparison between DVM/WCM pressure well (left) and an experimental pressure well (right) [5, 9, 11, 12].

The DVM/WCM code was used to perform free shear layer simulations given a range of upper and lower Mach number flows. The simulations provide a tool for characterizing the optical nature of the shear layer as well as a fast and efficient way of analyzing the feasibility of the proposed AO control system. The following Chapter describes the implications that a shear layer has on an optical system in more detail. It uses results obtained from the weakly-compressible model to investigate the relationship between a shear layer's vorticity thickness and its optical characteristics. An analysis of the shear layer's response to forcing is also presented. The results from several simulations, performed using the DVM/WCM model, are summarized providing a means of optically characterizing a free shear layer using non-intrusive small aperture laser beams.

CHAPTER 3:

SHEAR LAYER CHARACTERIZATION

3.1 Unforced Shear Layer

The development of turbulent shear layers, also referred to as mixing layers, has been the subject of considerable amounts of investigation throughout the past several decades [4, 5, 10, 13, 14, 15, 17, 33, 34, 36]. Shear layers are found in several different devices and flow regimes including combustion jet engines, supersonic ejection pumping, and separated flows between a free stream flow and recirculation region. Free shear layers also play a critical role in the development of laser transmission systems. Due to the detrimental optical effects caused by density variations within the shear layer through which a laser signal is propagated, knowledge of the flow fields structures, topology and dynamics is of great importance.

A free shear flow is characterized as a flow *free* from boundary conditions. The general form of a shear layer, as depicted in Fig. 3.1, is given by two flows merging after initially being separated by a splitter plate. The upper and lower stream velocities are represented by U_1 and U_2, respectively. As the flows merge, the velocity gradient between the two streams in combination with local instabilities cause shearing to occur between fluid elements at the interface increasing vorticity and eventually leading to a fully-developed turbulent flow field. The two streams are characterized as planar flows

where the mean velocity in the streamwise direction is considerably larger than the mean velocity in the spanwise direction. Similarly, gradients in the spanwise direction significantly outweigh gradients in the streamwise direction. These conditions may be applied to the Navier-Stokes equations to obtain Reynold's transport and vorticity transport equations specific to a free shear layer flow.

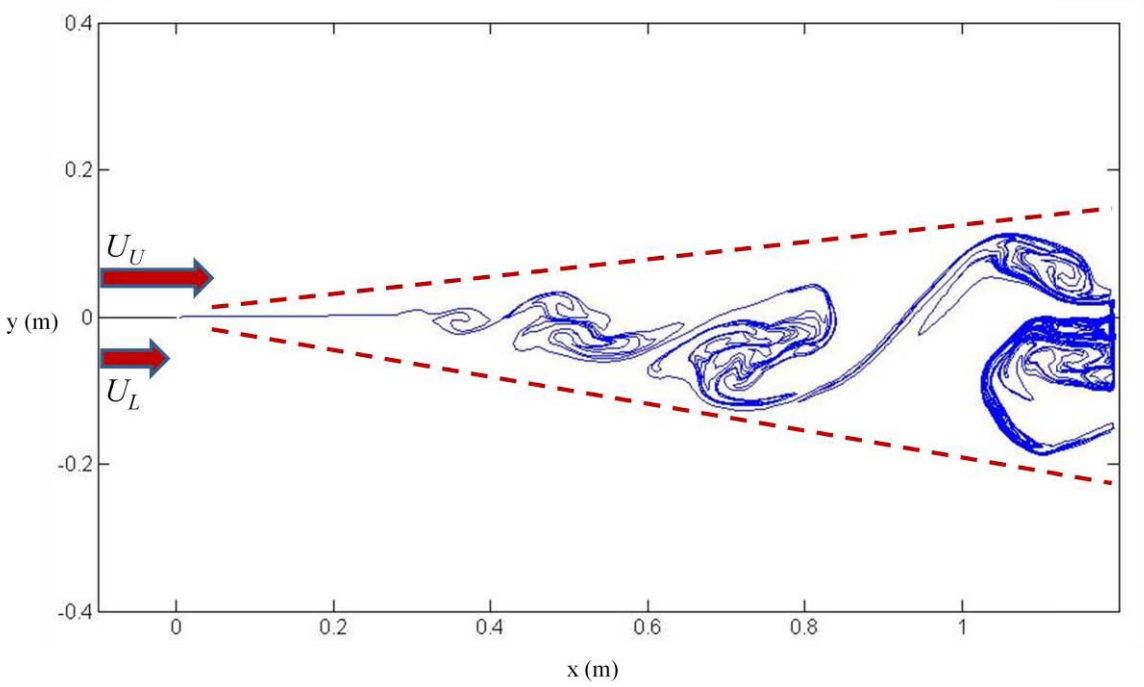

Figure 3.1: Vortex contour plot of a numerically simulated free shear layer, where U_U = 261 m/s and U_L = 35 m/s, with dotted lines showing the on-average linear growth rate of large-scale structures in the cross-stream direction.

It is well known that turbulence contains a wide range of length scales, where the largest scales are a characteristic of the mean flow and the smallest scales, also referred to as Kolmogorov scales, are the mechanism through which energy is finally dissipated [32]. As the flow convects downstream, nonturbulent irrotational fluid in the freestream

is entrained into the turbulence through a "gulping" mechanism. Dimotakis describes this process by three separate steps. Firstly, irrotational fluid near the shear layers boundary begins engaging in large-scale motions through the Biot-Savart law. This step is referred to as *induction*. The second stage is termed *diastrophy* and involves the introduction of vorticity through the straining of fluid elements as they cascade down towards the viscous, or Kolmogorov scales. Finally, other diffusive processes may take place through *infusion* depending on the type of flow [15]. Due to this continual entrainment of fluid, the mean shear layer thickness grows linearly (although not symmetrically) with downstream distance as shown by the dotted lines in Fig. 3.1. This linear growth rate is known to be a function of both velocity and density ratios [15, 33]. The growth rate can be seen to vary with changing upper and lower Mach numbers, which (for the matched total-temperature case) leads to variations in the temperature and density of each stream.

Linear stability analysis has also been used extensively to gain insight into the initial transition to turbulence. Small instabilities within the flow interact with the surrounding fluid creating random motions eventually leading to fully-developed turbulent flow through the Kelvin-Helmholtz instability mechanism. Linear stability theory describes this process as small disturbances upstream in the flow being amplified at the shear layers most unstable frequencies or wavelengths. Monkewitz and Huerre [17] showed that the maximum growth rate of a mixing layer more or less scales proportionally with velocity ratio by applying a linear stability analysis of both the *tanh* and *Blassius* profiles. These results supported prior findings, indicating that a shear layers spreading rate is also related to its velocity ratio.

3.1.1. Shear Layer Implications

A turbulent shear layer is an unstable flow susceptible to small perturbations which cause the layer to spread and advance into fully-developed turbulence. The flow is irreversible with energy being dissipated through viscous effects at the small scales. Due to their stochastic nature, statistical methods have been commonly used to analyze turbulent flows [44]. Such studies have offered much insight into their development including the mechanisms through which turbulence is intensified and dissipated. In 1974, Brown and Roshko observed an interesting feature about shear flows in experimental shadowgraphs taken of a different density mixing layer [13]. In their study, as well as in several subsequent studies by other authors [33, 17, 34, 35, 36], large-scale spanwise coherent structures have been shown to dominate the flow topology. These structures, also called "Brown-Roshko rollers", reveal a "quasi-ordered" flow that is not completely deterministic or stochastic [10]. These findings unveiled a new way of analyzing a free shear layer.

In addition to the discovery that large-scale structures were an intrinsic property of shear layer flows [13], Winant and Browand proposed that the growth rate of the shear layer was not only dependent upon the entrainment process, but also the interaction between these structures within the flow [36]. As the structures propagate downstream, two or more rollers begin interacting with one another eventually coalescing into a larger coherent structure. This merging mechanism is known as *pairing* when only two structures are involved. This process subsequently recurs creating larger and larger structures with downstream distance. Several studies have focused on the prediction of these pairing locations using a pairing parameter first introduced by Huang and Ho [37].

Experimental measurements have shown both pressure and density deficits within these large-scale coherent structures. However, for quite some time pressure fluctuations were viewed as negligible. Using the DVM/WCM code described in Chapter 2, Fitzgerald and Jumper [5] were able to shed some light on this flawed notion. Growth rates and velocity profiles obtained using this model showed good agreement with both theoretical predictions and experimental data, respectively. Large-scale coherent structures in experimental flow visualizations were also shown to exhibit a similar form and curvature as those computed using the weakly-compressible model [9]. Furthermore, the model confirmed the presence of significant pressure wells measured experimentally, refuting previous claims of negligible static pressure fluctuations within a high speed shear layer [5]. It is now acknowledged that these pressure wells are necessary to support the considerable amounts of curvature present in a shear layers velocity field. These results have made a significant impact on our understanding of the coherent structures that exist in free shear layers.

Moreover, these pressure wells and density deficits within the large-scale structures are the cause of significant optical aberrations induced on a laser beam projecting through the flow. In addition, saddle points in the shear layer produce high pressure/density regions between coherent structures causing further aberrations. For a projecting system mounted to the end of an aircraft, the severity of such aberrations increases as the beam is directed further backward (i.e., for larger azimuth angles) encountering more of the shear layer (refer to Fig. 1.4). Figure 3.2 illustrates an example of the detrimental effect a shear layer has on system performance [27]. Figure 3.2 is an early prediction by Dr. Demos Kyrazis of how the Strehl ratio of a large aperture beam

on the ABL would be affected based on shear layer optical data from Jumper and Hugo [11] and Fitzgerald and Jumper [5] for laser projection through a Mach 0.8/0.1 shear layer at Arnoold Engineering Development Center (AEDC). It shows an estimate of Strehl ratio, used to quantify system performance, versus azimuth angle. For azimuth angles between 0 and 90 degrees system performance depreciates by approximately 10%. However, once the azimuth angle exceeds 100 degrees dramatic reductions occur. Between 100 degrees and 120 degrees system performance reduces from approximately 90% to approximately 30%, a crippling effect to an AO system. The emerging optical beam becomes virtually, if not completely, ineffective. As a result, overcoming these shear layer implications on an AO system becomes crucial to solving the aero-optic mitigation problem.

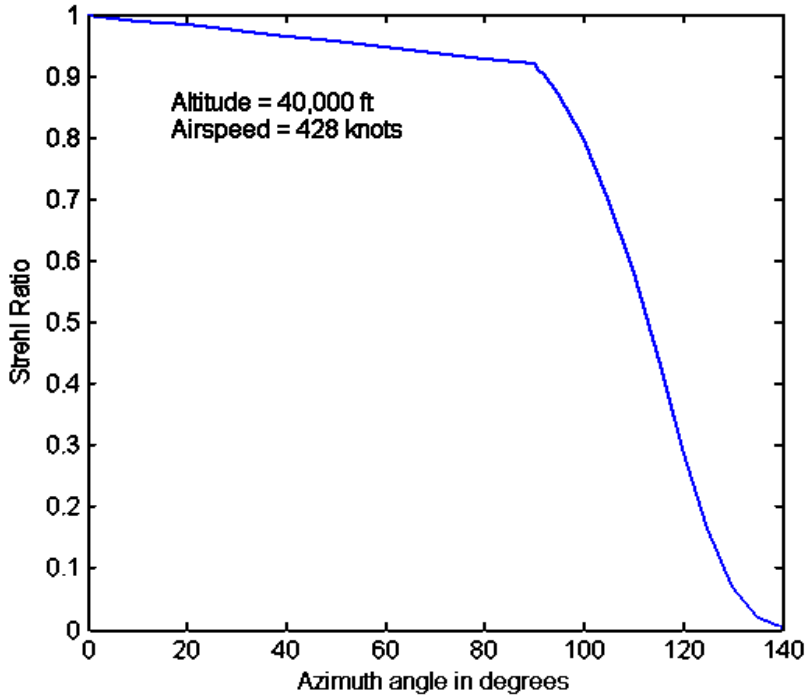

Figure 3.2: Demos Kyrazis' prediction of Strehl ratio versus azimuth angle in degrees.

3.1.2. Shear Layer Thickness

In general, most experimental shear layer studies report their results in terms of measures of the shear layer's thickness, the most common of which are either vorticity thickness, δ_ω, or momentum thickness, θ, given respectively by

$$\delta_\omega = \frac{U_U - U_L}{\left.\frac{dU}{dy}\right|_{\max}} \tag{3.1}$$

and

$$\theta = \int_{-\infty}^{+\infty} \frac{U(y) - U_L}{U_U - U_L}\left(1 - \frac{U(y) - U_L}{U_U - U_L}\right)dy\,. \tag{3.2}$$

These two measures are approximations of the on-average structure size in the vertical or cross-stream direction. Although highly turbulent, a shear layer experiences a linear growth rate in terms of its vorticity thickness and momentum thickness due to the pairing process undergone by the large-scale vortical structures convecting downstream. This linear growth rate is shown in Fig. 3.1 by the dotted lines bounding the vortex contours. Extensive experimental results for the growth rate of shear layers with matched density in the two streams at the splitter plate and with convective Mach numbers less than ~0.45 was conducted by Brown and Roshko [13]. The convective Mach number is defined as $(U_U - U_L)/(a_U + a_L)$ where U and a are the free stream velocity and speed of sound, respectively and the subscripts *'U'* and *'L'* represent the upper and lower streams, respectively. In another study by Brown [14], an analytical prediction for the growth rate of a temporally growing shear layers is given by

$$\frac{\delta_\omega}{x} = C_\delta \frac{(1-R)\left(1+s^{\frac{1}{2}}\right)}{\left(1+R\,s^{\frac{1}{2}}\right)} \tag{3.3}$$

where $R = U_L/U_U$, $s = \rho_L/\rho_U$, and $C_\delta = 0.085$. This relation is further supported by Dimotakis' shear layer growth rate prediction which reduces to Eq. (3.3) when the vortical structure size is small compared to position [15].

With the goal of developing a relationship between a shear layer's optical properties and its vorticity thickness, several simulations were performed comparing the weakly-compressible model vorticity results to the corresponding predicted growth rate given by Eq. (3.3). Figure 3.3 shows vorticity thickness versus downstream distance for the simulated shear layer shown above in Fig. 3.1. The numerically computed vorticity thickness (shown by ▲'s in Fig. 3.3) has an approximate growth rate of 0.131, closely agreeing with the predicted growth rate from Eq. (3.3) of 0.13 (shown by a solid line in Fig. 3.2). These results are similar to those computed by Jumper and Fitzgerald shown previously in Fig. 2.16 (B) for varying initial half shear layer thicknesses, $\delta_i/2$. In each of the computations referred to in this paper, a series of approximately 8,000 timesteps was run, with approximately 33 μs between timesteps. Simulations were performed using an initial vortex core size (initial half shear layer thickness) of 0.01725 meters and a rectangular velocity grid spacing in both the *x*- and *y*- directions of 0.005 meters.

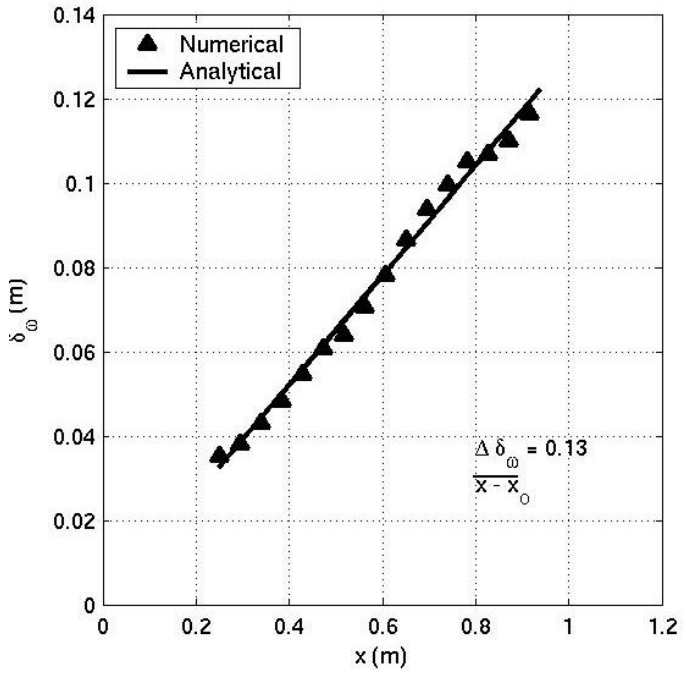

Figure 3.3: Vorticity thickness versus downstream distance from the splitter plate for the simulated shear layer shown in Fig. 3.1 where the ▲'s represent the numerically computed vorticity thickness and the solid line represents the predicted vorticity thickness according to Eq. (3.3).

Due to the optical nature of this research it became important to characterize the shear layer in terms of its optical characteristics. The goal was to perform a "system identification" of the unforced shear layer in terms of its dominant frequencies and relate this back to the commonly used experimental measure of vorticity thickness. In addition, such an optical characterization provides a non-intrusive means of measuring and classifying shear layer flow characteristics for future research.

3.1.3. Optical Characterization

This section outlines the procedure used to derive another thickness measure in terms of the shear layer's optical characteristics. The goal of this analysis was to provide a means of characterizing a shear layer's optical properties and link those back to the

commonly used vorticity thickness measure defined above in section 3.1.2. An optical characterization was performed by numerically propagating several small-aperture laser beams perpendicularly through a simulated shear layer at various locations downstream from the splitter plate. When a small-aperture beam is projected through the experimental turbulent flow field, its emerging angle, $\theta_j(x,t)$, can be recorded at rates exceeding 100 kHz. This time series of angles, referred to as the beam's "jitter", was used to determine the *natural* frequencies present within the shear layer flow. Thermodynamic properties, including time-dependant density fields, were computed from the series of velocity fields and used to determine the effect of the laser propagating through the shear layer. Jitter signals were obtained from the weakly-compressible model by first calculating a time series of *OPL* and *OPD* from the density field using Eqs. (2.2) and (2.3). The jitter angles were then computed using Eq. (2.4). Finally, a spectral analysis was conducted to determine the frequency content of the jitter signals. Since the beam's deflection is caused primarily by the density deficit present in the large-scale structures followed by the surplus density between structures [5], these signals provide information about the coherence lengths of the aberrating structures convecting through the beam.

Figure 3.4 (A) gives the power spectral density (PSD) of the jitter signals at several locations downstream from the splitter plate. A weighted average or "natural optical frequency" at each x-location was computed from the PSD's using,

$$f_n(x) = \frac{\int PSD(f,x)\, f\ df}{\int PSD(f,x)\ df} \tag{3.4}$$

where f_n represents the "natural" unforced optical frequency in the shear layer at each particular x-location and df indicates frequency is the variable of integration [16]. Figure 3.4 (B) shows a plot of the natural optical frequency versus downstream distance from the splitter plate. The results displayed in Figs. 3.4 (A) and 3.4 (B) were obtained using a numerical sample rate of approximately 33 μs. At each x-location, the PSD was calculated for a series of 4,096 consecutive timesteps. Twenty different runs, each consisting of 4,096 timesteps, were averaged to obtain the PSD plots shown in Fig.3.4 (A) for a given set of flow field conditions. Figure 3.4 (B) shows a 1/x relationship between the natural optical frequency, f_n, and downstream location, x, where the highest frequencies occur closest to the splitter plate corresponding to the smallest large-scale structures. As the structures grow with downstream distance, the corresponding frequencies of a small-aperture beam traversing the flow decreases.

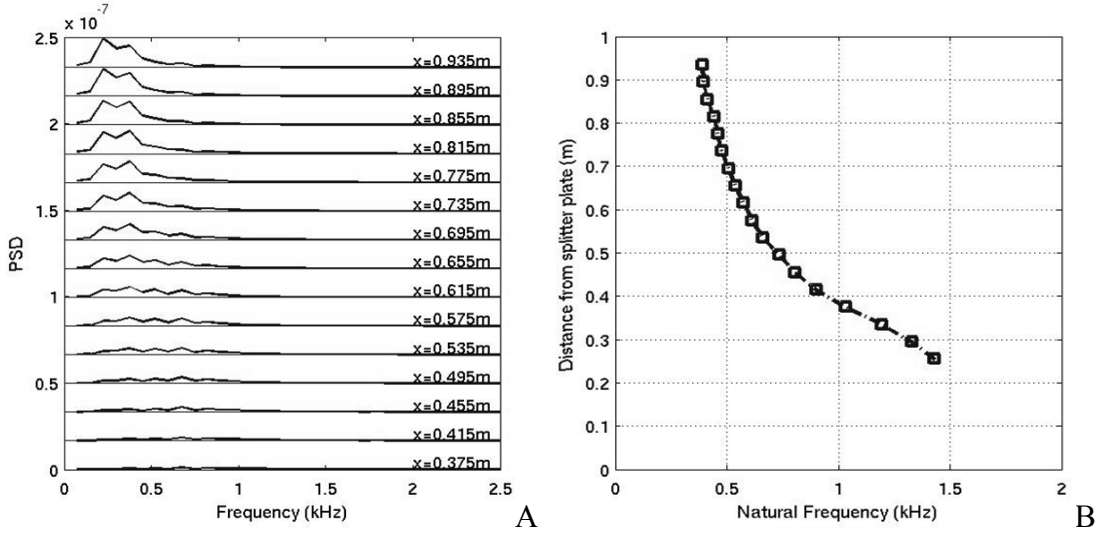

Figure 3.4: (A). PSD for flow-induced jitter angles at various downstream distances from the splitter plate for an unforced shear layer (B). Natural optical frequency, f_n, versus downstream distance from the splitter plate for an unforced shear layer.

It should be noted that Eq. (3.4) provides a means of calculating the average frequency versus downstream distance based upon numerical data. Therefore, when applying this method to experimental data, great care must be taken in filtering out any frequencies not associated with the shear layer dynamics themselves [31].

As mentioned above, these frequencies can be related to an average *optical* coherence length by dividing the convection velocity, U_c (in this case 147.87 m/s), by the natural optical frequency, f_n;

$$\Lambda_n(x) = \frac{U_c}{f_n(x)}. \tag{3.5}$$

As each coherent vortical structure passes through one of the small-aperture lasers, the beam undergoes one full cycle of beam jitter corresponding to one full wavelength of optical coherence length. This means that optical coherence length, as defined in Eq. (3.5), is a measure of the statistical, on-average, streamwise size of the large-scale vortical structures passing through the laser beam (i.e., spacing between large-scale structures). Figure 3.5 shows a plot of optical coherence length versus downstream distance. As expected, the range of natural optical frequencies and consequently optical coherence lengths vary with differing shear layer conditions, corresponding to the relationship between a shear layers growth rate and its velocity ratio [17, 18].

Similar to vorticity thickness, the unforced shear layer structures also experience a linear growth rate in terms of optical coherence length. However, when comparing Fig. 3.5 to Fig. 3.3, a difference between growth rates is evident. For the shear layer case shown in these two figures, a numerical optical coherence growth rate of 0.37 compared to a numerical vorticity thickness growth rate of 0.131 was computed. Therefore the

spacing between structures grows at a faster rate than their "thickness" in the cross-stream direction.

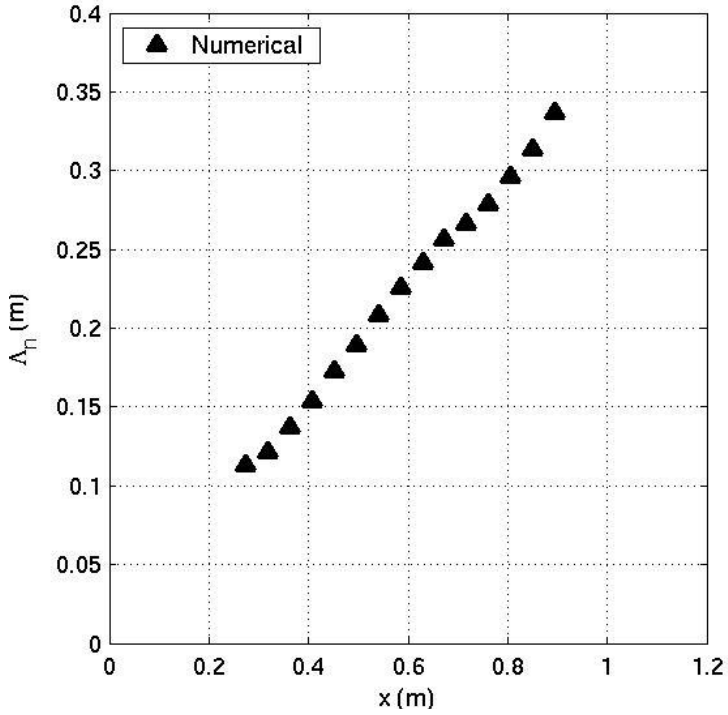

Figure 3.5: Optical coherence length (meters) versus distance downstream from the splitter plate given the shear layer shown in Fig. 3.1.

Several more shear layer cases were simulated with varying upper and lower stream velocities to further investigate this difference between growth rates. Each case was simulated using a rectangular grid with 0.005 meter spacing in the *x*- and *y*-directions. Time-averaging was calculated using a sample size of approximately 8,000 timesteps given an approximate timestep of 33 μs. Each jitter signal was evaluated at a single location in space, simulating an "infinitesimal" small-aperture beam. Time-averaged vorticity thicknesses and time-averaged optical coherence lengths were numerically computed to determine the relationship between these two measures of

structure size. Figures 3.6 (A) and (B) show vorticity thickness versus downstream distance for six different cases while Figs. 3.7 (A) and (B) show optical coherence length versus downstream distance for the same case studies. The three sets of simulation results shown in Fig. 3.6 (A) and Fig. 3.7 (A) correspond to a convective velocity of 147.87 m/s, while Fig. 3.6 (B) and Fig. 3.7 (B) correspond to a convective velocity of 117.5 m/s. As shown, the structure growth rate for both vorticity thickness and optical coherence length varies with differing shear layer Mach numbers. Given a common convective velocity, both vorticity thickness and optical coherence length increase at a greater rate as the upper Mach number is increased. It was also noted that in each case the optical coherence length increased at a faster rate than its corresponding vorticity thickness. Further computations were performed to determine a relationship between these growth rates.

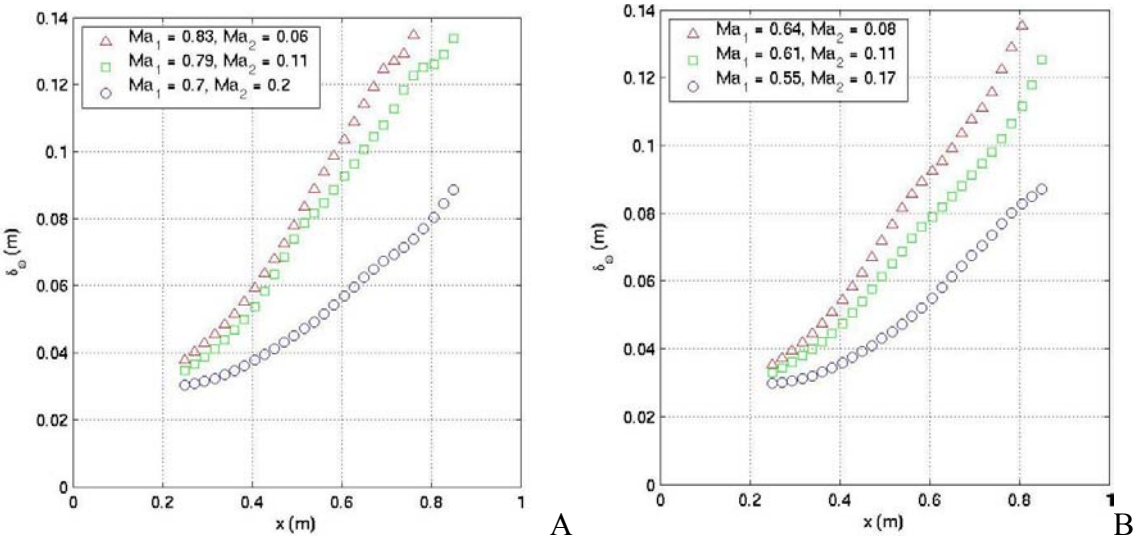

A B

Figure 3.6: (A). Vorticity thickness versus downstream distance for three different shear layer cases each with a convective velocity of approximately 147.87 m/s (B). Vorticity thickness versus downstream distance for three different shear layer cases each with a convective velocity of approximately 117.5 m/s.

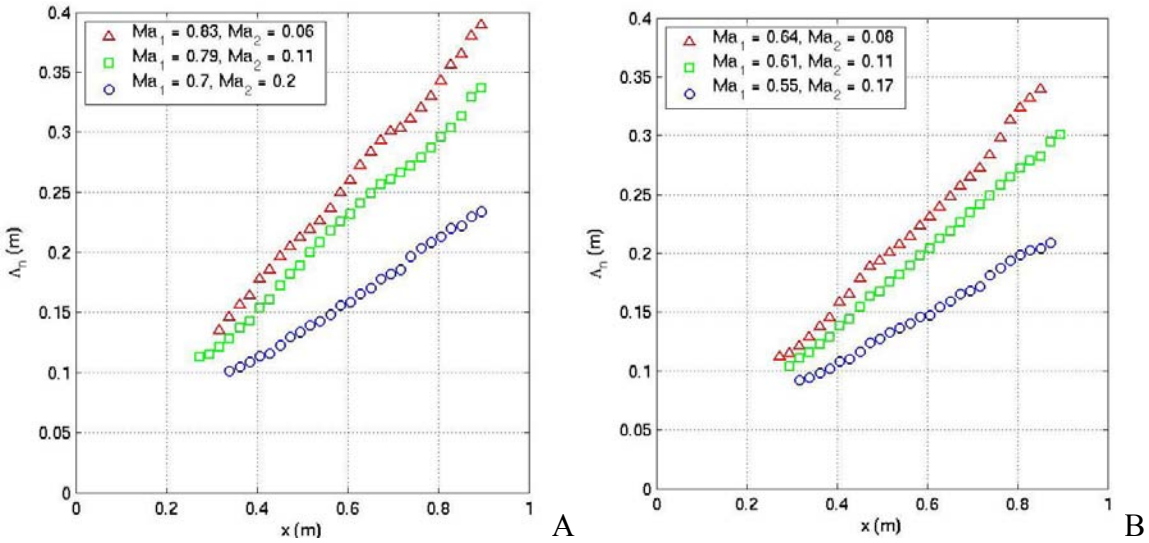

Figure 3.7: (A). Optical coherence length versus downstream distance for three different shear layer cases each with a convective velocity of approximately 147.87 m/s (B). Optical coherence length versus downstream distance for three different shear layer cases each with a convective velocity of approximately 117.5 m/s.

An average growth rate for each case shown above was computed and used to determine a relationship between vorticity thickness and optical coherence length. Figure 3.8 shows a plot of optical coherence length growth rates versus vorticity thickness growth rates. A linear fit was used to determine the factor relating these two shear layer measures, where the norm of the residuals was approximately 0.026. As seen from Fig. 3.8, the unforced shear layer structures grow at a rate approximately 3.18 times greater in the streamwise direction as compared to the normal direction. Therefore, optical coherence length closely defines the measure of vorticity thickness with a factor of 3.18 being the relationship between the coherence length in the *x*-direction (related to vortex spacing) and the shear layer thickness in the normal or *y*-direction (related to vortex size). It is important to notice that this factor of 3.18 is larger than the factor of 1.5 – 2.0 found in Ref. [13] describing the relationship between coherent-structure scale size, δ_ω, in

a shear layer and the visual shear layer thickness, δ_{vis}. Equation (3.4) uses a weighted average based upon the energy or power contained in the spectrum of frequencies present at each *x*-location. This creates an optical response which increases approximately linearly with streamwise structure size resulting in a natural optical frequency emphasizing the large-scale structures. Therefore, this difference is attributable to fact that the natural optical frequency defined in Eq. (3.4) is essentially a measure of the vortex spacing in the *x*-direction rather than the visual shear layer thickness in the y-direction, referred to in Ref. [13]. However, the factor of 3.18 does agree with results given in Refs. [20] and [13], where it is noted that a shear layer's large-scale structures are typically *spaced* a distance approximately three times the shear layer's thickness at each respective *x*-location.

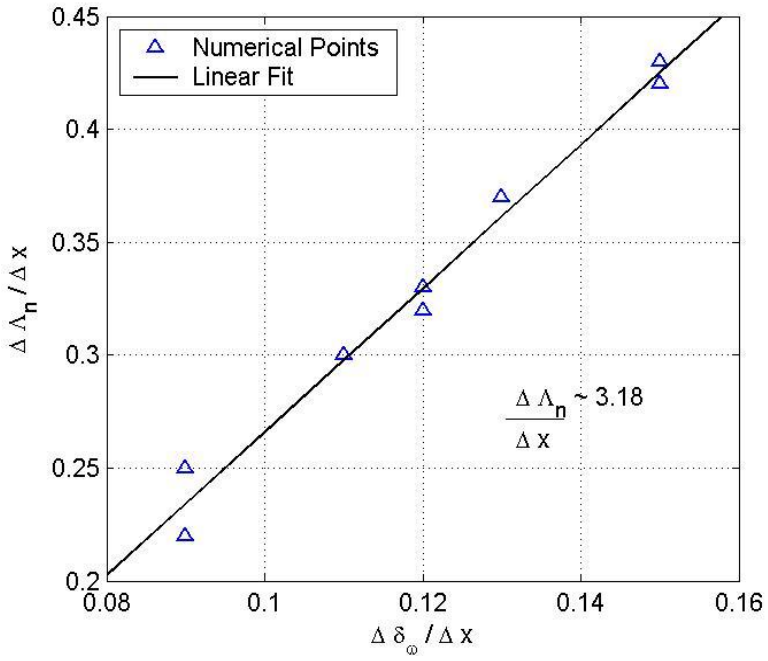

Figure 3.8: Averaged optical coherence length growth rates versus averaged vorticity thickness growth rates given varying upper and lower stream velocities computed numerically.

The results shown in Fig. 3.8 are listed below in Table 3.1 along with their respective convective velocities and velocity ratios. On average, both the optical coherence length growth rate and the vorticity thickness growth rate increase as the ratio of lower stream velocity to upper stream velocity decreases. In other words, as the difference in velocity between the upper and lower streams increases so do the rates at which the large-scale structures grow as well as the spacing between them.

Table 3.1

NUMERICAL AND ANALYTICAL SHEAR LAYER CHARACTERISTICS WITH CORRESPONDING CONVECTIVE VELOCITIES AND VELOCITY RATIOS (s = 1.0)

U_c (m/s)	R	$\Delta\Lambda_n/\Delta x$	$\Delta\delta_\omega/\Delta x$
106	0.06	0.42	0.15
147.9	0.08	0.43	0.15
147.9	0.13	0.37	0.13
148.5	0.15	0.32	0.12
117.5	0.18	0.33	0.12
127.5	0.19	0.30	0.11
147.9	0.28	0.25	0.09
117.5	0.31	0.22	0.09

Although a density ratio, *s*, of 1.0 has been assumed throughout this numerical study, it seems reasonable that the form of the well-established vorticity thickness growth rate equation (Eq. (3.3)) [13, 15], would also be relevant for optical coherence length growth rates. Therefore, optical coherence growth rate may be predicted by

$$\frac{\Lambda_n}{x} = C_\Lambda \frac{(1-R)\left(1+s^{\frac{1}{2}}\right)}{\left(1+R\,s^{\frac{1}{2}}\right)} \tag{3.6}$$

where the new constant, C_Λ, is equal to 0.27 (this value was obtained by multiplying the vorticity thickness constant [13] by the scaling factor 3.18 derived above). While the experimental value of C_Λ should also be close to 0.27, since the DVM slightly over predicts observed experimental shear layer growth rates one would expect that the value of C_Λ be slightly different if determined either by experiment or another type of numerical method. As a result, a correction factor of 0.86 was computed based on the numerical results given in Table 3.1 and the analytically calculated growth rates using Eq. (3.6) (assuming a density ratio of 1.0). After applying this correction factor to Eq. (3.6), the predicted optical coherence length for the previously studied shear layer case (Fig. 3.5) was computed and plotted against the numerically computed growth rate. Figure 3.9 shows good correspondence between the analytically computed optical coherence growth rate of 0.36 and the numerical optical coherence growth rate of approximately 0.37. Note this comparison essentially provides an assessment between numerical and experimental optical coherence growth rates since the analytical equation (Eq. (3.6)) may be linked back to experimental data reported in Ref. [14].

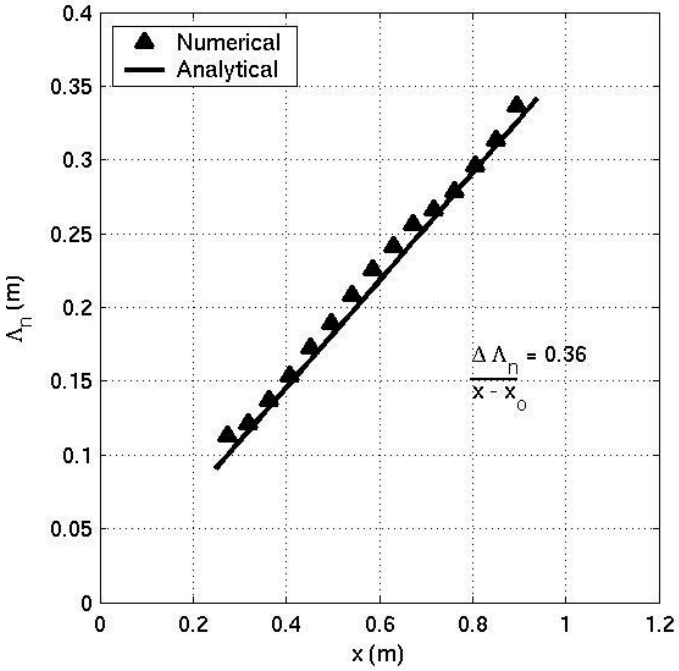

Figure 3.9: Natural coherence length versus downstream distance for an unforced shear layer with U_U = 261.04 m/s and U_L = 34.7 m/s.

For applications in which optical (non-intrusive) measuring techniques become more appropriate, optical coherence length provides a means of analyzing and characterizing the shear layer's flow dynamics. It also affords a link between commonly used thickness characteristics and optical characteristics of a free shear layer. In addition, such a relationship becomes beneficial when analyzing the optical response of a shear layer to forcing described in the following section.

3.2. Forced Shear Layer

One means of gaining a better appreciation for a shear layer's dynamics is to study its response to prescribed flow perturbations. Several studies have shown that

forcing a shear layer produces distinct alterations to the flow structures and the pairing process within a certain region of the flow [10, 18, 19, 20, 16]. Ho and Huang [10] demonstrated the ability to manipulate the shear layers growth rate in which two, three, and even four vortices were observed to merge. A global feedback mechanism in accord with the flows local stability was thought to control the amalgamation process. Oster and Wygnanski [18] also state that forcing enhances the coalescence of neighboring vortices, increasing the initial growth rate of the layer. This produces a "regularized" region where the Reynolds stress changes sign indicating an extraction of energy from the flow, while the fluctuating intensity in the spanwise direction decreases causing the flow to become more two-dimensional. Freud and Wei [19] used a wave-packet model to determine whether or not small perturbations may be used to produce a more regular and hence quieter flow. It is shown that the two most energetic POD modes calculated from the flow seem to organize themselves or become more regular in the presence of forcing.

As described in Section 1.1.2 and expanded upon in Section 2.3, bandwidth constraints associated with current conventional AO systems limit, and in many cases prevent, the ability to successfully correct for optical aberrations resulting from shear layers. In addition, the disparity between frequencies present within high-speed aero-optic flows and the bandwidth capabilities of state-of-the-art technology suggests an insurmountable challenge in the near future. In contrast, over the past several years work at Notre Dame has made progress towards overcoming the current bandwidth limitations by altering the flow field itself in a "predictable" manner. If a region of "regularized" flow could be produced, then a control system may be able to perform predictive AO corrections based upon *a priori* knowledge about the organized large-scale structures.

The following section presents regularization results based upon several numerical studies, which in turn led to a successful regularization experiment performed at the University of Notre Dame for a high-speed shear layer [39, 41].

3.2.1. Background of the Forced Shear Layer

Dating back to the 1800's, observations were first made that external excitation could influence a flow [46, 47]. In 1857, Count Schaffgotsch performed an experiment with a single gas-flame surrounded by a tube. While standing at some distance away from the flame, Schaffgotsch noticed that the flame would "quiver" when he raised his voice to a note corresponding with the tube [46]. Shortly after, John Le Conte attended a musical performance where he noted a similar acoustic influence to an open flame. He writes,

> "Soon after the music commenced, I observed that the flames in the gas-lit wall sconces exhibited pulsations which were exactly synchronous with the audible beats . . . It was exceedingly interesting to observe how perfectly even the trills of this instrument [violoncello] were reflected on the sheet of flame. A deaf man might have seen the harmony . . . I likewise determined, by experiment, that the effects were not produced by jarring or shaking the floor and walls of the room . . . but must have been produced by the direct influence of aerial sonorous pulses on the jet." [47]

Afterwards Tyndall performed a series of subsequent experiments further confirming these observations [46]. Learning that a flow could be influenced, or furthermore controlled, through external excitation was indeed a significant finding. Since that time several studies have been conducted investigating the regularizing effect forcing has on shear-layer flows [10, 18, 19, 20, 41, 45]. Several different methods of forcing, including free-stream velocity perturbations, acoustic waves, and mechanical vibrations, have been

shown to successfully alter a shear layers' original state. In each case, a region of large-scale structures becomes more regular maintaining a similar shape and size while convecting downstream. The location of this region appears to be dependent on both the shear-layer's flow conditions and the forcing parameters.

In a paper written in 1982, Oster and Wygnanski showed the susceptibility of a two-dimensional turbulent mixing layer to periodic forcing [18]. While varying both the forcing amplitude and forcing frequency they observed three distinct regions of development within the forced flow. Figures 3.10 (A) and (B) give the experimental shear layer response to single-frequency forcing reported by Oster and Wygnanski. As shown, the momentum thickness initially grows at a faster rate than the unforced case until leveling off over a region of "regularization" where pairing is inhibited. Finally, the shear layer begins growing at a rate similar to the unforced case further downstream.

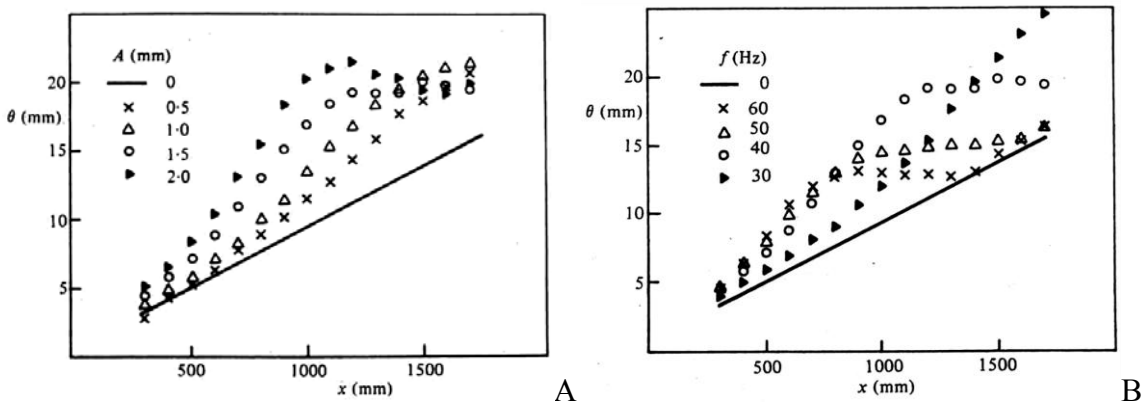

Figure 3.10: (A). Effect of amplitude of oscillation on the shear-layer momentum thickness for a trailing-edge flap, 1.0 cm long, located at the trailing edge of the splitter plate, forced at 40 Hz, (B). Effect of frequency of oscillation on the shear-layer momentum thickness for a trailing-edge flap, 1.0 cm long, located at the trailing edge of the splitter plate, forced at an amplitude of 1.5 mm [18].

In a later paper, de Zhou and Wygnanski [45] were able to perform hot-wire measurements of a forced shear layer to observe more closely the detailed forcing effect that gave rise to the flattening of the momentum thickness. A selected result from that paper is shown in Fig. 3.11, for the phase-lock averaged vorticity field of a shear layer under single frequency forcing. On average, Fig. 3.11 shows that the shear layer's stabilization in growth is the result of "regularizing" the coherent structures in the shear layer.

Figure 3.11: Phase-lock averaged vorticity plots of a low speed shear layer under single frequency forcing [45].

While each of these studies demonstrated an ability to regularize or control a shear layers large-scale structures through external excitation for low-speed flows, the same effect for high-speed shear layers remained in question. Since that time, work at the University of Notre Dame began to address this area of uncertainty. In 2000, Hugo and Jumper published a paper in which acoustic forcing was used to control a heated jet. They were able to improve their conditional-sampling method by producing a flow that repeated every other cycle. Although still a low-speed flow, natural frequencies present within the shear layer were on the order of two to three hundred hertz [48]. Later, Duffin was able to successfully regularize the same jet through acoustic forcing in a similar experiment. The heated jet was forced at approximately 240 Hz and a large-aperture beam traversing the flow was used to make wavefront measurements. Duffin found that

the waveform pattern, while containing the forcing frequency, also contained the subharmonic. Duffin's results showed that the waveform pattern was near periodic at 120 Hz. The repeatable wavefronts were then used in a manual feed-forward method of performing AO corrections [8]. Finally, in 2008 Rennie and Duffin were able to regularize a high-speed shear layer through mechanical forcing, confirming the numerical results presented in the following section [41]. The success of this experiment was a critical piece in establishing the feasibility of the automated alternative AO system presented throughout this dissertation.

3.2.2. Regularization Results

In Section 3.1.3 it was shown that a shear layer contains a range of optical natural frequencies which can be used to define the average optical coherence length or structure size in the streamwise direction. At each location downstream from the splitter plate, the shear layer contains a dominant "natural" frequency. This frequency may be excited, or forced, in order to organize the large-scale structures within a region of the flow. In a numerical study performed by Freund *et. al.* it was shown that the most effective forcing of a shear layer is done by displacing the edge of the splitter plate in the direction normal to the its surface [19]. In the case of the discrete-vortex code, forcing was simulated by inserting the first vortex into the shear layer displaced from the splitter-plate edge in the vertical, y, direction by

$$d = A\sin 2\pi f_f \tag{3.7}$$

where A is the forcing amplitude and f_f is the forcing frequency. By forcing the shear layer at a selected "natural" frequency, a region of regularization is achieved upstream from the point where the forcing frequency is equivalent to the unforced shear layer's optical natural frequency. A range of frequencies, each with varying amplitudes, were applied to several different shear layer cases in order to establish the response of the shear layer to forcing as predicted by the DVM/WCM numerical model.

Figures 3.12 (A) and (B) show plots of vorticity thickness versus downstream distance for a shear layer forced with varying frequencies and amplitudes. Figures 3.13 (A) and (B) show optical coherence length versus downstream distance for the same set of varying forcing conditions. In Fig. 3.12 (A) and Fig. 3.13 (A) the shear layer has been forced at a constant frequency of 650 Hz while varying the amplitude. Fig. 3.12 (B) and Fig. 3.13 (B) show results for a shear layer forced with varying frequencies ranging from 525 Hz to 1 kHz while the amplitude remains fixed at 2.5 mm. The numerical results found in both sets of figures (Figs. 3.12 and Figs. 3.13) are for a shear layer with upper and lower Mach numbers of 0.79 and 0.11, respectively and a convective velocity of 147.87 m/s.

When comparing Figs. 3.12 with Figs. 3.13, it is clear that the information displays similar trends. The obvious effect of forcing is to abruptly increase the shear layers growth rate and then "stabilize" its thickness for a region preceding the position where the shear layer thickness would have been in the unforced case; at this point the forced shear layer becomes more irregular once again growing at a rate similar to the unforced shear layer. The shear layer's spreading rate is therefore slightly suspended before pairing and continuing to spread again. Increasing the forcing amplitude moves

the sudden thickening of the shear layer, related to the structure roll-up, closer to the splitter plate. Consequently, the flow reaches its full extent of regularization earlier extending the region of coherent, predictable structures. These results agree with previous research studies which measure the growth of shear layers under the influence of forcing [18, 19, 20]. Although the flow conditions differ, the resulting behavior is very similar to the experimental response reported by Oster and Wygnanski (Figs. 3.10 (A) and (B)) [18]. In both cases, increasing the forcing amplitude resulted in an earlier and more robust stabilization of the mixing layer, while decreasing the forcing frequency moved the region of regularization further downstream.

In contrast, Figs. 3.12 and 3.13 differ in that the vorticity thickness shows a flatter slope in the "region of regularization" than the optical coherence length. This is due to the fact that as the structures evolve and convect, the spacing between them grows slightly in the flow direction while retaining approximately the same thickness in the *y*-direction, thus causing the optical coherence length to maintain a slight increase with downstream distance in the regularized region. It is important to note that the forcing amplitudes shown in Fig. 3.13 may not be representative of the actual values necessary to achieve regularization in an experimental setup. Due to grid spacing and the initial size of vortices, the simulation seems to require larger amplitude values to achieve a well regularized response in comparison to forcing experiments that have been performed [41]. However, the overall trends, associated with increasing the forcing amplitude and frequency, do illustrate a shear layers response to forcing.

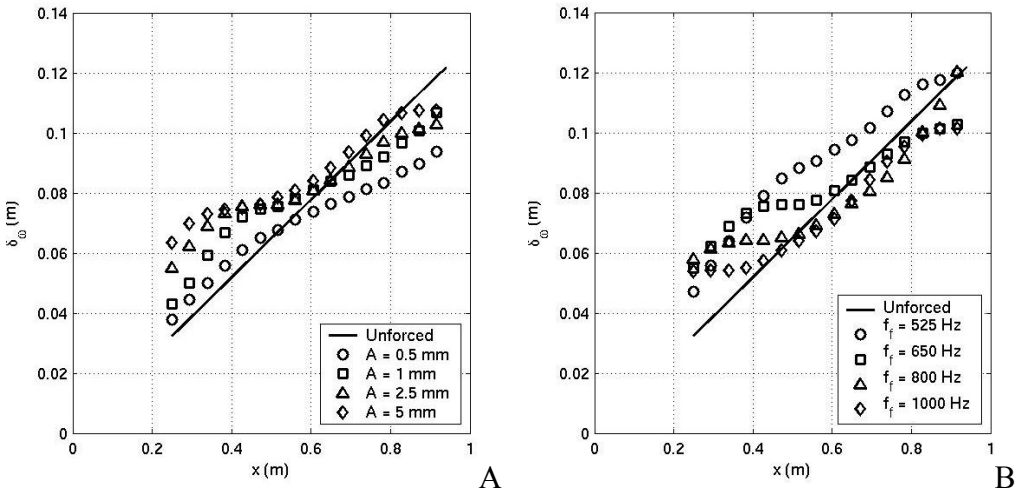

Figure 3.12: (A). Vorticity thickness versus downstream distance for a shear layer with an upper Mach number of 0.79 and lower Mach number of 0.11 forced at a range of frequencies with a fixed amplitude of 0.5 mm (B). Vorticity thickness versus downstream distance for a shear layer with an upper Mach number of 0.79 and lower Mach number of 0.11 forced at 650 Hz while varying the amplitude.

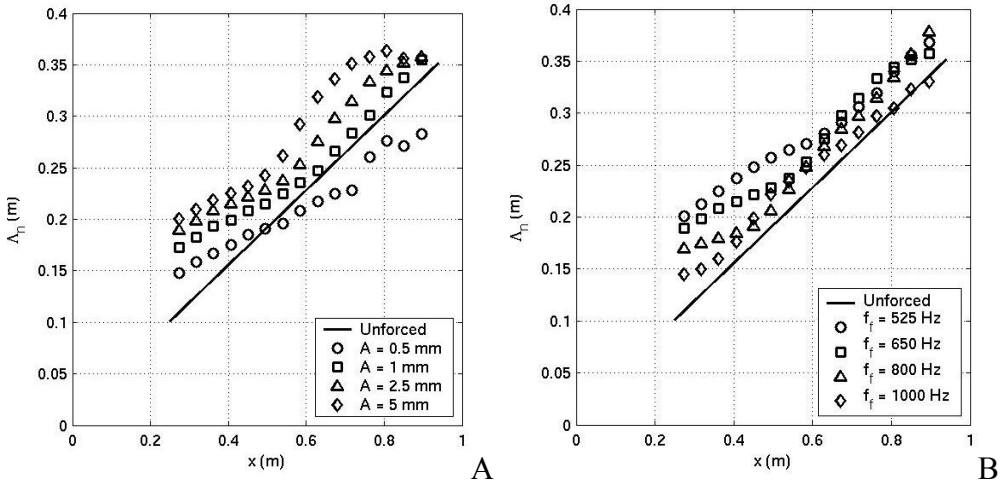

Figure 3.13: (A). Optical coherence length versus downstream distance for a shear layer with an upper Mach number of 0.79 and lower Mach number of 0.11 forced at a range of frequencies with a fixed amplitude of 0.5 mm (B). Optical coherence length versus downstream distance for a shear layer with an upper Mach number of 0.79 and lower Mach number of 0.11 forced at 650 Hz while varying the amplitude.

Vorticity contours were also created to provide a more visual means of studying the regularizing effect on the shear layers coherent structures. Figure 3.14 shows three realizations of instantaneous vorticity plots given a free shear layer forced at 650 Hz with a forcing amplitude of 2.5 mm. The three vorticity contour plots were captured at equal time delays corresponding to the same phase angle with respect to the 650 Hz forcing.

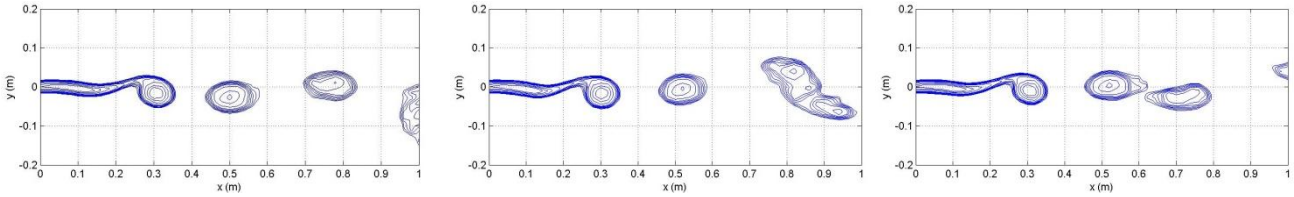

Figure 3.14: Single realizations of vorticity plots for a DVM/WCM simulated high-speed shear layer forced at 650 Hz, captured at the same phase angles of three successive cycles with respect to the forcing frequency.

The fixed phase-angle vorticity plots (shown in Fig. 3.14) were averaged to produce the results shown in Fig. 3.15. A comparison of Fig. 3.14 and Fig. 3.15 reveals that on average, as in de Zhou and Wygnaski's experiment (Fig. 3.11, [45]), the shear layer has been regularized by single frequency forcing; however, phase-lock averaging can be deceptive. It is important to note the decreasing vorticity contours in the downstream region of the shear layer shown in Fig. 3.15, also present in Zhou and Wygnanski's experimental results (Fig. 3.11). The decrease in contours is not an indication of preserving a single vortex, but rather the fact that single frequency forcing controls only the roll-up for which the forcing frequency is tailored. It is clear that the first roll-up location has been "locked" by the forcing while in the downstream region,

the normal process of pairing and merging continues to progress under the influence of the Kelvin-Helmholtz instability [16].

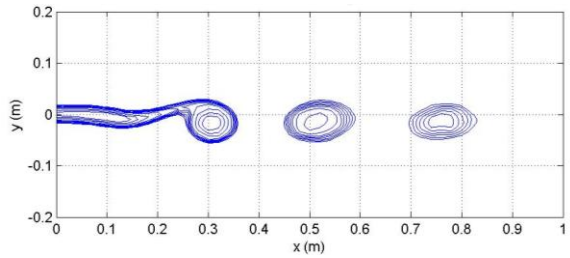

Figure 3.15: Phase-lock averaged vorticity plot for a DVM/WCM simulated high-speed shear layer forced at 650 Hz.

Another way of studying the codes results is to look at a locus of points indicating the locations of discrete vortices that define the undulation of the shear layers "contact surface". Figures 3.16 and 3.17 show two such sets of "shear-layer loci"; Fig. 3.16 shows nine successive realizations of loci for the unforced case and Fig. 3.17 shows nine successive realizations of loci for the forced case (Mach 0.79/0.11 shear layer forced at 650 Hz). Each set of figures have been taken at the same phase angle with respect to the forcing frequency of 650 Hz. The plots extend over the region for which the shear layer shows reasonably good control. An examination of the results shown in Fig. 3.17 reveals that the shear layer is extremely well controlled up to the first roll-up, and relatively well controlled up to the point where the first vortices begin to merge (second roll-up). These results imply that single-frequency forcing has successfully regularized the shear layer out to approximately 0.5 meters with some marginally-well controlled behavior slightly beyond 0.6 meters. These findings agree with the phase-averaged vorticity contours shown in Fig. 3.15. It is also consistent with the progression of vorticity thickness shown in Fig. 3.12 for the 650 Hz forced case indicating that the shear layer begins growing

again around 0.6 meters. The regularized spacing of the first roll-up allows for greater vorticity accumulation (circulation) contained in the larger, paired vortex creating a single structure which eventually merges into an agglomerated vortex consisting of three initial vortex structures. This is followed by the formation of another single vortex, after which pairing ensues and the process repeats.

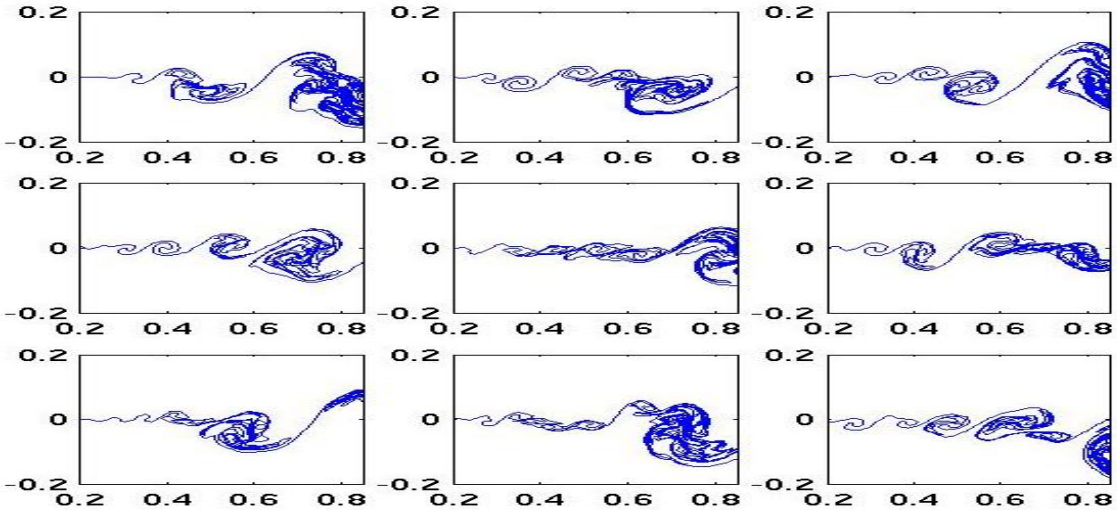

Figure 3.16: Nine successive cycles of shear layer loci for an unforced DVM/WCM simulated high-speed shear layer.

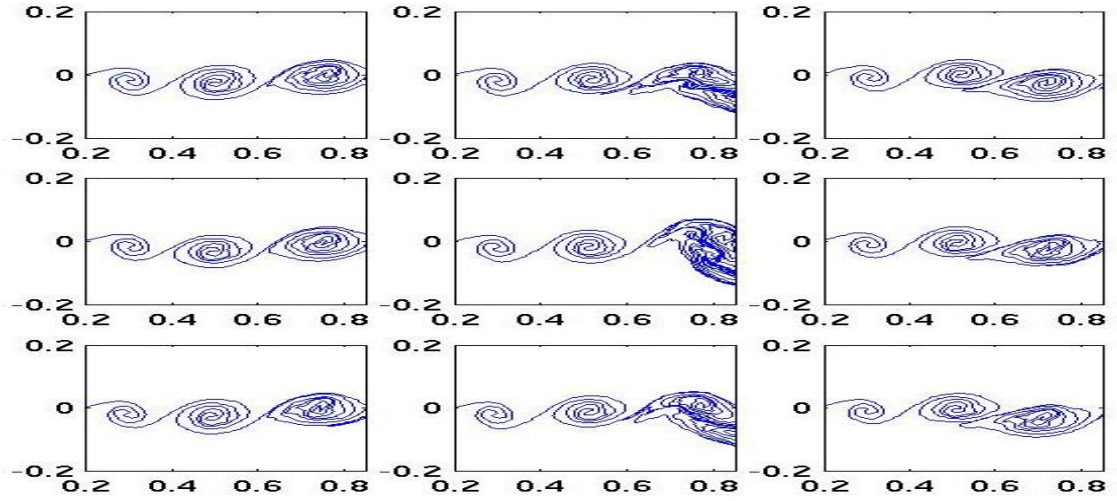

Figure 3.17: Nine successive cycles of shear layer loci for a DVM/WCM simulated high-speed shear layer forced at 650 Hz.

The differences between successive frames in Fig. 3.17 are caused by the encroachment of the "vortex-merging" phenomenon. For this particular DVM/WCM simulation, it is interesting to note that every third cycle is strikingly similar. In response to this observed three cycle repeat, phase-locked average vorticity plots were created from every third cycle of shear layer loci. Figure 3.18 shows phase-locked average vorticity contour plots for the same phase angles as the single realization shear layer loci plots displayed above in Fig. 3.17. Upon comparing the vorticity contours shown in Fig. 3.15 with those shown in Fig. 3.18 it becomes evident that a three-cycle repeat at 1/3rd the forcing frequency does a better job of capturing the actual downstream progression of the coherent structures. But even on a three-cycle repeat, regularization persists only up to the point where the forced shear layer matches the unforced shear layer thickness, after which pairing and vortex merging causes the shear layer to begin growing again. After performing several DVM/WCM simulations of a forced shear layer with varying upper and lower free stream velocities and different forcing frequencies, two- and three-cycle repeats were shown to exist in many cases becoming more dominant at the higher Mach numbers. As such, possible approaches for handling harmonics present within the regularized flow will be addressed later (Chapter 7).

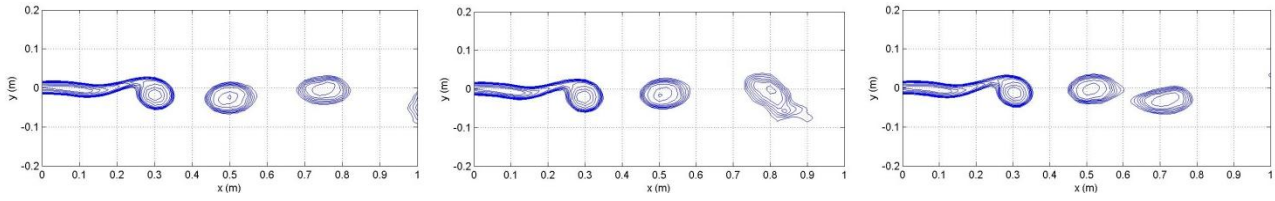

Figure 3.18: Three phase-locked average vorticity plots at the same phase angles as shown in Fig. 3.17 for every third cycle give a DVM/WCM simulated high-speed shear layer forced at 650 Hz.

The results displayed above in Figs. 3.12 and 3.13 also agree well with Oster and Wygnanski's prediction of a mixing layer's spatial extent of regularization. In Ref. [18], a regularized region, delineated by an array of quasi-two-dimensional large scale vortices that do not interact with one another, is defined by the locations, *x*, satisfying the following inequality,

$$1 < \frac{\lambda f_f}{U_c} x < 2, \tag{3.8}$$

where λ is a dimensionless velocity ratio defined as,

$$\lambda = \frac{u_U - u_L}{u_U + u_L}. \tag{3.9}$$

Given a Mach 0.79/0.11 simulated shear layer shown in Figs. 3.14, 3.15, 3.17, and 3.18, where the forcing frequency is equal to 650 Hz, Eq. (3.8) predicts a regularized region between 0.3 and 0.6 meters downstream from the splitter plate. This prediction corresponds well with the region of regularized coherent large-scale structures shown by the shear layer loci plots in Fig. 3.17 and the phase-locked average vorticity contours in Fig. 3.18.

Numerical analyses conducted as a part of this research effort also suggested that the pairing or merging mechanism was sensitive to two-frequency forcing. Specifically, the phase angle of the fundamental with respect to the subharmonic forcing frequency was shown to affect the pairing location further regularizing the shear layer. These results agree with a jet shear layer case studied by Gordeyev and Thomas [50]. Figure 3.19 shows nine successive cycles at fixed phase delays of a Mach 0.79/0.11 DVM/WCM simulated shear layer forced at 650 Hz and 325 Hz where the phase angle between

forcing frequencies is 320 degrees. It is clear from the images shown in Fig. 3.19 that in this case a two-cycle repeat exists and that regularization has been extended further downstream.

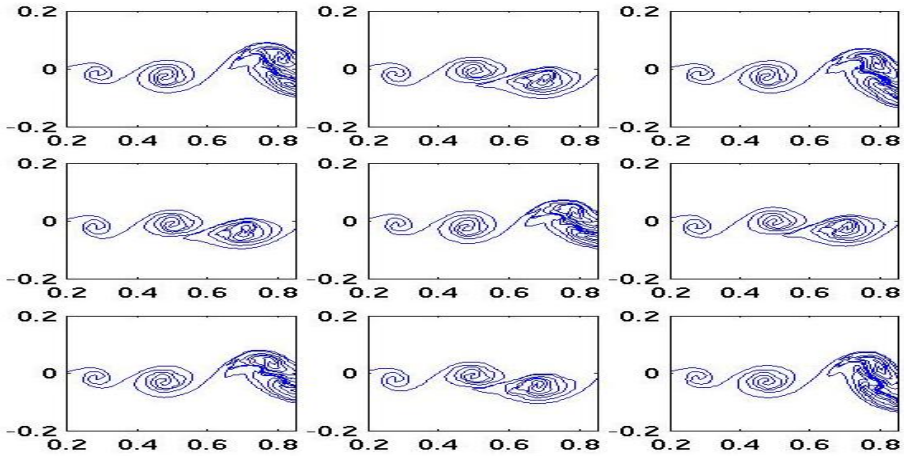

Figure 3.19: Nine successive realizations of shear layer loci for a DVM/WCM simulated high-speed shear layer forced at two frequencies, 650 Hz and 325 Hz, where the phase delay between frequencies is 320 degrees.

Although some amount of regularization may be achieved by forcing the shear layer at any of its inherent optical natural frequencies, there seems to exist a smaller range of forcing frequencies that are most effective for each shear layer case. Similar conclusions have been reported by Ho and Huang [10] and by Ho and Huerre [20]. Ho and Huang describe what they call „collective interaction' between vortices, the coalescence of several vortices rather than the typical pairing event of two vortex structures. They note the ability to manipulate the merging process of structures within a mixing layer with fairly small amounts of forcing. Ho and Huerre describe amplification rates for the range of frequencies present in an experimental mixing layer showing a clear point of maximum amplification. The numerical results presented in this section along

with the experimental results found in Refs. [10, 18, 20] indicate that the forcing frequency may be chosen based upon the desired region to be regularized. This selection depends on flow conditions for the unforced shear layer. It was also shown that two- and sometimes three-cycle repeats often develop during forcing. And the influence of these harmonics within the flow field seems to prevail more at the higher Mach numbers.

3.2.3. Bandwidth Reductions

The purpose of using flow control to force the shear layer is to produce a more periodic flow. By creating a repeating flow pattern the corresponding optical wavefronts emerging from the flow become more predictable, effectively reducing the bandwidth requirements for an AO system. Using *a priori* knowledge of the flows optical characteristics, a real-time correction may be "fed forward" in an automated control scheme. An approximation of the cyclically repeating aberrated wavefront may be determined given a set of shear layer and forcing conditions. Phase and amplitude adjustments may then be applied to the DM's wavefront correction using simple control techniques. A phase-lock-loop control approach, detailed in Chapter 4, has been proposed. It will be used to synchronize the predicted wavefront correction with the shear layer's actual emerging wavefront.

The alternative AO control strategy described throughout this dissertation would no longer require the use of a WFS, but rather two small aperture laser beams used to provide optical feedback information. Therefore, the bandwidth limiting step (WFS capture rate) may be circumvented altogether. This means the previously uncorrectable example described in Section 2.4.3 of a high-speed shear layer whose natural frequencies

approach 800 Hz now becomes feasible. The significant reduction in the bandwidth constraint for the AO system represents a momentous breakthrough in the pursuit of correcting high-speed aero-optic disturbances.

It should be noted here that the phase-lock-loop control scheme, as defined in this dissertation, is designed to operate in the case where periodic regularization occurs within the shear layer. When the large-scale structures begin experiencing a more dominant two- or three- cycle repeat, as shown above in Fig. 3.19 and Fig. 3.17, the AO correction constructed from the phase-lock-loop will render less effective. Since the phase-lock-loop produces an output signal based upon a single fundamental frequency, it is incapable of accounting for any subharmonics present within the emerging optical wavefront. However, the phase-lock-loop controller should provide an effective means of performing AO corrections on a forced shear layer whose character is dominated by a single frequency. The phase-lock-loop control strategy itself should also afford subsequent research efforts, following this dissertation work, a basis for tackling the two- or three-cycle repeat condition. Suggestions for handling these cases are outlined in Chapter 7.

3.3. Summary of Optical Characterization

The DVM/WCM model was used to study the optical characteristics of the unforced and forced free shear layer. The results reported above demonstrate that an optical interrogation of a variable-index-of-refraction shear layer yields similar information to other methods of documenting the shear layer's characteristics. Optical

coherence length, a statistical measure of the on-average large-scale structure size in the streamwise direction showed a linear growth rate of approximately 3.18 times that of the vorticity thickness growth rate. This factor agrees with previously reported vortex spacing discussions [13, 20]. Because a linear relationship exists between the shear layer's vorticity thickness, δ_ω, and its optical coherence length, Λ_n, optical measurements provide a non-intrusive means of measuring the shear layer's local structure spacing in the *x*-direction and could be useful when intrusive ways of measuring thickness are difficult or impossible, as in chemically- or thermally-hostile environments (jet-engine exhaust, for example).

In addition, this numerical study demonstrated the feasibility of optically regularizing a high-Mach subsonic shear layer. Results showed that stabilizing the fluid mechanics of the shear layer also regularized its optical characteristics. By mechanically forcing the shear layer's origin (or vertically displacing the first vortex in the numerical shear layer's free vortex sheet), a region of more regular large-scale coherent structures were formed. Consequently, the optical wavefront emerging from that region was also regularized creating a waveform more amenable to wavefront estimation. The following chapter describes an alternative control method for constructing AO corrections based on a phase-lock-loop. While this control strategy is designed for a regularized shear layer containing primarily one fundamental frequency, it may also offer possible avenues for addressing subharmonics within the flow field.

CHAPTER 4:

ALTERNATIVE AO CONTROL SYSTEM

4.1.Control Objective

One of the primary goals of this research was to develop a means of performing real-time AO corrections to an aberrated beam emerging from a high-speed aero-optic shear layer. Since current technology prevents the conventional AO system from being capable of such corrections due to bandwidth limitations, the problem was approached from a different angle. Realizing that the necessary bandwidth improvements to system components (such as the WFS) posed a seemingly insurmountable task at present, an alternative approach was proposed. This alternative AO approach incorporates flow control and a phase-lock-loop controller. Flow control is used to "regularize" the shear layer's large-scale structures and consequently it's optically aberrating character as described in Section 3.2.2. Real-time corrections are then performed based upon an estimation of the aberrating optical wavefront. Rather than incorporate the bandwidth limiting WFS measurements, this technique uses small-aperture jitter signals for gathering amplitude and phase feedback information. The estimated wavefront is synchronized with the shear layer's actual aberrating wavefront by adjusting the amplitude and phase of the estimation. By predicting the optical character of the shear layer's emerging wavefront, fewer measurements are necessary thereby reducing the

bandwidth requirements placed on the AO system. Instead of performing real-time measurements of the wavefront's amplitude, spatial frequency, and temporal frequency at capture rates consistent with the stability and update requirements discussed previously in Section 2.3.1 and Section 2.4.3, this method uses *a priori* knowledge of the regularized waveform in conjunction with sparse sensing techniques [7]. An estimation of the shear layer's emerging wavefront may be predicted from the flow's optical response characteristics (detailed in Section 3.1.3) reducing the amount of information needed to construct the appropriate conjugate correction in real-time.

Figure 4.1 (A) shows a depiction of a large-aperture beam propagating through an unforced shear layer. The aberrations induced on the emerging beam contain high-frequencies and are largely unpredictable. Figure 4.1 (B) shows a depiction of a forced shear layer whose conjugate correction may be estimated based upon flow conditions and forcing parameters. Once the estimated correction is synchronized with the regularized shear layer, the emerging beam will ideally become less aberrated (i.e., residual error will decrease) thereby increasing on-axis intensity and improving overall system performance.

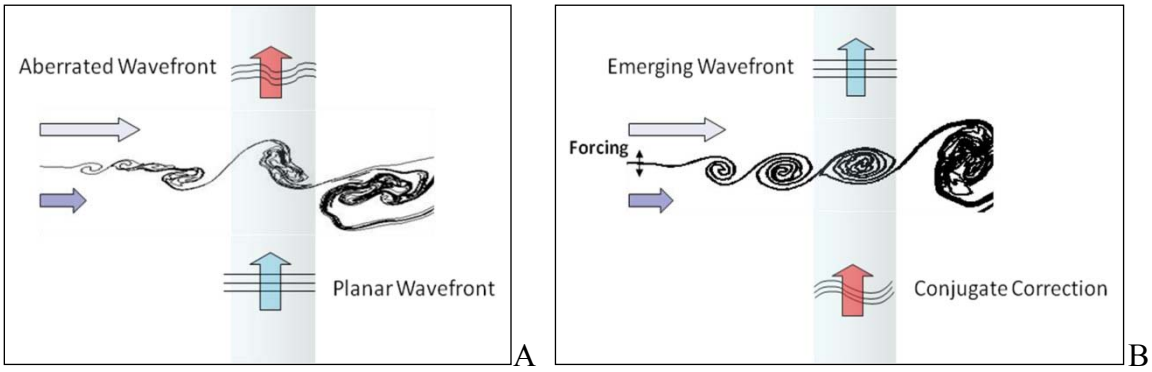

Figure 4.1: (A). Depiction of a large-aperture beam propagating through an unforced shear layer (B). Depiction of a forced shear layer where an estimated conjugate correction has been synchronized with the flows structures producing an ideally emerging planar wavefront.

While regularizing a shear-layer flow through forcing has been used for several decades, combining this technique with a synchronization control strategy represents a novel AO control approach introduced at the University of Notre Dame. In 2005, this concept was first examined using a flow-control-based AO experiment performed by Duffin [8]. A two-dimensional, planar heated jet was acoustically forced at 240 Hz with acoustic waves from a speaker placed approximately 1.0 meter from the jet. Phase-lock wavefronts averaged over one full cycle for the two-cycle repeat (i.e., at the subharmonic of the forcing frequency) of the jet's response were computed from a time series of experimental OPD measurements. Phase-lock averaged wavefronts were calculated for several different phase angles and applied to the DM during an AO correction experiment. The conjugate corrections were *manually* synchronized to the experimental aberrating wavefront. The experiment proved successful in correcting the optical aberrations of the forced heated jet, increasing the time averaged Strehl ratio from 0.64 without AO corrections (Fig. 4.2 (A)) to 0.93 with AO corrections (Fig. 4.2 (B)). These tests were performed using a wavelength of $\lambda = 0.63$ μm.

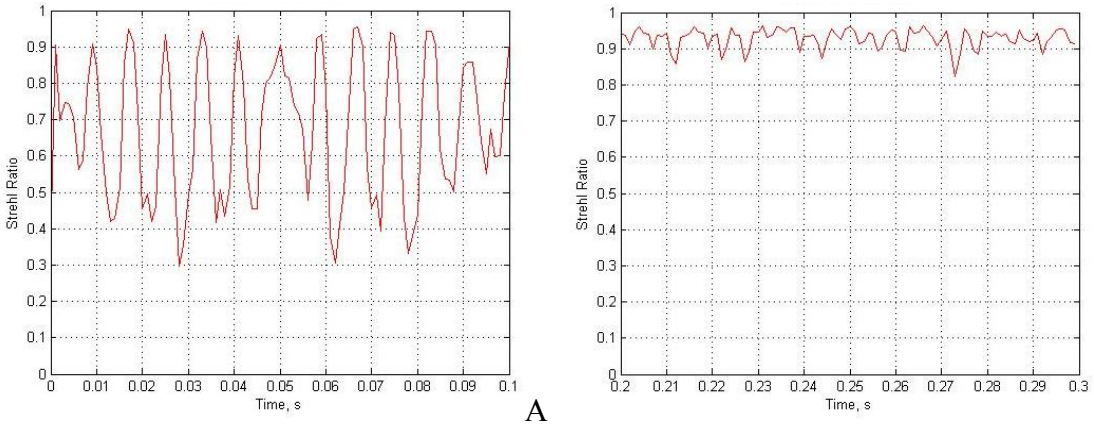

A B

Figure 4.2: (A). Time history of Strehl ratio without correction for a 240 Hz forced heated jet (B). Time history of Strehl ratio with correction for a 240 Hz forced heated jet (at $\lambda = 0.63$ μm) [8].

Then in July of 2006, a similar experiment was performed on a high-speed subsonic shear layer with an upper Mach number of 0.8 [27]. The shear layer was forced at 750 Hz and a 3-inch aperture beam was propagated through the flow approximately 0.4 meters downstream from the splitter plate. Phase-lock averaged wavefronts were computed from a series of measurements taken at phase angles between 0 and 360 degrees at 30 degree phase increments with respect to the subharmonic. First the phase-lock averaged wavefronts were subtracted from the time series of wavefront measurements in a post-process analysis to calculate the expected increase. Finally, the phase-lock averaged wavefronts were programmed into the DM and manually synchronized with the shear layer aberrations during an AO correction experiment. Real-time AO corrections were applied to the 3-inch beam propagating through the forced flow. Wavefront measurements of both the uncorrected and corrected beams were recorded and post-processed revealing an increase in time-averaged Strehl ratio from approximately 0.14 to 0.66, based on a laser wavelength of 1.0 μm. These results, as reported by Duffin [27], are shown below in Fig. 4.3. This historic experiment of a successful human-in-the-loop AO correction became the basis for developing the alterative AO controller presented in this dissertation; the goal being to automate the synchronization process without resorting to a "human-in-the-loop".

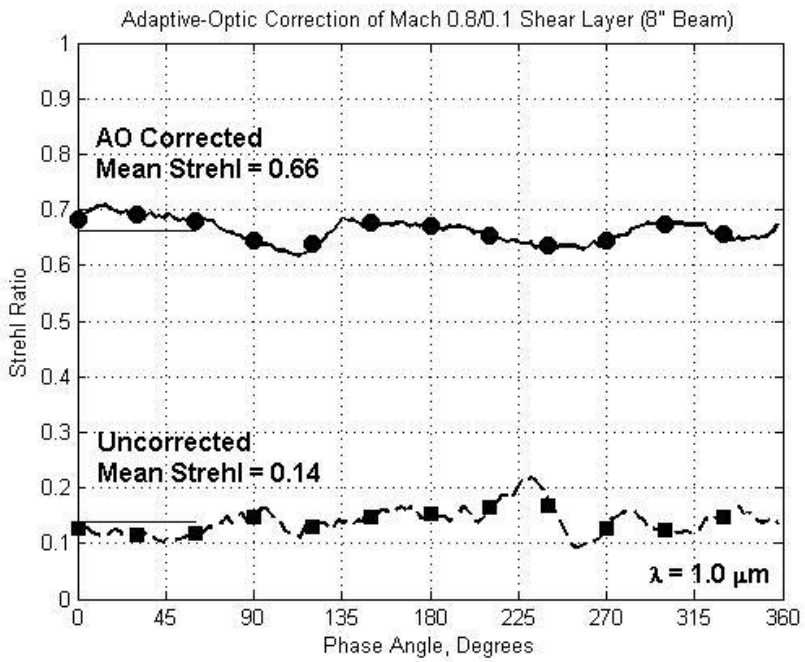

Figure 4.3: Post-processed Strehl ratio results for a man-in-the-loop aero-optic AO correction of a Mach 0.8/0.1 shear layer performed by Daniel Duffin in July of 2006 [27].

4.2. Phase-Lock-Loops (PLLs)

Phase-lock-loops (PLLs) are one of the most common feedback control systems designed and built by engineers. The PLL is a common control technique used to synchronize its output signal with a reference signal [23, 24]. First developed in the 1930's, PLLs serve a wide range of applications including radios, telephones, televisions, and computers. They are used to perform frequency synthesis, demodulation of frequency or phase modulated signals, and carrier recovery processes. By adjusting its frequency the PLL is able to synchronize itself with a reference source or input signal. A simple example, analogous to the operation of a PLL process, is the use of a tuning fork to tune an instrument. The tuning fork provides a standard of pitch acting as a reference frequency signal. The desired note is struck on the instrument while the tension on the

string is adjusted. When the note is "out of tune", there exists a discrepancy between the frequency of the tuning fork and the frequency of the note itself. The two waves interfere with one another creating an audible beat frequency. As the instrument is tuned and its frequency approaches that of the tuning fork the beats become less frequent until finally becoming inaudible. Duffin used this same concept in both his experiments when manually phasing the conjugate correction with the shear layer's *reference* wavefront [8, 27]. This idea provided the foundation for using a PLL to automate the correction process.

The typical PLL is comprised of a phase detector (or multiplier), low pass filter and loop filter, and a voltage-controlled oscillator (VCO). The loop filter provides a useful design tool for the control engineer to create the desired system tracking response. Second and third order closed loop transfer functions are commonly designed due to their stability and tracking characteristics. Figure 4.4 shows a block diagram depicting the basic PLL. PLLs respond to both frequency and phase variations that exist between the reference signal and the local output signal by adjusting the frequency of the VCO until the two signals become synchronized. The VCO operates at a center frequency which can be varied based on an externally applied signal. This provides a means of synchronizing the output signal with the reference signal [23, 24].

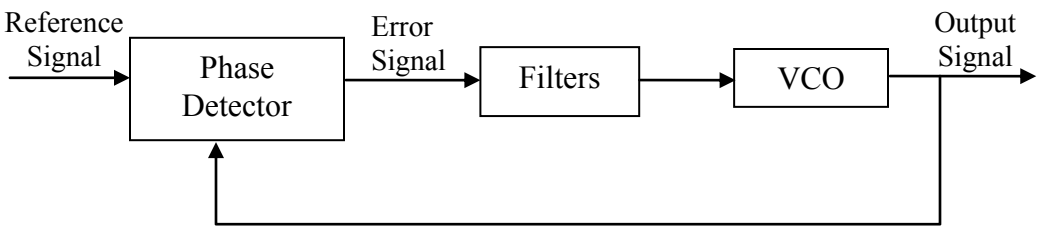

Figure 4.4: Block diagram of a basic PLL process.

The basic PLL operates similar to the tuning fork example described previously. The output signal is compared to the reference signal and a difference in frequency is detected producing an error voltage (rather than an audible beat). The VCO's output frequency is adjusted accordingly until the error approaches zero, when the PLL is said to be phase-locked [24]. There exist several different types of phase detectors, one of which is a frequency mixer. When the reference signal is mixed, or multiplied, with the VCO's output signal, the resulting signal is comprised of both a *baseband* component and a *double harmonic* component. The baseband portion is a function of the phase difference between the two input signals and as such contains important information for synchronization. Since the double harmonic portion does not contain any vital information it is filtered out isolating the baseband portion. If the phase difference between the original two signals is zero the output will also be zero requiring no change to the VCO's output. However, if the two original input signals differ in phase from one another, the filtered output signal will maintain a value other than zero. This value is directly related to the phase difference and therefore becomes the input signal controlling the VCO once appropriate filtering has taken place. The VCO then converts this input voltage to a clock signal operating at a proportional frequency. This creates a small variation in the VCO's output frequency allowing it to "catch up" or "fall back" with respect to the reference signal. Once the two signals are synchronized, the filtered baseband signal becomes zero, locking the two signals in phase.

In order to apply linear control techniques to the PLL, a more conceptual model must be used. Figure 4.5 shows the block diagram for a conceptual PLL model. A

summation block represents the mixing function of the phase detector. The output phase signal or phase-locked signal, *Y(s)*, is subtracted from the reference phase signal, *R(s)*, generating an error signal, *E(s)*. The error is scaled by K_{PD}, representing the gain magnitude of the phase detector and passed through a low pass filter, *F(s)*. The loop filter, $L_F(s)$, performs any other necessary filtering actions while maintaining closed loop system stability. Finally, the VCO acts as an integrator, where K_{VCO} represents the sensitivity constant related to that device.

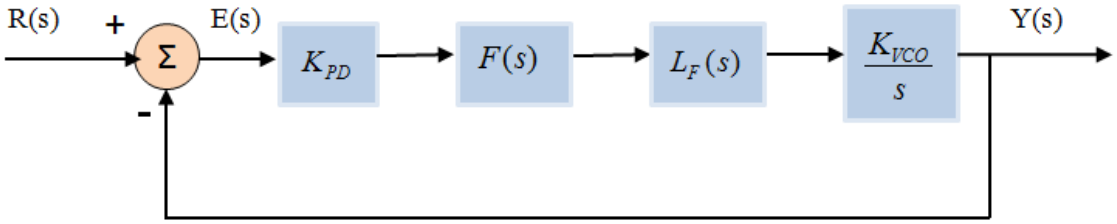

Figure 4.5: Block diagram of a conceptual or linearized model of the basic PLL.

The closed loop transfer function for the system shown in Fig. 4.5 is given by the Laplace transform:

$$T(s) = \frac{Y(s)}{R(s)} = \frac{K_{PD}K_{VCO}F(s)L_F(s)}{s + K_{PD}K_{VCO}F(s)L_F(s)}, \tag{4.1}$$

where *F(s)* represents the low pass filter and $L_F(s)$ the loop filter function designed by the engineer to meet desired response characteristics. For the given aero-optic application, the phase of the shear layer's emerging regularized wavefront is the reference source, *R(s)*, and the phase of the wavefront estimation model used to control the DM is the phase-locked signal, *Y(s)*. Further details outlining the design of the PLL used in this AO controller application follow.

4.3. AO Control System Design/Layout

This section describes the basic setup of the proposed alternative AO system while further detailing the controller's PLL process. The alternative AO system will consist of a DM, two small aperture position sensing devices, and feed-forward and feedback control circuits as shown in Fig. 4.6.

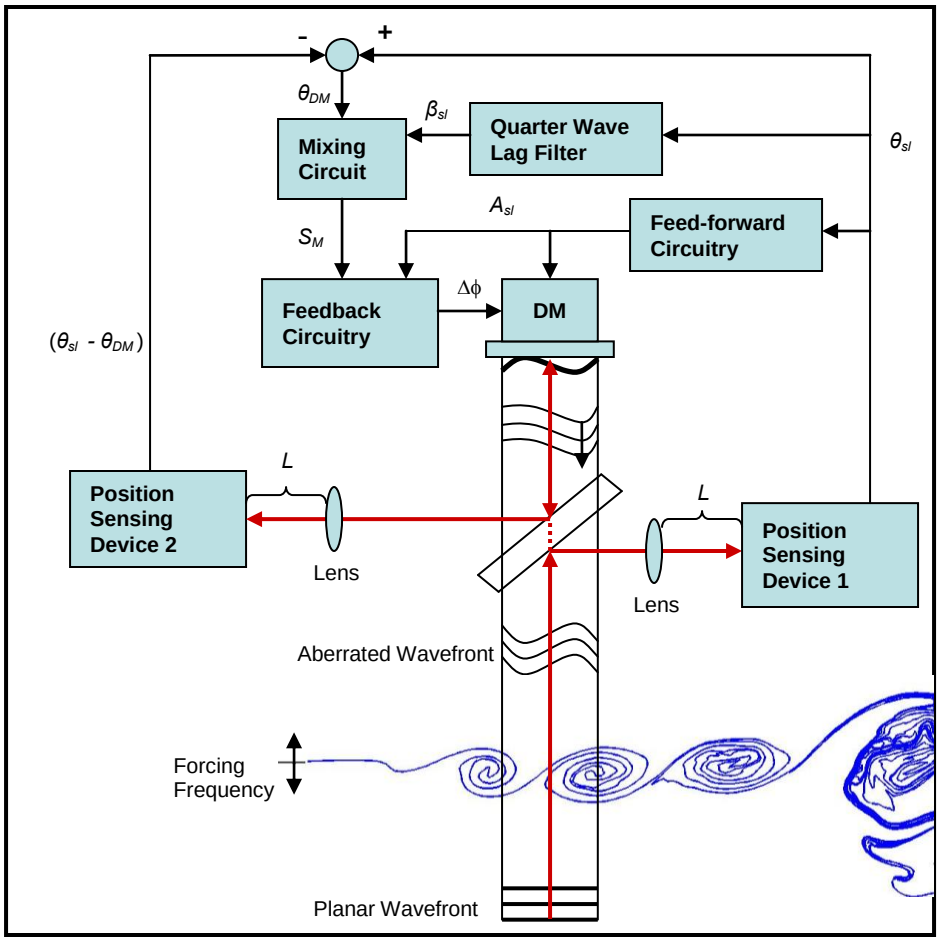

Figure 4.6: Depiction of the alternative AO system's components and setup.

The purpose of this system is to perform real-time AO corrections to an aberrating wavefront emerging from the forced shear layer using a DM; the ultimate goal being to reduce outgoing wavefront aberrations in order to increase on-target intensity. Although

no WFS is needed to operate the control loop, as in Duffin's manual phasing experiment, a WFS could be used to directly measure the residual error remaining on the beam. As such, the WFS acts only as a scoring sensor and can operate at very low frequencies for this purpose.

As indicated in the previous chapter, this alternative AO approach uses non-intrusive small-aperture beams to gather feedback information. This increases the system's bandwidth capabilities as compared to the conventional AO system which uses a WFS. A small aperture laser beam associated with a planar wavefront is propagated through a shear layer being forced at a frequency, f_f, to regularize the vortical structures as described in the Section 3.2. The emerging jitter signal (time varying signal due to the aberrating wavefront) passes through a beam splitter, directing part of the incident beam onto a position sensing device whose output can then be notch filtered. Such a method has been demonstrated at Notre Dame by M. Rennie for a Mach 0.8/0.1 forced shear layer producing a near-sinusoidal signal at the forcing frequency after notch filtering. The filtered signal generated by this sensor is then input into an analog feed-forward circuit that estimates the amplitude of the aberrated wavefront. This signal is also used in the feedback circuitry to determine the phase difference between wavefronts. The part of the beam which passes through the beam splitter is reflected off the DM and redirected by the beam splitter onto another position sensing device producing a signal equivalent to the shear layer jitter minus the DM jitter (θ_{sl} - θ_{DM}) [21]. Assuming the shear layer has been regularized and contains a single dominant optical frequency, the emerging wavefront will be akin to a traveling sinusoidal wave with an angular frequency given by

$$\omega_{sl} = 2\pi f_f \tag{4.2}$$

and a wave number,

$$k_{sl} = \frac{\omega_{sl}}{U_c} \tag{4.3}$$

where the convective velocity, U_c, may be determined by cross-correlating two small aperture beams propagating perpendicularly through the flow [22] a distance Δx apart with a time delay, τ:

$$\mathrm{U_c} = \frac{\Delta \mathrm{x}}{\tau}. \tag{4.4}$$

The shear layer's associated OPD will have an assumed form,

$$OPD_{sl}(t,x) = A_{sl}\sin(k_{sl}x - \omega_{sl}t + \phi_{sl}). \tag{4.5}$$

It is important to note that the only unknown parameters in Eq. (4.5) are the amplitude, A_{sl}, and phase, ϕ_{sl}, of the shear layer's optical wavefront. The parameters, ω_{sl} and k_{sl}, are determined from the flow and forcing conditions and will be used to drive the DM actuators. The DM's estimated conjugate correction will be of the form,

$$OPD_{DM}(t,x) = A_{DM}\sin(k_{sl}x - \omega_{sl}t + \phi_{DM}), \tag{4.6}$$

assuming the DM membrane can form the desired sinusoidal waveform. In Eq. (4.5) and Eq. (4.6), the subscripts „*sl*" and „*DM*" refer to *shear layer* and *deformable mirror*, respectively. The goal is to use estimates of A_{sl} and ϕ_{sl} to determine the amplitude, A_{DM}, and phase, ϕ_{DM}, of the DM such that $|\mathrm{OPD_{DM}} - \mathrm{OPD_{sl}}|$ is minimized. This is accomplished through a feedback control system using a PLL. An estimate of the phase difference between the shear layer's aberrating wavefront and the DM's wavefront is used to synchronize the two waveforms. Figure 4.7 shows a block diagram depicting the alternative AO control system.

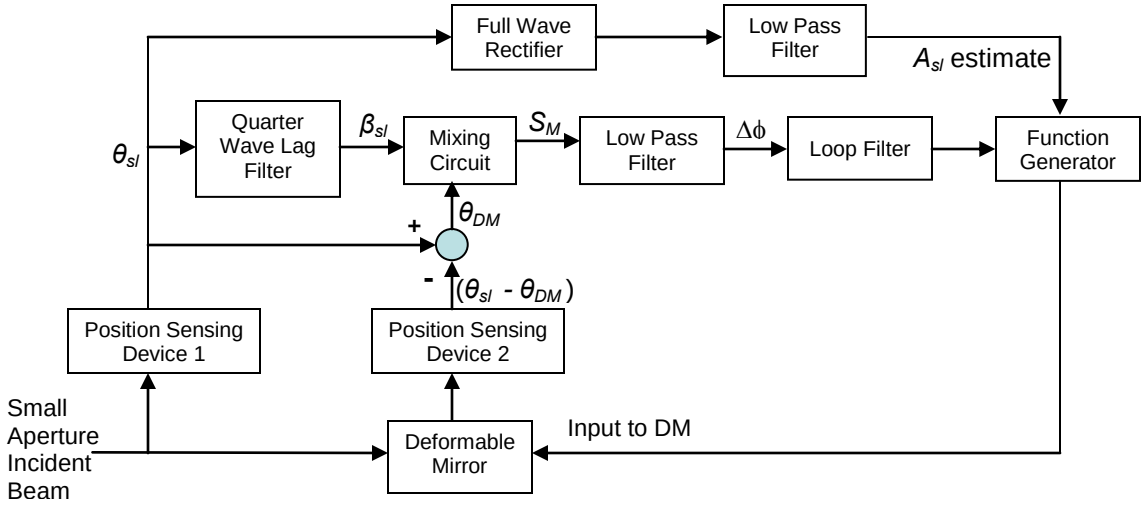

Figure 4.7: Block diagram depicting the alternative AO control system.

Referring back to Eq. (2.4), the jitter angles associated with the shear layer and DM may be expressed as,

$$\theta_{sl}(t, x_o) = -A_{sl} k_{sl} \cos(k_{sl} x_o - \omega_{sl} t + \phi_{sl}) \tag{4.7}$$

and

$$\theta_{DM}(t, x_o) = -A_{DM} k_{sl} \cos(k_{sl} x_o - \omega_{sl} t + \phi_{DM}) \tag{4.8}$$

where θ_{sl} is measured via the first position sensing device (located at the focal distance, L, of the lens shown in Fig. 4.6), and θ_{DM} is the jitter angle corresponding to the location on the DM where the beam is reflected ($x = x_o$). The second position sensing device measures the jitter angle of a small aperture beam propagated through the shear layer and reflected off of the DM producing a signal equivalent to the difference between θ_{sl} and θ_{DM}. This signal is subtracted from the shear layer jitter signal to recover θ_{DM}. The shear layer jitter signal, θ_{sl}, is then passed through a quarter wave lag filter. This filter has a unit gain and applies a $\pi/2$ phase lag at the frequency, ω_{sl}. In other words the resulting

signal may be described using a sine function rather than the original cosine function. The phase shifted signal, β_{sl}, is then multiplied with θ_{DM} in a mixing circuit to generate the output,

$$S_M = A_{DM} k_{sl} \cos(k_{sl} x_o - \omega_{sl} t + \phi_{DM}) A_{sl} k_{sl} \sin(k_{sl} x_o - \omega_{sl} t + \phi_{sl}). \tag{4.9}$$

Using a trigonometric identity Eq. (4.9) may be expressed as the sum of two sinusoids given by,

$$S_M = \tfrac{A_{DM} A_{sl} k_{sl}^2}{2} \sin(2k_{sl} x_o - 2\omega_{sl} t + \phi_{sl} + \phi_{DM}) + \tfrac{A_{DM} A_{sl} k_{sl}^2}{2} \sin(\phi_{sl} - \phi_{DM}). \tag{4.10}$$

Therefore, the mixed signal, S_M, is composed of a DC bias whose magnitude is proportional to the sine of the phase difference between the DM's waveform and the shear layer's aberrated wavefront. The mixed signal also contains a harmonic term at twice the shear layer's angular frequency, $2\omega_{sl}$. As described in the previous section, the double harmonic term is removed using an active low pass filter. As a result the filtered signal, consisting of a baseband component, has a significantly lower bandwidth than the original jitter signals.

For small angles, $\phi_{sl} - \phi_{DM}$, the filtered signal may be approximated by

$$S_{DC} \cong \frac{A_{DM} A_{sl} k_{sl}^2}{2} (\phi_{sl} - \phi_{DM}). \tag{4.11}$$

Thus, the phase difference may be extracted by rearranging Eq. (4.11) to produce

$$\Delta\phi = (\phi_{sl} - \phi_{DM}) = \frac{2 S_{DC}}{A_{DM} A_{sl} k_{sl}^{\,2}}. \tag{4.12}$$

A loop filter is then used to obtain a desired system response before the signal is finally applied to the VCO's input.

The amplitude of the estimated wavefront, A_{sl}, used to control the DM is obtained via a separate feed-forward amplitude estimator circuit. The shear layer's jitter signal, measured by the first position sensing device (refer to Fig. 4.6 and Fig. 4.7), serves as the input. The "sinusoidal" jitter signal is sent through a *True RMS-to-DC Converter* chip. The chip computes the true root-mean-square value of the AC input signal generating a DC output equivalent to

$$V_{out} = \sqrt{avg.(V_{in})^2} \,. \tag{4.13}$$

where V_{in} represents the input signal (the shear layer's jitter signal in this case) and *avg.* indicates an average magnitude or amplitude. The resulting DC signal is passed through an amplifier circuit used for calibration, applying the appropriate gain to the signal. The final output represents the amplitude of the shear layer's regularized jitter signal. This signal is used to apply amplitude adjustments to the wavefront estimation model as well as to provide the amplitude information necessary in the PLL's analog phase error computation (Eq. 4.12).

4.4. Compensator Analysis

A PLL controller was designed to synchronize the DM's conjugate correction with the regularized aberrating wavefront emerging from a forced shear layer. As depicted in Fig. 4.6, the jitter signal from a small-aperture beam projected through the flow acts as the PLL's reference source used for phase-locking. The response characteristics of the phase-locking process are dependent upon the control parameters used in the control system. System response, stability, and robustness are all key issues

that must be considered when designing an appropriate compensator for this AO control system, where the compensator is described by the transfer function:

$$G_C(s) = \frac{K_{PD}K_{VCO}F(s)L_F(s)}{s}. \tag{4.14}$$

The compensator contains two different filters designed to achieve a set of specified criteria; the predetermined filter function, F(s), is used to filter out the double harmonic described in the previous section and the loop filter, $L_F(s)$, is chosen to produce a desired closed-loop system response. A set of design criteria was chosen to aid in the design selection of the compensator parameters. Specifically, tracking error, phase margin, settling time, percent overshoot, and absolute error were analyzed in the design process of the proposed alternative AO controller.

4.4.1. Tracking Error

One of the primary control objectives for this application is to have zero steady-state error given a step change in the phase or frequency of an incoming reference signal. In other words, the PLL is designed to track both step and ramp phase inputs with zero tracking error. Consider a sinusoidal signal with frequency, ω, and phase shift, ϕ, where the frequency is a function of time and the phase shift is constant,

$$\zeta(t) = \sin(\omega(t)t + \phi). \tag{4.15}$$

The argument of the sinusoidal function given in Eq. (4.15) may also be expressed as a general phase angle varying with respect to time given by,

$$\theta(t) = \omega(t)t + \phi. \tag{4.16}$$

By taking the time derivative of the time-varying phase angle $\theta(t)$,

$$\frac{d}{dt}\left(\theta(t)\right) = \omega(t) + t\frac{d\omega}{dt} \tag{4.17}$$

it becomes clear that the frequency of a sinusoidal signal is directly related to its time-varying phase angle. More specifically, a step change in frequency is equivalent to a steady ramp change in the signals phase given zero initial conditions. Knowing this, consider the general feedback system depicted in Fig. 4.8.

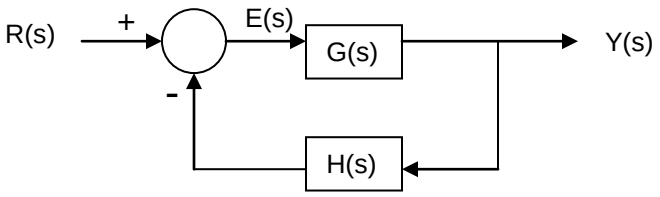

Figure 4.8: Block diagram depicting a general feedback control loop.

Using block diagram transformations and reduction techniques [29, 42] the error signal may be defined as

$$E(s) = \frac{R(s)}{1 + G(s)H(s)}. \tag{4.18}$$

The open-loop transfer function will be expressed in the following general form

$$G(s)H(s) = \frac{K(s+z_1)(s+z_2)\cdots(s+z_m)}{s^q(s+p_1)(s+p_2)\cdots(s+p_n)}, \tag{4.19}$$

where K is the gain constant, z_i and p_j are the zero's and pole's of the open-loop system respectively, *m* represents the number of zeros, *n* represents the number of left-half plane poles, and *q* represents the number of poles on the imaginary axis. The final value theorem,

$$e_{ss} = \lim_{t\to\infty} e(t) = \lim_{s\to 0} sE(s) \tag{4.20}$$

was used to determine the steady-state error, e_{ss}, of the system. Given a ramp input

$$R(s) = \frac{1}{s^2}, \tag{4.21}$$

the steady-state error simplifies to

$$\begin{aligned} &= \lim_{s\to 0} \frac{1}{s^2} \frac{s}{1+G(s)H(s)} \\ &= \lim_{s\to 0} \frac{1}{s+sG(s)H(s)} \end{aligned} \tag{4.22}$$

Therefore, $e_{ss} \to 0$ when $\lim_{s\to 0}\left[sG(s)H(s)\right] \to \infty$. This can only occur if $q \geq 2$ which means there must be at least two poles on the imaginary axis, requiring a double integrator be present in the open-loop transfer function. The presence of a double integral (poles at zero) ensures that the system is capable of asymptotically tracking step and ramp changes in phase with zero tracking error. However, due to the instability that arises from this type of function in the closed-loop form, a minimum phase zero must also be included to maintain closed-loop system stability.

Since the VCO is modeled as a single integrator,

$$V(s) = \frac{K_{VCO}}{s} \tag{4.23}$$

one of the filters must additionally contain an integrator to ensure zero steady-state error in the presence of a ramp input. The purpose of the low-pass filter function is to attenuate the double harmonic present after mixing along with higher order noise. A first order low-pass filter was chosen to achieve this task described by the transfer function

$$F(s) = \frac{K_{PD}\omega_p}{s+\omega_p}, \tag{4.24}$$

where ω_p represents the pole location (also referred to as the filter's cutoff frequency), and K_{PD} is the overall gain constant for the phase detector (mixer and low-pass filter combination). Thus, the loop filter must contain both a pole at zero and a minimum phase zero to satisfy the requirements discussed above. Its transfer function is given by,

$$L_F(s) = \frac{K_{LF}(s+\omega_z)}{s\omega_z}, \tag{4.25}$$

where K_{LF} is the gain constant and ω_z represents the location of the minimum phase zero. Since both the low-pass filter and the loop filter are first degree transfer functions, unity feedback results in a third-order PLL whose closed-loop transfer function is defined as

$$T(s) = \frac{G_C(s)}{1+G_C(s)} = \frac{K'\omega_p(s+\omega_z)}{\omega_z s^3 + \omega_p\omega_z s^2 + K'\omega_p s + K'\omega_p\omega_z}, \tag{4.26}$$

and whose open-loop transfer function is

$$G(s)H(s) = G_C(s) = \frac{K'\omega_p(s+\omega_z)}{\omega_z s^2(s+\omega_p)}, \tag{4.27}$$

where $K' = K_{PD}K_{LF}K_{VCO}$, representing the overall open-loop gain constant.

The two PLL components with design flexibility are the low-pass filter and the loop filter; the low pass filter is modeled based upon the expected reference frequency while the loop filter is designed to meet specific closed-loop response characteristics. The PLL AO controller described here was designed to accommodate input frequencies ranging from approximately 600 Hz to 1200 Hz; therefore the low-pass filter's open-loop pole was placed at approximately 80 Hz (or 500 rad/s). The pole placement was selected in order to adequately attenuate the double harmonic while largely retaining the form of

the DC component. The following sections outline the design process based upon several common metrics used to assess the system's response characteristics: phase margin, settling time, percent overshoot, and absolute error. The analysis was conducted using the transfer functions given in Eq. (4.26) and Eq. (4.27), where $\omega_p \approx 500$ rad/s, in order to determine the minimum phase zero placement, ω_z, as well as the overall gain constant, K'.

4.4.2. Phase Margin

Phase margin provides a measure of a systems relative stability defined as the difference in phase between the system's output and -180° when the loop gain is unity. It is a commonly used metric when analyzing a closed loop control system. Larger positive values of phase margin correspond to a more stable system where the output has fewer tendencies to oscillate in response to an input, such as a step input. Phase margin may be easily determined from a Bode plot by evaluating the system's phase angle at the unity magnitude point, $|GH(j\omega_u)| = 1$. The phase angle for the open-loop system given in Eq. (4.27) is,

$$\angle GH(j\omega) = \tan^{-1}\left[\frac{-\omega(\omega_z - \omega_p)}{\omega_p\omega_z + \omega^2}\right]. \tag{4.28}$$

Phase margin is calculated by evaluating Eq. (4.28) at the cross-over frequency, ω_u, and comparing the resulting phase angle to -180°. Figure 4.9 shows phase margin measured in degrees versus the minimum phase zero placement (ω_z) for several different K' values. The *matlab* code used to create the results shown in Fig. 4.9 may be found in Appendix B.

It is clear from the results shown in Fig. 4.9 that there exists an optimal range for the minimum zero placement corresponding to each K' value based upon relative stability. It should also be noted that placing the minimum phase zero beyond the predetermined low-pass filter cutoff frequency, such that $\omega_z \geq \omega_p$, has no stabilizing effect independent of the overall gain constant, K'. While this phase margin investigation affords a necessary first step in selecting ω_z and K', the following analyses provide a more thorough basis in the design selection process.

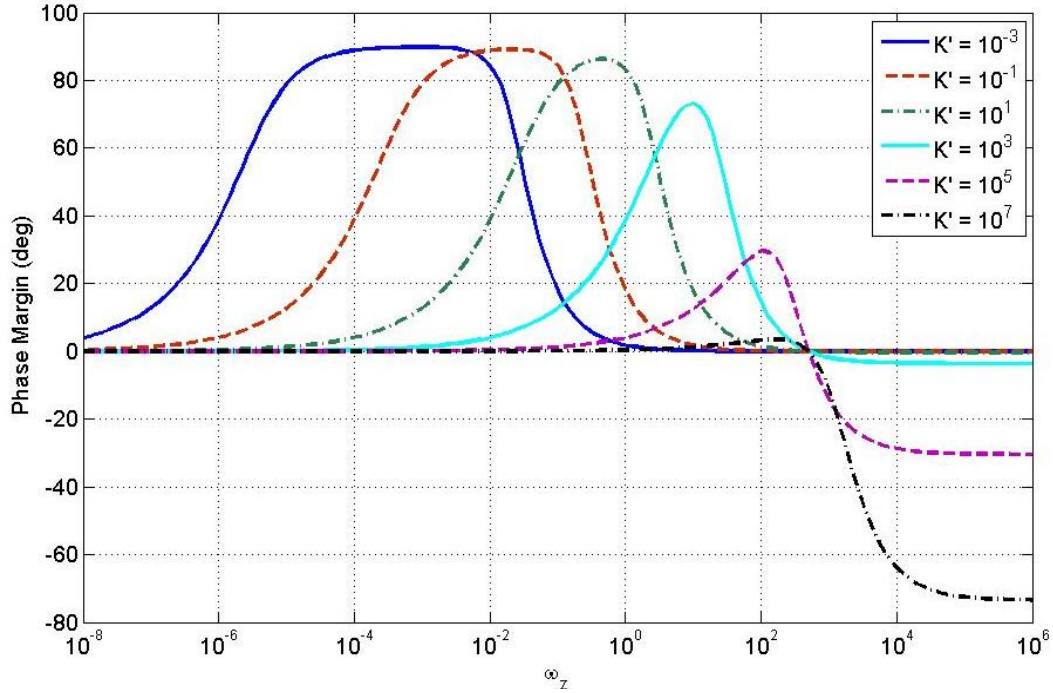

Figure 4.9: Phase margin (degrees) verses the placement of the loop function's minimum phase zero (ω_z) given a range of overall gain constant values (K').

4.4.3. Settling Time

The second metric used to analyze the performance of the PLL controller was settling time (T_s), defined as the time required for a system's output to *remain* within a certain percentage of the desired response [42]. A step input was applied to the PLL

controller for each combination of control parameters (ω_z and K') studied in Section 4.4.2. The system response was examined and compared to the unit step input to determine settling time. The results shown in Fig. 4.10 represent the settling time taken for each system to remain within 1% of the final value. In all six cases of K' values, there exists a threshold of approximately 0.015 seconds, below which the settling time never reduces. In each case, the results show a range of ω_z values for which the settling times remain at or near this threshold before rapidly increasing past a certain breaking point. Regardless of the K' value, when the minimum phase zero exceeds the low-pass filters cutoff frequency (500 rad/s for this particular study) the settling time approaches infinity. This corroborates with the phase margin results, indicating instability where the output response never decays to its desired value.

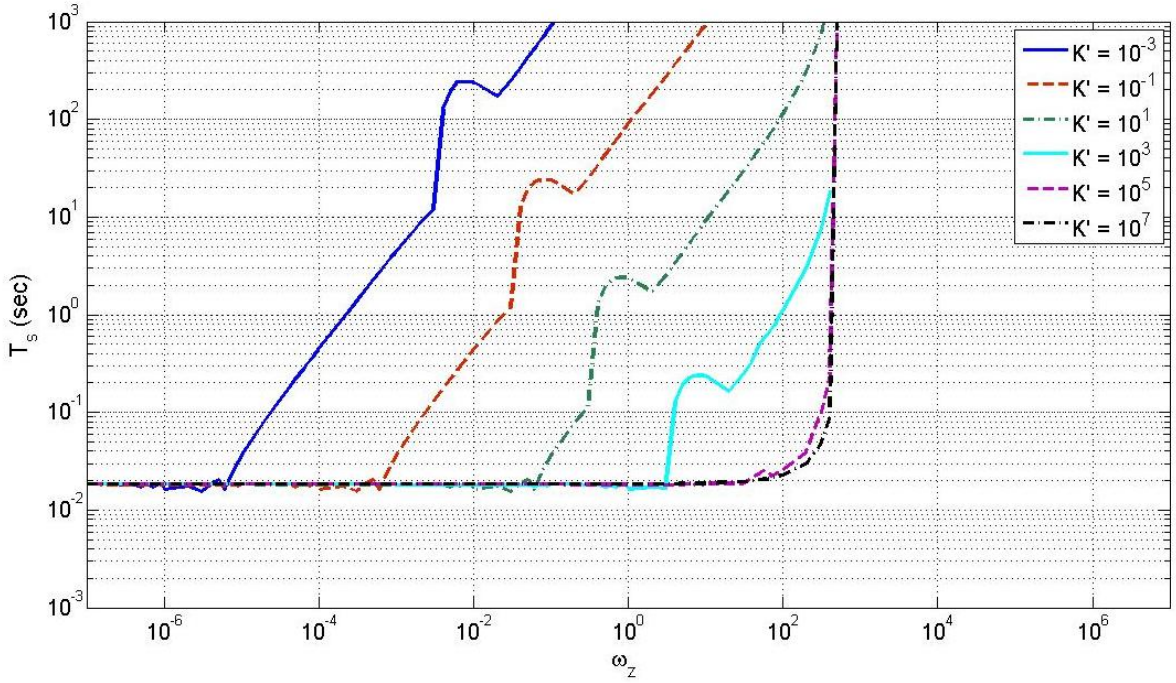

Figure 4.10: Settling time (T_s) given a unit step input verses the placement of the loop function's minimum phase zero (ω_z) given a range of overall gain constant values (K'); the settling time is given by the time it takes the output to remain within 1% of its final value.

Since the PLL controller is also being designed to accommodate ramp changes in phase, it is necessary to assess the system's ramp response. For this investigation the PLL output was simulated given a ramp input, defined as $u(t) = t$. The absolute error between the ramp input and the system output was examined and a settling time computed. Due to lesser absolute error values, settling time was calculated based on a 0.1% limit. Therefore the results in Fig. 4.11 show settling time, defined as the amount of time taken before the output remains within 0.1% of its final value, verses minimum phase zero placement for a range of gain constants.

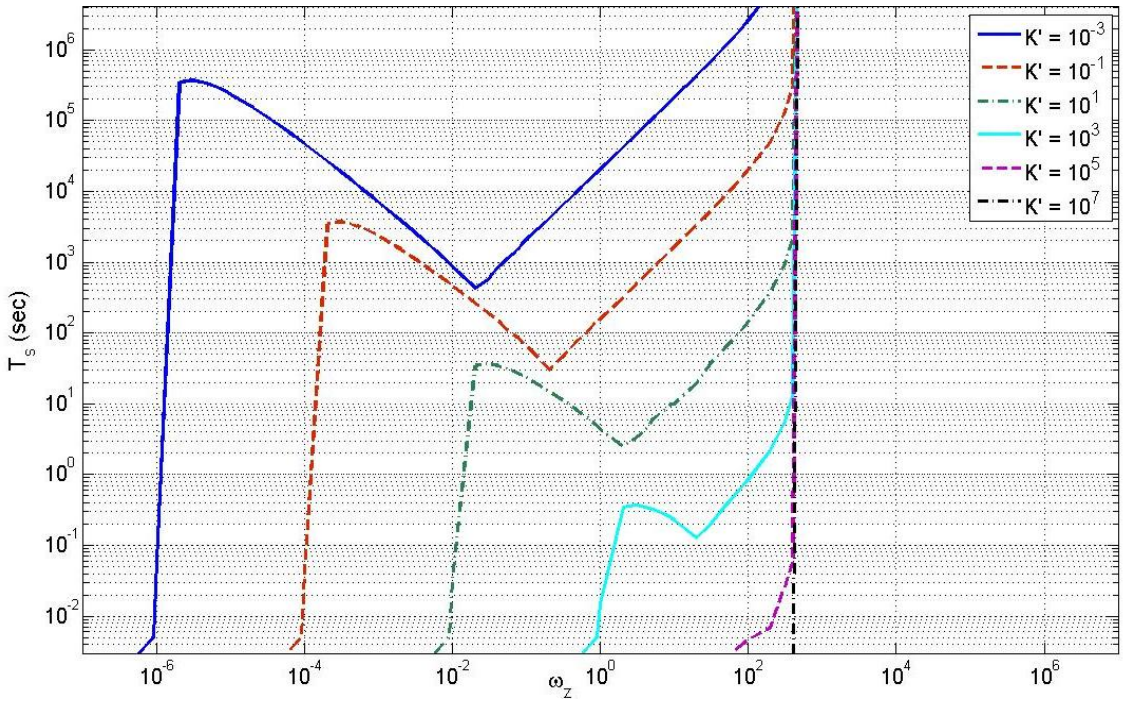

Figure 4.11: Settling time (T_s) given a ramp input verses the placement of the loop function's minimum phase zero (ω_z) given a range of overall gain constant values (K'); the settling time is given by the time it takes the output to remain within 0.1% of its final value.

While Fig. 4.11 indicates little to zero settling time (based on the selected 0.1% limit) as ω_z approaches 10^{-6} for each K' case, there exists considerable amounts of

oscillation within these regions. It is important to consider both the phase margin results shown in Fig. 4.9 along with the settling times given in Fig. 4.11 to obtain a more complete picture of the ramp response. Although the settling time given a ramp input is small over some areas of each curve, marginal stability may produce an extremely oscillatory response. *Matlab* code used to create these plots may be found in Appendix B.

4.4.4. Percent Overshoot

While settling time provides some very useful information concerning the PLL's response, the extent of oscillation remains uncertain at this point. Thus, percent overshoot was computed to create a clearer picture of the overall system response. Percent overshoot is the maximum percentage by which the output exceeds the response's final value [42]. Figure 4.12 shows the percent overshoot corresponding to the settling times shown in Fig. 4.10. These results reveal the PLL's tendency to oscillate for ω_z values both above and below a certain range of more stable frequencies. As the overall gain constant K' increases so do the system's oscillations. Together, the results shown in Figs. 4.10 and 4.12 illustrate the character of the PLL's output given a unit step input. For low ω_z frequencies, the system has a significant oscillatory response that settles down quickly. For high ω_z frequencies, the system also responds with large oscillations which take considerable more time to dampen out. Once the value of ω_z exceeds a value at or near the low-pass filter's cutoff frequency, the system response becomes completely unstable without decay. In each case shown in Fig. 4.12, there

exists a range of "optimal" ω_z frequencies in which the response maintains the least amount of oscillation. *Matlab* code used to create this plot may be found in Appendix B.

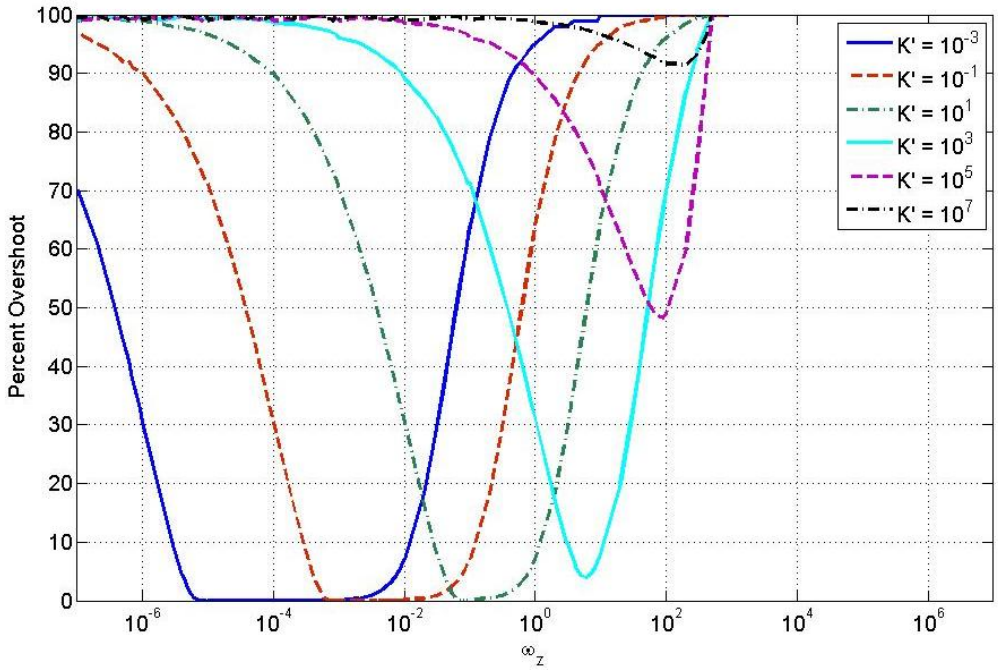

Figure 4.12: Percent overshoot versus the placement of the loop function's minimum phase zero (ω_z) given a range of overall gain constant values (K').

4.4.5. Integral Error

Integral error was the final performance index evaluated in this compensator analysis. Both ITAE (integral of time multiplied by absolute error) defined as,

$$ITAE = \int_0^T t|e(t)|dt \tag{4.29}$$

and ISE (integral of the square of the error) defined as,

$$ISE = \int_0^T e^2(t)dt \tag{4.30}$$

were computed as measures of the system's error accumulated over time [42]. For both calculations, error was measured as the difference between the system output and the unit step input. The upper limit, *T*, was a chosen finite time exceeding the settling time for each case study. Figure 4.13 shows the computed ITAE results as a function of minimum phase zero placement, and Fig. 4.14 shows the computed ISE results as a function of minimum phase zero placement. (*Matlab* code used to create these plots may be found in Appendix B.)

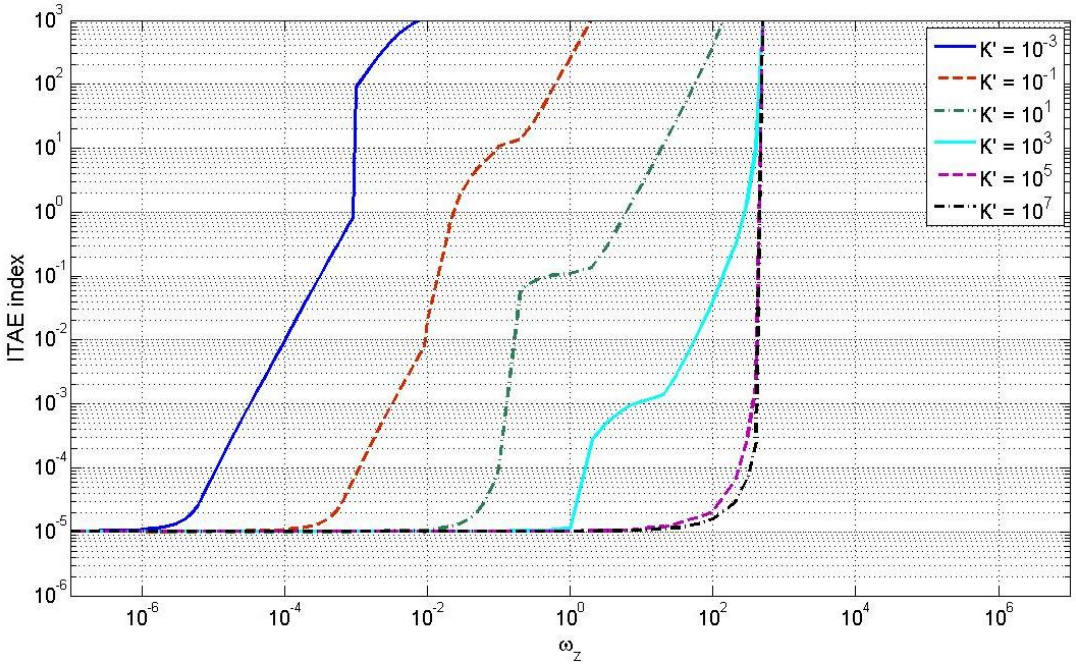

Figure 4.13: ITAE performance criterion versus the placement of the loop function's minimum phase zero (ω_z) given a range of overall gain constant values (K').

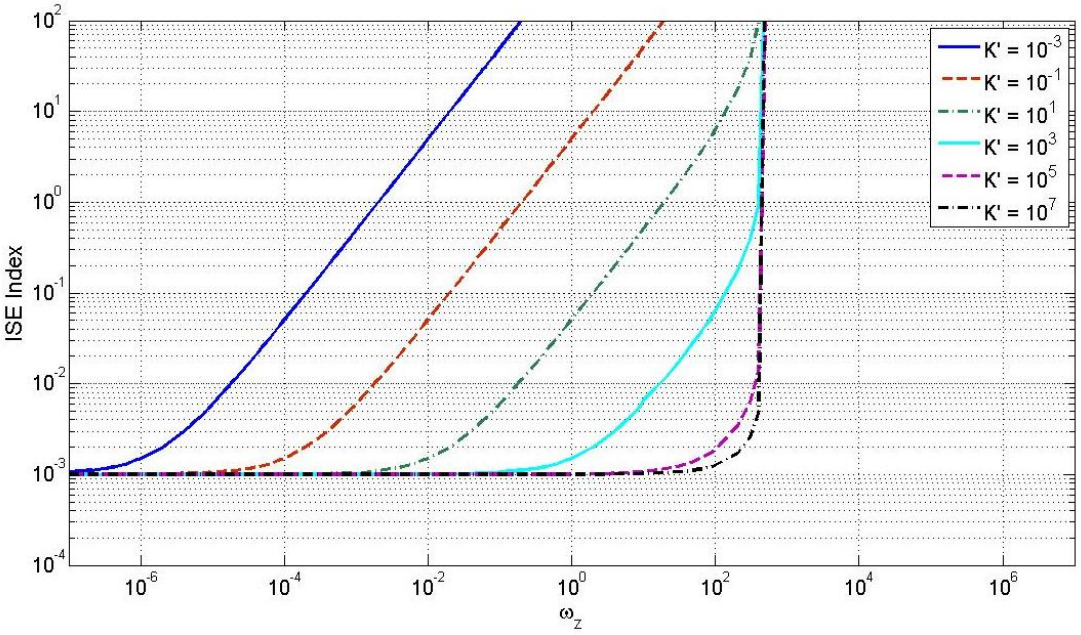

Figure 4.14: ISE performance criterion versus the placement of the loop function's minimum phase zero (ω_z) given a range of overall gain constant values (K').

In both cases the integrated error increases with increasing ω_z values suggesting that smaller ω_z values are the most desirable. While placing the minimum phase zero close to the real axis does in fact minimize the integrated error, such a selection may not ultimately be the best choice. Furthermore, it may result in a marginally stable or unstable system. Consequently, the analyses presented in Sections 4.4.2 – 4.4.5 must be examined collectively when selecting the most appropriate control parameters. The chosen values are given in the following section along with the controller's simulated response.

4.4.6. PLL Design Summary

The analyses reported in Sections 4.4.2 – 4.4.5 were assessed collectively when selecting the control parameter values for ω_z and K'. The goal was to minimize settling time, percent overshoot, and integrated error while maximizing the amount of phase margin. After evaluating system response characteristics and system stability, the PLL control parameters were chosen; an overall gain constant (K') of 10,000 and a minimum phase zero frequency (ω_z) of 55 rad/s was selected. The open-loop controller is given by

$$G(s)H(s) = G_C(s) = \frac{5{,}000{,}000(s+55)}{55s^2(s+500)}, \tag{4.31}$$

recalling the low-pass filter frequency of 500 rad/s, determined previously. These values result in a phase margin of approximately 53 degrees at 179 rad/s, depicted in the open-loop bode diagram shown below in Fig. 4.15. By placing the minimum phase zero at a frequency of 55 rad/s, the open-loop phase increases to -127 degrees at the unity gain bandwidth providing stability to an otherwise unstable system. While the primary aim of this parameter selection process was to create a control system that responded to step and ramp inputs in a minimal amount of time while maintaining closed-loop system stability, the effects of percent overshoot and integrated error were also taken into consideration. By selecting this gain constant and minimum phase zero combination, the percent overshoot was reduced to less than 25 % and the ITAE index and ISE index were kept below approximately 0.0003 and0.00 4, respectively.

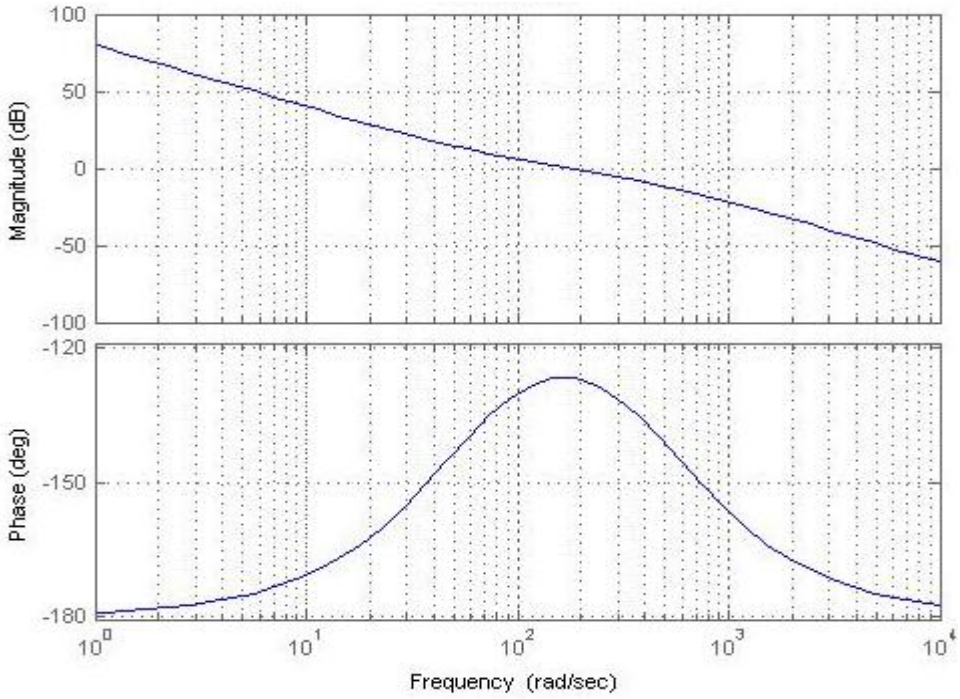

Figure 4.15: Bode diagram for the finalized open-loop controller given in Eq. (4.31).

In order to accommodate both step and ramp changes in phase, a second order PLL controller was designed for this application. This required two integrators in the controller's forward path. As such, a minimum phase zero was necessary to ensure system stability. In addition, a first-order low-pass filter was used in the design adding a left-half plane pole to the transfer function as well. By keeping the filter first-order this resulted in a second order PLL. One of the benefits of designing a second order PLL as oppose to a higher order model is that parameters designed to ensure stability of the linearized model also apply to the actual nonlinear PLL [24]. The responsiveness of the finalized controller can best be seen from the simulated step and ramp responses shown below in Figs. 4.16. These figures show the response error verses time given a unit step input (Fig. 4.16 (A)) and a ramp input (Fig. 4.16 (B)). As shown, for the step and ramp

inputs, the output settles to within 1% and 0.01% of their final values in less than 0.05 seconds, respectively, and the PLL controller responds with less than 25 % overshoot given a step input.

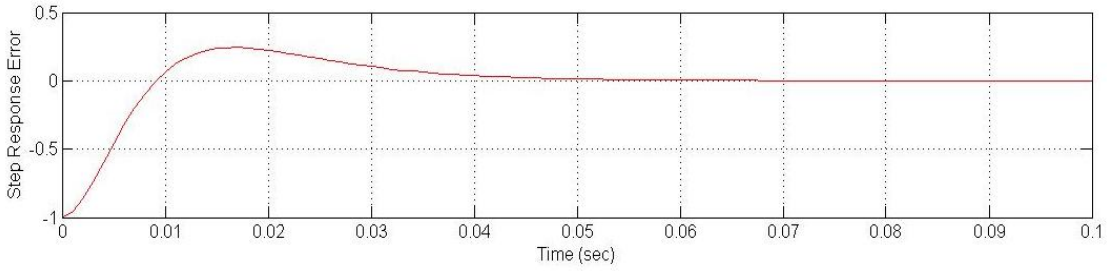

A

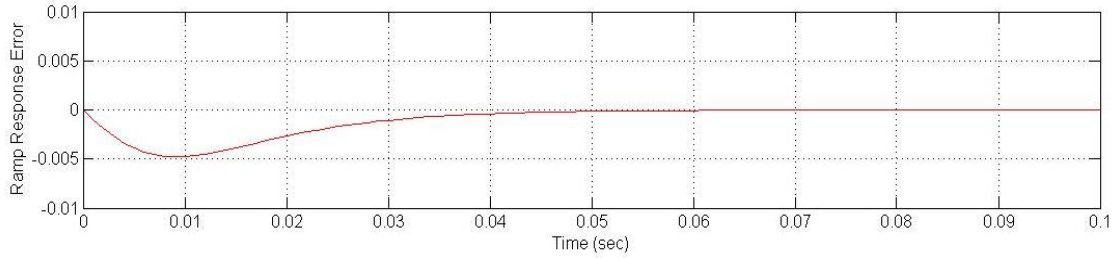

B

Figure 4.16: (A). Finalized PLL controller's simulated response error verses time given a unit step input (B). Finalized PLL controller's simulated response error verses time given a ramp input.

4.5. PLL AO Simulation Results

The finalized PLL controller was modeled in Matlab and used to analyze the control system response given a simulated shear layer. The discrete vortex method and Weakly Compressible Model described in Section 2.5 were used to simulate a forced shear layer and its emerging optical wavefront. The results presented in this section involve three different high-speed simulated shear layer cases with upper Mach numbers ranging from approximately 0.55 to 0.8 and lower Mach numbers ranging from approximately 0.1 to 0.2. In each case forcing was applied to regularize the shear layer's

large-scale vortical structures within a certain range of downstream distances. The PLL controller described above was simulated and used to apply AO corrections to the shear layer's regularized wavefront. OPD error and Strehl Ratio were computed, providing a means of assessing this new alternative control technique.

These preliminary simulations were conducted to investigate the PLL controller's effectiveness when used in a high-speed shear layer application. While these tests were not experimental, the Weakly-Compressible Model's ability to predict the large-scale structures within the flow field [5, 9, 12, 31] provide a good means of initially assessing the alternative AO controller. Before performing the AO simulation, a succession of optical wavefronts and a time series of Strehl ratios were computed using the Weakly-Compressible Model prior to forcing. This provided a point of reference by which to compare the final AO corrections. Once the benchmark results were computed, the simulated shear layers were forced and AO corrections applied using the PLL controller described in this chapter. A 633 nm wavelength beam was used in each of the following four simulations discussed in this section.

4.5.1. Simulation Case Study #1

The first simulation involved a high speed shear layer with upper and lower Mach numbers of approximately 0.55 and 0.17, respectively. Forcing was applied at 1100 Hz. Wavefronts were computed by simulating a 0.15 meter aperture optical beam propagating through the flow centered 0.38 meters downstream from the point of origin. Figure 4.17 shows six consecutive numerical wavefronts taken approximately 0.00015 seconds apart, prior to both forcing and AO corrections.

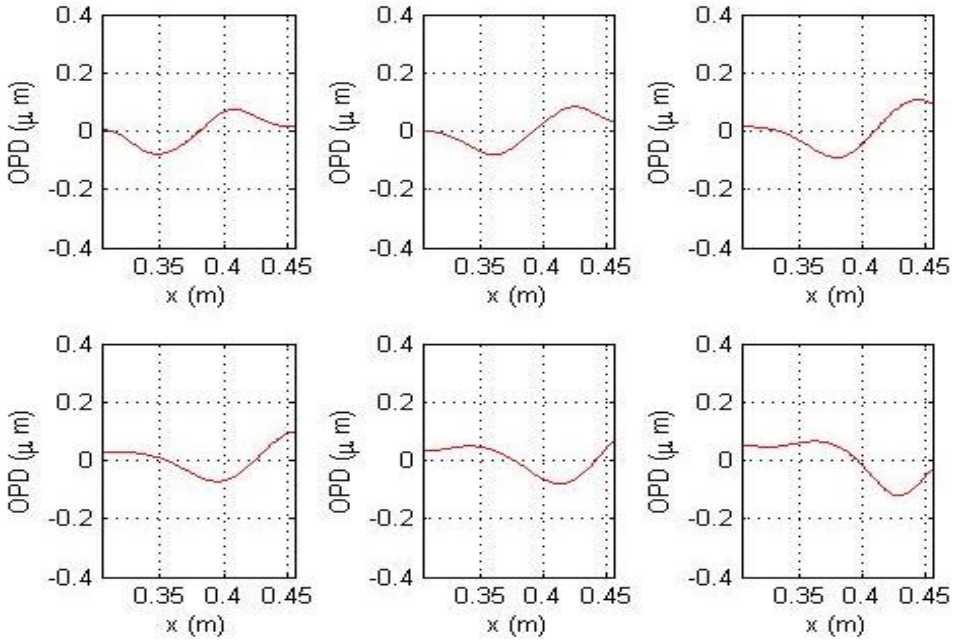

Figure 4.17: Six successive numerical wavefronts computed for an unforced shear layer with upper and lower Mach numbers of approximately 0.55 and 0.17, respectively.

Figure 4.18 shows a similar set of consecutive wavefronts after forcing is applied. The solid curves in Fig. 4.18 represent the regularized wavefronts emerging from the forced shear layer and the dashed curves represent the DM waveform used to apply conjugate corrections to the regularized aberrating wavefronts. The numerical results shown in Fig. 4.18 represent six consecutive wavefronts after which phase-locking has occurred. The good agreement between the simulated forced shear layer's wavefronts and the PLL controller's simulated correction can best be seen by the wavefront error curves shown in Fig. 4.19.

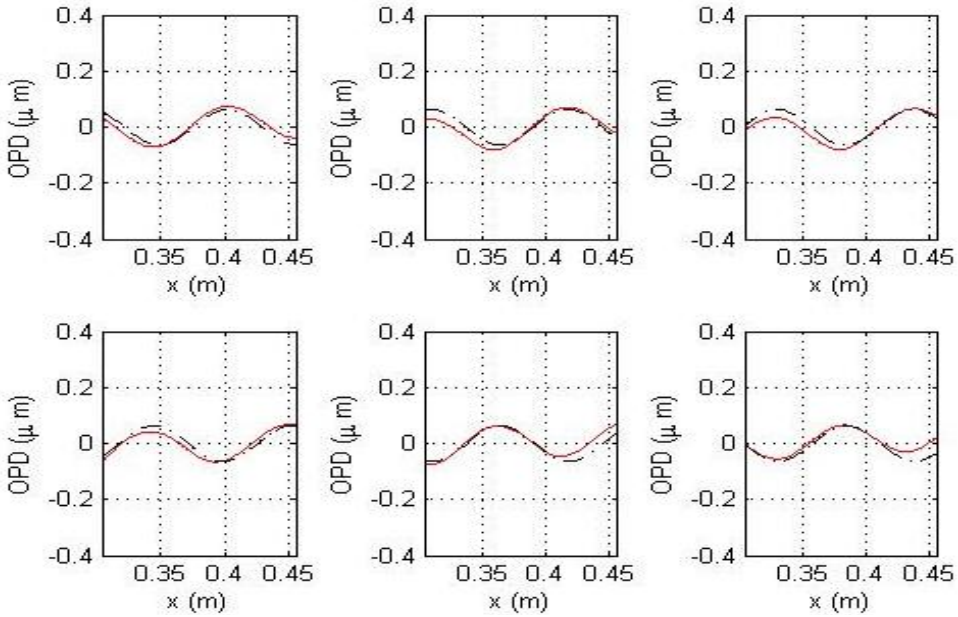

Figure 4.18: Six successive numerical wavefronts computed for an 1100 Hz forced shear layer (solid curves) with upper and lower Mach numbers of approximately 0.55 and 0.17, respectively along with the controller's six corresponding conjugate corrections (dashed curves).

The two curves shown above in Fig. 4.18 (the solid curves represent the forced shear layer's numerical wavefronts, and the dashed curves represent the DM's conjugate correction) were subtracted from one another producing the simulated residual wavefront errors shown in Fig. 4.19. The spacing between wavefronts in all three figures (Fig. 4.17, Fig. 4.18, and Fig. 4.19) is equivalent to one sixth the forcing wavelength; therefore, the six successive wavefronts represent data from one full cycle of forcing.

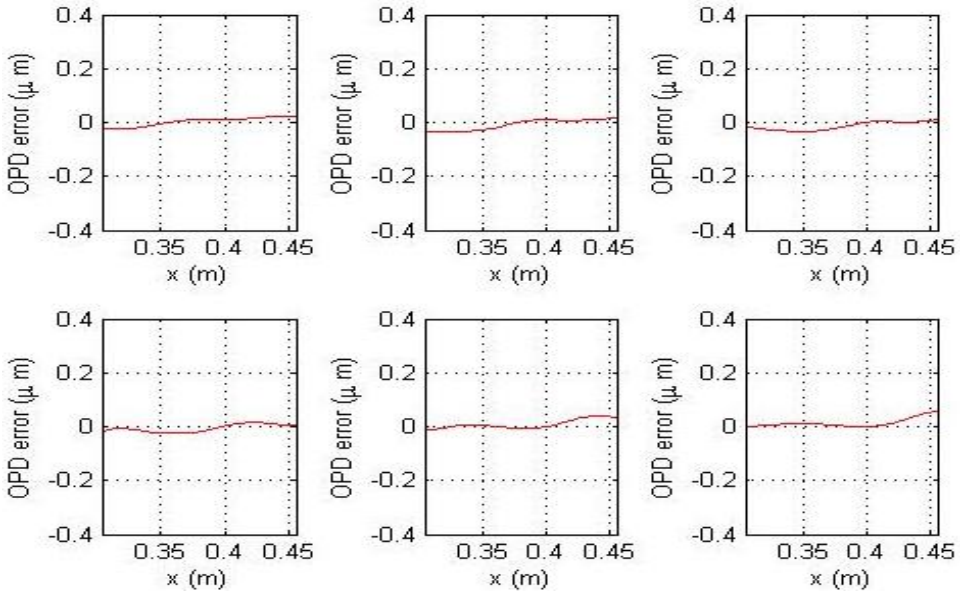

Figure 4.19: Six successive numerical wavefronts computed for an 1100 Hz forced shear layer with upper and lower Mach numbers of approximately 0.55 and 0.17, respectively, after AO corrections have been applied using the proposed PLL controller (i.e., residual wavefront error).

Comparing the wavefronts from Fig. 4.17 with those from Fig. 4.19 reveals a significant amount of wavefront reduction. The time-averaged root-mean-squared OPD error reduces from approximately 0.037 μm in the unforced case to 0.021 μm after numerical AO corrections are applied to the forced case (time-averaging for the second case was computed after phase-locking occurred). It should be noted in Fig. 4.19 that the residual OPD error might further be improved by removing tilt (see later results). A time series of Strehl ratios was also computed to evaluate the controller's effectiveness. A one dimensional far field diffraction pattern was constructed at each time step and the Strehl ratio computed from the center intensity value. Figure 4.20 shows Strehl ratio verses time prior to both forcing and AO corrections. The time-averaged Strehl ratio for the given duration is approximately 0.85. While this value is fairly high, it is clear from Fig. 4.20 that the instantaneous Strehl ratio frequently drops below 0.7.

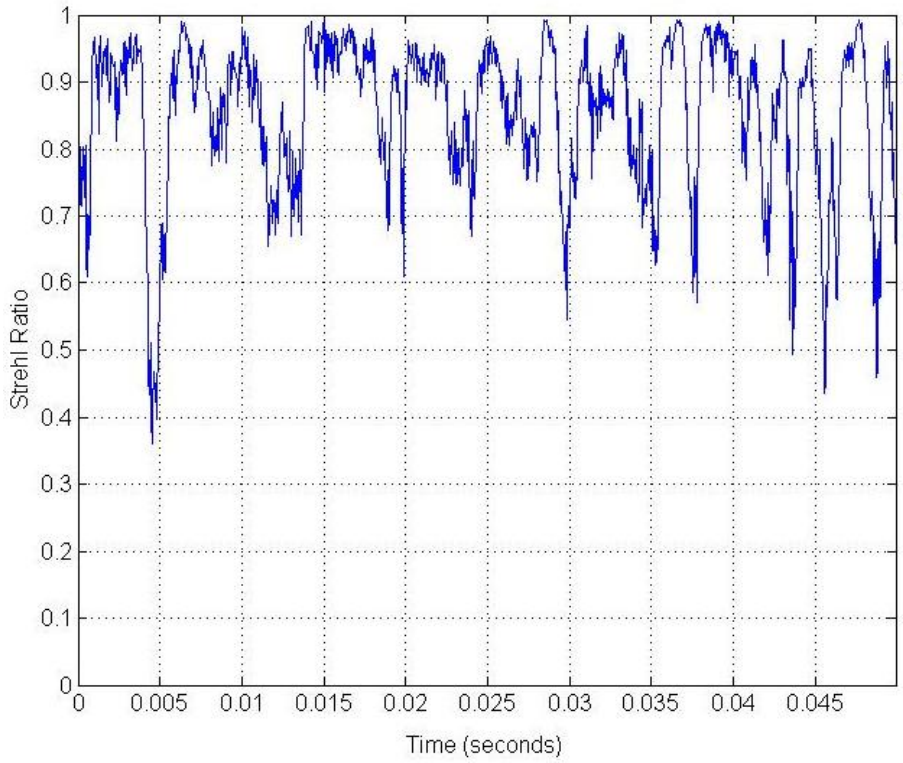

Figure 4.20: Strehl ratio verses time for the unforced shear layer with upper and lower Mach numbers of approximately 0.55 and 0.17, respectively.

AO corrections were applied to this simulated shear layer in order to further improve upon the Strehl ratio results shown above (Fig. 4.20). Figure 4.21 shows both the controller's phase response verses time and the corresponding Strehl ratio verses time during the process of applying AO corrections. It is clear from Fig. 4.21 (A) that phase-locking occurs after approximately 0.023 seconds. At this point the PLL has adjusted for the original 140 degree phase difference between the shear layer's wavefront and the conjugate correction. Note that prior to phase-locking the Strehl ratio is significantly lower than the unforced case (Fig. 4.21 (B)) due to additive error occurring initially. As the AO controller's conjugate correction phase-locks with the shear layer's emerging

wavefront, the Strehl ratio improves significantly resulting in a time-averaged Strehl ratio of approximately 0.96 once phase-locked.

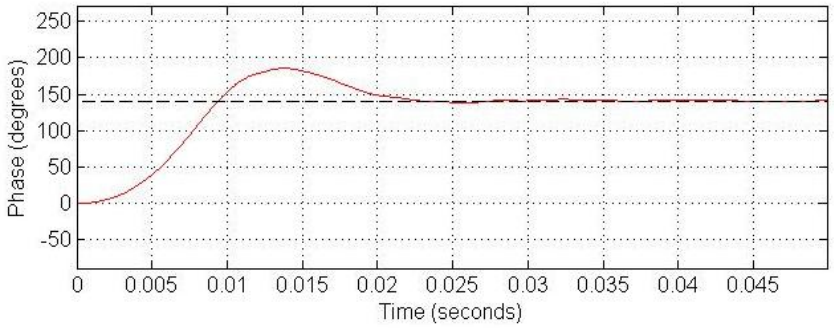

A

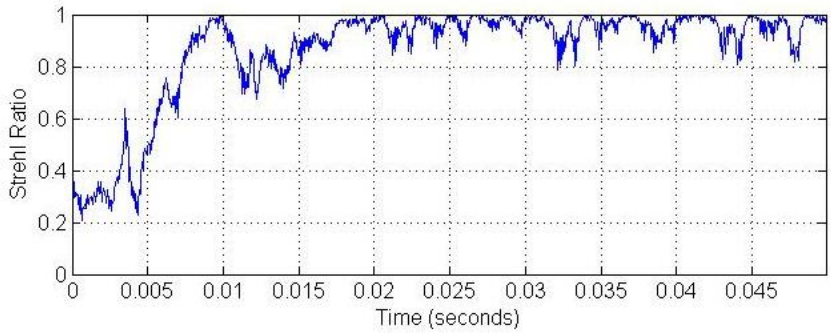

B

Figure 4.21: (A). PLL controller's phase response verses time given an initial step phase error of approximately 140 degrees (B). Strehl ratio verses time while AO corrections are being applied to an 1100 Hz forced shear layer with upper and lower Mach numbers of approximately 0.55 and 0.17, respectively.

By further removing tip/tilt, as is typically done via a separate control loop, the time-averaged Strehl ratio improves even further to approximately 0.99 producing an overall increase of 16.5% (refer to Fig. 4.22). For lower Mach number flows, such as the one studied in this section, tip/tilt removes most of the subharmonics creating favorable results. However, in higher Mach flows subharmonics become more dominant such that an alternative method of creating the conjugate correction may be necessary.

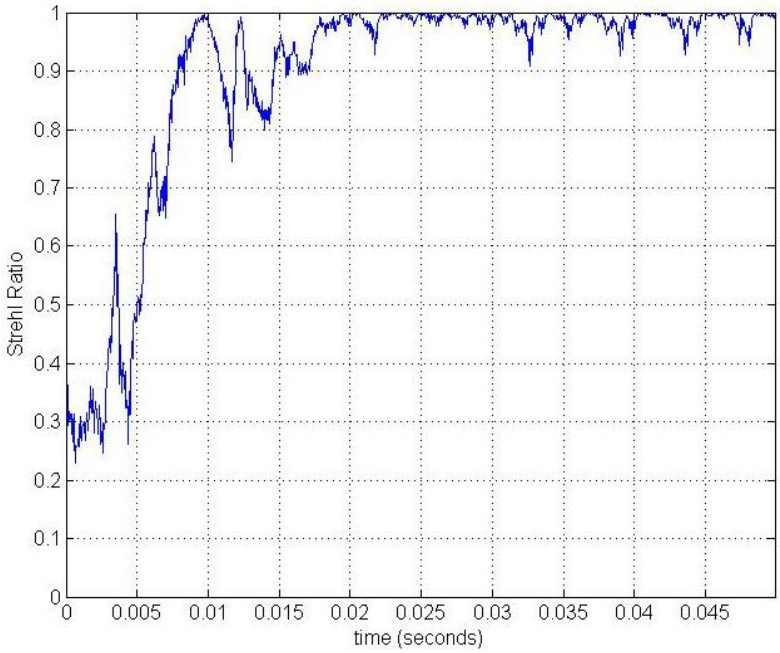

Figure 4.22: Strehl ratio verses time after tip/tilt has been removed given the results shown above in Fig. 4.21 (B).

One-dimensional far-field patterns were also created for each case study to provide a more visual means of assessing the applied correction. The electric field was computed numerically based on Eq. (2.5) from the residual wavefront error for the one-dimensional case. The electric field was squared and scaled producing an intensity pattern normalized to one. A series of intensity patterns were created from the residual error corresponding to four different timesteps. Figure 4.23 shows the one-dimensional intensity patterns for the first case studied in this section. An ideal one-dimensional intensity pattern given a perfectly planar wavefront is also shown in each figure by a dashed curve serving as a reference. The upper left figure corresponds to 0.0025 seconds (refer to Fig. 4.22) where the Strehl ratio is approximately 0.311. The upper right figure corresponds to 0.005 seconds and a Strehl ratio of approximately 0.497. The lower left

and lower right figures correspond to 0.04 and 0.045 seconds with respective Strehl ratios of approximately 0.969 and 0.996. Once phase-locking is achieved, approximately 0.018 seconds after the simulation begins, the time-averaged tip/tilt removed Strehl ratio approaches 0.99 as seen from the two lower intensity patterns shown below in Fig.4.23.

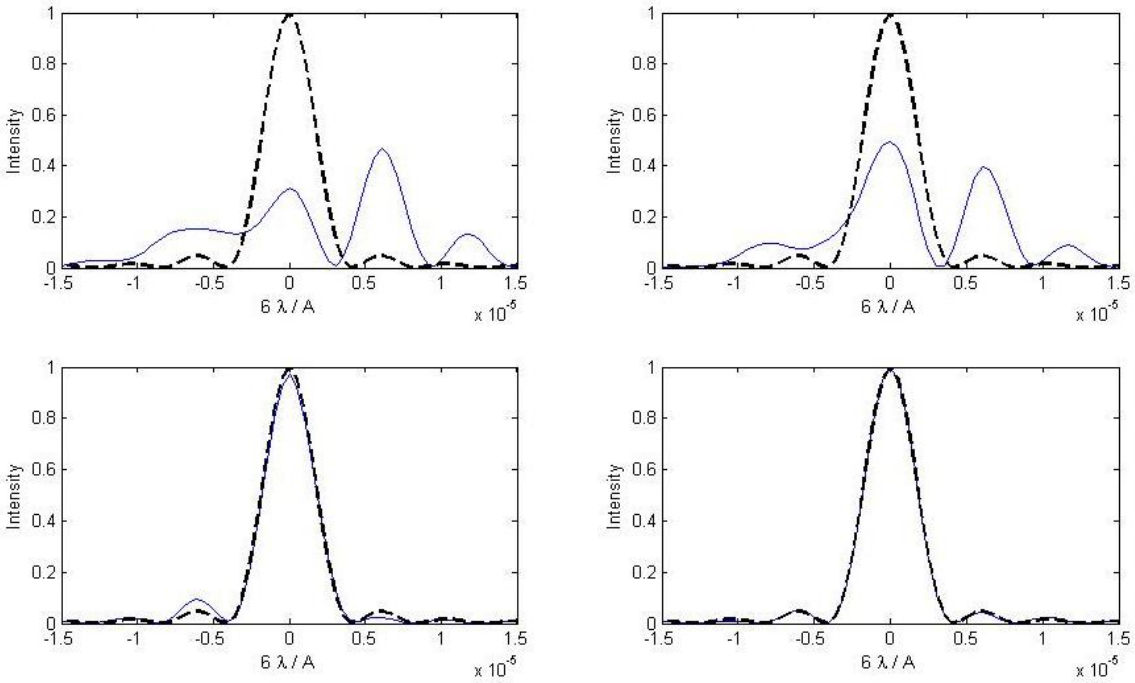

Figure 4.23: A series of four one-dimensional intensity patterns constructed from residual wavefront errors induced by a Mach 0.55/0.17 numerical shear layer (refer to Fig. 4.19) at times 0.0025 seconds (upper left), 0.005 seconds (upper right), 0.04 seconds (lower left), and 0.045 seconds (lower right).

4.5.2. Simulation Case Study #2

The second simulated high-speed shear layer had an upper Mach number of approximately 0.7 and a lower Mach number of approximately 0.2. A 0.15 meter aperture beam was numerically propagated through the shear layer approximately 0.35 meters downstream from the point of origin. Six consecutively spaced wavefronts shown below in Fig. 4.24 represent the OPD error present in the unforced case. A time-averaged

root-mean-squared OPD error of approximately 0.068 μm was computed. The alternative AO approach was then employed. The shear layer was forced at 1200 Hz and corrections were applied using the simulated PLL controller. Figure 4.25 shows both the forced shear layer's regularized wavefronts (solid curves) and the PLL controller's conjugate corrections (dashed curves). The resulting residual wavefront errors shown in Fig. 4.26 represent the difference between the regularized wavefronts and the conjugate corrections. Once the numerical AO corrections were applied and phase-locking occurred, the time-averaged root-mean-squared OPD error reduced to approximately 0.038 μm.

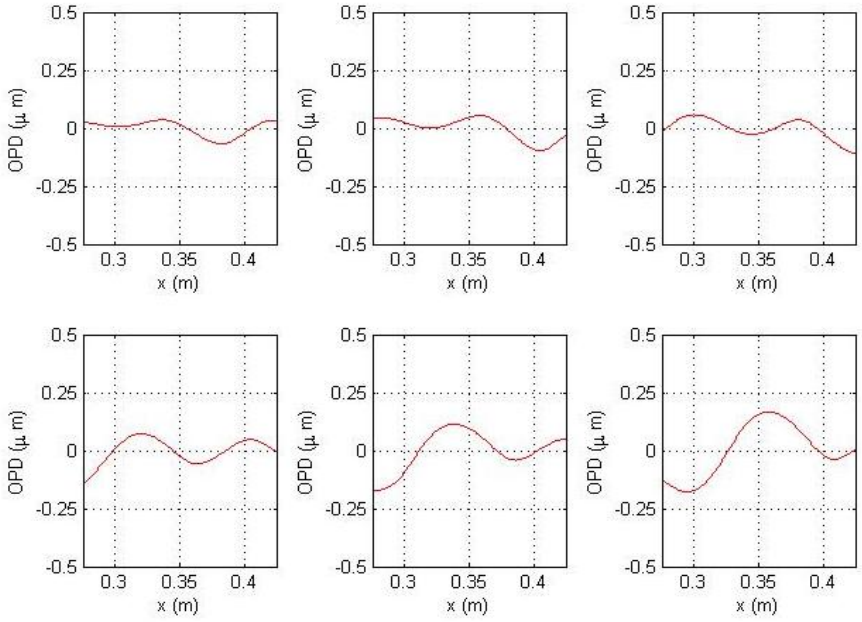

Figure 4.24: Six successive numerical wavefronts computed for an unforced shear layer with upper and lower Mach numbers of approximately 0.7 and 0.2, respectively.

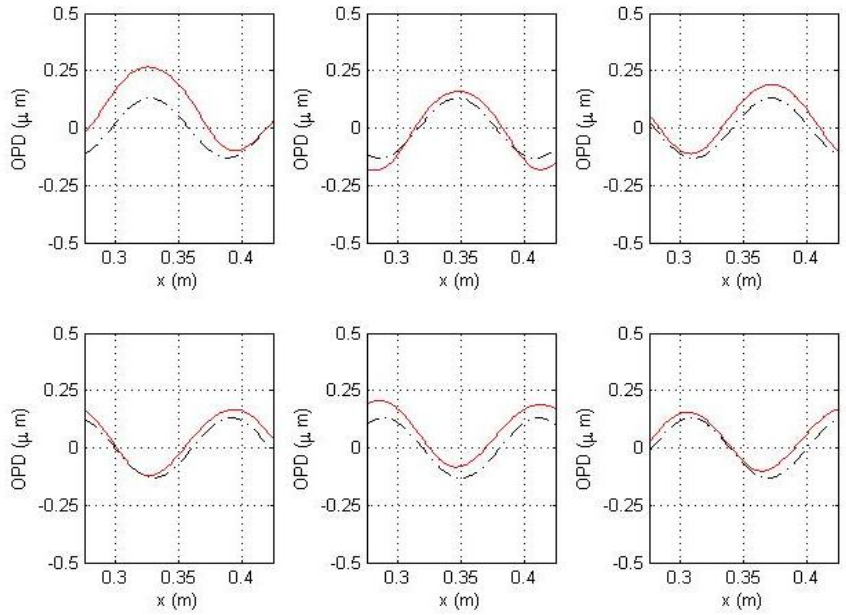

Figure 4.25: Six successive numerical wavefronts computed for a 1200 Hz forced shear layer (solid curves) with upper and lower Mach numbers of approximately 0.7 and 0.2, respectively along with the controller's six corresponding conjugate corrections (dashed curves).

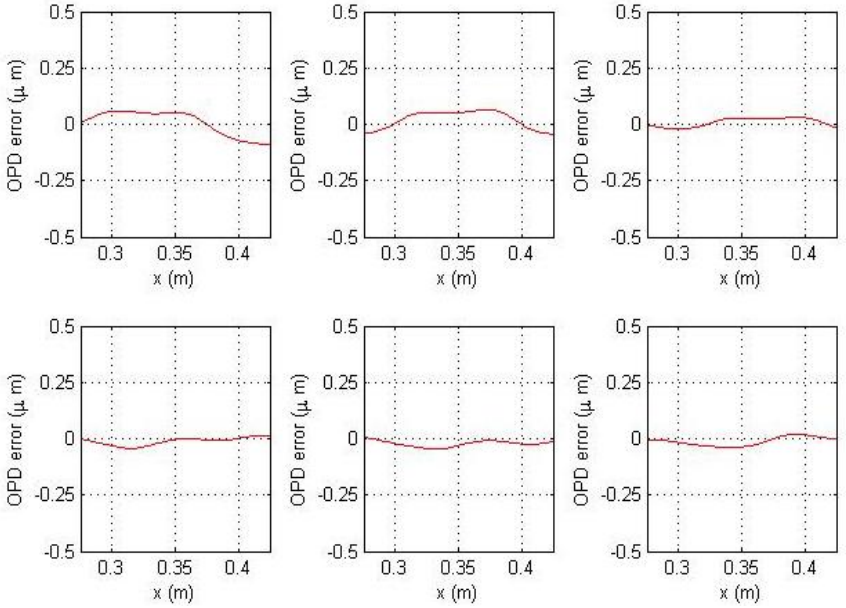

Figure 4.26: Six successive numerical wavefronts computed for a 1200 Hz forced shear layer with upper and lower Mach numbers of approximately 0.7 and 0.2, respectively, after AO corrections have been applied using the proposed PLL controller (i.e., residual wavefront error).

A time series of Strehl ratios was also computed for the unforced case as shown below in Fig. 4.27. Prior to forcing, the time-averaged Strehl ratio was approximately 0.63 consistently dropping below 0.2. After regularizing the large-scale structures within the indicated range of downstream distances, corrections were applied. An original phase error between the shear layer's emerging regularized wavefront and the conjugate correction was approximately 102 degrees. As shown in Fig. 4.28 (A), phase-locking occurred after approximately 0.015 seconds producing a time-averaged Strehl ratio of 0.87 (Fig. 4.28 (B)). Once tip/tilt was removed from each wavefront the Strehl ratio improved further to approximately 0.96 as seen in Fig. 4.29. This represents a 52 % increase in average Strehl ratio while the instantaneous value no longer drops below approximately 0.75.

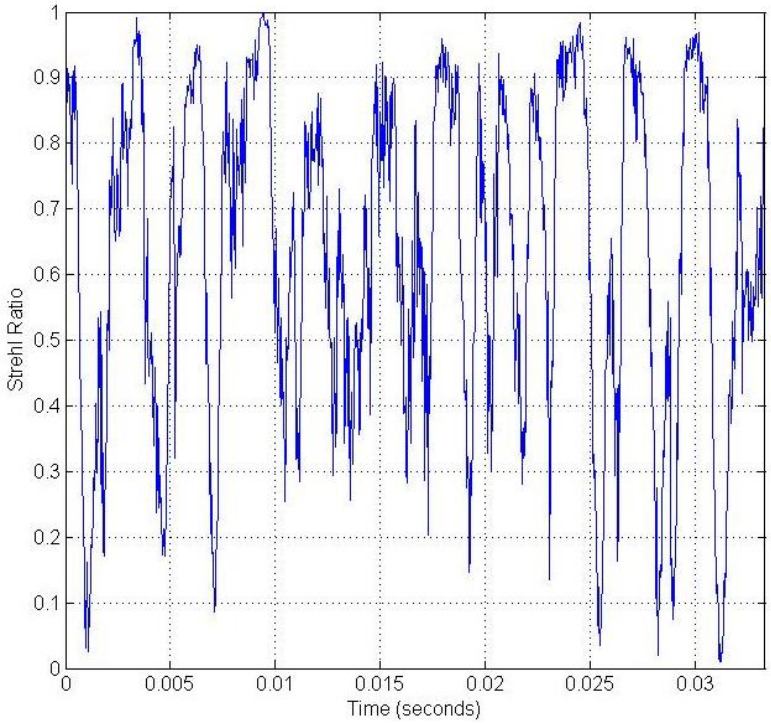

Figure 4.27: Strehl ratio verses time for the unforced shear layer with upper and lower Mach numbers of approximately 0.7 and 0.2, respectively.

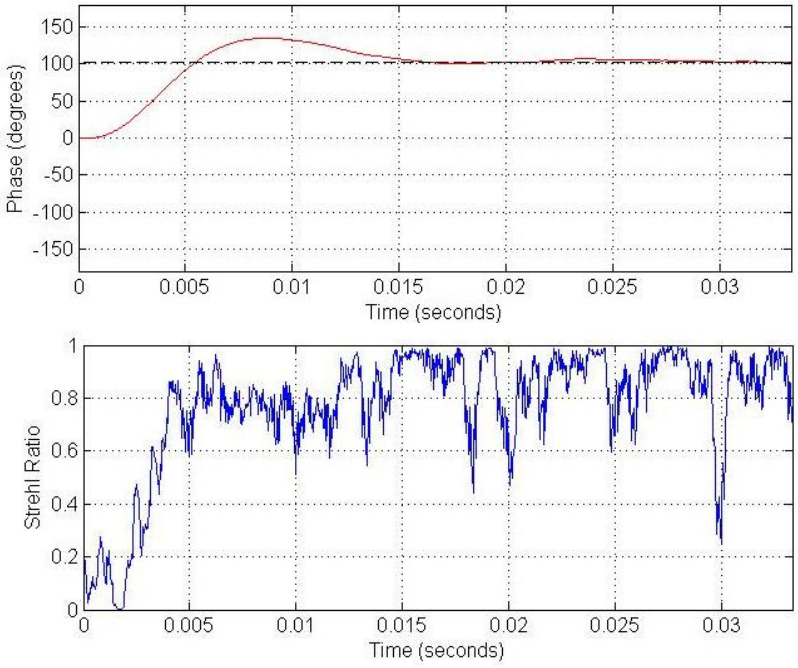

Figure 4.28: (A). PLL controller's phase response verses time given an initial step phase error of approximately 102 degrees (B). Strehl ratio verses time while AO corrections are being applied to a 1200 Hz forced shear layer with upper and lower Mach numbers of approximately 0.7 and 0.2, respectively.

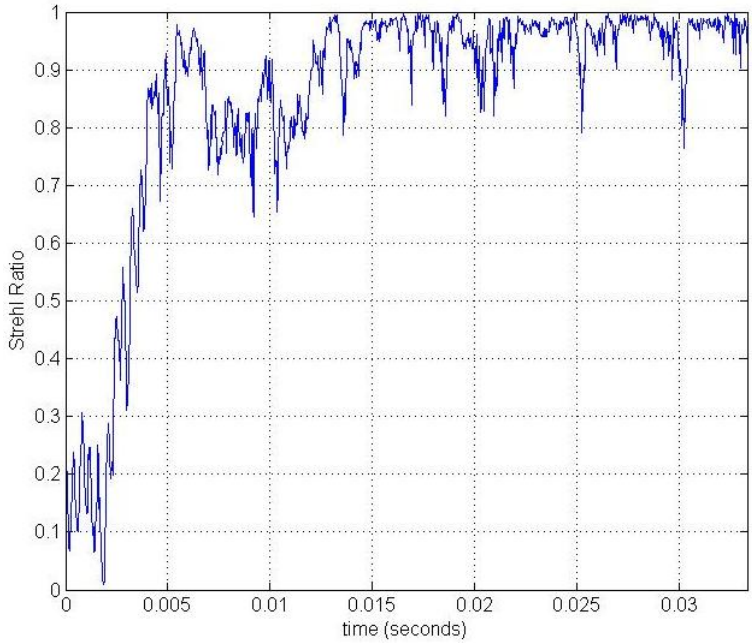

Figure 4.29: Strehl ratio verses time after tip/tilt has been removed given the results shown above in Fig. 4.28 (B).

One-dimensional far-field intensity patterns were constructed from the residual wavefront error (refer to Fig. 4.25) post AO corrections and tip/tilt removal. Four intensity patterns are shown below in Fig. 4.30 at times 0.0015 seconds (upper left), 0.0025 seconds (upper right), 0.02 seconds (lower left), and 0.025 seconds (lower right). The Strehl ratios corresponding to each of these figures are 0.082, 0.432, 0.907, and 0.961, respectively. As before, the ideal one-dimensional intensity pattern is shown by the dashed curves in each figure. It is clear from these intensity patterns that a significant amount of correction is achieved after phase-locking occurs, approximately 0.015 seconds after the simulation begins.

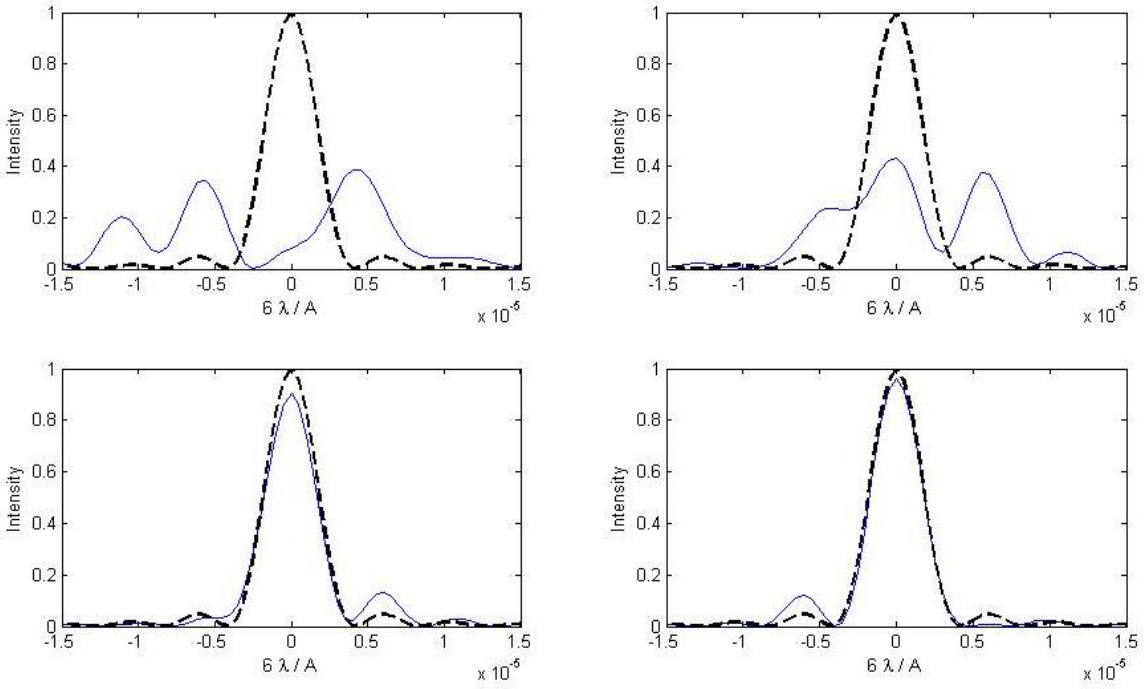

Figure 4.30: A series of four one-dimensional intensity patterns constructed from residual wavefront errors induced by a Mach 0.7/0.2 numerical shear layer (refer to Fig. 4.25) at times 0.0015 seconds (upper left), 0.0025 seconds (upper right), 0.02 seconds (lower left), and 0.025 seconds (lower right).

4.5.3. Simulation Case Study #3

The third simulation involved a high speed shear layer with upper and lower Mach numbers of 0.79 and 0.11, respectively. A 0.12 meter aperture beam was numerically propagated through the shear layer approximately 0.38 meters downstream from its point of origin. Initial wavefront measurements were computed for the unforced case and are shown below in Fig. 4.31. After completing the preliminary calculations, forcing was applied to the simulated shear layer at 700 Hz and another set of wavefronts were computed. Figure 4.32 shows six consecutive wavefronts over one full cycle of forcing. The solid curves represent the forced shear layer's emerging wavefront while the dashed curves represent the PLL controller's conjugate correction. It is important to note two key features in these figures. First, the regularized wavefronts experience OPD values considerably higher than those produced in the previous two simulation studies. Secondly, the regularized wavefronts for this particular case are not nearly as sinusoidal in nature. These aspects render the PLL controller less effective. As a result, the residual wavefront error shown in Fig. 4.33 is higher than the previous cases due in part to subharmonics present within the regularized flow. Removing tip/tilt does provide further improvement; however in a case such as this where harmonics are more dominant a conjugate correction based solely on the fundamental forcing frequency is not sufficient. Suggestions to address these issues are presented in Chapter 7.

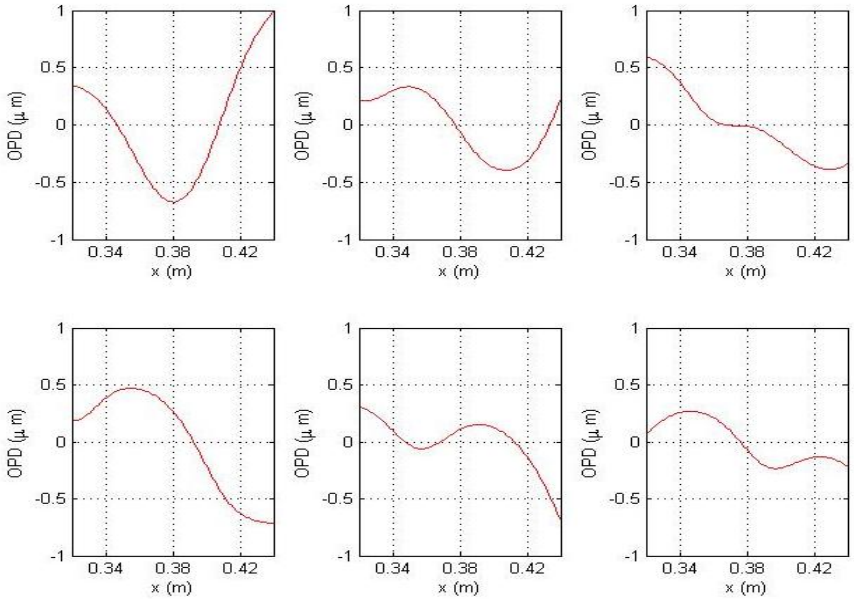

Figure 4.31: Six successive numerical wavefronts computed for an unforced shear layer with upper and lower Mach numbers of approximately 0.79 and 0.1, respectively.

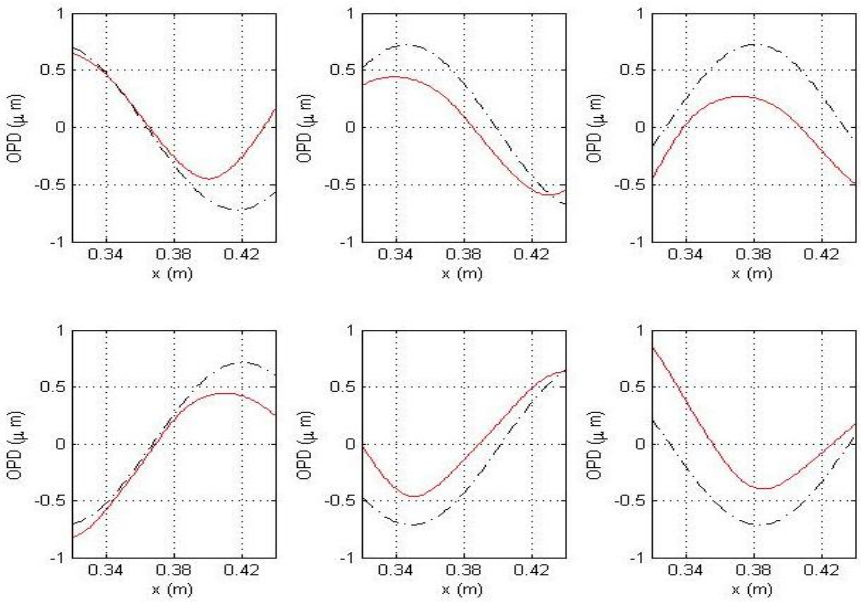

Figure 4.32: Six successive numerical wavefronts computed for a 700 Hz forced shear layer (solid curves) with upper and lower Mach numbers of approximately 0.79 and 0.1, respectively along with the controller's six corresponding conjugate corrections (dashed curves).

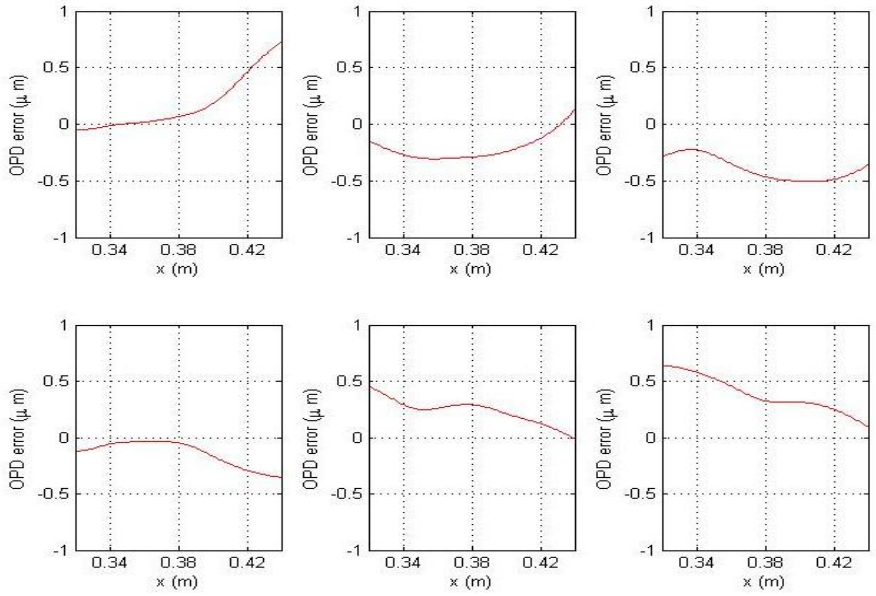

Figure 4.33: Six successive numerical wavefronts computed for a 700 Hz forced shear layer with upper and lower Mach numbers of approximately 0.79 and 0.1, respectively, after AO corrections have been applied using the proposed PLL controller (i.e., residual wavefront error).

Strehl ratios were also computed prior to and after AO corrections were applied. Figure 4.34 shows Strehl ratio verses time for the numerical unforced shear layer studied here. The time-averaged Strehl ratio for the unforced case is approximately 0.13. Once numerical AO corrections are applied and phase-locking occurs the Strehl ratio does show some improvement. Figure 4.35 shows both Strehl ratio verses time (Fig. 4.35 (A)) and the corresponding phase response verses time for the PLL controller (Fig. 4.35 (B)) during the AO correction process. As shown, phase-locking occurs after approximately 0.015 seconds at which point the time-averaged Strehl ratio improves to approximately 0.37. Once tip/tilt is removed the time-averaged Strehl ratio improves to approximately 0.64 (Fig. 4.36).

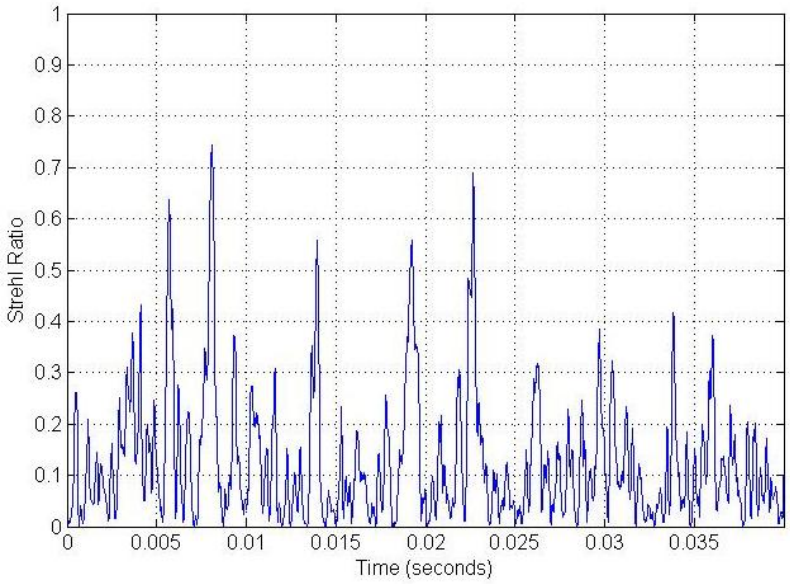

Figure 4.34: Strehl ratio verses time for the unforced shear layer with upper and lower Mach numbers of approximately 0.79 and 0.1, respectively.

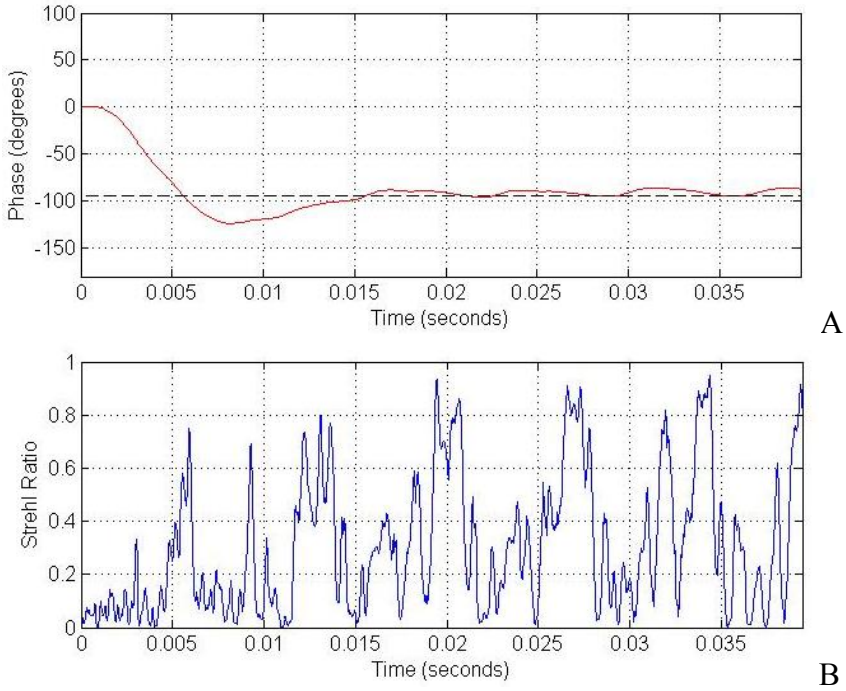

Figure 4.35: (A). PLL controller's phase response verses time given an initial step phase error of approximately 94 degrees (B). Strehl ratio verses time while AO corrections are being applied to a 700 Hz forced shear layer with upper and lower Mach numbers of approximately 0.79 and 0.1, respectively.

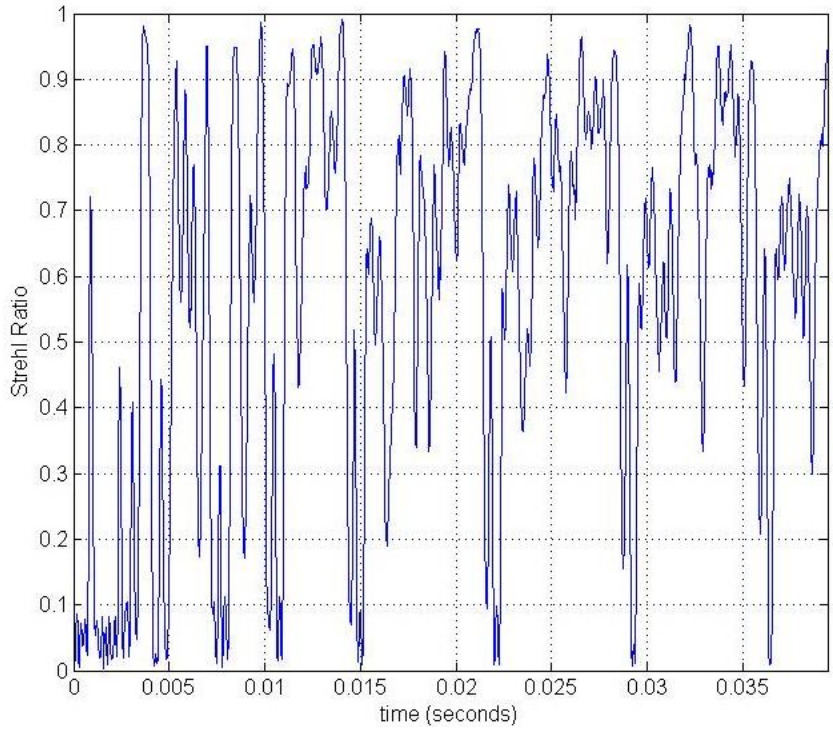

Figure 4.36: Strehl ratio verses time after tip/tilt has been removed given the results shown above in Fig. 4.35 (B).

One-dimensional far-field intensity patterns were again constructed from the residual wavefront error (refer to Fig. 4.33) post AO corrections and tip/tilt removal. The four intensity patterns shown below in Fig. 4.37 correspond to times 0.002 seconds (upper left), 0.01 seconds (upper right), 0.015 seconds (lower left), and 0.025 seconds (lower right). The Strehl ratios at each of these instances are 0.042, 0.421, 0.009, and 0.798, respectively. As before, the ideal one-dimensional intensity pattern is shown by a dashed curve in each figure.

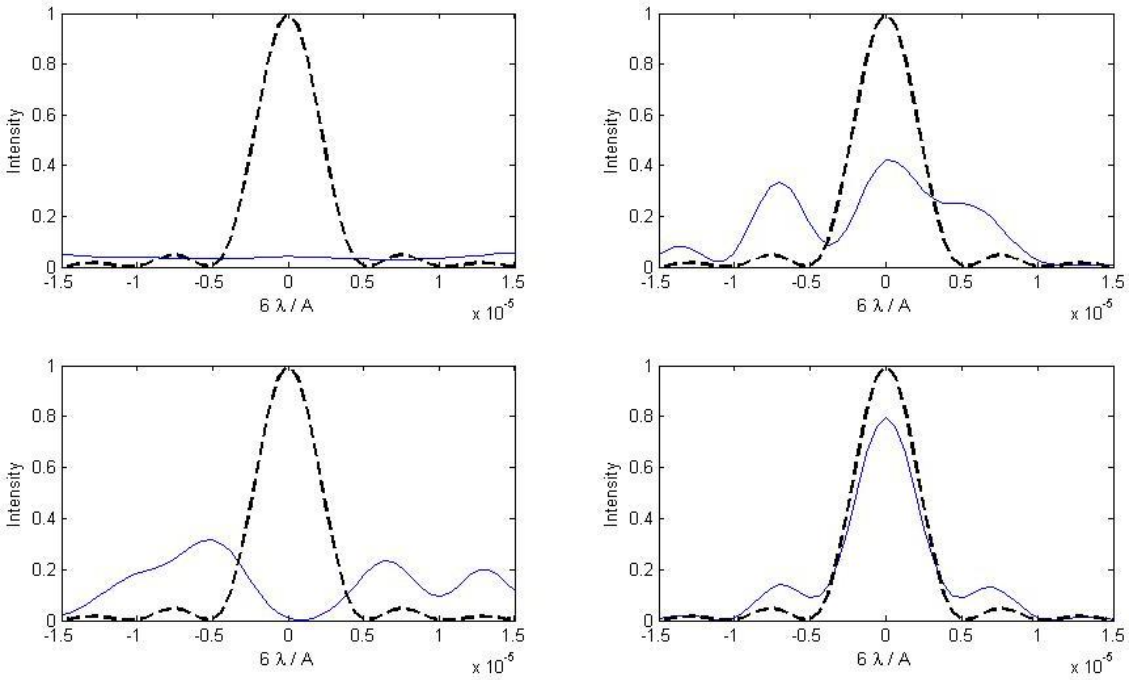

Figure 4.37: A series of four one-dimensional intensity patterns constructed from residual wavefront errors induced by a Mach 0.79/0.11 numerical shear layer (refer to Fig. 4.36) at times 0.002 seconds (upper left), 0.01 seconds (upper right), 0.015 seconds (lower left), and 0.025 seconds (lower right).

While the PLL controller is able to achieve phase-lock with the shear layer's aberrating wavefront in this case, the resulting Strehl ratio continues to experience less than desirable drops below 0.1. These drops in Strehl ratio seem to occur periodically as a result of subharmonics present within the flow field (refer to Fig. 4.36). Since the alternative AO controller is based upon a single frequency wavefront correction, subharmonics such as those found in this case inhibit the controller's ability to produce consistent results. As stated earlier, the success of the alternative AO control method relies highly on the shear layer's susceptibility to regularization. More specifically, favorable results occur when the emerging wavefront is both highly regular and sinusoidal in form, containing little to no harmonics. However, the advantages of the

PLL approach introduced in this dissertation may still be exploited in such high-speed shear layer cases where subharmonics become more dominant. In these instances, it may be possible to construct a conjugate correction containing more than one frequency while still using a PLL controller for phase-locking purposes. This recommendation would be very similar to the man-in-the-loop experiment conducted by Duffin [27] at the University of Notre Dame. Only instead of manually phasing the wavefronts, a PLL controller would be used to phase-lock the forcing signal with the fundamental or a subharmonic signal contained in the DM's conjugate correction. This idea is discussed further in Chapter 7 (Section 7.2). It should also be noted that maintaining lesser OPD values upon regularization is advantageous. If possible it is recommended to force the shear layer with higher forcing frequencies, in an effort to minimize the size of the regularized large-scale structures while keeping the region of regularization close to the shear layer's point of origin.

4.5.4. Ramp Response Simulation

In addition to studying the PLL controller's step response to phase errors, a ramp change in phase between the conjugate correction and the shear layer's regularized wavefront was also investigated. A Mach 0.7/0.2 shear layer was forced at 1200 Hz, while the AO PLL controller was simulated with an operating frequency of 1150 Hz. This created a constant 50 Hz frequency difference between the conjugate correction and the shear layer's emerging wavefront corresponding to a ramp changing phase (refer to Eq. (4.17)). Figure 4.38 (A) shows the PLL's phase response verses time as the controller compensates for a ramp change in phase along with an initial constant phase

error. As shown in Fig. 4.38 (B), once the controller locks onto the ramp changing phase the corresponding Strehl ratio improves resulting in a time-averaged Strehl ratio of approximately 0.82.

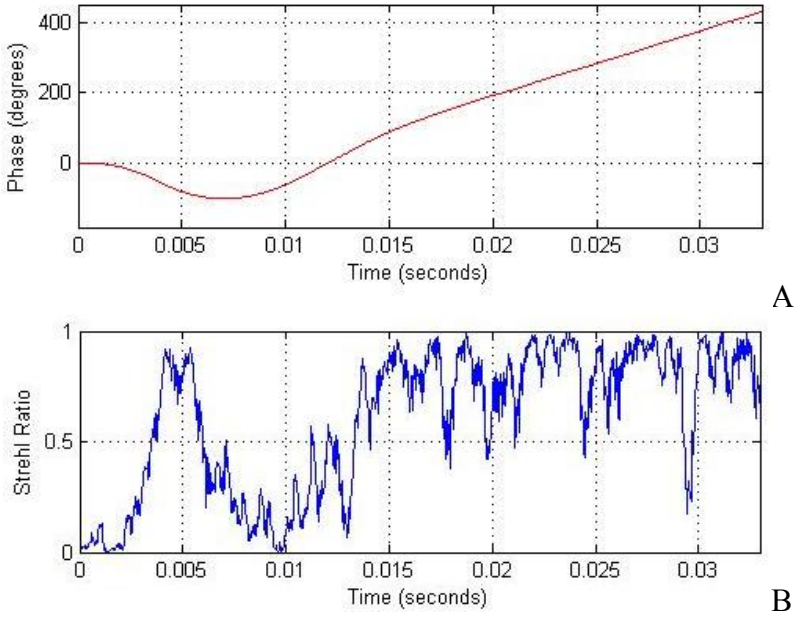

Figure 4.38: (A). Controller's phase response to a ramp change in phase corresponding to a 50 Hz frequency difference (B). Strehl ratio verses time as the controller compensates for phase errors given a Mach 0.7/Mach 0.2 shear layer forced at 1200 Hz.

4.5.5. Simulation Summary

The results shown above throughout Section 4.5 clearly demonstrate the feasibility and potential benefits of using the alternative AO approach and PLL controller proposed in this dissertation. By combining shear layer regularization with a PLL control strategy, an otherwise seemingly insurmountable bandwidth limitation may be circumvented. In creating a regularized shear layer and consequently its emerging wavefront whose form is highly periodic, a PLL controller may be used to synchronize a sinusoidal wavefront estimation with the shear layer. For cases that involve harmonics or

whose form varies slightly from a pure sinusoid, an alternative estimation model might be employed while still utilizing the PLL control strategy presented throughout this dissertation to achieve phase-lock between wavefronts.

After reviewing the successful simulations reported in Section 4.5, the PLL AO controller described above was constructed electronically. The following chapter (Chapter 5) details the controller's individual circuitry components and transfer functions along with the overall analog PLL circuit. Finally, Chapter 6 describes experimental results obtained from testing the PLL controller and Chapter 7 provides concluding remarks and further recommendations.

CHAPTER 5:

ALTERNATIVE AO CONTROLLER CIRCUITRY

5.1. Analog AO Controller Circuit

This chapter describes the analog circuitry used to create the AO controller outlined in Chapter 4. The controller consists of two main components, the PLL circuit and the amplitude estimator circuit. The PLL circuit can be further separated into its phase detector, loop filter, and voltage-controlled oscillator components. Figure 5.1 displays a schematic of the overall AO controller circuitry. The shear layer jitter signal acts as the reference source. The signal is first scaled to produce an output amplitude of approximately two. Then the signal is input into the phase detector circuitry. This reference signal is multiplied with the PLL output after the PLL signal has been phase-lagged by approximately 90°. It should be noted that the 90° phase-shift circuit shown below in Fig. 5.1 is for an 800 Hz input signal and must be designed based upon the input frequency. However, when the PLL circuit is applied to the final AO controller for wind tunnel testing the phase-shift circuit will be omitted since the measured jitter signal (reference signal) is a derivative of the DM actuator's driving signal.

Once the two signals are mixed (or multiplied) the resulting output is passed through a low-pass filter circuit to detect their phase difference. Next, the loop filter acts as a regulator ensuring zero tracking error for both step and ramp phase changes while

maintaining closed-loop system stability. The loop filter's output represents the phase adjustment needed to begin synchronizing the two wavefronts. This voltage signal is summed with the waveform generators *FM bias* signal; the voltage required for the waveform generator to operate at its center frequency. Finally, the output is inverted serving as the waveform generators *FM sweep* input. The VCO produces a sinusoidal output signal whose amplitude is scaled to unity before closing the PLL's feedback loop.

A separate loop is used to estimate the appropriate amplitude for the conjugate correction. The amplitude of the shear layer's jitter signal is approximated using a *RMS-to-DC converter* chip. The output is scaled by a correction factor closely approximating the shear layer jitter signals actual amplitude. This signal is then multiplied with the VCO output, whose amplitude is roughly unity after being scaled itself. The final output represents a sinusoidal voltage signal whose amplitude and phase are continually being adjusted to match the shear layer's jitter signal until phase-locking occurs.

The PLL's phase-locked output may be used to control the DM in a real-time AO correction. Once the output has been scaled appropriately, a series of phase-shifter circuits represent a possible means of constructing the two-dimensional conjugate correction from the one-dimensional PLL output. The following sections describe each circuitry component in more detail. Further specifications pertaining to each major component or chip, shown below in Fig. 5.1, can be found in Appendix C. Detailed data sheets may also be referenced at each of the manufacturer's website for more information and circuitry examples.

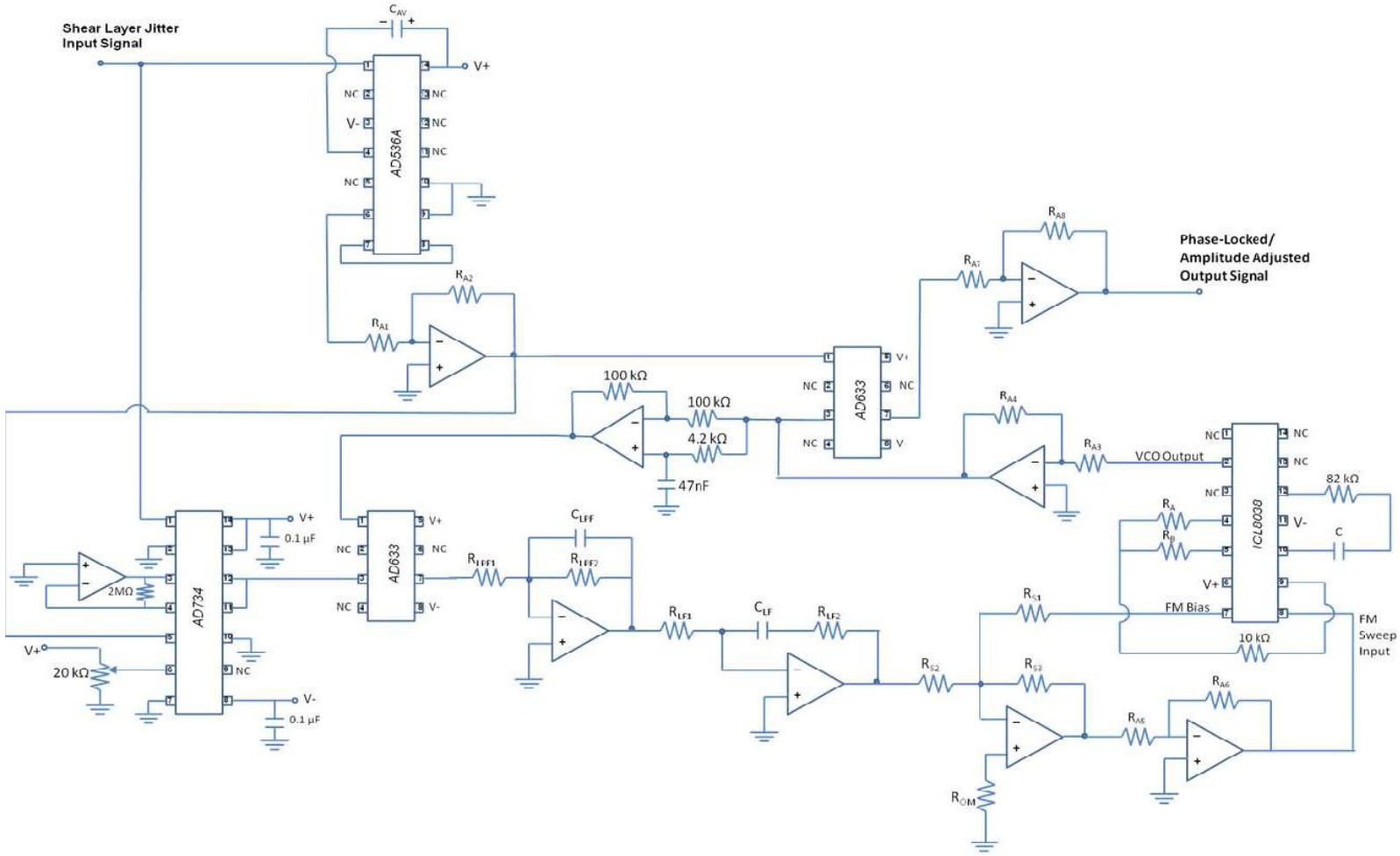

Figure 5.1: Schematic showing the overall circuitry for the AO controller.

5.2. PLL Circuit

As mentioned previously, the PLL circuit is comprised of three main components: the phase detector circuit, the loop filter circuit, and the voltage-controlled oscillator circuit. Each piece plays a critical role in the overall performance of the PLL controller. The phase detector is used to determine the phase difference between the reference input and the PLL output. The loop filter is the component with the most design flexibility, constructed to achieve certain response characteristics. In this case the loop filter was designed to ensure zero tracking error given a step or ramp input while maintaining closed-loop system stability. The voltage-controlled oscillator circuit produces an oscillatory output based upon its center frequency and the loop filter's output: a voltage signal related to phase error. A more thorough description of the circuitry and corresponding transfer functions follows.

5.2.1. Scaling Reference and Feedback Signals

In an effort to isolate the PLL control from the amplitude estimator control, both the reference signal (shear layer jitter signal) and the feedback signal (PLL output) are scaled before being fed into the phase detector. Recall that two terms are produced upon mixing the two sinusoidal input signals: a double harmonic and DC component whose amplitude is approximately equivalent to half the product of the incoming signal's amplitudes (Eq. (4.10)). Therefore, by scaling the PLL output amplitude to unity and the reference signal amplitude to approximately 2, the mixed signals DC component will more accurately represent the unknown phase difference.

While the PLLs output may be scaled by a constant using a basic op amp inverter amplification circuit, the reference signal must be scaled by a value that may vary. Consequently, a four-quadrant multiplier/divider chip (AD734) is used to perform this operation. Figure 5.2 shows the circuit connections for the AD734 used as a three-variable multiplier/divider with a fixed scale factor of approximately 2.

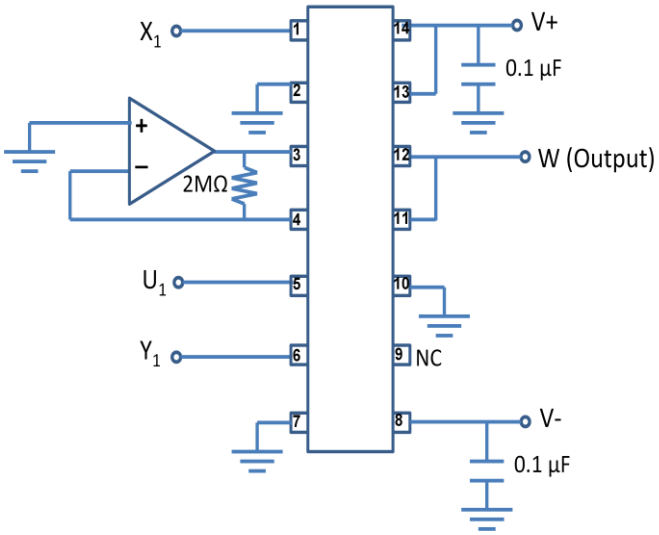

Figure 5.2: Circuit diagram of the four-quadrant multiplier/divider connections (AD734).

For the connections shown in Fig. 5.2, the output from the AD734 is given by,

$$W = \frac{(X_1 - X_2)(Y_1 - Y_2)}{(U_1 - U_2)} + Z_2 . \tag{5.1}$$

where the X_2 (pin 2), Y_2 (pin 7), U_1 (non-inverting input of the op amp connected to pin 3), and Z_2 (pin 10) inputs have all been grounded. For the dissertation application depicted in Fig. 5.1, the shear layer jitter signal represents the X_1 input, a scale factor approximately equal to 2 is applied to the Y_1 input, and the shear layer's approximated

amplitude (output from the amplitude estimator circuitry) is connected to the U_2 input. As a result the output amplitude maintains an approximate value of 2 accounting for the factor found in Eq. (4.10) and Eq. (4.12). Further specifications for the AD734 chip shown in Fig. 5.2 can be found in Appendix C.5.

5.2.2. Phase Detector Circuitry

Phase detection is achieved through a simple multiplication and low-pass filtering combination. A four-quadrant multiplication chip (AD633) has the capability of receiving four different inputs. The difference between pin 1 and pin 2 is multiplied with the difference between pin 3 and pin 4. The product generated from this chip has a scale factor of 10 Volts; therefore the gain of the phase detector, K_{PD}, is 1/10. The AD633 chip also has the capability of adding two or more multiplier outputs through a summing node, although not used for this specific application. The transfer function for the AD633 multiplication chip is given by,

$$W = \frac{(X_1 - X_2)(Y_1 - Y_2)}{10} + Z \tag{5.2}$$

where X_1 is the input for pin 1, X_2 is the input for pin 2, Y_1 is the input for pin 3, Y_2 is the input for pin 4, Z is the input for pin 6, and W is the output from pin 7.

For the PLL testing discussed in Section 6.1, the scaled PLL output (directly related to the DM's conjugate correction) is connected to pin 1 and the scaled shear layer's jitter signal (or function generator signal) is connected to pin 3. For the proposed high-speed AO correction experiments following the completion of this dissertation (outlined in Section 6.2), the shear layer's jitter signal will be connected to both pin 1 and

pin 3, while the other jitter signal (representing the difference between the shear layer jitter and the DM jitter) will be connected to pin 2. The product generated from the multiplication chip is sent through a low-pass filter designed to attenuate both the double harmonic and any higher order noise. The result is to isolate the signal's DC component which is directly related to the phase difference between inputs. An active low-pass filter with a cutoff frequency of approximately 500 rad/s (80 Hz) was created using a low-noise operational amplifier (NE5534A). Figure 5.3 shows a circuit diagram of the low-pass filter.

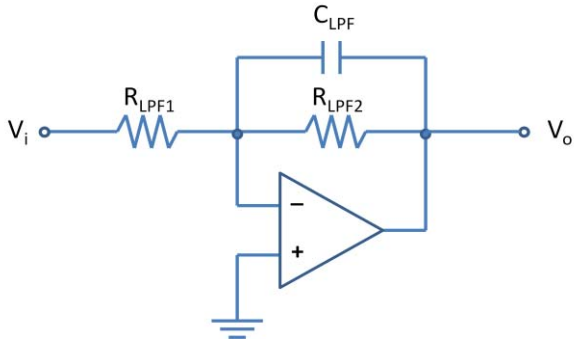

Figure 5.3: Circuit diagram of the phase detector's low-pass filter.

The overall transfer function for this circuit is given by,

$$\frac{V_o(s)}{V_i(s)} = -\frac{R_{LPF2}}{R_{LPF1}}\left(\frac{1}{1+sR_{LPF2}C_{LPF}}\right) \tag{5.3}$$

where R_{LPF1} is a 10 kΩ resistor, R_{LPF2} is a 100 kΩ resistor, and C_{LPF} is a 22 nF capacitor. These values were selected based on the compensator analysis described in Section 4.4.6. It should be noted that these resistor values produce a low-pass filter gain constant of approximately 10. This was designed to accommodate for the multiplier chip's gain constant of 1/10, therefore resulting in an overall unity gain constant for the entire phase

detector circuit. Key specifications for the four-quadrant multiplier chip (AD633) and the low-noise operational amplifier (NE5534A) can be found in Appendix C.1 and Appendix C.2, respectively.

5.2.3. Loop Filter Circuitry

As discussed in Section 4.4.1, the loop filter must contain both a pole at zero (integrator) and a minimum phase zero in order to meet the specified design requirements. This was achieved using a low-noise operational amplifier (NE5534A) in combination with a capacitor and two resistors. Figure 5.4 shows the circuit diagram for the loop filter whose transfer function is given by,

$$\frac{V_o(s)}{V_i(s)} = -\left(\frac{1+sR_{LF2}C_{LF}}{sR_{LF1}C_{LF}}\right). \tag{5.4}$$

Resistor and capacitor values were chosen based upon the design summary described in Section 4.4.6. The resistor values for R_{LF1} and R_{LF2} are approximately 150 kΩ and 180 kΩ, respectively, while a 100 nF capacitor was chosen for C_{LF}. These values result in an overall gain constant for the loop filter of approximately 67.

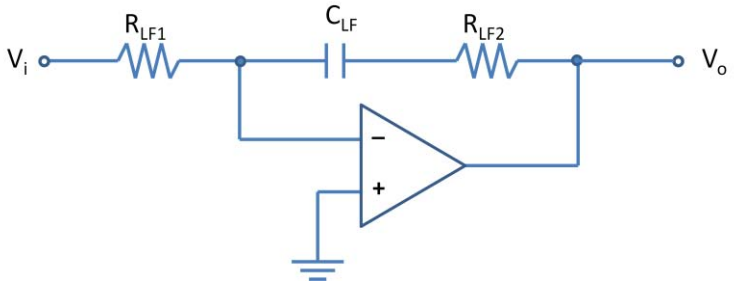

Figure 5.4: Circuit diagram of the loop filter containing both a pole at zero and a minimum phase zero.

5.2.4. Voltage-Controlled Oscillator Circuitry

The voltage-controlled oscillator (VCO) represents the final step in the PLL process. It produces an oscillatory response based upon its center frequency and a sweep input. The VCO uses a phase input to adjust its output frequency, therefore acting as an integrator in the circuit. The gain constant of the VCO corresponds to its sensitivity; a value referring to the change in instantaneous frequency as a function of the change in input amplitude (*FM Sweep* input) such that

$$K_{VCO} = \frac{d\omega}{dv}. \tag{5.5}$$

A precision waveform generator (NTE864) chip capable of producing sinusoidal waveforms with high accuracy was purchased for this task. The center frequency is selected externally using a combination of resistors and capacitors while frequency modulation and sweeping is accomplished through an external voltage signal (*FM Sweep* input). Figure 5.5 shows a diagram of the waveform generator circuit connections.

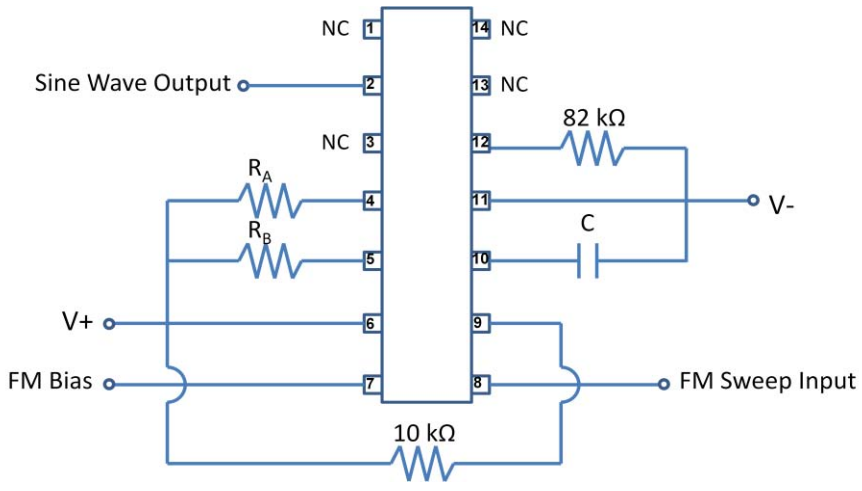

Figure 5.5: NTE864 waveform generator circuit connections for the PLL application described in this dissertation.

A series of experimental tests were performed at varying center frequency values in order to determine the gain constant for this particular waveform generator chip. Different combinations of resistor values (R_A and R_B) and capacitor value (C) were used to create varying center frequencies where the center frequency of the VCO is given by

$$f_c = \frac{0.33}{RC} \tag{5.6}$$

where $R=R_A=R_B$. The resistors, R_A and R_B, were selected with equivalent values to achieve a 50% duty cycle. In order to determine the center operating frequency, the VCO was initially tested using each combination of resistors and capacitor, with pin 7 (*FM Bias*) and pin 8 (*FM Sweep*) directly connected. A series of subsequent tests were performed in which pin 7 was left with no connection and a range of input voltages was applied to pin 8. The VCO's output frequency was recorded for each input voltage. The change in output frequency was plotted as a function of change in input voltage. Finally, the VCO's sensitivity was determined by examining the slope of the line created for each set of resistor/capacitor combination. Figure 5.6 shows the VCO's sensitivity verses center operating frequency. Recalling that the sensitivity refers to the VCO gain constant, the curve shown in Fig. 5.6 may be described by the following equation:

$$K_{VCO} = -0.205 f_c . \tag{5.7}$$

In other words when the VCO has a center operating frequency of 830 Hz, the gain constant, K_{VCO}, is approximately 170.

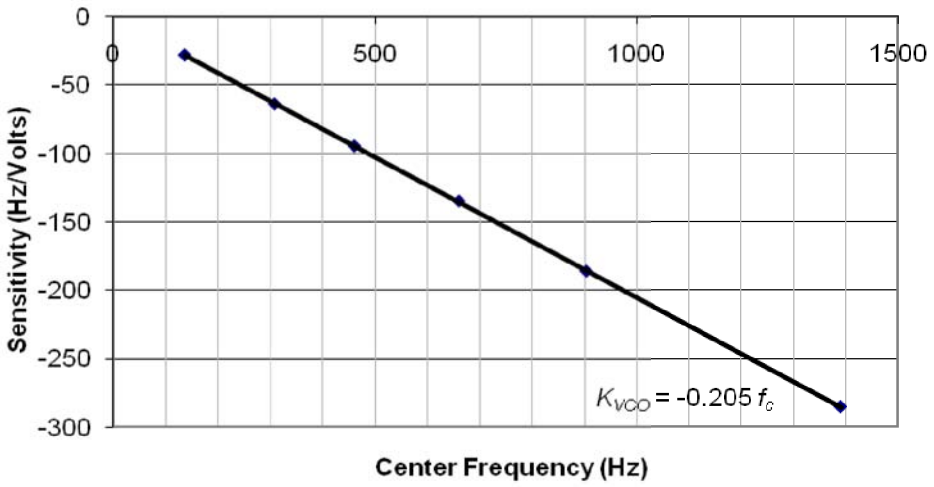

Figure 5.6: Voltage-controlled oscillator (NTE864) sensitivity verses its center operating frequency obtained through experimental testing.

The following resistor and capacitor values were used for the function generator testing described and reported in Section 6.1. Resistor values of approximately 12 kΩ were chosen for R_A and R_B, similar to the test circuits shown in the NTE864 data sheet (the data sheet may be found at the manufacturer's website referred to in Appendix C.3). A 33 nF capacitor was used for C producing a center operating frequency of approximately 830 Hz (Eq. (5.6)); the combination of resistor and capacitor values produce a specific *FM Bias* voltage signal which regulates the chip's operating frequency. The *FM Bias* signal is summed with the PLL's phase error signal (output from the loop filter discussed previously) through an op amp summation circuit where R_{S1}, R_{S2}, and R_{S3} are each 100 kΩ resistors and R_{OM} is a 33kΩ resistor. Finally, the signal is inverted before being used as the *FM Sweep* input. This was achieved using a basic op amp inverter with unity gain where R_{A5} and R_{A6} are each 10 kΩ resistors (refer back to Fig. 5.1).

The VCO's oscillating output has an amplitude equivalent to approximately 0.22 times the supply voltage, V_S. Testing reported throughout this dissertation, specifically in Section 6.1, was conducted using a supply of +/- 12 Volts. Therefore, the VCO's output maintained an amplitude of approximately 3.3 Volts. In order to create an output whose amplitude approaches unity, the VCO's output is scaled by a factor of $\frac{1}{0.22V_S}$, approximately equivalent to 0.38 for these tests. This was achieved using 100 kΩ and 39 kΩ resistors for R_{A3} and R_{A4}, respectively (refer to Fig. 5.1). Key specifications for NTE864 may be found in Appendix C.3.

5.3. Amplitude Estimator Circuit

A separate control loop is used to estimate the appropriate amplitude for the conjugate correction. The jitter signal emerging from the regularized shear layer is sent through a *True RMS-to-DC Converter* chip (AD536A). The chip produces a DC output equivalent to the true root-mean-square of the incoming AC signal; given a sinusoidal input this equates to approximately 0.707 times the signal's amplitude. Consequently, the output from AD536A is scaled by approximately 1.414 generating an estimate of the original signal's amplitude. This scaling is achieved using a basic op amp inverting amplifier circuit shown below in Fig. 5.7 where R_{A1} and R_{A2} are 70.8 kΩ and 100 kΩ resistors, respectively. It should be noted that when the PLL circuit is used to construct the conjugate correction sent to the DM for real-time wavefront corrections an additional scaling factor of $1/k_{sl}^2$ must be added due to the relationship between an optical wavefront (OPD) and its corresponding jitter signal (refer back to Eq. (2.4) and Eq. (4.7)).

Once the amplitude is estimated, the DC signal is multiplied with the scaled VCO output (whose amplitude should be approximately 1) using an AD633 analog multiplier chip introduced previously. Due to the $1/10$ scale factor associated with AD633, a final amplification must be performed where R_{A7} and R_{A8} are 10 kΩ and 100 kΩ resistors, respectively. The resulting output now resembles the initial reference signal, or shear layer jitter signal, in both phase and amplitude. Figure 5.7 shows a circuit diagram of the *RMS-to-DC Converter* connections as well as the scaling and multiplication circuitry discussed above. Further specifications for AD536A may be found in Appendix C.4.

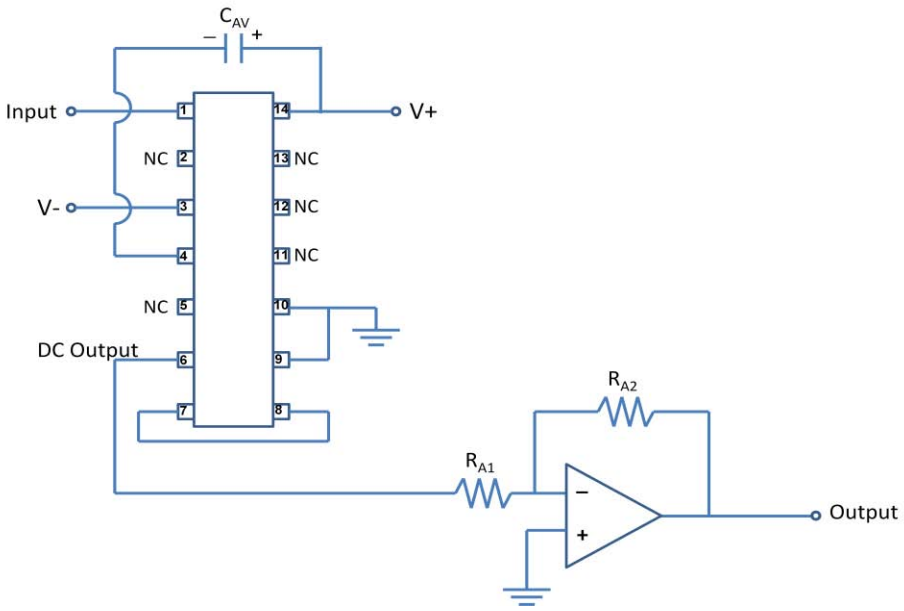

Figure 5.7: Amplitude estimator circuitry including the *RMS-to-DC Converter* (AD536A) circuit connections.

When applying this circuit to future experimental tests in which the DM will be used to perform AO corrections, resistors R_{A7} and R_{A8} must be modified appropriately. Before the phase-locked output may be sent to the DM, the signal must be amplified by the proper scale factor compensating for the following: the AD633 $1/10$ scale factor, the

DM amplifier's 3X amplification factor, and the DM's voltage to stroke conversion (+/- 10 Volts to +/- 4 μm). The scaled phase-locked output may then be used to control the DM actuators used to create the appropriate conjugate correction.

5.4. DM Waveform Construction

For the high-speed shear layer AO correction experiments following the completing of this dissertation, the PLL's single output signal must be used to construct a two-dimensional conjugate correction. Assuming the shear layer has been regularized, its emerging optical wavefront acts like a traveling sinusoidal waveform (see further discussion in Chapter 7). The seven rows of actuators composing the DM will be used to create this traveling sinusoid. The center row will be controlled by the PLL's phase-locked output since the shear layer's jitter signal (PLL reference signal) is measured at the same center location. Each of the remaining six rows of actuators will also be controlled by this signal after being appropriately phase-shifted. The phase-shift between consecutive rows should be equivalent to

$$\Delta\gamma = k_{sl}\delta, \tag{5.8}$$

where δ represents the physical spacing between actuators rows (7 mm multiplied by the magnitude change due to the telescope) and k_{sl} refers to the regularized wavefront's wave number (Eq. 4.3).

A series of simple analog phase-shift circuits is suggested to create the additional six signals as shown in Fig. 5.8; however, it may be advantageous to explore a more accurate solution in subsequent work supporting this dissertation research. One such

recommendation would be to drive the DM with a predetermined waveform, possibly containing a subharmonic similar to the experimental testing performed by Duffin [27], while achieving synchronization using the PLL's phase-locked output (see Chapter 7 for further discussion).

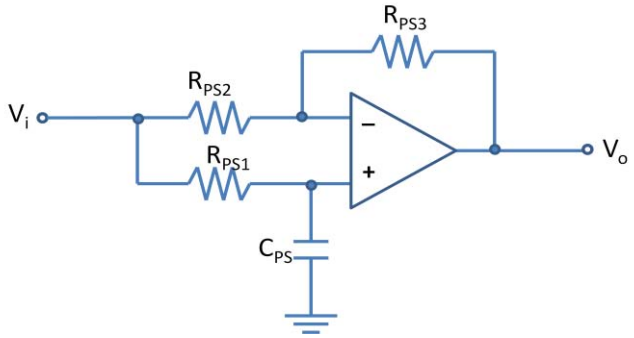

Figure 5.8: Single phase-shift circuit suggested to create the signals used to control the remaining six rows of actuators on the DM.

CHAPTER 6:

ALTERNATIVE AO CONTROLLER EXPERIMENTS

6.1. Function Generator "Jitter" Testing

After testing the individual circuit components described in Chapter 5, the alternative AO controller was constructed on a prototype board pictured below in Fig. 6.1. Upon completion of the PLL circuit, a series of experimental tests were performed using a function generator as the reference input. The purpose of these experiments was to test the PLL's phase-locking capability and evaluate the amplitude estimator circuit response. The following sections outline the experimental procedure used in testing and describe the results obtained.

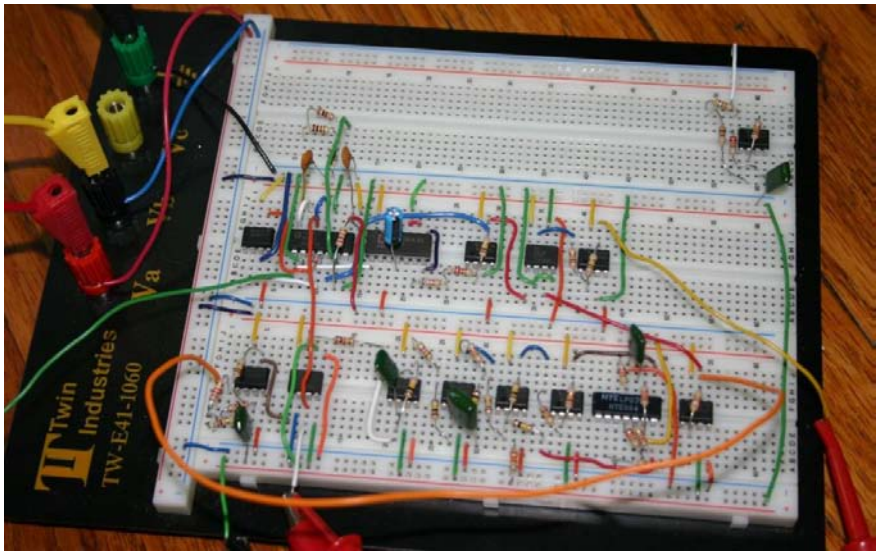

Figure 6.1: Photograph of the alternative AO controller prototype board circuitry.

6.1.1. Experimental Setup

The experimental testing described in this section was performed using a GW Dual Tracking Laboratory DC Power Supply set to +/- 12 Volts operating in series. A function generator provided the reference input allowing for variable input frequency and amplitude during testing. The function generator signal was connected to the reference input, identified as the „Shear Layer Jitter Input Signal' in Fig. 5.1. A two channel oscilloscope was used to monitor the input reference signal in conjunction with the PLL's phase-locked output signal. Channel 1 was connected to the „Shear Layer Jitter Input Signal' and served as the trigger for testing. Channel 2 was connected to the „Phase-Locked/Amplitude Adjusted Output Signal' (see Fig. 5.1). A data acquisition system was used to record several signals within the circuit including the *Shear Layer Jitter Input Signal*, the scaled *Shear Layer Jitter Input Signal*, the *Phase-Locked/Amplitude Adjusted PLL Output Signal*, the scaled *PLL output signal*, and the *amplitude estimation output*. Once the experiment was set up, power was supplied to the prototype circuit board commencing each experimental test and data was recorded.

A series of experimental tests were performed in order to examine the alternative AO controller's response to input variations in both phase and amplitude. Upon powering the AO controller, an unknown phase difference exists between the function generator's sinusoidal input and the VCO's sinusoidal output. In addition to any initial constant phase error, ramp changes in phase were also investigated. A constant frequency difference between the function generator's input signal and the PLL's operating frequency represents a steady change in phase over time. The results presented in Section 6.1.2 demonstrate the PLL's ability to track such phase differences. The AO

controller's ability to compensate for amplitude fluctuations was also examined. Throughout several tests, the function generator's input amplitude was varied abruptly in order to assess the ability of the amplitude estimator circuit to track changes in amplitude. These test results may be found below in Section 6.1.3.

As described in the previous chapter, the PLL circuit tested here was designed with a center operating frequency of approximately 830 Hz. Thus, function generator testing was conducted using a range of frequencies at or near the circuits operating frequency while input amplitudes ranged from 0.5 Volts up to 5 Volts. The following experimental data was obtained using a six channel data acquisition system. Data was recorded at a rate of 200 kHz over a period of 5 seconds for each test. Power was supplied to the circuit board shortly after acquiring began. Figure 6.2 shows a picture of the experimental setup described above.

Figure 6.2: Photograph of the experimental setup for the function generator testing performed on the AO controller circuit.

6.1.2. Phase Response Results

A series of experimental tests were conducted to assess the PLL controller's phase-locking capability. Input reference frequencies, representing the shear layers regularized jitter frequencies, ranged from 500 Hz up to 1500 Hz. Several tests were performed at each input frequency using a variety of amplitudes. Data was collected at a rate of 200 kHz over a period of 5 seconds. The sixth channel from the data acquisition system was connected to the power supply's positive supply voltage providing a reference signal for determining the commencement of each test. Consistent phase-locking results were observed for frequencies between approximately 700 Hz and 1200 Hz representing the PLL's capture range given this particular operating frequency. Phase-locking outside of this frequency range remained inconsistent.

The following results display the phase-locking data obtained over a series of experimental tests. The figures show phase error, expressed in Volts, as a function of time. Each set of data corresponds to a given reference frequency and input amplitude. The analog signals were acquired simultaneously during testing and post-processed to determine phase error. A matlab code was written to evaluate the phase difference between signals based upon the rising cross-over locations. Since the two signals do not always maintain the same frequency with one another the resulting phase error does not always appear to vary smoothly.

In addition, it should be noted that since the 90° phase-shift circuit (referred to in Section 5.1) was constructed specifically for an 800 Hz operating frequency, any departures from that frequency result in small amounts of phase error after phase-lock has occurred. However, when the PLL circuit is applied to the final high-speed aero-optic

experiments the 90° phase-shift circuit will be eliminated since the PLL's output will ultimately be used to control the DM wavefront, a derivative of the input jitter signal (Eq. (2.4)). Thus once removed, the steady-state phase errors shown below should no longer be present.

The first set of phase results are shown in Fig. 6.3. The reference frequency and amplitude provided by the function generator for this test were 700 Hz and 4 Volts, respectively. Phase-locking occurs after approximately 0.09 seconds and although a negative 10 degree steady-state error exists upon phase-locking this should be eliminated once the phase-shift circuit has been removed. Similar results were obtained for this reference frequency given input amplitudes ranging from 0.5Volts to 5 Volts.

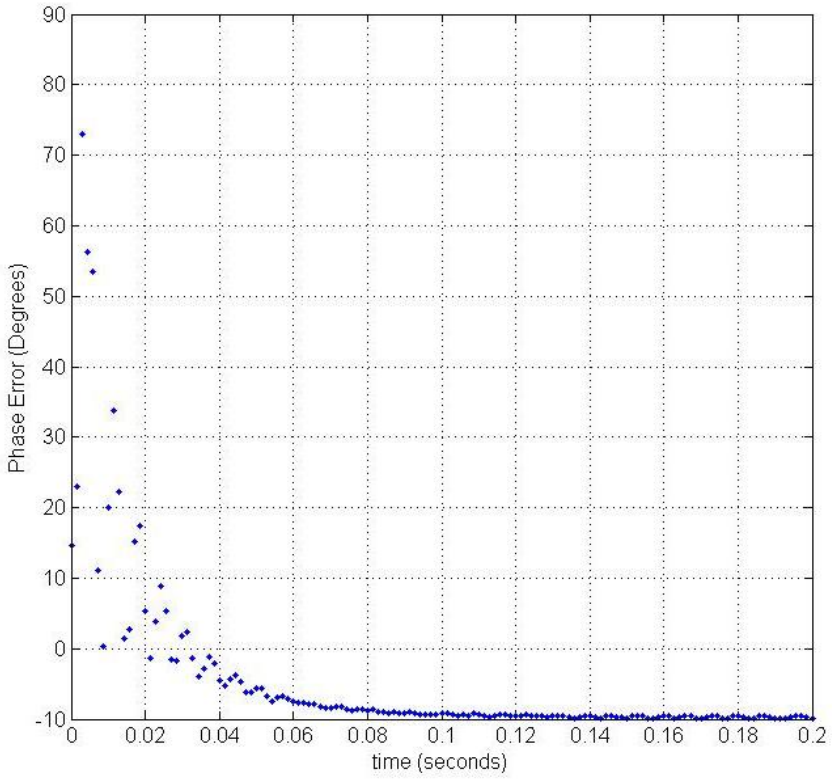

Figure 6.3: Phase error (degrees) verses time (seconds) for a PLL experimental test given a reference frequency and amplitude of 700 Hz and 4 Volts, respectively with an operating frequency of approximately 830 Hz.

The second set of results shown below is for a reference frequency and amplitude of 800 Hz and 1 Volt, respectively. In this case phase-locking occurs after approximately 0.05 seconds with very little steady-state error as shown in Fig. 6.4. This makes sense since the function generator's reference frequency is very near the PLL's operating frequency of 830 Hz. Similar phase error results were obtained for input amplitudes ranging from 0.5 Volts to 5 Volts.

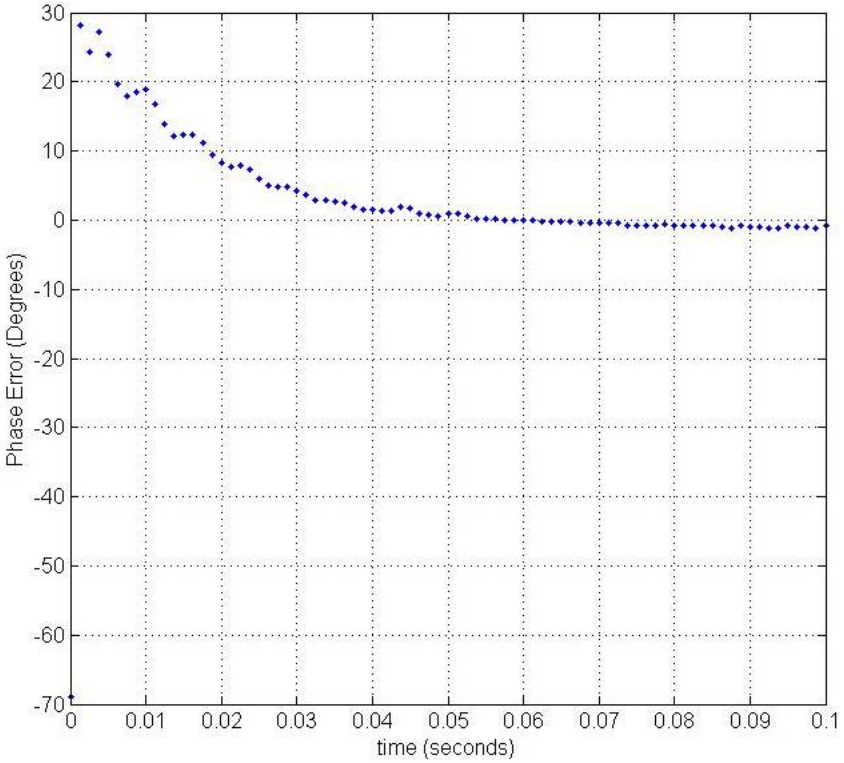

Figure 6.4: Phase error (degrees) verses time (seconds) for a PLL experimental test given a reference frequency and amplitude of 800 Hz and 1 Volt, respectively with an operating frequency of approximately 830 Hz.

The results shown in Fig. 6.5 are for a reference frequency and amplitude of 900 Hz and 5 Volts, respectively. Phase-locking occurs after approximately 0.04 seconds. Since the reference frequency is greater than the PLL's operating frequency, the phase-

shift circuit induces a positive steady-state phase error of approximately 7 degrees on the PLL's output signal. Figure 6.6 shows the phase-locking results given a reference frequency and amplitude of 1000 Hz and 0.5 Volts, respectively. Phase-lock is achieved in less than 0.03 seconds with approximately 9 degrees of steady-state phase error. Once again, similar phase error results were obtained for input amplitudes ranging from 0.5 Volts up to 5 Volts in both cases. The phase responses shown in Figs. 6.3, 6.4, 6.5, and 6.6 demonstrate the PLL's tracking ability within the capture range. In all four cases phase-locking is achieved within 0.1 seconds or less.

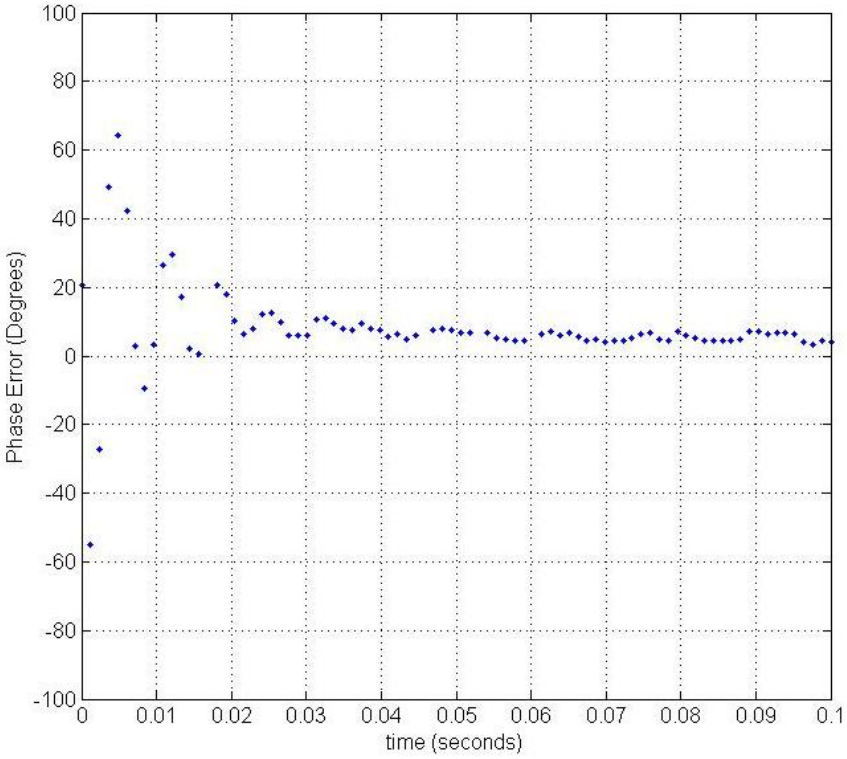

Figure 6.5: Phase error (degrees) verses time (seconds) for a PLL experimental test given a reference frequency and amplitude of 900 Hz and 5 Volts, respectively with an operating frequency of approximately 830 Hz.

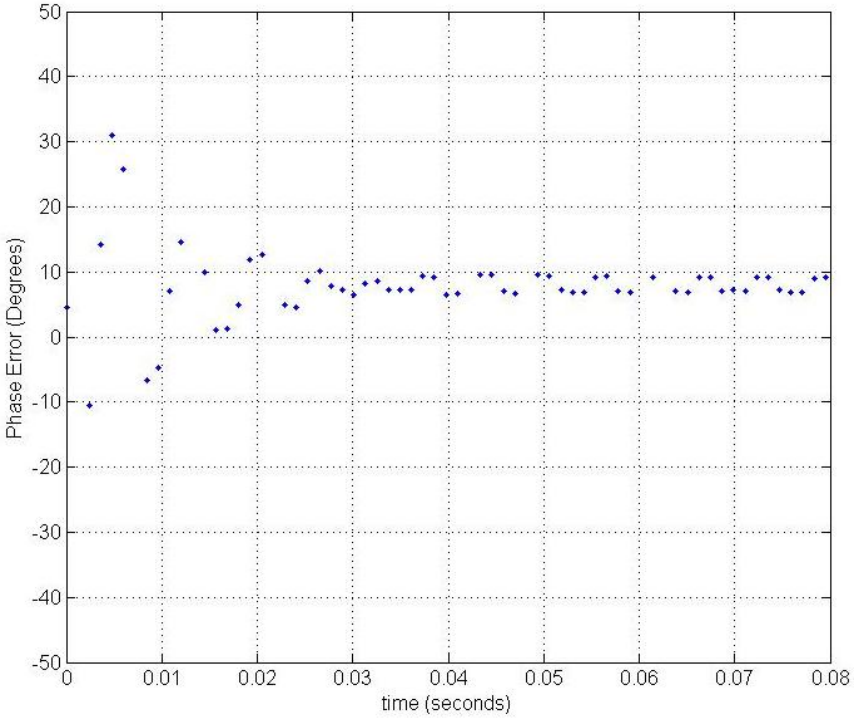

Figure 6.6: Phase error (degrees) verses time (seconds) for a PLL experimental test given a reference frequency and amplitude of 1000 Hz and 0.5 Volts, respectively with an operating frequency of approximately 830 Hz.

The results shown below in Fig. 6.7 demonstrate one set of data recorded outside the PLL's capture range. For this experiment the function generator's reference signal had a frequency of 1300 Hz and an amplitude of 2 Volts. As shown by the recurring fluctuations in phase difference between the two signals over the given time interval, phase-locking is not achieved in this case.

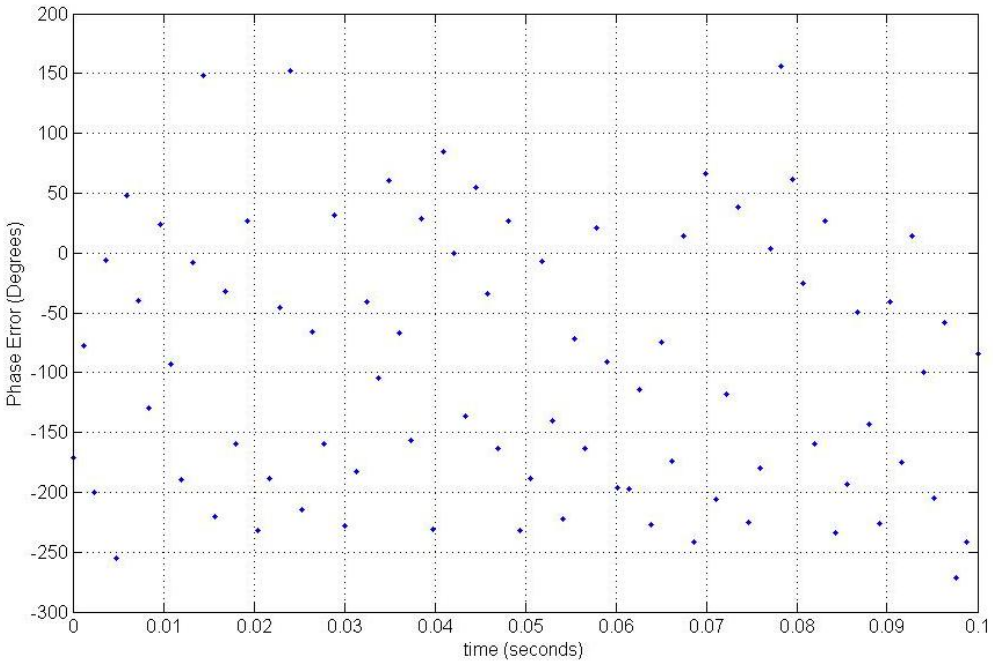

Figure 6.7: Phase error (degrees) verses time (seconds) for a PLL experimental test given a reference frequency and amplitude of 1300 Hz and 2 Volts, respectively with an operating frequency of approximately 830 Hz.

6.1.3. Amplitude Response Results

The amplitude response of the alternative AO controller was also examined experimentally. During each experiment the output from the amplitude estimator circuit was measured and compared to the function generator's input amplitude. The amplitude estimator output represents the jitter signal's amplitude calculated via the control circuit. Amplitude response results for each of the four phase-locking tests reported in Section 6.1.2 are shown in Figs. 6.8 – 6.11. The first case had a reference frequency of 700 Hz and an input amplitude of 4 Volts. The control circuit approximated the appropriate amplitude within 0.4 seconds as shown below in Fig. 6.8.

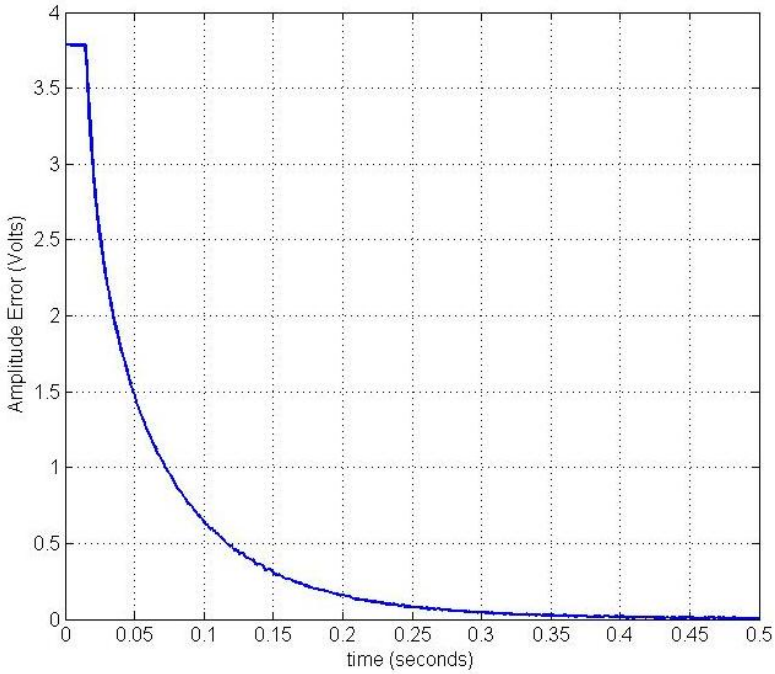

Figure 6.8: Amplitude error (Volts) verses time (seconds) for a PLL experimental test given a reference frequency and amplitude of 700 Hz and 4 Volts, respectively with an operating frequency of approximately 830 Hz.

Three more cases are shown below in Figs. 6.9 – 6.11. The amplitude results displayed in all four figures (Figs. 6.8-6.11) correspond to the phase error experiments reported in Figs. 6.3-6.6, respectively. In all four case studies the final amplitude is estimated within 0.4 seconds or less of the circuit power turning on. The small amounts of error shown in each case are due primarily to the inexact nature of the basic op amp inverting amplifier used to scale the RMS-to-DC Converter's output (Section 5.3). The ratio of resistor values, R_{A1} and R_{A2} (see Fig. 5.7), along with the precision of the RMS-to-DC Converter chip control the accuracy of this estimation. The controller's ability to track amplitude changes during testing was also investigated by manually varying the function generator's input amplitude. The output signal showed good tracking ability to any sudden amplitude variations.

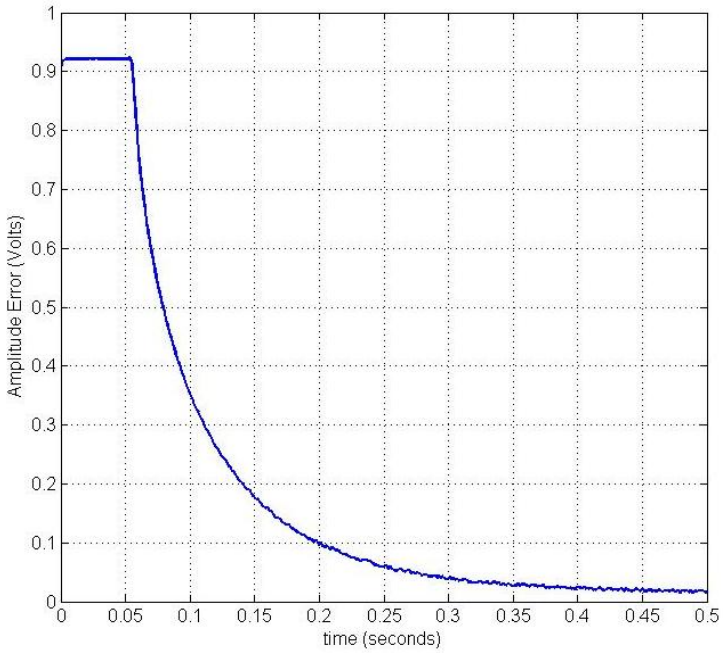

Figure 6.9: Amplitude error (Volts) verses time (seconds) for a PLL experimental test given a reference frequency and amplitude of 800 Hz and 1 Volt, respectively with an operating frequency of approximately 830 Hz.

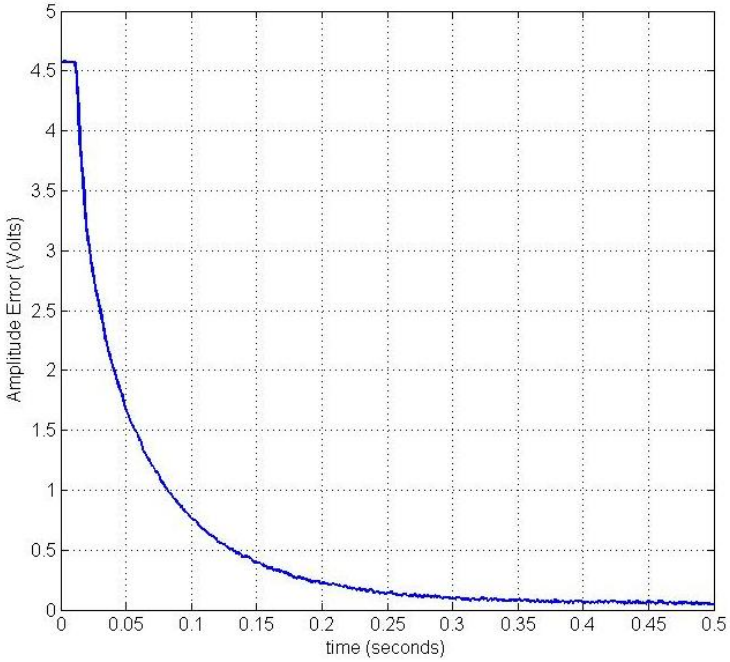

Figure 6.10: Amplitude error (Volts) verses time (seconds) for a PLL experimental test given a reference frequency and amplitude of 900 Hz and 5 Volts, respectively with an operating frequency of approximately 830 Hz.

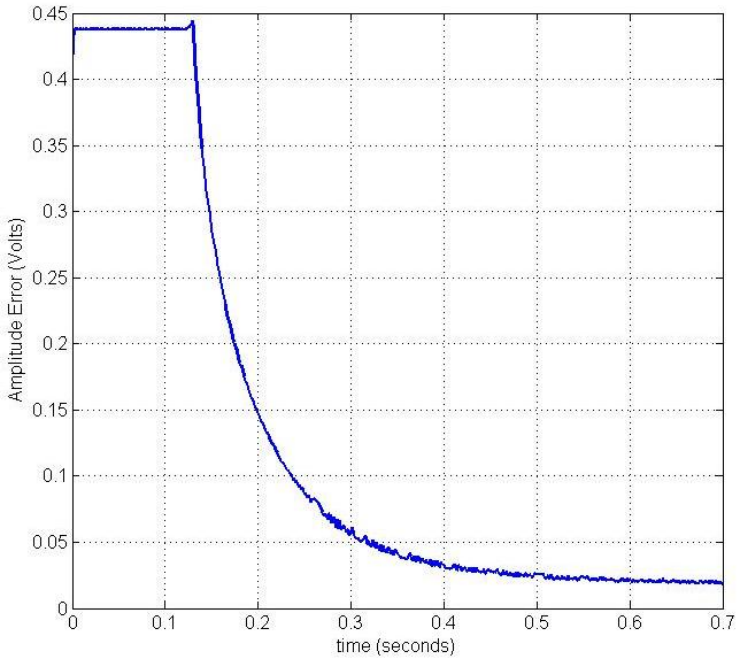

Figure 6.11: Amplitude error (Volts) verses time (seconds) for a PLL experimental test given a reference frequency and amplitude of 1000 Hz and 0.5 Volts, respectively with an operating frequency of approximately 830 Hz.

6.1.4. Jitter Error

This section provides a visual comparison between each set of jitter signals investigated above along with their respective jitter error over a specified time interval. The first experiment shown below in Fig. 6.12 and Fig. 6.13 was conducted using a 700 Hz sinusoidal signal whose input amplitude was 4 Volts. The analog input signal was produced using a function generator and is represented by the dashed curve shown in Fig. 6.12. The solid curve displays the PLL's output signal after both amplitude estimation and phase synchronization has been achieved. Figure 6.13 was produced by subtracting the PLL output from the function generator input. The solid curve represents the jitter error present after synchronization. While the initial jitter signal's amplitude was

approximately 4 Volts, maximum jitter error was reduced to less than 0.7 Volts. Recall that the PLL's center operating frequency for these experimental tests was approximately 830 Hz which results in increased phase error with larger variances from the input frequency due to the phase shift circuit; however, as discussed earlier the phase error induced by the phase-shift op amp circuit should all but be eliminated when this component is removed for the ultimate high-speed shear layer wavefront experiments.

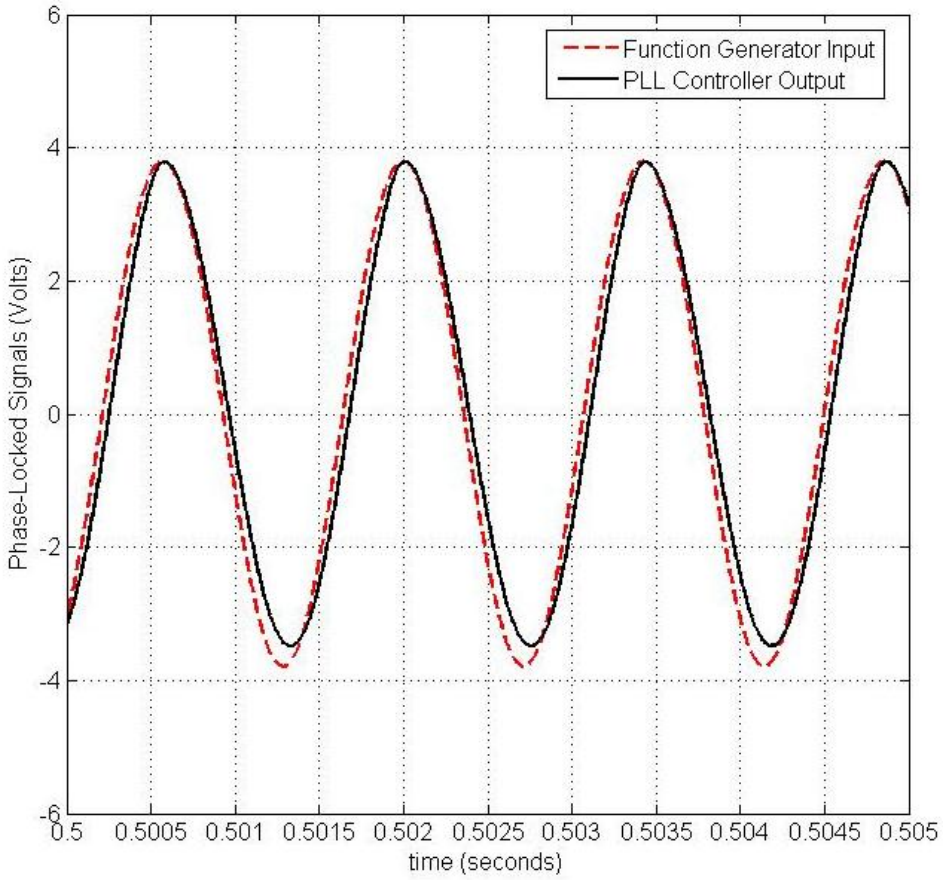

Figure 6.12: Measured jitter signal (Volts) verses time (seconds) for a PLL experimental test given a reference frequency and amplitude of 700 Hz and 4 Volts, respectively after amplitude and phase synchronization has been achieved. The dashed curve represents the function generator's input signal and the solid curve represents the measured PLL output signal.

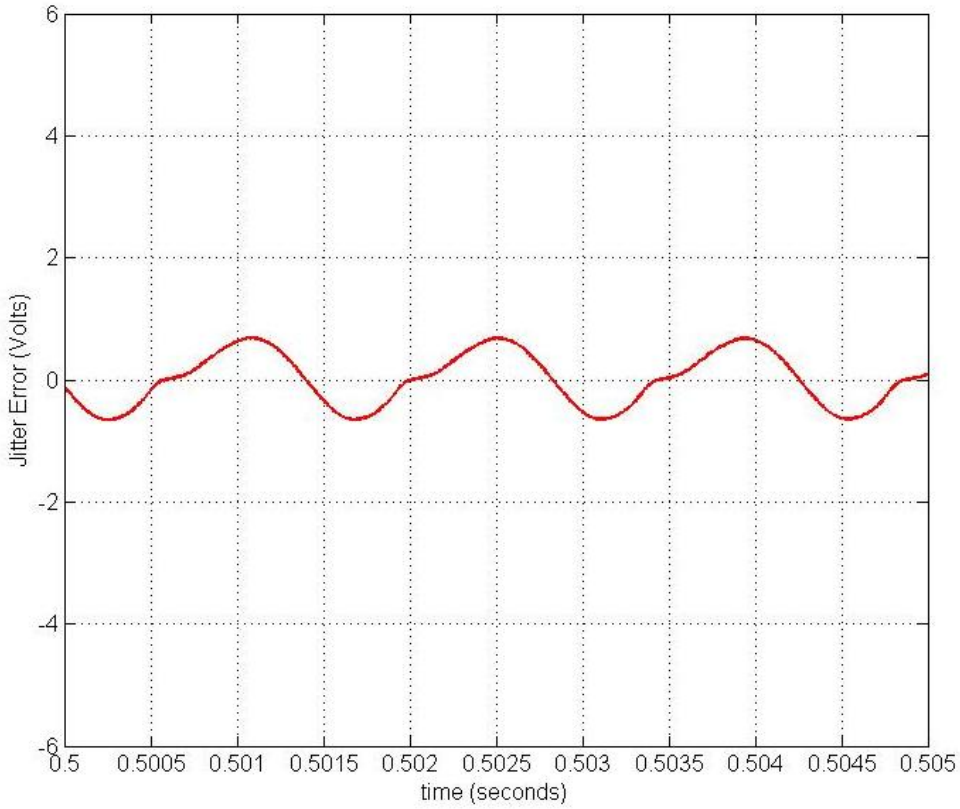

Figure 6.13: Computed jitter error (Volts) verses time (seconds) for a PLL experimental test given a reference frequency and amplitude of 700 Hz and 4 Volts, respectively after amplitude and phase synchronization has been achieved.

Figures 6.14 – 6.19 show similar results to those shown above. In each case the jitter signals and jitter error are shown after amplitude and phase synchronization has occurred. It is clear from the figures that the best results were obtained given an input frequency of 800 Hz which is expected since this frequency most closely resembles the PLL's operating frequency of 830 Hz. In this experiment the maximum jitter error reduces to approximately 0.1 Volts. When the input amplitude is increased to 5 Volts, given an input frequency of 800 Hz, the jitter error still remains less than 0.5 Volts.

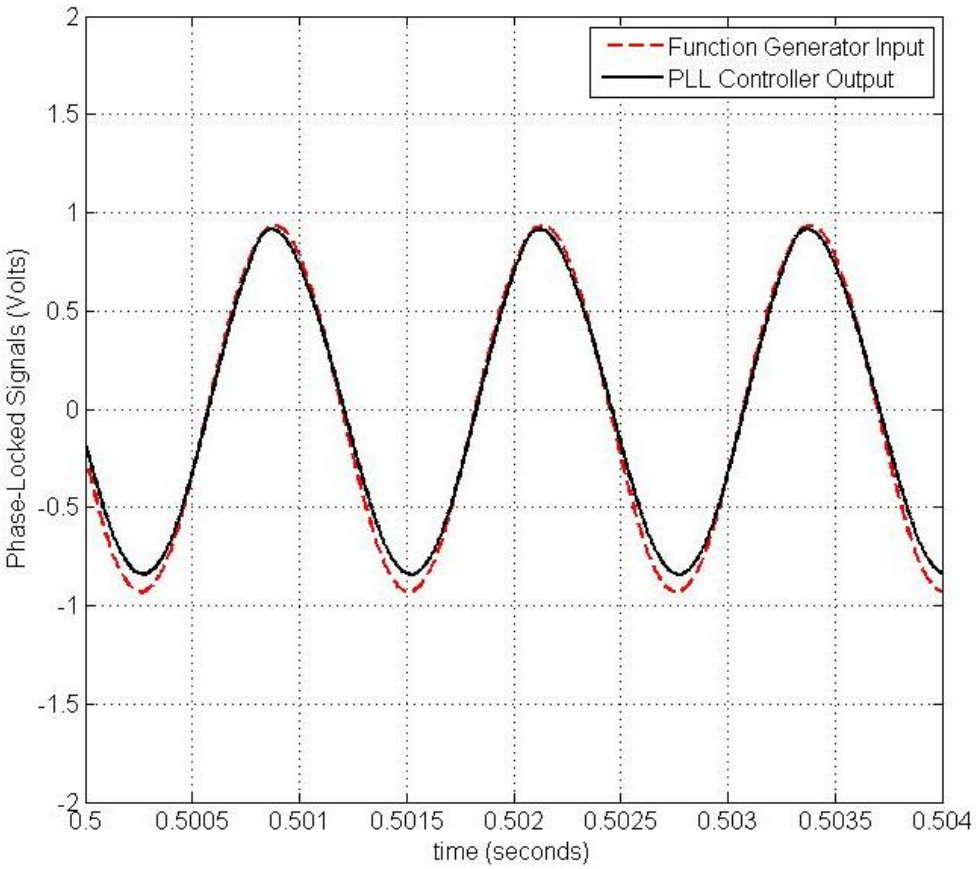

Figure 6.14: Measured jitter signal (Volts) verses time (seconds) for a PLL experimental test given a reference frequency and amplitude of 800 Hz and 1 Volt, respectively after amplitude and phase synchronization has been achieved. The dashed curve represents the function generator's input signal and the solid curve represents the measured PLL output signal.

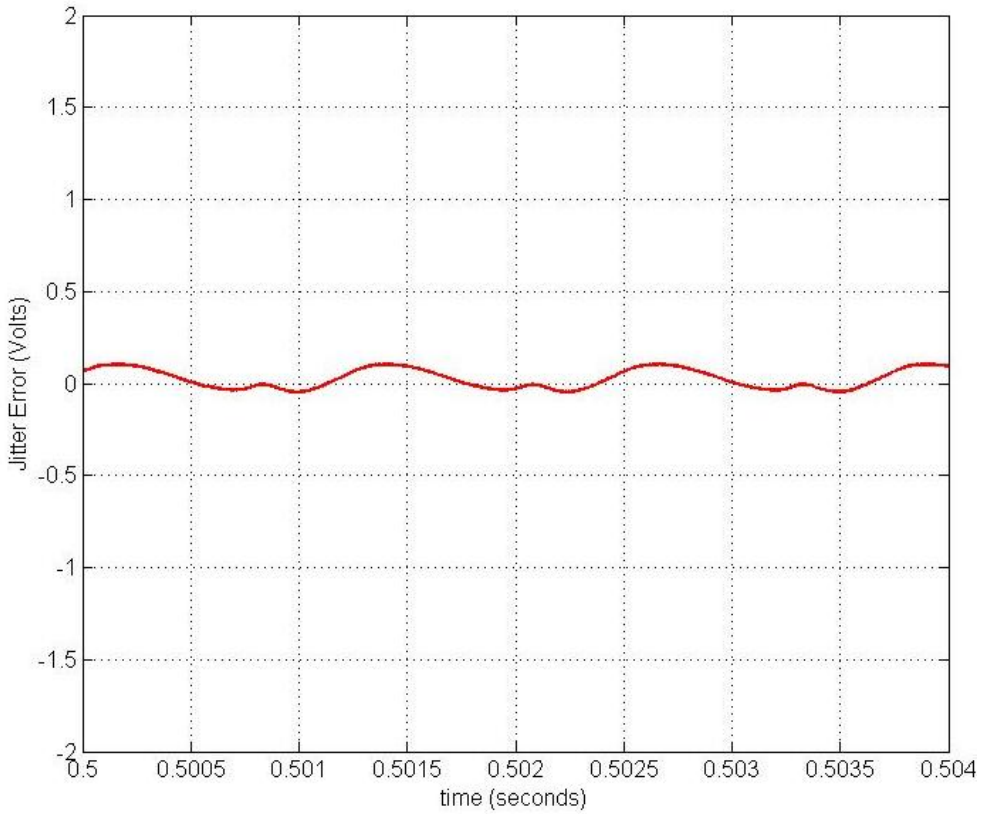

Figure 6.15: Computed jitter error (Volts) verses time (seconds) for a PLL experimental test given a reference frequency and amplitude of 800 Hz and 1 Volt, respectively after amplitude and phase synchronization has been achieved.

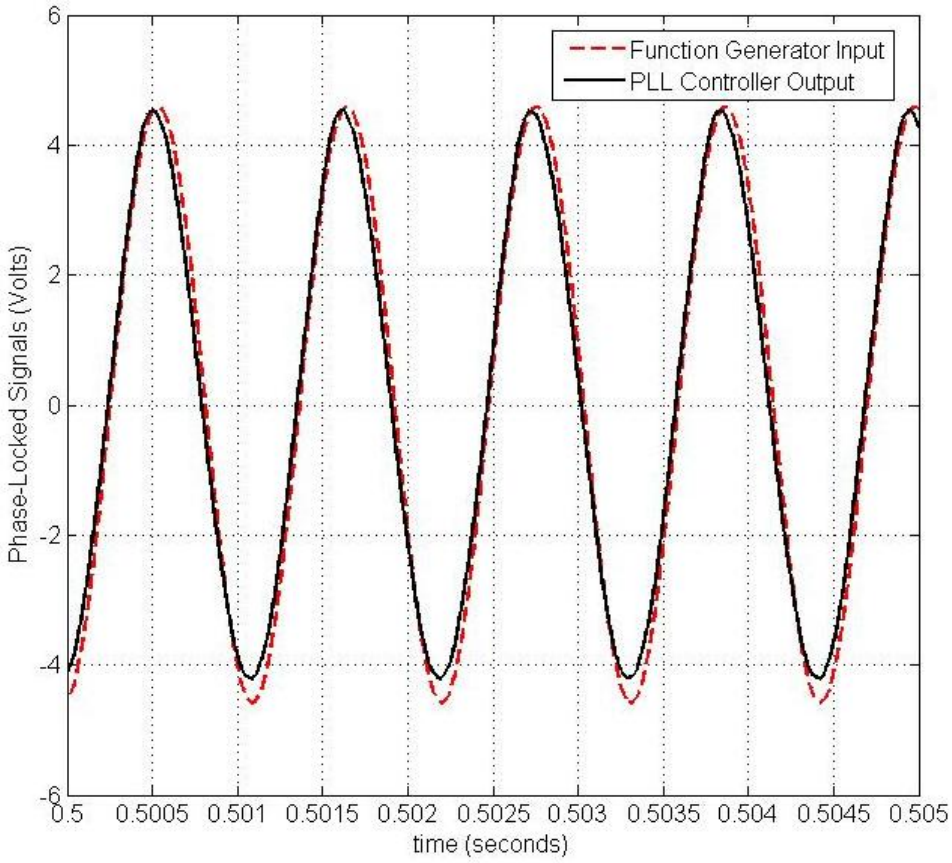

Figure 6.16: Measured jitter signal (Volts) verses time (seconds) for a PLL experimental test given a reference frequency and amplitude of 900 Hz and 5 Volts, respectively after amplitude and phase synchronization has been achieved. The dashed curve represents the function generator's input signal and the solid curve represents the measured PLL output signal.

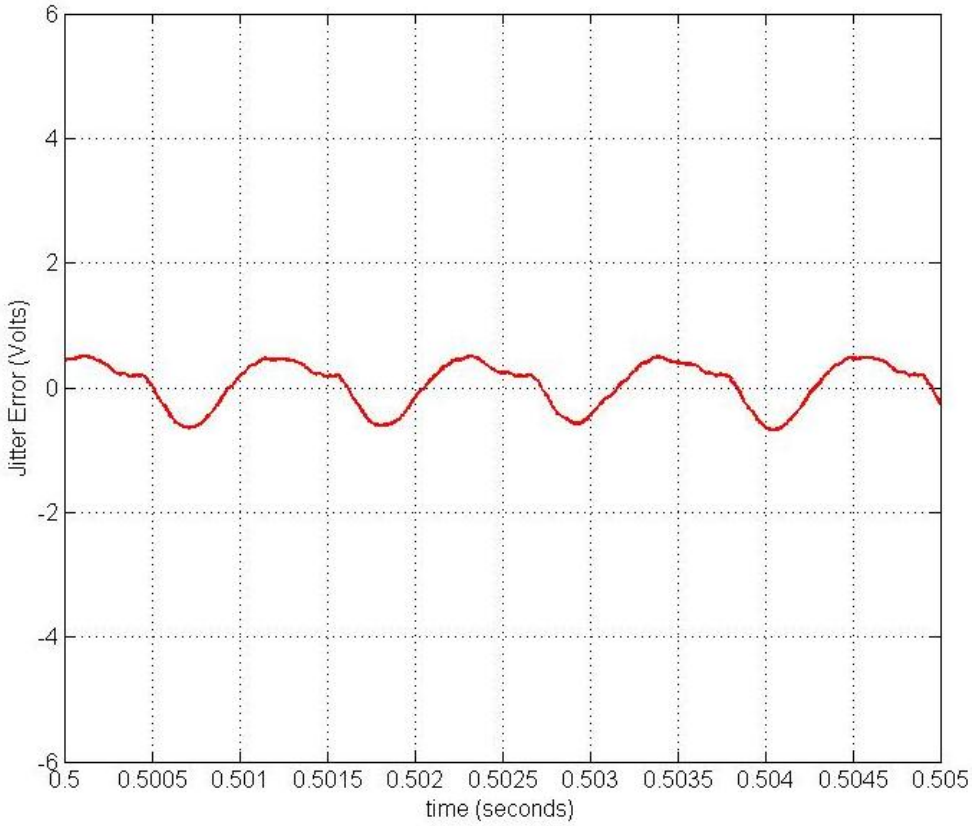

Figure 6.17: Computed jitter error (Volts) verses time (seconds) for a PLL experimental test given a reference frequency and amplitude of 900 Hz and 5 Volts, respectively after amplitude and phase synchronization has been achieved.

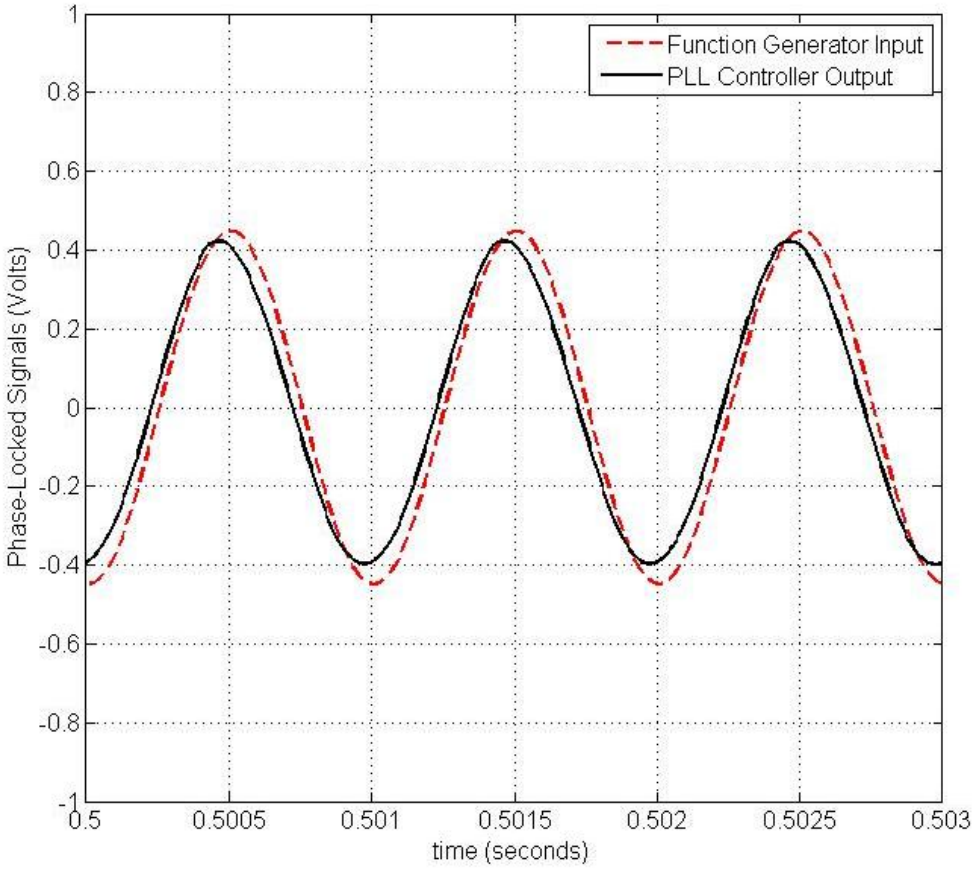

Figure 6.18: Measured jitter signal (Volts) verses time (seconds) for a PLL experimental test given a reference frequency and amplitude of 1000 Hz and 0.5 Volts, respectively after amplitude and phase synchronization has been achieved. The dashed curve represents the function generator's input signal and the solid curve represents the measured PLL output signal.

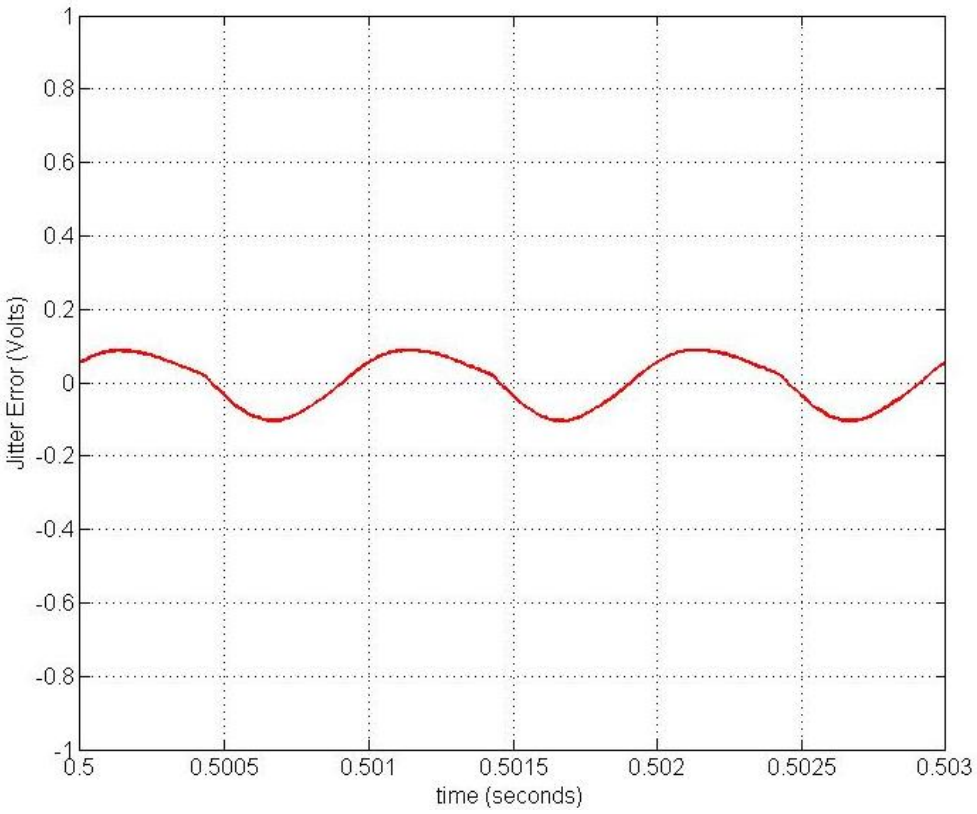

Figure 6.19: Computed jitter error (Volts) verses time (seconds) for a PLL experimental test given a reference frequency and amplitude of 1000 Hz and 0.5 Volts, respectively after amplitude and phase synchronization has been achieved.

6.1.5. Summary of PLL Experiments

In summary, analog experimental tests were performed to investigate the PLL circuit's ability to track amplitude and phase variations of an incoming sinusoidal signal. The PLL circuit was designed with a center operating frequency of approximately 830 Hz, which can be modified by changing a few resistor and capacitor values. A function generator was used to produce a sinusoidal input signal representing the shear layer jitter signal that will eventually be measured using a small-aperture position sensing device in the ultimate high-speed shear layer experiment. A data acquisition system acquired the

analog signals during testing at a rate of 200 kHz. Phase and amplitude response data was collected and reported above in Sections 6.1.2 and 6.1.3, respectively. Finally, jitter error was computed from the "jitter" signals themselves and shown in Section 6.1.4.

For the given center operating frequency of 830 Hz, a capture range between approximately 700 Hz and 1200 Hz was established. Phase-locking consistently occurred between 0.03 and 0.1 seconds after testing was initiated. The amplitude estimation response commonly took approximately 0.4 seconds or less. While maximum jitter error reached values close to 0.5 Volts in some cases due to the error induced by the phase-shift circuit, actual "jitter" errors should be closer to 0.05 Volts after accounting for this induced phase error. Overall, these results are very promising. Taken in combination with Duffin's manual phase-locking wavefront experiments [8, 27], the alternative AO approach appears to be a feasible and innovative way of overcoming the bandwidth limitations inhibiting current AO systems.

It should also be noted that any latency associated with individual components of the AO system, as discussed in Chapter 2, are irrelevant using this alternative approach. This is because the mirror's phasing and amplitude adjustments are a result of the reference and compensated beams being mixed in real time. The actual phase delay between the DM input signal and the DM's response is accounted for by the compensated signal. The exact phase delay induced by the DM amplifier on the input signal is therefore irrelevant. In a conventional AO system, these latencies make correction ineffective or even damaging as discussed in Chapter 2.

6.2. Proposed High-Speed Shear Layer Small-Aperture Jitter Test

Several wind tunnel experiments must be performed in follow-on work to completely evaluate the PLL circuit and alternative AO controller. The first test outlined here will be designed to further assess the PLL's tracking capabilities of both amplitude and phase variations, a continuation of the experimental tests discussed above. Similar to the tests reported in Section 6.1, the PLL's response to changes in amplitude and phase of an incoming jitter signal will be investigated. However, in this set of experiments, an actual small-aperture laser beam will be projected through the high-speed shear layer. The emerging jitter signal will be measured using a small-aperture position sensing device and filtered as discussed earlier. Then the filtered, near-sinusoidal signal will be applied to the PLL circuit. The goal of these tests will be to evaluate the PLL's ability to track phase and amplitude variations of an actual incoming jitter signal emerging from a forced high-speed shear layer. When evaluating the results of these tests, two important items should be considered; first the effect of having an input signal whose form is no longer dominated by a single harmonic sinusoid, and second the effect of noise present on the input signal induced by the boundary layer within the wind tunnel, mechanical vibrations, and other aspects of the experiment.

This small-aperture jitter experiment will require the use of a high-speed wind tunnel, optical bench, and PLL controller. A high-speed free shear layer will be generated using a transonic in-draft, wind-tunnel located in Notre Dame's Hessert Laboratory. This facility consists of an inlet nozzle, test section with viewing windows to allow for propagation of the laser beam, diffuser section, and vacuum pumps. High- and low-speed flows are fed through the inlet nozzle separated by a splitter plate. Once the

two flows merge a free shear layer forms within the test section. Voice-coil actuators affixed to the edge of the splitter plate will be used to incorporate flow control, regularizing a region of the large-scale structures as discussed in Section 3.2 of this dissertation. A small-aperture laser beam will be propagated up through the regularized region of the forced shear layer and then directed back onto an optical bench where a small-aperture position sensing device will be used to acquire the resulting jitter signal. Once filtered, the analog signal produced from the position sensing device will serve as the PLL's reference input. Both the shear layer's jitter signal and the PLL's phase-locked output will be recorded via a data acquisition system during testing. Post-processing will be used to assess the PLL's tracking response to both amplitude and phase. AO corrections should first be tested using only a fast steering mirror to determine if the jitter signal alone can be properly compensated similar to the experimental circuitry tests described earlier.

Full AO correction capabilities of this alternative method may be further analyzed by post-processing wavefronts created from the phase-locked PLL output. An estimation of residual error could be computed by comparing post-processed wavefronts to wavefront measurements taken of a large-aperture bean projected through the regularized shear layer. This could serve as a preliminary investigation to the following high-speed shear layer AO correction experiment described below in Section 6.3.

6.3. Proposed High-Speed Shear Layer AO Correction Experiment

Once phase-locking has been successfully demonstrated in the small-aperture jitter experiments discussed previously (Section 6.2), the final high-speed shear layer AO correction experiment can be conducted. The goal of this experiment will be to test and demonstrate system performance capabilities of the alternative AO control system presented throughout this dissertation. Similar to the experiments presented in the previous section, a transonic in-draft, wind-tunnel located in Notre Dame's Hessert Laboratory will be used to create a free shear layer. Again, voice-coil actuators affixed to the edge of the splitter plate will be used to mechanically force the shear layer's origin in an effort to regularize a downstream region of the flow. A small aperture laser beam along with a large aperture beam will be propagated through the test section within the region of regularization. The small aperture laser beam will again be measured via a small-aperture position sensing device and its filtered signal will serve as the PLL's reference input signal. Real-time AO corrections will be applied to the large aperture laser beam using Notre Dame's deformable mirror controlled by the alternative AO controller. Two-dimensional wavefront measurements will be acquired using a WFS of the large aperture beam before and after AO corrections have been applied as a means of evaluating the system's performance.

Before conducting this high-speed shear layer AO experiment, a few modifications must be made to the PLL circuit shown in Fig. 5.1. First, since the PLL output will be used to generate a two-dimensional wavefront characterizing the DM's conjugate correction, the 90° phase-shift circuit must be removed. This will cause the PLL output to be locked 90° out of phase with the reference input signal. The basis for

this necessary phase lag originates from the definition of *jitter* (Eq. (2.4)). The reference input corresponds to the shear layer jitter while the PLL output characterizes the optical wavefront, therefore the two signals must be 90° out of phase in order to create the proper conjugate correction.

Secondly, a method of phase-shifting the PLL output signal must be devised to produce the desired DM waveform. A series of operational amplifier phase-shift circuits, as described in Section 5.4, is proposed as an initial approach to create the two-dimensional wavefront extended across the aperture in the off-axis direction (each row of actuators will carry the same control signal); however, other possibilities should be explored such as digital phase-shift options, RF-Lambda phase shifters, *etc*. Finally, the op amp inverting amplifier circuit shown in Fig. 5.7 must be modified to account for the amplification factor of the DM amplifier and the DM's voltage to stroke conversion.

Once successful AO corrections have been demonstrated for forcing frequencies at or near the given PLL operating frequency, subsequent shear layer cases may be examined. The waveform generator circuit may be modified to create varying center operating frequencies by adjusting the resistor and capacitor values shown in Fig. 5.5. This series of AO wind tunnel testing will constitute a final validation of the alternative AO control method proposed in this dissertation.

CHAPTER 7:

CONCLUSIONS AND RECOMMENDATIONS

Optical wavefront aberrations induced by variations in a flow field's index-of-refraction field cause significant performance reductions to an AO system making use of such an optical signal. Conventional AO systems are currently being used to successfully correct for atmospheric disturbances; however, they are bandwidth limited in the case of aero-optic disturbances. Due to high frequencies present within a free shear layer, commonly exceeding 1 kHz, the current AO system is inhibited by its ability to close the loop within the necessary timeframe. Over the past several years Notre Dame has been working towards a solution to this previously underestimated problem.

The research reported in this dissertation, in concert with the high-speed AO testing completed and documented by Duffin in 2009 [27], signifies a significant breakthrough in the area of aero-optics. The goal of this research was to automate the manual phasing process in Duffin's experiments. More specifically, to develop an alternative AO approach using a combination of flow control to regularize the shear layer's large-scale structures and a PLL controller to synchronize an estimated waveform with the shear layer's emerging wavefront.

7.1. Contributions

The first phase of this research involved a numerical investigation. A discrete vortex method along with a Weakly-Compressible model developed by Fitzgerald [5, 12], was used to simulate a high-speed free shear layer. The well known linear growth rate of a free shear layer, commonly characterized by vorticity thickness measurements, was examined from a different angle through an optical analysis. A series of small-aperture beams numerically propagated perpendicularly through the shear layer were used to generate a new measure of growth based upon the induced jitter. The new shear layer measure introduced in this dissertation, defined by Eq. (3.4) and Eq. (3.5), is called optical coherence length [16, 49]. Similar to vorticity thickness, it reveals a linear growth rate with downstream distance exhibited by an unforced free shear layer. However, the difference being that optical coherence length measures large-scale structure size in the streamwise direction rather than the cross-stream direction. It was also shown that the large-scale coherent structures which dominate a free shear layer flow grow at a more rapid rate in the streamwise direction compared to the cross-stream direction [49]. It was found that the growth rates differed by a factor of approximately 3.18 in agreement with previous work [13, 20].

The numerical simulations performed for this research also revealed a dominant *natural* frequency present within the flow field at each downstream location. These natural optical frequencies, related to optical coherence length, were shown to be directly related to the shear layer's most susceptible forcing frequency for a given location. Numerical simulations reported in this dissertation were also used to illustrate a shear layer's susceptibility to forcing. Numerical findings corroborated experimental tests

conducted at the University of Notre Dame [39, 41] and provided a better understanding of a shear layer's range of effective forcing frequencies.

The second and most significant contribution of this research was the development of an alternative AO controller that will replace the "person-in-the-loop" in Duffin's AO experiment [27]. Upon confirming the shear layer's periodic structure when forcing is applied, a PLL control strategy was proposed. Through wavefront regularization, a small-aperture laser beam may be used as a reference signal with which to phase-lock. The major achievement made by this approach is to effectively remove the need for a two-dimensional wavefront sensor thereby reducing the required system bandwidth. Instead of the hundred fold update requirement presently constraining current AO systems, the issue now becomes one of phase-locking two one-dimensional jitter signals. Another benefit of the alternative AO approach presented in this dissertation is the fact that time delays associated with individual mechanical components within the control loop will be accounted for during the phase-locking process.

Basic control techniques were used to design a filter function for the PLL controller. The PLL generates an output signal whose frequency and phase is synchronized with the shear layer's large-scale vortical structures. The phase-locked output will be used to estimate a conjugate correction applied to the DM. The next logical research phase, as a follow-on to this work, would be to investigate and develop a means of constructing the proper conjugate waveform based upon the PLL output signal. Once the conjugate correction is formed, the wavefront must be broken down into individual analog signals which will be sent through the DM amplifier directly to the DM

actuators themselves. Recommendations for this process are outlined in the following section.

7.2. Recommendations

The following recommendations are intended to help facilitate the completion of the proposed alternative AO controller. In order to carry on the research presented throughout this dissertation and create a controller that will eventually be used in a high-speed aircraft experiment, a series of wind tunnel tests must be performed in addition to the finalization of the controller circuitry. This section includes some recommendations for those experimental tests as well as ways of handling harmonics which turn out to be more dominant in some of the higher speed shear layer cases.

7.2.1. High-Speed Shear Layer Experiments

A series of high-speed shear layer experiments are recommended to aid in the completion and verification of the proposed alternative AO controller. These experiments include both small-aperture beam testing and large-aperture beam testing. Before the AO controller is finalized, as per the recommendations found in Section 7.2.2, the PLL circuit should be tested under the actual high-speed shear layer conditions. The sinusoidal function generator input (refer to Chapter 6) will be replaced by an actual shear layer jitter signal. A small-aperture beam propagating perpendicularly through the regularized region of the forced shear layer will be measured using a position sensing device. After appropriately filtered, the measured shear layer jitter signal will serve as

the PLL input. An experimental overview of the setup and procedure is described in Section 6.2. The purpose of this experiment will be to test the PLL circuit's ability to perform phase-locking under less than ideal conditions where the reference input is not a simple single-frequency sinusoid and may also contain additional noise. A subsequent set of tests will then be performed using Notre Dame's fast steering mirror (tip/tilt mirror) to apply one-dimensional tip/tilt corrections to the shear layer's regularized jitter signal.

The second set of experimental tests should be performed after the small-aperture testing has been completed and the alternative AO controller has been finalized. In this high-speed shear layer experiment, real-time AO corrections will be applied to a large-aperture beam while a small-aperture beam is used as the PLL's reference input. Wavefront measurements of the large-aperture beam will be recorded using a WFS with and without corrections as a means of scoring. A general description of the wind tunnel testing facility and suggested experimental setup may be found in Section 6.3.

7.2.2. Finalizing the Alternative AO Controller

The last step necessary to finalize the proposed alternative AO controller is to apply the appropriate conjugate correction to a DM based upon the PLL output signal. This waveform will ultimately be used to perform high-speed shear layer AO corrections to a large-aperture beam propagating through a regularized region of the flow field. The PLL output will be used to create seven signals corresponding to each of the DM's seven rows of actuators. Together the signals will represent a traveling sinusoidal waveform used to perform conjugate corrections. As described in Section 5.4, a series of op amp

phase-lag circuits could provide a sufficient means of generating the seven input signals. In addition, it is recommended that digital options be explored. This may include, but should not be limited to, digital phase-shifters and RF-Lambda phase shifters. A digital phase-shift circuit may be a more reliable method of phase-lagging; however, the frequency of this particular application may prove to be limiting. Once preliminary testing has been completed and a method of constructing the DM waveform has been selected, it must be integrated with the PLL circuit presented in this dissertation. Resistors, R_{A7} and R_{A8}, in the op amp inverting amplifier shown in Fig. 5.1, must be adjusted to provide the appropriate scaling. In addition to the amplitude estimation factor, the op amp circuit must account for both the DM amplifier's 3X amplification constant and the DM's conversion factor from input voltage to actuator stroke length (+/- 10 Volts to +/- 4 μm), as well as any factor associated with the phase-lag circuitry chosen above.

It should also be noted that the DM waveform is based upon both the free shear layer's convection velocity and the forcing frequency as described in Section 4.3. In other words the structure of the conjugate correction changes as the wind tunnel conditions vary. Thus, a process of constructing the DM wavefront that will adapt or adjust to testing conditions would be beneficial. A second small aperture beam propagating through the test section a small distance downstream from the original shear layer jitter signal could provide a means of computing the convection velocity. The two jitter signals could be cross-correlated with one another to recover the time delay between signals. The convection velocity could then be computed according to Eq. (4.4) based upon the established time delay and the known horizontal spacing between beams.

Finally, the phase shift between adjacent rows of actuators could be computed according to Eq. (4.3) and Eq. (5.8).

One final recommendation for the AO controller is to consider replacing the current resistors R_A and R_B, in the waveform generator circuit (refer to Fig. 5.5), with potentiometers. This may allow the user a simpler means of adjusting the VCO center operating frequency for varying testing conditions.

7.2.3. Handling Harmonics within the Regularized Wavefronts

Both numerical [16, 49] and experimental [27, 41] results seem to indicate that harmonics other than the fundamental forcing frequency become more dominant within the shear layer flow field at higher Mach numbers. In lower speed cases, where forcing produces a regularized region primarily dominated by a single frequency, the alternative AO approach proposed in this dissertation should prove to be successful. However, in some regularized shear layers, often occurring in higher Mach number flows, the wavefronts contain one or more harmonics largely contributing to its overall form. In these cases, a different method of constructing the conjugate correction may be necessary. Rather than a purely sinusoidal conjugate correction governed by a single frequency, a more complex waveform may be required.

Harmonics that influence the optical wavefront's character will also affect the shape of the measured shear layer jitter signal itself. This could render the alternative AO controller described in this dissertation less effective. The current PLL circuit outputs a sinusoidal signal at a single frequency without any harmonics. This signal is used to construct the conjugate correction based on a traveling sinusoid. If unaltered, the absence

of harmonics may result in discrepancies between the conjugate correction and the shear layer's actual emerging wavefront. If the regularized shear layer's large-scale structures contain dominant frequencies other than the fundamental forcing frequency, a more substantial amount of wavefront error results. Therefore, it may become necessary to construct the DM's conjugate correction by different means in these cases. One possible solution may be to construct the conjugate correction using a POD (proper orthogonal decomposition) analysis. An investigation by Duffin [27] suggests that most of the energy contained within the flow is described by the first three modes. Duffin also notes that the modal temporal coefficients, used to reconstruct the optical wavefronts, vary slightly from one realization to the next [27]. Therefore, reconstruction based on an average of several temporal coefficients for the first few modes may provide a good wavefront approximation. It may also be possible to design a separate control loop assigned the task of continually updating the time averaged temporal coefficients via wavefront slope measurements. In this case synchronization may still be achievable through a PLL control loop. As mentioned above the wavefront reconstruction, or some variation of it, may be phase-locked with the forcing signal while a simple phase-lag circuit could be added to the controller if a constant phase error existed between signals.

APPENDIX A:

SYSTEM IDENTIFICATION

A.1. Constructing an Uncertainty Model

System identification, the process of constructing a model based on experimental data, measurements, and observations, is an important aspect of this research effort. The alternative AO control system developed for this research consists of several different components including optical sensors, mirrors, electrical circuitry, *etc.* It becomes necessary to model system response characteristics for some of the individual components in order to properly analyze and design the AO controller. The system identification procedure described here is based on robust control theory. A component is modeled using an unstructured multiplicative uncertainty model given by,

$$G(s) = G_o(s)[I + \Delta(s)] \tag{A.1}$$

where G_o represents the nominal plant and Δ the uncertainty associated with the actual plant, or model, G. The average magnitude and phase response data is plotted versus input frequency, where each averaged data point contains an associated range of values corresponding to its uncertainty. The nominal plant, G_o, can then be determined by finding a transfer function which most closely models the average magnitude and phase response characteristics.

In order to access the uncertainty of both magnitude and phase in conjunction with one another, phasor notation must be used. Therefore, a Nyquist plot is generated from the nominal plant's transfer function. Uncertainty regions are constructed using the maximum and minimum values of both magnitude and phase from the experimentally-measured data for a given input frequency. Uncertainty circles are then constructed, centered along the nominal plant's Nyquist plot and encompassing each corresponding uncertainty region. Given the multiplicative model expressed in Eq. (A.1), the radius of each circle corresponds to the magnitude of the nominal plant multiplied by the uncertainty as shown in Fig. A.1. Therefore, the uncertainty may be determined by multiplying the radius values for each respective input frequency by the inverse of the nominal plant's magnitude.

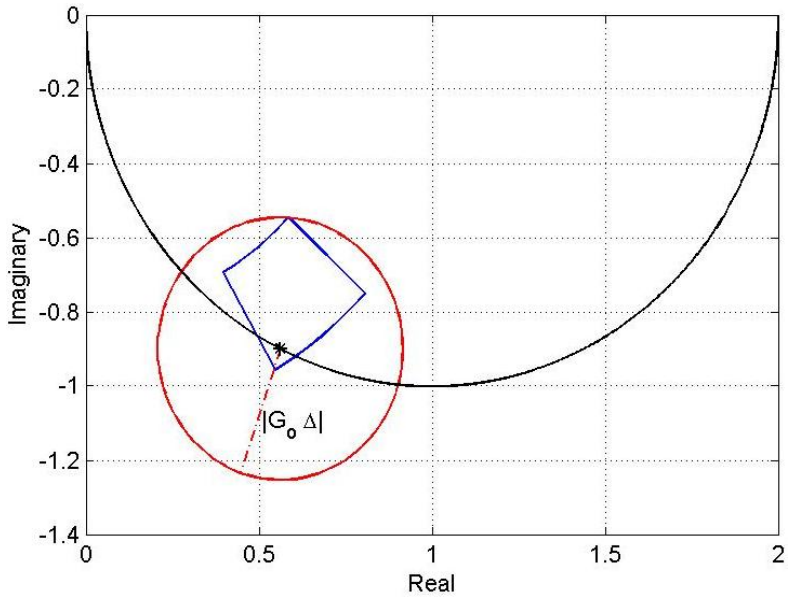

Figure A.1: Example of a Nyquist plot given a multiplicative uncertainty model.

Over bounding the uncertainty with a stable proper rational transfer function is one method of modeling system uncertainty [28, 29]. In this approach, a multiplicative bound, *W(s)*, is constructed such that

$$\left\| W_{\Delta}^{-1} \Delta \right\|_{\infty} < 1 \,, \tag{A.2}$$

where the $\mathcal{H}_{\infty}$ norm is the supremum of the maximum singular value of a complex valued matrix, or in this case a single complex valued function. This type of model accounts for uncertainties within the plant and provides a useful form for further robust control analysis [28, 29]. The following section uses the uncertainty model described here to model the DM Amplifier's frequency response.

A.2. DM Amplifier

One specific electrical component often creating the primary bandwidth limitation within a circuit is the amplifier. The DM Amplifier is one of the key components in Notre Dame's current AO system used to transfer the conjugate correction signal to the DM actuators. It amplifies each input signal by three times its input voltage while maintaining a 70 volt bias (i.e., when the input is 0.0 Volts, the output is 70 Volts). The amplifier accepts a maximum input signal of +/- 10 Volts, resulting in an output signal with maximum fluctuations of +/- 30 Volts centered on the bias.

Frequency response measurements were taken to identify and construct a transfer function as well as determine corresponding bandwidth limitations for Notre Dame's DM amplifier using the uncertainty model discussed above in Section A.1. Testing was conducted using sinusoidal input waveforms with amplitudes ranging from 1 Volt to 8

Volts. Input frequencies ranged from 100 Hz to 20 kHz. In order to test the amplifier under conditions similar to those experienced during normal operation, a 2.2 μF capacitor was connected to the output of the amplifier, simulating the effects of an individual piezoelectric actuator. The sinusoidal signals were input into the amplifier using a function generator and the output voltage was measured across the simulated actuator (capacitor) using a data acquisition system. The input and output signals were acquired at a 500 kHz sampling rate. Figure A.2 shows the ratio of output to input amplitude versus frequency for eight different input amplitudes. Figure A.3 shows the corresponding phase delays encountered between the input and output signals over the same range of input amplitudes and frequencies.

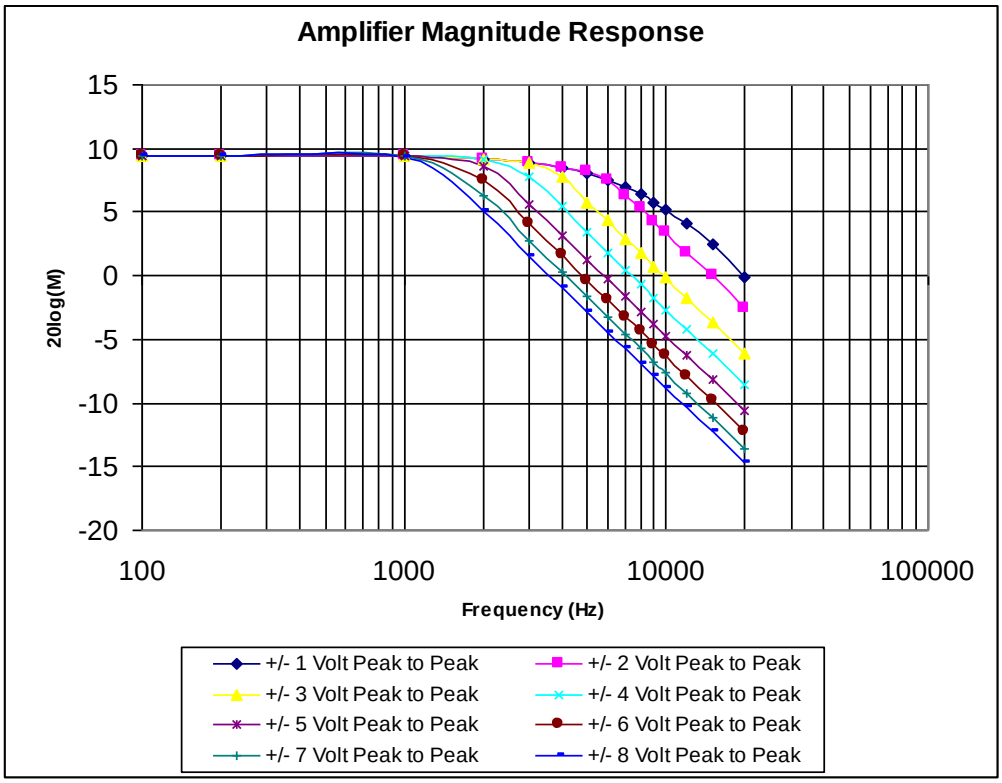

Figure A.2: Experimental magnitude response for the DM Amplifier.

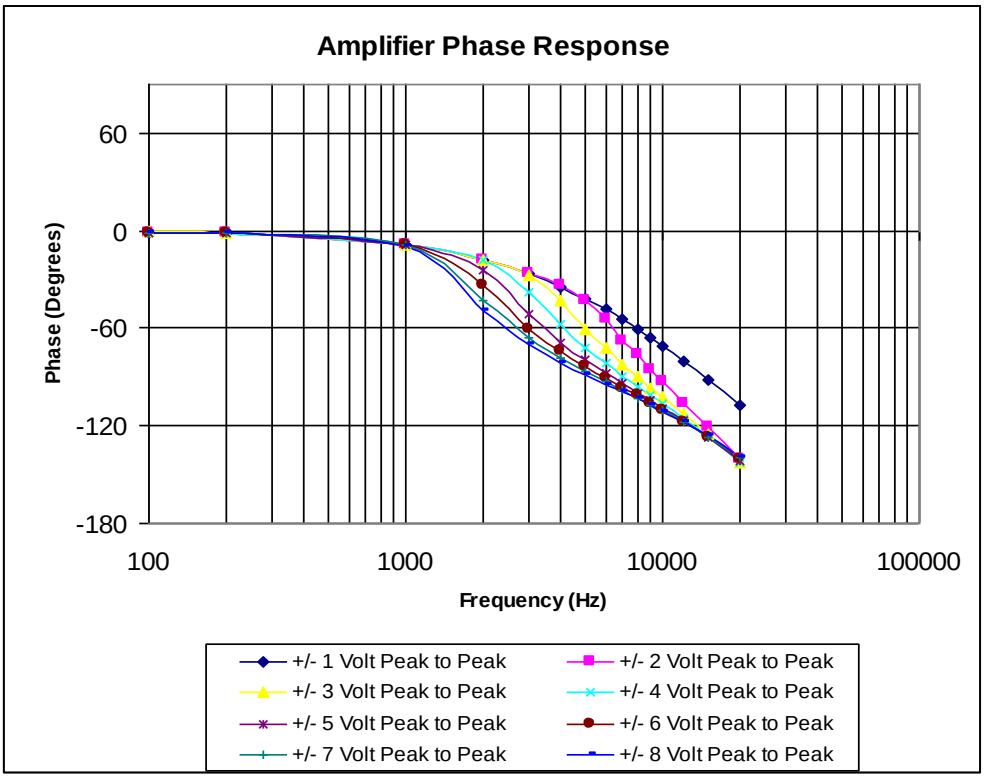

Figure A.3: Experimental phase response for the DM Amplifier.

As is evident from Fig. A.2 and Fig. A.3, the DM Amplifier exhibits linear characteristics to approximately 1 kHz, at which point both the magnitude and phase begin to significantly fall off for large input amplitudes. Although the magnitude response seems to be linear for frequencies below 1 kHz, the linear negative slope in the Fig. A.3 phase plot between 100 Hz and 1 kHz suggests that the amplifier operates with a pure time delay.

The experimental magnitude and phase data shown in Figs. A.2 and A.3 were averaged and a transfer function was fit to the set of nominal data points. Figure A.4

displays the averaged magnitude and phase data (x's in Fig. A.4) for the DM amplifier along with the bode plot for the associated nominal plant (solid line in Fig. A.4) given by,

$$G_o(s) = 3.2\frac{2\pi(3000)}{s + 2\pi(3000)}. \tag{A.3}$$

A low pass filter with a cutoff frequency of 3 kHz was first determined to be the best fit for the averaged magnitude data. The larger phase delays observed in the averaged data at higher frequencies was modeled using the uncertainty analysis described previously in Section A.1.

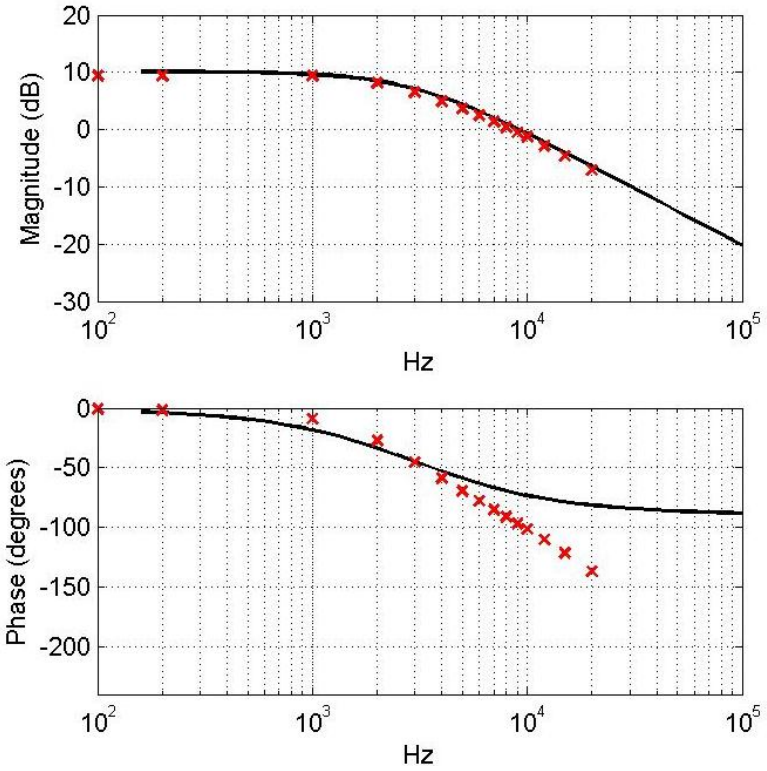

Figure A.4: Averaged magnitude and phase response data points for the DM Amplifier plotted against the bode diagram for its associated nominal plant.

The next step involved modeling the measurement uncertainty [28, 29]. Although the nominal plant, shown above in Fig. A.4, seems to model the averaged magnitude data points very well, there remains a certain amount of uncertainty between the averaged data points and actual system response. Consequently, a Nyquist plot was generated for the nominal plant to access the frequency response of both the magnitude and phase data in combination. Figure A.5 shows the Nyquist plot for the nominal plant, G_o, given in Eq. (A.3).

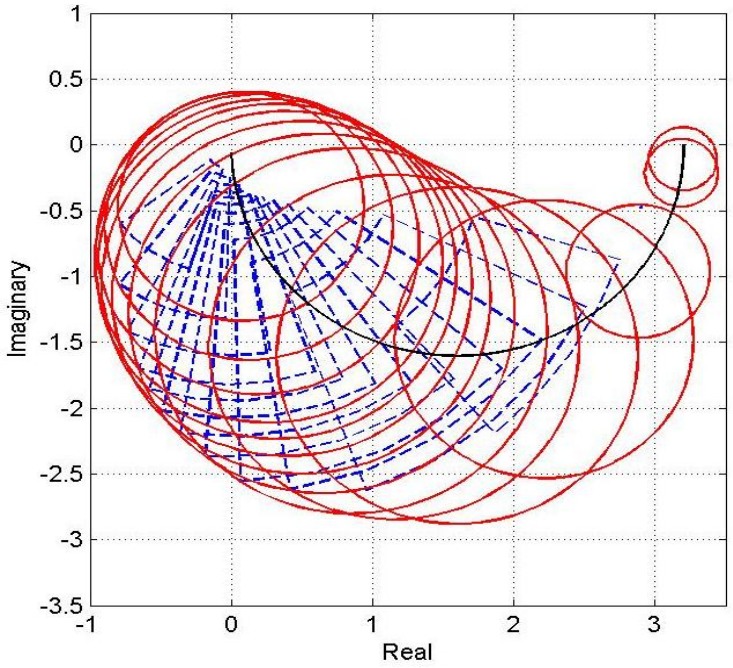

Figure A.5: Nyquist plot for the nominal plant given in Eq. (A.3) (solid black curve) along with the uncertainty circles bounding the regions of magnitude and phase (dashed curves) for each input frequency.

The range of experimental values associated with each data point for varying input amplitudes have been swept out by dotted lines. Circles were constructed, centered along the nominal plant's Nyquist plot and encompassing the corresponding uncertainty

regions. These circles represent the amount of uncertainty present at a given frequency for the DM Amplifier. As described in the preceding section, the radius of each circle represents the magnitude of the nominal plant multiplied by the uncertainty at a given frequency, $|G_o(j\omega)\Delta(j\omega)|$. Given the nominal plant described in Eq. (A.3) and the radius values of the uncertainty circles shown in Fig. A.5, the uncertainty of the amplifier was determined and plotted versus input frequency.

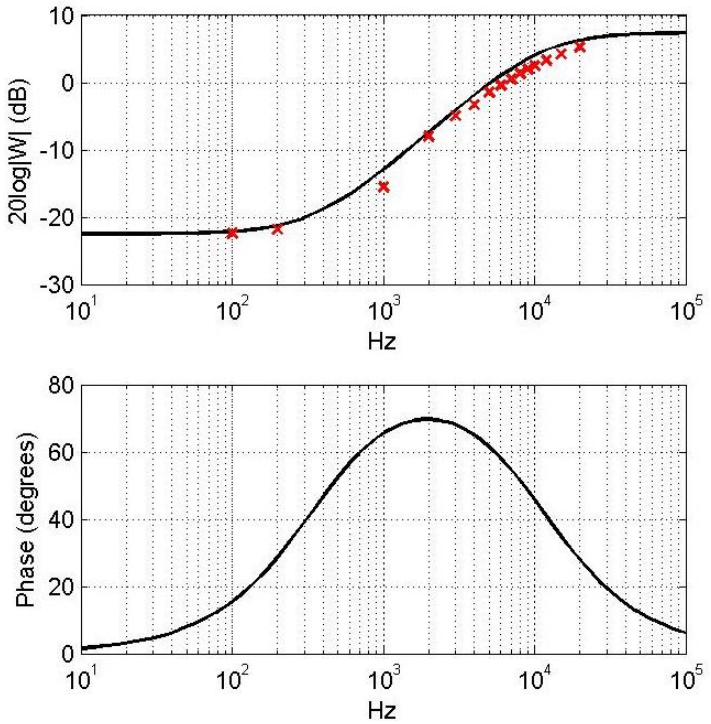

Figure A.6: Gain-magnitude plot of the stable rational transfer function, *W(s)*, over bounding the uncertainty values obtained from Fig. A.5 (circle radii).

Figure A.6 is a plot of the uncertainty values along with the gain-magnitude response for the following transfer function,

$$W(s) = 0.75\left[\frac{31.43[s + 2\pi(350)]}{s + 2\pi(11{,}000)}\right], \tag{A.4}$$

representing the multiplicative bound. The DM Amplifier may therefore be conservatively modeled as,

$$G(s) = 3.2\frac{2\pi(3000)}{s + 2\pi(3000)}\left[1 + \Delta(s)\right], \tag{A.5}$$

where

$$\left|\Delta(s)\right| < \left|W(s)\right|. \tag{A.6}$$

APPENDIX B:

MATHEMATICAL CODE FOR NUMERICAL ANALYSES

A significant portion of the research conducted for this dissertation consisted of numerical analyses and computations. A two-dimensional free shear layer was simulated using the DVM and WCM codes referred to in Chapter 2, Section 2.5. The DVM and WCM fortran codes were developed by E. Fitzgerald, a former Notre Dame graduate student, and may be found in Ref. [12]. Several matlab codes were written as a part of this dissertation work in order to perform jitter computations and frequency analyses, as well as to evaluate control parameters and performance. The following sections include several matlab codes central in the completion of this dissertation.

B.1. Beam Jitter and Spectral Analysis

The mathematical code found in Section B.1.1 was used to compute jitter angles for several small-aperture beams propagating perpendicularly through a DVM/WCM free shear layer at various downstream locations. A frequency analysis was then performed on the jitter signal at each downstream location. The code found in Section B.1.2 computes the PSD of each signal and then calculates a weighted average based on frequency. The weighted average is used to determine optical natural frequency, a term introduced and defined in Chapter 3 of this dissertation (Eq. (3.5)).

B.1.1. Jitter Computations

```
%-------------------------------------------------------------
%  Alice Nightingale
%  May 24, 2005
%  This program loads the OPD data and the Vortex position data
%  to compute jitter angles versus time at several locations
%  downstream from the shear layer's origin.  It also performs
%  a PSD analysis of the jitter signal at a selected location.
%-------------------------------------------------------------

clear all;
format long;

dir='C:\Users\Guest2\Desktop\ANightingale\MatlabFiles\Uc_147A\unforced\
';
%dir='/home/anightingale/research/';

% Input parameters %
uupper=261.04; % m/s
ulower=34.7; % m/s
r=0.01725;  % m - vortex core radius
rk=3.5;
udpv=(uupper+ulower)/2;
dt=(r/rk)/udpv;     % time step

first_file=2100;
last_file=2799;
j=1;

for ifile=first_file:last_file;

    if ifile>2099 && ifile<=2109
        % Vort=load([dir,'Vortmap_',int2str(ifile),'.txt']);
        A=load([dir,'OPDcmp4PVT0_Hess_E0',int2str(ifile-2100),'.txt']);

    elseif ifile>2109 && ifile<=2199
        % Vort=load([dir,'Vortmap_',int2str(ifile),'.txt']);
        A=load([dir,'OPDcmp4PVT0_Hess_E',int2str(ifile-2100),'.txt']);

    elseif ifile>2199 && ifile<=2209
        % Vort=load([dir,'Vortmap_',int2str(ifile),'.txt']);
        A=load([dir,'OPDcmp4PVT0_Hess_F0',int2str(ifile-2200),'.txt']);

    elseif ifile>2209 && ifile<=2299
        % Vort=load([dir,'Vortmap_',int2str(ifile),'.txt']);
        A=load([dir,'OPDcmp4PVT0_Hess_F',int2str(ifile-2200),'.txt']);

    elseif ifile>2299 && ifile<=2309
        % Vort=load([dir,'Vortmap_',int2str(ifile),'.txt']);
        A=load([dir,'OPDcmp4PVT0_Hess_G0',int2str(ifile-2300),'.txt']);

    elseif ifile>2309 && ifile<=2399
        % Vort=load([dir,'Vortmap_',int2str(ifile),'.txt']);
        A=load([dir,'OPDcmp4PVT0_Hess_G',int2str(ifile-2300),'.txt']);
```

```
    elseif ifile>2399 && ifile<=2409
        % Vort=load([dir,'Vortmap_',int2str(ifile),'.txt']);
        A=load([dir,'OPDcmp4PVT0_Hess_H0',int2str(ifile-2400),'.txt']);

    elseif ifile>2409 && ifile<=2499
        % Vort=load([dir,'Vortmap_',int2str(ifile),'.txt']);
        A=load([dir,'OPDcmp4PVT0_Hess_H',int2str(ifile-2400),'.txt']);

    elseif ifile>2499 && ifile<=2509
        % Vort=load([dir,'Vortmap_',int2str(ifile),'.txt']);
        A=load([dir,'OPDcmp4PVT0_Hess_I0',int2str(ifile-2500),'.txt']);

    elseif ifile>2509 && ifile<=2599
        % Vort=load([dir,'Vortmap_',int2str(ifile),'.txt']);
        A=load([dir,'OPDcmp4PVT0_Hess_I',int2str(ifile-2500),'.txt']);

    elseif ifile>2599 && ifile<=2609
        % Vort=load([dir,'Vortmap_',int2str(ifile),'.txt']);
        A=load([dir,'OPDcmp4PVT0_Hess_J0',int2str(ifile-2600),'.txt']);

    elseif ifile>2609 && ifile<=2699
        % Vort=load([dir,'Vortmap_',int2str(ifile),'.txt']);
        A=load([dir,'OPDcmp4PVT0_Hess_J',int2str(ifile-2600),'.txt']);

    elseif ifile>2699 && ifile<=2709
        % Vort=load([dir,'Vortmap_',int2str(ifile),'.txt']);
        A=load([dir,'OPDcmp4PVT0_Hess_K0',int2str(ifile-2700),'.txt']);

    elseif ifile>2709 && ifile<=2799
        % Vort=load([dir,'Vortmap_',int2str(ifile),'.txt']);
        A=load([dir,'OPDcmp4PVT0_Hess_K',int2str(ifile-2700),'.txt']);
    end

    N=size(A,1);
    OPD=A(:,2);
    x=A(:,1);
    dx=x(2)-x(1);

    % Interpolating between data points
    h=dx/10;
    xx=x(1):h:x(N);
    opd_fit=spline(x,OPD,xx);

    [r,NN]=size(opd_fit);

    % Jitter Calculation %
    for k = 1:(NN-1)
        Theta(j,k) = atan(-(opd_fit(k+1)-opd_fit(k))/h);
        dist(k) = (xx(k+1)+xx(k))/2;
    end

    time(j)=dt*j;
    j=j+1;
end
```

```
save(['/afs/nd.edu/user22/aduesing/research/Jitter_Data/r01725m_Uc147_8
7/x1_120cm/Jitter_unf.mat'],'time','Theta');
```

B.1.2. Power Spectral Density Analysis of Jitter Signals

```
%-------------------------------------------------------%
%  Alice Nightingale                                    %
%  August 6, 2004                                       %
%  The following program uses Discrete Fourier          %
%  Transform to perform a spectrum analysis for the     %
%  jitter angle output developed from the DVM code and  %
%  plots the optical natural frequency versus downstream%
%  distance.                                            %
%-------------------------------------------------------%

clear all;
format long;

%dir='H:\research\Jitter_Data\';
dir='/afs/nd.edu/user22/aduesing/research/Jitter_Data/';

load([dir,'Unforced_sl/r01725m_Uc147_87/x1_120cm/Jitter_unf.mat']);

% Input parameters %
uupper=261.04; % m/s
ulower=34.7;  % m/s
r=0.01725;     % m - vortex core radius
rk=3.5;
udpv=(uupper+ulower)/2; % Convective velocity
dt=(r/rk)/udpv;         % Time step

for j=1:19              % Selecting data at specified position from the
splitter plate

    [N,p]=size(Theta);      % Number of data points, number of columns
(distance from splitter plate)
    T=time(N)-time(1);      % Total sampling time
    y1=Theta(:,j);

    ndp=512;
    N_interval=37;
    %N_interval=25;          % Number of time intervals %
    %ndp=(N)/N_interval;     % Number of data points per interval %

    % Loop to determine the mean average fft magnitude curves %
    for i=1:N_interval*2-1

        y_interval=y1((i-1)*ndp/2+1:(i+1)*ndp/2);
        time_interval=time((i-1)*ndp/2+1:(i+1)*ndp/2);
        [NN,pp]=size(y_interval);
        TT=time_interval(NN)-time_interval(1);
        Y_fft=fft(y_interval);
```

```
        Y_fft(1)=[];
        P(:,i)=((Y_fft(1:(NN/2)-1)).*conj(Y_fft(1:(NN/2)-1))/((NN/2)-
1));
    end

    mean_P=mean(P');
    freq=(1/TT)*(1:(NN/2)-1);

    % Calculating a weighted average natural frequency at each x
location %
    d0=0.215;                   % Starting distance from splitter plate
for calculations
    d(j)=d0 + 0.04*(j-1);       % Locations away from splitter plate
where numerical beam jitter calculations take place

    weighted_freq=mean_P.*freq;
    num=sum(weighted_freq);
    den=sum(mean_P);
    f_avg(j)=num/den;
end

% Plotting the average natural frequency squared %

figure('PaperUnits','centimeter','PaperPosition',[0 0 10 10]);
%axes('XMinorTick','on','YMinorTick','on');
plot(d,udpv./f_avg,'ko');
title('Progression of Dominant Natural frequency');
xlabel('Distance from splitter plate (m)');
ylabel('\Lambda_{n} (m)');
xlim([0,1]);ylim([0,0.4]);
legend('\delta_i /2 = 17.25 mm')
str1(1) = {'\Delta \Lambda_n = 0.42'};
str1(2) = {'x-x_o'};
text(0.7,0.1,str1);

%print -djpeg linear_nat_freq
```

B.2. Compensator Analysis

The control parameters which compose the third order PLL controller discussed throughout this dissertation were selected based upon four main measures of merit; phase margin, settling time, percent overshoot, and integral error. The matlab code used in these analyses may be found below. The first code, shown in Section B.2.1, determines phase margin based upon varying PLL control parameters. The codes found in Section B.2.2 and B.2.3, were used to assess response characteristics given a step and ramp input,

respectively. Finally, Section B.2.4 contains the matlab code used to compute the integral of time multiplied by absolute error (ITAE) and the integral of the square of the error (ISE) for varying control parameters.

B.2.1. Phase Margin

```
%------------------------------
%  Alice Nightingale
%  Sept. 13, 2009
%  Phase Margin investigation
%  for a 3rd order PLL design
%  while varying the minimum
%  phase zero placement.
%------------------------------

clear all;
format long;

% Low-pass filter cutoff frequency based on input frequency
wp = 500;

% Values for K prime (K_PD * K_LF * K_VCO)
Kpr = [10e-4, 10e-2, 10e0, 10e2, 10e4, 10e6];

% Varying minimum phase zero placement
wz = logspace(-8,6,149);

figure(1)
% Phase Margin Calculation for varying zero locations
for ii = 1:length(Kpr)

    for jj = 1:length(wz)

        % Open-Loop Transfer function
        GH_num=[Kpr(ii)*wp Kpr(ii)*wp*wz(jj)];
        GH_den=[wz(jj) wz(jj)*wp 0 0];
        GH=tf(GH_num,GH_den);
        [Gm(ii,jj),Pm(ii,jj),Wgm(ii,jj),Wpm(ii,jj)] = margin(GH);

%         wu = Kpr(ii)/wz(jj);
%         if wz(jj) > Kpr(ii)
%             wu = Kpr(ii)^(0.5);
%         end
%
%         PM(ii,jj) = atan((-wu*(wz(jj) - wp))/(wp*wz(jj) + wu^2));

    end

    % Plotting the Phase Margin versus minimum phase zero placement for
```

```
    % varying K' values

    semilogx(wz, Pm(ii,:))
    xlabel('\omega_z'),ylabel('Phase Margin (deg)');
    xlim([wz(1),wz(length(wz))]);
    grid on;
    hold on;

end

%save('PhaseMargin.mat','Kpr','wz','PM');
```

B.2.2. Settling Time and Percent Overshoot Given a Step Input

```
%----------------------------------------
%  Alice Nightingale
%  Sept. 15, 2009
%  This file computes the settling time
%  and percent overshoot given a step
%  input for a range of K' values and
%  omega_z values.
%----------------------------------------

clear all;
format long;

% Low-pass filter cutoff frequency based on input frequency
wp = 500;

% Values for K prime (K_PD * K_LF * K_VCO)
Kpr = [0.0001, 0.01, 1, 100, 10000, 1000000];

% Varying minimum phase zero placement
wz = logspace(-8,6,83);

% Defining time intervals
dt = 0.0001;
Tfinal = 10;
time=[0:dt:Tfinal]';

% Defining settling time limit (within 0.1% of the final value)
limit = 0.01;

figure(1)
%Calculating step and ramp responses
for ii = 1:length(Kpr)

    for jj = 1:length(wz)

        % Transfer functions
        GH_num=[Kpr(ii)*wp Kpr(ii)*wp*wz(jj)];
        GH_den=[wz(jj) wz(jj)*wp 0 0];
```

```
        GH=tf(GH_num,GH_den);           % open-loop Transfer function
        CL_sys=feedback(GH,1);          % closed-loop Transfer function

        u_step = ones(size(time));          % Step Input
        Y1 = step(CL_sys,time);             % Step Response

        % Computing percent overshoot
        PO(ii,jj) = ((max(Y1) - 1)/1)*100;  % Percent overshoot
        if max(Y1) < 1
            PO(ii,jj) = 0;
        end

        % Computing Settling Time
        e_step = Y1 - u_step;               % Step response error
        Test_step = abs(e_step) <= limit*ones(size(time));

        stop_test1 = 0;
        if sum(Test_step) ~= 0

            for kk = 1:length(time)

                Flag = length(time)+ 1 - kk;

                if sum(Test_step(kk:length(time)))==Flag&&stop_test1==0
                    Ts_step(ii,jj) = time(kk);
                    stop_test1 = 1;
                end
            end
        end

        if stop_test1 == 0
            Ts_step(ii,jj) = Tfinal*10;
        end
    end

    semilogx(wz, Ts_step(ii,:));
    xlabel('\omega_z'),ylabel('Settling Time (sec)');
    xlim([wz(1),wz(length(wz))]);
    ylim([0, Tfinal]);
    grid on;
    hold on;
end

%save('SettlingTime_step.mat','Kpr','wz','Ts_step');
```

B.2.3. Settling Time and Peak Value Given a Ramp Input

```
%-----------------------------------------------
% Alice Nightingale
% Sept. 15 2009
% Computes settling time given a ramp input
%-----------------------------------------------
```

```
clear all;
format long;

% Low-pass filter cutoff frequency based on input frequency
wp = 500;

%Kpr = [10e-4, 10e-2, 10e-1, 10e0, 10e1, 10e2, 10e4, 10e6];
%wz = [10e-8, 40e-8, 10e-7, 40e-7, 10e-6, 40e-6, 10e-5, 40e-5, 10e-4,
       40e-4, 10e-3, 40e-3, 10e-2, 40e-2, 10e-1, 40e-1, 10e0, 40e0,
       10e1, 40e1,10e2, 10e3, 10e4, 10e5, 10e6];

Kpr = 10e2;
wz = 20e0;
%wz = [10e-1, 20e-1, 30e-1, 40e-1 50e-1, 60e-1, 70e-1, 80e-1, 90e-1];


% Defining time intervals
dt = 0.00001;
Tfinal = 0.5;
time=[0:dt:Tfinal]';

% Defining settling time limit (within 0.1% of the final value)
limit = 0.001;

for ii = 1:length(wz)

    %Calculating step and ramp responses
    % Transfer functions
    GH_num=[Kpr*wp Kpr*wp*wz(ii)];
    GH_den=[wz(ii) wz(ii)*wp 0 0];

    GH=tf(GH_num,GH_den);               % open-loop Transfer function
    CL_sys=feedback(GH,1);              % closed-loop Transfer function

    u_ramp=time;                        % Ramp Input
    [Y2,T2]=lsim(CL_sys,u_ramp,time);   % Ramp Response

    % Computing Settling Time
    e_ramp = Y2 - u_ramp;               % Ramp response error
    Test_ramp = abs(e_ramp) <= limit*ones(size(time));

    % Computing peak value of error
    PVe(ii) = max(abs(e_ramp));         % Peak Value of error

    for kk = 1:length(time)

        Flag = length(time)+ 1 - kk;

        if sum(Test_ramp(kk:length(time))) == Flag
            Ts_ramp(ii) = time(kk);
            break;
        end
    end
end
```

```
plot(time, e_ramp);
```

B.2.4. Integral Error

```
%-----------------------------------
%  Alice Nightingale
%  Sept. 15, 2009
%  This file computes the ITAE index
%  and ISE index given a step input.
%-----------------------------------

clear all;
format long;

% Low-pass filter cutoff frequency based on input frequency
wp = 500;

% Values for K prime (K_PD * K_LF * K_VCO)
%Kpr = [0.0001, 0.01, 1, 100, 10000, 1000000];
Kpr = 0.0001;

% Varying minimum phase zero placement
%wz = logspace(-8,6,70);
wz = [10e-7, 30e-7, 10e-6, 30e-6, 10e-5];
%wz = [ 30e-5, 10e-4, 30e-4, 10e-3, 30e-3, 10e-2, 30e-2];

% Defining time intervals
dt = 0.000001;
Tfinal = 10;
time=[0:dt:Tfinal]';

%Calculating step and ramp responses
for ii = 1:length(Kpr)

    for jj = 1:length(wz)

        % Transfer functions
        GH_num=[Kpr(ii)*wp Kpr(ii)*wp*wz(jj)];
        GH_den=[wz(jj) wz(jj)*wp 0 0];

        GH=tf(GH_num,GH_den);           % open-loop Transfer function
        CL_sys=feedback(GH,1);          % closed-loop Transfer function

        u_step = ones(size(time));          % Step Input
        Y1 = step(CL_sys,time);             % Step Response

        % Computing Integral errors given a step input
        e_step = Y1 - u_step;               % Step response error
        ITAE_step(ii,jj) = dt*sum(time.*abs(e_step)); % ITAE index
        ISE_step(ii,jj) = dt*sum(e_step.^2);          % ISE index

    end
end
```

```
% Plotting the ITAE index
figure(2)
for mm = 1:length(Kpr)

    loglog(wz, ITAE_step(mm,:));
    xlabel('\omega_z'),ylabel('ITAE index');
    xlim([wz(1),wz(length(wz))]);
    grid on;
    hold on;

end

% Plotting the ISE index
figure(3)
for mm = 1:length(Kpr)

    loglog(wz, ISE_step(mm,:));
    xlabel('\omega_z'),ylabel('ISE index');
    xlim([wz(1),wz(length(wz))]);
    grid on;
    hold on;

end

save('ITAE_Step.mat','Kpr','wz','ITAE_step');
save('ISE_Step.mat','Kpr','wz','ISE_step');
```

B.3. Finalized PLL Analysis

The following matlab code creates a bode diagram, root locus, step and ramp response plots for the third order PLL controller designed and described in this dissertation.

```
%---------------------------------------
%  Alice Nightingale
%  Sept. 14, 2009
%  This file plots the root locus, gain
%  and phase margin, step response and
%  ramp response for a specific 3rd order
%  PLL controller.
%---------------------------------------

clear all;
```

```
format long;

% Check Phase Margin Calculation by evaluating system's bode plot for
% various omega_z values.
Kpr = 10000;     % 10e2 = 10^3 = 1000
wp=500;
wz = 55;        % 20e0 = 2*10^1 = 20

% Transfer function
GH_num=[Kpr*wp Kpr*wp*wz];
GH_den=[wz wz*wp 0 0];
GH=tf(GH_num,GH_den)            % Open-loop TF
CL_sys=feedback(GH,1);          % Closed-loop TF

% figure(5)
% rlocus(GH)

figure('PaperUnits','centimeter','PaperPosition',[0 0 8 4])
margin(GH)
grid on;

time1=[0:0.001:0.5];
u1=ones(size(time1));
[Y1,T1]=lsim(CL_sys,u1,time1);
error1 = Y1 - u1';

figure(7)
subplot(2,1,1),plot(time1,error1,'r');
xlabel('Time (sec)'),ylabel('Step Response Error');
grid on;

time2=[0:0.001:0.5];
u2=10*time2;
[Y2,T2]=lsim(CL_sys,u2,time2);
error2 = Y2 - u2';
subplot(2,1,2),plot(time2,error2,'r');
%ylim([-0.01, 0.01]);
xlabel('Time (sec)'),ylabel('Ramp Response Error');
grid on;

% figure(8)
% bode(CL_sys)
% grid on;
```

B.4. AO Controller Simulations

The following matlab code performs conjugate corrections to a beam emerging from the DVM/WCM free shear layer by numerically approximating the PLL controller designed for this dissertation.

```
%-------------------------------------------------------------
%  Alice Nightingale
%  June 22, 2004
%  This program simulates a closed loop controller that adjusts
%  the amplitude and phase of a sinusoidal wave with the goal of
%  syncing the sine wave to the numerical OPD waveform.
%-------------------------------------------------------------

clear all;
format long;

% dir='/afs/nd.edu/user22/aduesing/research/PLL/Uc_147B/1200Hz/';
dir='C:\Users\Guest2\Desktop\ANightingale\MatlabFiles\Uc_147A\700Hz\';

% Input parameters %
%  uupper=258.4; % m/s
%  ulower=40.8; % m/s

% Uc_117B
% uupper=180;
% ulower=55;

% Uc_117_5C
% uupper=210;
% ulower=25;

% Uc_147A
 uupper=261.04; % m/s
 ulower=34.7; % m/s

% Uc_147_87B
% uupper=231;     % m/s
% ulower=64.74;   % m/s

r=0.01725;  % m - vortex core radius
rk=3.5;
udpv=(uupper+ulower)/2;
dt=(r/rk)/udpv;     % time step

% Choose position between 0.25m and 0.94m %
location = 0.38;    % meters
aperture = 0.12;    % meters
lambda=0.633e-6;    % meters
```

```
Length=1;           % distance between position sensing device and
shear layer (meters)
L=101;
t_final=0.1;
degree=4;           % degree of polynomial fit

% Initial waveform parameters %
A_DM(1) = 0.5e-06;
Ff = 700;                   % wave speed
omega_sl = 2*pi*Ff;
k_sl = (2*pi*Ff)/udpv;       % wave freq
phase(1) = 0;
delta_phi(1)=0;
Period = round((1/Ff)/dt);

% Amplitude Feedforward control parameters %
RC1 = 0.0055;   % RC circuit used to determine amplitude of full
rectified wave
RC2 = 0.0085;
Ka = 0.2;       % Amplitude proportional gain constant

% Third order PLL control parameters
RC=0.002;
Ko=1000;
R1C=0.026;
R2C=0.011;

Kp=Ko*R2C/R1C;
Ki=Ko/R1C;

Th0(1)=0;
Th0_dot(1)=0;

A_sl(1) = A_DM(1);
Sm_out(1) = 0;
TT2(1)=0;
tau=1/(4*Ff*dt);
shift=round(tau);
dtau=tau-shift;

% % Transvers coordinates of the sourse
% xs=0;
% ys=0;
% Ro=10000;     % Distance from source to aperture
%
% % Grid points in the aperture plane (must be same length as
OPD_ap2(j,:))
% N_OPDap=91;
% xy_pr_o=0.09;
% dx_pr=xy_pr_o/((N_OPDap-1)/2);
% dy_pr=dx_pr;
% [x_pr,y_pr]=meshgrid([-xy_pr_o:dx_pr:xy_pr_o],[-
xy_pr_o:dy_pr:xy_pr_o]);
%
% % Grid points in the observation plane
```

```
% x_ob=-20:0.5:20;
% y_ob=-20:0.5:20;
% [X,Y]=meshgrid(x_ob,y_ob);
% Ro_pr=2000000;   % Distance from aperture to observation plane
%
% % Derived Parameters %
% Nx=size(X,2);
% Ny=size(Y,2);
% k_laser=(2*pi)/lambda;
%
% alpha=-xs/Ro;       % Direction cosine from source to aperture
% beta=-ys/Ro;        % Direction cosine from source to aperture
% alpha_pr=x_ob/Ro_pr;   % Dir. cosine from ap. to observation plane
% beta_pr=y_ob/Ro_pr;    % Dir. cosine from ap. to observation plane
%
% u=(alpha-alpha_pr);
% v=(beta-beta_pr);
%
% % Calculating the field numerically %
% Eo=exp(-i*k_laser*Ro)/Ro;
%
% % Defining the Trasmission Function at the aperture%
% radius=0.05;
%
% for jj=1:size(x_pr,2)
%     for kk=1:size(y_pr,2)
%         if abs(x_pr(jj,kk))>radius
%             tr(jj,kk)=0;
%         elseif y_pr(jj,kk)>=0 && y_pr(jj,kk)<=sqrt(radius^2-
x_pr(jj,kk)^2)
%             tr(jj,kk)=1;
%         elseif y_pr(jj,kk)<0 && y_pr(jj,kk)>=-sqrt(radius^2-
x_pr(jj,kk)^2)
%             tr(jj,kk)=1;
%         else
%             tr(jj,kk)=0;
%         end
%     end
% end

f_file=1616;
l_file=2799;
j=1;
m=0;

for ifile=f_file:l_file;

    if ifile<=999
        % % Vort=load([dir,'Vortmap_',int2str(ifile),'.txt']);
        A=load([dir,'OPDcmp4PVT0_Hess_',int2str(ifile),'.txt']);

    elseif ifile>999 && ifile<=1009
        % % Vort=load([dir,'Vortmap_',int2str(ifile),'.txt']);
        A=load([dir,'OPDcmp4PVT0_Hess_:0',int2str(ifile-1000),'.txt']);
```

```
    elseif ifile>1009 && ifile<=1099
        % Vort=load([dir,'Vortmap_',int2str(ifile),'.txt']);
        A=load([dir,'OPDcmp4PVT0_Hess_:',int2str(ifile-1000),'.txt']);

    elseif ifile>1099 && ifile<=1109
        % Vort=load([dir,'Vortmap_',int2str(ifile),'.txt']);
        A=load([dir,'OPDcmp4PVT0_Hess_;0',int2str(ifile-1100),'.txt']);

    elseif ifile>1109 && ifile<=1199
        % Vort=load([dir,'Vortmap_',int2str(ifile),'.txt']);
        A=load([dir,'OPDcmp4PVT0_Hess_;',int2str(ifile-1100),'.txt']);

    elseif ifile>1199 && ifile<=1209
        % Vort=load([dir,'Vortmap_',int2str(ifile),'.txt']);
        A=load([dir,'OPDcmp4PVT0_Hess_<0',int2str(ifile-1200),'.txt']);

    elseif ifile>1209 && ifile<=1299
        % Vort=load([dir,'Vortmap_',int2str(ifile),'.txt']);
        A=load([dir,'OPDcmp4PVT0_Hess_<',int2str(ifile-1200),'.txt']);

    elseif ifile>1299 && ifile<=1309
        % Vort=load([dir,'Vortmap_',int2str(ifile),'.txt']);
        A=load([dir,'OPDcmp4PVT0_Hess_=0',int2str(ifile-1300),'.txt']);

    elseif ifile>1309 && ifile<=1399
        % Vort=load([dir,'Vortmap_',int2str(ifile),'.txt']);
        A=load([dir,'OPDcmp4PVT0_Hess_=',int2str(ifile-1300),'.txt']);

    elseif ifile>1399 && ifile<=1409
        % Vort=load([dir,'Vortmap_',int2str(ifile),'.txt']);
        A=load([dir,'OPDcmp4PVT0_Hess_ee0',int2str(ifile-
1400),'.txt']);

    elseif ifile>1409 && ifile<=1499
        % Vort=load([dir,'Vortmap_',int2str(ifile),'.txt']);
        A=load([dir,'OPDcmp4PVT0_Hess_ee',int2str(ifile-1400),'.txt']);

    elseif ifile>1499 && ifile<=1509
        % Vort=load([dir,'Vortmap_',int2str(ifile),'.txt']);
        A=load([dir,'OPDcmp4PVT0_Hess_ff0',int2str(ifile-
1500),'.txt']);

    elseif ifile>1509 && ifile<=1599
        % Vort=load([dir,'Vortmap_',int2str(ifile),'.txt']);
        A=load([dir,'OPDcmp4PVT0_Hess_ff',int2str(ifile-1500),'.txt']);

    elseif ifile>1599 && ifile<=1609
        % Vort=load([dir,'Vortmap_',int2str(ifile),'.txt']);
        A=load([dir,'OPDcmp4PVT0_Hess_@0',int2str(ifile-1600),'.txt']);

    elseif ifile>1609 && ifile<=1699
        % Vort=load([dir,'Vortmap_',int2str(ifile),'.txt']);
        A=load([dir,'OPDcmp4PVT0_Hess_@',int2str(ifile-1600),'.txt']);

    elseif ifile>1699 && ifile<=1709
```

```
    % Vort=load([dir,'Vortmap_',int2str(ifile),'.txt']);
    A=load([dir,'OPDcmp4PVT0_Hess_A0',int2str(ifile-1700),'.txt']);

elseif ifile>1709 && ifile<=1799
    % Vort=load([dir,'Vortmap_',int2str(ifile),'.txt']);
    A=load([dir,'OPDcmp4PVT0_Hess_A',int2str(ifile-1700),'.txt']);

elseif ifile>1799 && ifile<=1809
    % Vort=load([dir,'Vortmap_',int2str(ifile),'.txt']);
    A=load([dir,'OPDcmp4PVT0_Hess_B0',int2str(ifile-1800),'.txt']);

elseif ifile>1809 && ifile<=1899
    % Vort=load([dir,'Vortmap_',int2str(ifile),'.txt']);
    A=load([dir,'OPDcmp4PVT0_Hess_B',int2str(ifile-1800),'.txt']);

elseif ifile>1899 && ifile<=1909
    % Vort=load([dir,'Vortmap_',int2str(ifile),'.txt']);
    A=load([dir,'OPDcmp4PVT0_Hess_C0',int2str(ifile-1900),'.txt']);

elseif ifile>1909 && ifile<=1999
    % Vort=load([dir,'Vortmap_',int2str(ifile),'.txt']);
    A=load([dir,'OPDcmp4PVT0_Hess_C',int2str(ifile-1900),'.txt']);

elseif ifile>1999 && ifile<=2009
    % Vort=load([dir,'Vortmap_',int2str(ifile),'.txt']);
    A=load([dir,'OPDcmp4PVT0_Hess_D0',int2str(ifile-2000),'.txt']);

elseif ifile>2009 && ifile<=2099
    % Vort=load([dir,'Vortmap_',int2str(ifile),'.txt']);
    A=load([dir,'OPDcmp4PVT0_Hess_D',int2str(ifile-2000),'.txt']);

elseif ifile>2099 && ifile<=2109
    % Vort=load([dir,'Vortmap_',int2str(ifile),'.txt']);
    A=load([dir,'OPDcmp4PVT0_Hess_E0',int2str(ifile-2100),'.txt']);

elseif ifile>2109 && ifile<=2199
    % Vort=load([dir,'Vortmap_',int2str(ifile),'.txt']);
    A=load([dir,'OPDcmp4PVT0_Hess_E',int2str(ifile-2100),'.txt']);

elseif ifile>2199 && ifile<=2209
    % Vort=load([dir,'Vortmap_',int2str(ifile),'.txt']);
    A=load([dir,'OPDcmp4PVT0_Hess_F0',int2str(ifile-2200),'.txt']);

elseif ifile>2209 && ifile<=2299
    % Vort=load([dir,'Vortmap_',int2str(ifile),'.txt']);
    A=load([dir,'OPDcmp4PVT0_Hess_F',int2str(ifile-2200),'.txt']);

elseif ifile>2299 && ifile<=2309
    % Vort=load([dir,'Vortmap_',int2str(ifile),'.txt']);
    A=load([dir,'OPDcmp4PVT0_Hess_G0',int2str(ifile-2300),'.txt']);

elseif ifile>2309 && ifile<=2399
    % Vort=load([dir,'Vortmap_',int2str(ifile),'.txt']);
    A=load([dir,'OPDcmp4PVT0_Hess_G',int2str(ifile-2300),'.txt']);
```

```
elseif ifile>2399 && ifile<=2409
    % Vort=load([dir,'Vortmap_',int2str(ifile),'.txt']);
    A=load([dir,'OPDcmp4PVT0_Hess_H0',int2str(ifile-2400),'.txt']);

elseif ifile>2409 && ifile<=2499
    % Vort=load([dir,'Vortmap_',int2str(ifile),'.txt']);
    A=load([dir,'OPDcmp4PVT0_Hess_H',int2str(ifile-2400),'.txt']);

elseif ifile>2499 && ifile<=2509
    % Vort=load([dir,'Vortmap_',int2str(ifile),'.txt']);
    A=load([dir,'OPDcmp4PVT0_Hess_I0',int2str(ifile-2500),'.txt']);

elseif ifile>2509 && ifile<=2599
    % Vort=load([dir,'Vortmap_',int2str(ifile),'.txt']);
    A=load([dir,'OPDcmp4PVT0_Hess_I',int2str(ifile-2500),'.txt']);

elseif ifile>2599 && ifile<=2609
    % Vort=load([dir,'Vortmap_',int2str(ifile),'.txt']);
    A=load([dir,'OPDcmp4PVT0_Hess_J0',int2str(ifile-2600),'.txt']);

elseif ifile>2609 && ifile<=2699
    % Vort=load([dir,'Vortmap_',int2str(ifile),'.txt']);
    A=load([dir,'OPDcmp4PVT0_Hess_J',int2str(ifile-2600),'.txt']);

elseif ifile>2699 && ifile<=2709
    % Vort=load([dir,'Vortmap_',int2str(ifile),'.txt']);
    A=load([dir,'OPDcmp4PVT0_Hess_K0',int2str(ifile-2700),'.txt']);

elseif ifile>2709 && ifile<=2799
    % Vort=load([dir,'Vortmap_',int2str(ifile),'.txt']);
    A=load([dir,'OPDcmp4PVT0_Hess_K',int2str(ifile-2700),'.txt']);

end

N=size(A,1);
OPD=A(:,2);
x=A(:,1);
dx=x(2)-x(1);
time(j)=dt*j;

% Interpolating between data points %
h=0.001;
xx=x(1):h:x(N);
yy=spline(x,OPD,xx);
position=round((location-xx(1))/h + 1);
loc1 = position - round((aperture/2)/h);
loc2 = position + round((aperture/2)/h);
N_aperture = loc2 - loc1;

OPD_ap(j,:) = yy(loc1:loc2);
OPD_ap(j,:) = OPD_ap(j,:) - mean(OPD_ap(j,:));
xx_ap = xx(loc1:loc2);
OPD_ideal=0;

% Functions driving each of the 7 rows of actuators (Predicting the
```

```
    % optical wavefront)
    time(j)=(j-1)*dt;
    OPD_DM(j,:) = A_DM(j)*sin(k_sl.*xx_ap-omega_sl*time(j) - phase(j));
    x_DM = [xx_ap(1),xx_ap(1+N_aperture/6),xx_ap(1+2*N_aperture/6),
xx_ap(1+3*N_aperture/6), xx_ap(1+4*N_aperture/6),
xx_ap(1+5*N_aperture/6), xx_ap(1+6*N_aperture/6)];

%     f1 = A_DM(j)*sin(k_sl*x_DM(1) - omega_sl*time(j) - phase(j));
%     f2 = A_DM(j)*sin(k_sl*x_DM(2) - omega_sl*time(j) - phase(j));
%     f3 = A_DM(j)*sin(k_sl*x_DM(3) - omega_sl*time(j) - phase(j));
%     f4 = A_DM(j)*sin(k_sl*x_DM(4) - omega_sl*time(j) - phase(j));
%     f5 = A_DM(j)*sin(k_sl*x_DM(5) - omega_sl*time(j) - phase(j));
%     f6 = A_DM(j)*sin(k_sl*x_DM(6) - omega_sl*time(j) - phase(j));
%     f7 = A_DM(j)*sin(k_sl*x_DM(7) - omega_sl*time(j) - phase(j));
%
%     % Actuator Positions %
%     act1x = [x_DM(1), x_DM(1)];
%     act1y = [-1e-06, f1];
%     act2x = [x_DM(2), x_DM(2)];
%     act2y = [-1e-06, f2];
%     act3x = [x_DM(3), x_DM(3)];
%     act3y = [-1e-06, f3];
%     act4x = [x_DM(4), x_DM(4)];
%     act4y = [-1e-06, f4];
%     act5x = [x_DM(5), x_DM(5)];
%     act5y = [-1e-06, f5];
%     act6x = [x_DM(6), x_DM(6)];
%     act6y = [-1e-06, f6];
%     act7x = [x_DM(7), x_DM(7)];
%     act7y = [-1e-06, f7];
%
%     % Shape of the deformable mirror %
%     f = [f1,f2,f3,f4,f5,f6,f7];
%     coef = polyfit(x_DM,f,degree);
%     p = polyval(coef,xx_ap);

    % Jitter and OPD error %
    %OPD_error(j,:) = OPD_ap2(j,:) - p;
    OPD_error(j,:) = OPD_ap(j,:) - OPD_DM(j,:);
    Jitt_error(j) = -atan(((OPD_error(j,N_aperture/2+2)-
OPD_error(j,N_aperture/2+1))/h + (OPD_error(j,N_aperture/2+1)-
OPD_error(j,N_aperture/2))/h)/2);

    % Measurement from the small aperture position sensing device
    Jitt_sl(j) = -atan(((OPD_ap(j,N_aperture/2+2)-
OPD_ap(j,N_aperture/2+1))/h + (OPD_ap(j,N_aperture/2+1)-
OPD_ap(j,N_aperture/2))/h)/2);
    Pos_sen_device = Length*Jitt_sl(j);
    Jitt_DM(j) = -Jitt_error(j) + Jitt_sl(j);

    % Calculating the amplitude of the actual OPD waveform
    ThAmp(j) = -Jitt_sl(j)/k_sl;
    A_fwr(j) = abs(ThAmp(j));

    if j <= 2*tau
```

```
        A_DM(j+1) = A_DM(j);
        A_sl(j+1) = A_sl(j);
        phase(j+1) = phase(j);

    else

        m=m+1;

        % Applying phase shift to Jitt_sl and performing Signal mixing
        % to determine phase difference
        Jitt_ps(m) = Jitt_sl(j-shift) + sign(dtau)*dtau*(Jitt_sl(j-
(shift+sign(dtau))) - Jitt_sl(j-shift));
        Sm(m) = Jitt_ps(m)*Jitt_DM(j)/(k_sl^2);

        % Frequency content of mixing signal %
        [pp,NN]=size(Sm);
        TT(m)=(m-1)*dt;
        Y_fft=fft(Sm);
        PSD=(Y_fft.*conj(Y_fft))/NN;
        freq=(1/TT(m))*(0:ceil(NN/2)-1);

        % Rectifier and Capacitor circuit
        A_sl(j+1) = A_sl(j) + dt*(-A_sl(j)/RC2 + A_fwr(j)/RC1);
        delta_A = (A_sl(j) - A_DM(j));
        A_DM(j+1) = A_DM(j) + Ka*delta_A;

        % Simulating low-pass filter for frequencies above 200 Hz
        Sm_out(m+1) = Sm_out(m) + dt*(-Sm_out(m)/RC + Sm(m)/RC);
        delta_phi(m) = real(asin(2*Sm_out(m+1)/(A_DM(j+1)*A_sl(j+1))));

        % Simulating loop filter and VCO integrator (non-minimum phase
        % zero and two zero poles)
        if m==1
            delta_phi_dot(m) = 0;
        else
            delta_phi_dot(m) = (delta_phi(m) - delta_phi(m-1))/dt;
        end

        Th0_dot(m+1) = Th0_dot(m) + dt*((Ko/R1C)*delta_phi(m) +
(Ko*R2C/R1C)*delta_phi_dot(m));
        Th0(m+1) = Th0(m) + dt*Th0_dot(m);
        phase(j+1) = Th0(m+1);

       % Frequency content of filtered mixing signal %
       [pp2,NN2]=size(Sm_out);
       TT2(m+1)=m*dt;
       Y_fft2=fft(Sm_out);
       PSD2=(Y_fft2.*conj(Y_fft2))/NN2;
       freq2=(1/TT2(m+1))*(0:ceil(NN2/2)-1);

    end

    % Removing Tilt from OPD at each time step
    poly=polyfit(xx_ap,OPD_error(j,:),1);
```

```
    linear_fit=poly(1)*xx_ap+poly(2);
    OPD_tilt_removed = OPD_error(j,:) - linear_fit;

    % Calculating the Strehl ratio at each time step %
        th=linspace(-6*lambda/aperture,6*lambda/aperture,L);
    for k=1:size(th,2)
        theta=th(k);

Intens(k)=(abs(sum(exp(2*pi*i*((OPD_error(j,:)+theta*xx_ap)/lambda))))/
size(xx_ap,2))^2;

Intens_orig(k)=(abs(sum(exp(2*pi*i*((OPD_ap(j,:)+theta*xx_ap)/lambda)))
)/size(xx_ap,2))^2;

Intens_tr(k)=(abs(sum(exp(2*pi*i*((OPD_tilt_removed+theta*xx_ap)/lambda
))))/size(xx_ap,2))^2;

Intens_ideal(k)=(abs(sum(exp(2*pi*i*((OPD_ideal+theta*xx_ap)/lambda))))
/size(xx_ap,2))^2;
    end;

    psuedo_St(j)=max(Intens);
    St(j)=Intens((L+1)/2);
    mean_st=mean(St);

    psuedo_St_tr(j) = max(Intens_tr);
    St_tr(j) = Intens_tr((L+1)/2);
    mean_st_tr=mean(St_tr);

    St_orig(j) = Intens_orig((L+1)/2);

    if psuedo_St(j)>1
        j
    end

    rmsOPD(j) = sqrt(mean(OPD_error(j,:).^2));

%     figure(j)
%     plot(xx_ap,OPD_error(j,:),'r');
%     grid on;
%     ylim([-1e-6, 1e-6]);
%     xlim([xx(loc1),xx(loc2)]);
%     title('Wavefront Sensor');
%     xlabel('x (m)'),ylabel('OPD error (m)');

%     % Movie 1
%     handle=figure(1)
%     subplot(2,1,1),plot(time,phase(1:j).*(180/pi),'m',time,phi_act,
'k--');
%     grid on;
%     xlim([0,t_final]);
%     ylim([-180,90]);
%     %title('Phase Control');
%     xlabel('Time (seconds)'),ylabel('Phase (degrees)');
%
```

```
%     subplot(2,1,2),plot(time,St,'b');
%     %title('AO Corrected');
%     xlabel('Time (seconds)');
%     ylabel('Strehl Ratio');
%     ylim([0,1]);
%     xlim([0,t_final]);
%     grid on;
%     F(j)=getframe(handle);
%
%     % Movie 2
%     handle=figure(2);

figure(2)
subplot(2,1,1),plot(xx_ap,OPD_ap(j,:).*10^6,'k',xx_ap,OPD_DM(j,:).*10^6
,'b');
    grid on;
    ylim([-2, 2]);
    xlim([xx(loc1),xx(loc2)]);
    title('Waveform Comparison');
    legend('Numerical waveform','DM waveform');
    xlabel('x (m)'),ylabel('OPD (\mu m)');

    subplot(2,1,2),plot(th,Intens,'b',th,Intens_ideal,'k-.');
    xlim([-1.5e-5,1.5e-5]);
    ylabel('Intensity'),xlabel('6 \lambda / Ap');
%     F(j)=getframe(handle);
%
%
%     % Movie 3 %
%
%    OPD_ap2_rect=OPD_ap2(j,:);
%    OPD_er_rect=OPD_error(j,:);
%    for cc=1:N_aperture
%        OPD_ap2_rect=[OPD_ap2_rect; OPD_ap2(j,:)];
%        OPD_er_rect=[OPD_er_rect; OPD_error(j,:)];
%    end
%
%    for aa=1:Nx
%        aa
%        for bb=1:Ny
%            E_er(aa,bb)=sum(sum(tr.*exp(-
i*k_laser.*OPD_er_rect).*exp(-
i*k_laser*(u(aa).*x_pr+v(bb).*y_pr)))*dx_pr)*dy_pr;
%            E_ap(aa,bb)=sum(sum(tr.*exp(-
i*k_laser.*OPD_ap2_rect).*exp(-
i*k_laser*(u(aa).*x_pr+v(bb).*y_pr)))*dx_pr)*dy_pr;
%        end
%    end
%
%    Intens_er(:,:,j)=(abs((i/lambda)*Eo*(exp(-
i*k_laser*Ro_pr)/Ro_pr)*E_er)).^2;
%    Intens_ap(:,:,j)=(abs((i/lambda)*Eo*(exp(-
i*k_laser*Ro_pr)/Ro_pr)*E_ap)).^2;
%
%    handle=figure(3)
```

```
%    subplot(1,2,1)
%    h1=pcolor(X,Y,Intens_ap(:,:,j));
%    caxis([0,2e-12]);
%    title('Uncorrected Far Field');
%    subplot(1,2,2)
%    h2=pcolor(X,Y,Intens_er(:,:,j));
%    set(h1,'EdgeColor','interp');
%    set(h2,'EdgeColor','interp');
%    %colormap gray
%    caxis([0,2e-12]);
%    title('Corrected Far Field');
%
%    if j==1;
%        brighten(0.45);
%    end
%
%    F(j)=getframe(handle);
%

    j=j+1;
end

%save(['/home/anightingale/research/Results/AIAA_Conf_06/control_1100.m
at'],'F');
% movie2avi(F,'Phase_Step_Error','fps',40);

mean_rmsOPD=mean(rmsOPD(600:j-1))
%mean_orig=mean(St_orig)
mean_st=mean(St(600:j-1))
%mean_psuedo=mean(psuedo_St)
mean_st_tr=mean(St_tr(450:j-1))


% Figure 1 %
phi_act = -94;      % Initial phase error between shear layer and
conjugate correction

figure('PaperUnits','centimeter','PaperPosition',[0 0 12 10]);
subplot(2,1,2),plot(time,St,'b');
%title('AO Corrected');
xlabel('Time (seconds)','LineWidth',1.2);
ylabel('Strehl Ratio');
ylim([0,1]);
xlim([0,time(length(time))]);
grid on;

subplot(2,1,1),plot(time,phase(1:j-
1).*(180/pi),'r',time,ones(length(time)).*phi_act,'k--
','LineWidth',1.2);
grid on;
xlim([0,time(length(time))]);
ylim([-180,180]);
%title('Phase Control');
xlabel('Time (seconds)'),ylabel('Phase (degrees)');
```

```
% Figure 2 %
figure('PaperUnits','centimeter','PaperPosition',[0 0 10 10])
plot(time,St,'k',time,St_tr,'b-','LineWidth',1.2);
xlabel('time (seconds)');
ylabel('Strehl Ratio');
legend('Strehl Ratio', 'Tilt-Removed Strehl Ratio');
ylim([0,1]);
xlim([0,time(length(time))]),grid on;

% Figure 3 %
figure('PaperUnits','centimeter','PaperPosition',[0 0 10 10]);
plot(time,St_orig, 'LineWidth', 1.2);
xlabel('time (seconds)');
ylabel('Strehl Ratio');
ylim([0,1]);
xlim([0,time(length(time))]);
grid on;
title('Forced Shear Layer');

figure(10)
for qq = 1:6

subplot(2,3,qq),plot(xx_ap,OPD_ap(700+round(qq*(1/Ff)/dt/6),:)*10^6,'r'
, xx_ap,OPD_DM(700+round(qq*(1/Ff)/dt/6),:)*10^6,'k-.');
    grid on;
    ylim([-1, 1]);
    xlim([xx(loc1),xx(loc2)]);
    xlabel('x (m)'),ylabel('OPD (\mu m)');
end

figure(11)
for qq = 1:6

subplot(2,3,qq),plot(xx_ap,OPD_error(700+round(qq*(1/Ff)/dt/6),:)*10^6,
'r');
    grid on;
    ylim([-1, 1]);
    xlim([xx(loc1),xx(loc2)]);
    xlabel('x (m)'),ylabel('OPD error (\mu m)');
end
```

APPENDIX C:

ALTERNATIVE AO CONTROLLER SPECIFICATIONS

This appendix contains specifications for the PLL circuit's primary electrical components described in Chapter 5. Each section includes a brief description of the component's function within the PLL circuit and a table of key electrical specifications. Further information may be found by referencing the manufacturer's website.

C.1. Four-Quadrant Analog Multiplier (AD633)

Two four-quadrant analog multiplier chips were used in the construction of the PLL circuit. The first AD633 chip, in conjunction with a low-pass filter, functions as a phase detector. The shear layer jitter signal is multiplied with the PLL output in an effort to determine the phase difference between signals. The second AD633 chip is used to create a phase-locked output signal with the appropriate amplitude. The PLL phase-locked output previously scaled to unity is multiplied by an estimate of the shear layer's amplitude using this multiplier chip. The four-quadrant analog multiplier chip has high impedance inputs and operates with a supply voltage between ±8 Volts to ±18 Volts. Table C.1 includes a few key specifications for the AD633 four-quadrant analog multiplier chip.

TABLE C.1

SPECIFICATIONS FOR THE FOUR-QUADRANT

MULTIPLIER CHIP, AD633.

Model	AD633JN
Manufacturer	Analog Devices
Name	Low Cost Analog Multiplier
Transfer Function	$W = \frac{(X_1 - X_2)(Y_1 - Y_2)}{10} + Z$
Supply Voltage Operating Range	±8 Volts to ±18 Volts
Input Resistance	10 MΩ

C.2. Low-Noise Operational Amplifier (NE5534A)

Nine low-noise operational amplifiers were used in the construction of the PLL circuit described in Chapter 5. The eight pin amplifiers were used to perform several different operations within the circuit including scaling, filtering, and summing. Table C.2 shown below contains a few key specifications pertaining to these operational amplifiers. Further information including a complete data sheet may be found at the manufacturer's website.

TABLE C.2

SPECIFICATIONS FOR THE LOW-NOISE

OPERATIONAL AMPLIFIER, NE5534A.

Model	NE5534AP
Manufacturer	Texas Instruments
Name	Low-Noise Operational Amplifer
Supply Voltage Operating Range	±3 Volts to ±20 Volts
Input Resistance	100 kΩ

C.3. Waveform Generator (NTE864)

A precision waveform generator, also referred to as a voltage-controlled oscillator (VCO), is one of the primary components of the PLL circuit. The NTE864 chip is an integrated circuit designed to produce sine, square, triangular, sawtooth, and pulse waveforms. The chip is capable of both frequency modulation and sweeping with a frequency range from 0.001 Hz up to 300 kHz. The operating range for the chips supply voltage is between ±5 Volts to ±15 Volts. The PLL application described in this dissertation uses both frequency modulation and the sine wave output. Table C.3 provides a few key specifications for the waveform generator chip. Further details and examples of operation may be found at the manufacturer's website. It should be noted that the NTE864 is a replacement part for the ICL8038 chip which has become obsolete. The ICL8038 data sheets may also be referenced for additional information pertaining to operation and circuitry.

TABLE C.3

SPECIFICATIONS FOR THE PRECISION

WAVEFORM GENERATOR CHIP, NTE864

(REPLACEMENT CHIP FOR ICL8038).

Model	NTE864
Manufacturer	NTE Electronics, Inc.
Name	Integrated Circuit Precision Waveform Generator
Frequency Range	0.001 Hz to 300 kHz
Supply Voltage Operating Range	±5 Volts to ±15 Volts
Obsolete Model Number/Manufacturer	ICL8038, Intersil

C.4 RMS-to-DC Converter (AD536A)

The amplitude estimator circuit described in Section 5.3 is based upon a root-mean-squared (rms) approximation. An RMS-to-DC converter chip (AD536A) computes the true rms level of an input sinusoidal signal. In this case, the AD536A computes the rms of the shear layers regularized jitter signal producing a DC value corresponding to its input. The AD536A chip is a monolithic integrated circuit with fourteen leads. Table C.4 contains a few key specifications for the AD536A chip. Further information including detailed data sheets may be found at the manufacturer's website.

TABLE C.4

SPECIFICATIONS FOR THE RMS-TO-DC

CONVERTER CHIP, AD536A.

Model	AD536AJ
Manufacturer	Analog Devices
Name	Integrated Circuit True RMS-to-DC Converter
Transfer Function	$V_{out} = \sqrt{AVG\left(V_{in}{}^2\right)}$
Supply Voltage Operating Range	±3 Volts to ±18 Volts

C.5. Four-Quadrant Multiplier/Divider (AD734)

A four-quadrant multiplier/divider chip (AD734) was also used in the development of the AO controller. Before being fed into the PLL control circuit, the incoming shear layer jitter signal is scaled to unity. The AD734 chip performs analog division in this application. The shear layer jitter signal is divided by an estimate of the

signal's amplitude, the output from the RMS-to-DC converter and op-amp amplifying circuit. This fourteen lead multiplier/divider chip operates off a dual power supply and has multiplication, division, squaring and square root capabilities. Table C. 5 contains a few key specifications for the AD734 chip. Further information including detailed data sheets may be found at the manufacturer's website.

TABLE C.5

SPECIFICATIONS FOR THE FOUR-QUADRANT

MULTIPLIER/DIVIDER CHIP, AD734.

Model	AD734AN
Manufacturer	Analog Devices
Name	10 MHz, 4-Quadrant Multiplier/Divider
Transfer Function	$W = A_O\left\{\frac{(X_1 - X_2)(Y_1 - Y_2)}{U} - (Z_1 - Z_2)\right\}$
Supply Voltage Operating Range	±8 Volts to ±16.5 Volts

REFERENCES

[1] Lloyd-Hart, Michael, "Taking the Twinkle out of Starlight", *IEEE Spectrum*, **40** (12), Dec 2003, pp. 22-29.

[2] Tyson, R.K., *Principles of Adaptive Optics*, 2nd ed., Academic Press, Chestnut Hill Massachusetts, 1991.

[3] Jumper, E.J., and E.J. Fitzgerald, "Recent Advances in Aero-Optics", *Progress in Aerospace Sciences*, **37**, 2001, pp.299-339.

[4] Kyrazis, D., "Optical degradation by turbulent free shear layers", *SPIE*, **2005**, 1993.

[5] Fitzgerald, E.J. and Jumper E.J., "The Optical Distortion Mechanism in a Nearly Incompressible Free Shear Layer," *Journal of Fluid Mechanics*, **512**, 2004, pp. 153-189.

[6] Klein, Miles V., *Optics*, 1st ed., John Wiley & Sons, Inc., New York, London, Sydney, Toronto, 1970.

[7] Cicchiello, J.M., and E.J. Jumper, "Far-Field Optical Degradation due to Near-Field Transmission through a Turbulent Heated Jet," *Applied Optics*, **36** (25), pp. 6441-6452, September 1997.

[8] Duffin, D.A., "Feed-Forward Adaptive-Optic Correction of Aero-Optical Aberrations Caused by a Two-Dimensional Heated Jet," *AIAA Paper 2005-4776*, June 2005.

[9] Chouinard, M. Asghar, A., Kirk, J.F., Siegenthaler, J.P. and Jumper, E.J., "An Experimental Verification of the Weakly-Compressible Model", *AIAA Paper 2002-0352*, Jan 2002.

[10] Ho, C-M, and Huang, L-S., "Subharmonics and vortex merging in mixing layers," *Journal of Fluid Mechanics*, **119**, 1982, pp. 443-473.

[11] Jumper, E.J., and Hugo, R.J., "Quantification of Aero-Optical Phase Distortion Using the Small-Aperture Beam Technique," *AIAA Journal*, **33**(11), 1995, pp. 2151-2157.

[12] Fitzgerald, E. J., *The shear layer compressibility mechanism and its role in creating aero-optical distortions*, Ph.D. Dissertation, Department of Aerospace and Mechanical Engineering, Univ. of Notre Dame, Notre Dame, IN, 2000.

[13] Brown, G. L. and Roshko, A., "On density effects and large structure in turbulent mixing Layers," *Journal of Fluid Mechanics* **64**(4), pp. 775-816, 1974.

[14] Brown, G. L., "The entrainment and large structure in turbulent mixing layers," In *Fifth Australian Conf. on Hydraulics and Fluid Mechanics*, Christchurch, New Zealand, pp. 352-359, 1974.

[15] Dimotakis, P. E., "Two-Dimensional Shear Layer Entrainment", *AIAA Journal*, Vol. 24, No. 11, 1986, pp. 1791-1796.

[16] Nightingale, A. et. al, "Regularizing Shear Layer for Adaptive Optics Control Application," *AIAA Paper 2005-4774*, Toronto, June, 2005.

[17] Monkewitz, P. A. and Huerre, P., "The influence of the velocity ratio on the spatial instability of mixing layers," *Journal: Physics of Fluids*, **25**, 1982, pp. 1137-1143.

[18] Oster, D. and Wygnanski, I., "The Forced Mixing Layer between Parallel Streams," *Journal of Fluid Mechanics*, **123**, 1982, pp. 91-130.

[19] Freund, J.B. and Wei, M.," Some Small Changes that Make a Mixing Layer Very Quiet", *AIAA Paper 2005-0997*, Reno, Jan 2005.

[20] Ho, C-M, and Huerre, P., "Perturbed Free Shear Layers," *Annual Reviews of Fluid Mechanics*, **16**, 1984, pp. 365-424.

[21] Nightingale, A. et. al., "Adaptive-Optic Correction of a Regularized Weakly-Compressible Shear Layer," *AIAA Paper 2006-3072* , June, 2006.

[22] Gordeyev, S., Jumper, E.J., Ng, T., and Cain, A., "Aero-Optical Characteristics of Compressible, Subsonic Turbulent Boundary Layer," *AIAA Paper 2003-3606*, Jun 2003.

[23] Ziemer, R.E. and Peterson R.L., *Digital Communications and Spread Spectrum Systems*, MacMillan Publishing Co., New York New York, 1985.

[24] Abramovitch, D., "Phase-Locked Loops: A Control Centric Tutorial," *Proceedings of the American Control Conference*, **1**, 2002, pp. 1-15.

[25] Leland, R. P., "Stochastic Models for Laser Propagation in Atmospheric Turbulence," *Lecture Notes in Control and Information Sciences*, **133**, 1989, pp. 4-6.

[26] Greenwood, D., "Bandwidth specification for adaptive optics systems," *Optical Society of America Journal*, **67**, No. 3, 1977, pp. 390-393.

[27] Duffin, D. A., *Feedforward Adaptive-Optic Correction of a Weakly-Compressible High Subsonic Shear Layer*, Ph.D. Dissertation, Dept. of Aerospace and Mechanical Engineering, Univ. of Notre Dame, Notre Dame, IN, 2008.

[28] Zhou, K., and Doyle, J., *Essentials of Robust Control*, Prentice-Hall, 1998.

[29] Melsa, J., and Schultz, D., *Linear Control Systems*, McGraw-Hill Inc., 1969.

[30] Hugo, R. J., Jumper, E. J., Havener, G., and Stepanek, S. A., "Time-Resolved Wavefront Measurements through a Compressible Free Shear Layer," *AIAA Journal*, **35** (4), April 1997, pp. 671-677.

[31] Fitzgerald, E. J., and Jumper, E. J., "Aperture Effects on the Aero-Optical Distortions Produced by a Compressible Shear Layer," *AIAA Journal*, **40** (20), February 2002, pp. 267-275.

[32] Davidson, P. A., *Turbulence: An Introduction for Scientists and Engineers*, Oxford University Press, 2004.

[33] Papamoschou, D. and Roshko, A., "The Compressible Turbulent Shear Layer: an Experimental Study", *Journal of Fluid Mechanics*, **197**, 1988, pp. 453-477.

[34] Elliott, G. S., Samimy, M., and Arnette, S. A., "The Characteristics and Evolution of Large-Scale Structures in Compressible Mixing Layers", *Physics of Fluids*, **7** (4), April 1995, pp. 864-876.

[35] Thurow, B. Samimy, M., and Lempert, W., "Compressibility Effects on Turbulence Structures of Axisymmetric Mixing Layers", *Physics of Fluids*, **15** (6), June 2003, pp. 1755-1765.

[36] Winant, C. D., and Browand, F. K., "Vortex Pairing: the Mechanism of Turbulent Mixing Layer Growth at Moderate Reynolds Number", *Journal of Fluid Mechanics*, **63**, 1974, pp. 237-255.

[37] Huang, L. S., and Ho, C. M., "Small-Scale Transition in Plane Mixing Layer", *Journal of Fluid Mechanics*, **220**, 1990, pp. 475-500.

[38] Bernal, L. P., and Roshko, A., "Streamwise Vortex Structure in Plane Mixing Layer", *Journal of Fluid Mechanics*, **170**, 1986, pp. 499-525.

[39] Rennie, R. M., Siegenthaler, J. P., and Jumper, E. J., "Forcing of a Two-Dimensional, Weakly-Compressible Subsonic Free Shear Layer", *AIAA Paper 2006-0561*, Reno, Jan. 2006.

[40] Mahajan, V. N., Optical Imaging and Aberrations, Part II. Wave Diffraction Optics, SPIE Press Monograph Vol. PM103, Washington, 2001.

[41] Rennie, R. M., Duffin, D. A., and Jumper, E. J., "Characterization and Aero-Optic Correction of a Forced Two-Dimensional, Weakly Compressible Shear Layer," *AIAA Journal*, Vol. 46, No. 11, Nov., 2008, pp. 2787-2795.

[42] Dorf, R. C., and Bishop, R. H., Modern Control Systems: Ninth Edition, Prentice Hall, Inc., New Jersey, 2001.

[43] Duffin, D. A., *private communication*, 2007.

[44] Thomas, F.O., "Structure of Mixing Layers and Jets", *Applied Mech. Review*, Vol. 44, No. 3, March 1991, pp. 119-153.

[45] de Zhou, M. and Wygnanski, I., "The Response of a Mixing Layer Formed between Parallel Streams to a Concomitant Excitation at Two Frequencies," *Journal of Fluid Mechanics*, Vol. 441, 2001, pp. 139-168.

[46] Tyndall, J., *Sound: A Course of Lectures Delivered at the Royal Institute of Great Britain*, New York: D. Appleton and Co., 1867.

[47] Le Conte, J., "On the Influence of Musical Sounds on the Flame of a Jet of Coal-Gas," *Philosophical Magazine*, Vol. 15, 1858, pp. 235-239.

[48] Hugo, R. J., and Jumper, E. J., "Applicability of the Aero-Optic Linking Equation to a Highly Coherent, Transitional Shear Layer," *Applied Optics*, Vol. 39, no. 24, 2000, pp. 4392-4401.

[49] Nightingale, A. M., Gordeyev, S., Jumper, E. J., "Optical Characterization of a Simulated Weakly-Compressible Shear Layer: Unforced and Forced", *AIAA Journal*, Vol. 47, No. 10, October 2009, pp. 2298-2305.

[50] Gordeyev, S. V. and Thomas, F. O., "Temporal Subharmonic Amplitude and Phase Behavior in a Jet Shear Layer: Wavelet Analysis and Hamiltonian Formulation," *Journal of Fluid Mechanics*, Vol. 394, 1999, pp. 205-240.